A
PhD Thesis
titled

Soy flour based N-doped porous carbons for industrial waste water treatment

Submitted in the partial fulfillment of the requirement
for the award of degree
of
Doctor of Philosophy (Ph.D.)
under the guidance
of

Dr. Loveleen K. Brar
Assistant Professor, SPMS,
&
Dr. O. P. Pandey
Senior Professor, SPMS,
TIET, Patiala
by
Raveena
(Reg. no.: 901712004)

School of Physics and Materials Science
Thapar Institute of Engineering and Technology
(Deemed to be University)
Patiala-147004
September 2022

DECLARATION

I hereby certify that the work presented in thesis ***'Soy flour based N-doped porous carbons for industrial waste water treatment'*** as the partial fulfilment of the requirement for award of the degree of **DOCTOR OF PHILOSOPHY (Ph.D.)** in School of Physics and Materials Science, Thapar Institute of Engineering and Technology, Patiala is an authentic record of my own work carried out under the supervision of **Dr. Loveleen Kaur Brar** and **Dr. O.P. Pandey**. The matter embodied in this thesis has not been submitted in part or full to any other institute/university for the award of any degree.

Raveena
(Reg. no.: 901712004)

This is to certify that the above statement made by the candidate is true to the best of my knowledge.

Dr. Loveleen Kaur Brar
(Assistant Professor)
School of Physics and Materials Science
Thapar Institute of Engineering and Technology
Patiala (Punjab)-147004

Dr. O.P. Pandey
(Senior Professor)
School of Physics and Materials Science
Thapar Institute of Engineering and Technology
Patiala (Punjab)-147004

ACKNOWLEDGMENT

This thesis would not have been possible without the support of many people. It is my pleasure to express my deep sense of thanks to several individuals who journeyed with me and helped me to reach my destination. My first and foremost offering of thanks goes to my supervisors **Dr. Loveleen Kaur Brar** and **Dr. O.P. Pandey** for their excellent guidance, constant encouragement, valuable suggestions, blessings, extreme care and providing me with an excellent atmosphere for academic and personal growth. Furthermore, I would like to thank **Dr. Bhaskar Chandra Mohanty**, **Dr. Bhupendra N. Chudasama** and **Dr. Amjad Ali** for being part of my thesis committee, as well as for all the fruitful discussions. I also like to express my thanks to Head SPMS **Dr. Kulvir singh** for his continuous support and encouragement. I would like to thank **Dr. Aayush Gupta** for making me comfortable in the new techniques related to my work. The new techniques and fields to which I was introduced helped me a lot to master the analysis of the work done. I would like to acknowledge **SAI labs (TIET)**, **SAIF (Panjab University)**, **ACMS (IIT Kanpur)**, **AIRF (JNU)**, **IIC (IIT Roorkee)**, **Materials Characterization Facility (TIET)**, **Department of chemistry, IIT Madras** and **Dr. Soumen Basu** (SCBC-TIET) for performing various characterizations during this work. I thank my friends **Amanpreet Kaur**, **Kaveri**, **Aashima Mahajan**, **Jaskiran Kaur**, **Trisha Walia**, **Dr. Manju Rawat**, **Kaushlendra Pandey**, **Dr. Santhosh Mahadevan**, **Pradeep Kumar**, **Shubham**, **Sachin Jaidka**, **Yashpreet Kaur**, **Dr. Amandeep**, **Dr. Indu Gupta**, **Dr. Gaurav Sharma**, **Dr. Piyush Sharma**, **Dr. Shagun**, **Renuka**, **Sonika**, **Sakshi** and all other friends for their great support throughout the tough times, for being so positive, supportive and helpful. I would like to thank my seniors and all current labmates (PhD and M.Sc. students) at Hybrid Materials Lab and Functional Materials Lab. The encouraging and helpful atmosphere made my time in the lab a very interesting learning experience. I really cannot find words which can express my love, regard and thanks to my parents **Mr. Vijay Kumar** and **Mrs. Kavita Devi**, My grandparents **Mr. Gopi Ram** and **Mrs. Jhoomar Devi**, brother **Vipin** and sister-in-law **Kiran** for standing by me in this long journey. I would like to acknowledge my parents-in-law **Mr. Hetram Saharan** and **Mrs. Durga Devi** for their continuous support and love. I thank my loving husband **Mr. Suresh Kumar** for his love, care, and support and for making me feel comfortable and happy during important stages of this work. Above all, I am thankful to ***Almighty*** for giving me the good health and well-being needed to finish this thesis.

Raveena

CONTENT

LIST OF PUBLICATIONS

Ph.D. work publications:

1. **Raveena Choudhary**, O.P. Pandey, Loveleen K. Brar, *Influence of thermal treatment atmosphere on N-doped carbon spheres for wastewater treatment and supercapacitor applications*, *Materials chemistry and physics*, 284 (2022) 126037. https://doi.org/10.1016/j.matchemphys.2022.126037. (IF- 4.77)
2. **Raveena Choudhary**, O.P. Pandey, Loveleen K. Brar, *High yield glucose assisted carbonization of soy flour for dye removal applications*, *Materials chemistry and physics*, 260 (2021) 124174. https://doi.org/10.1016/j.matchemphys.2020.124174. (IF- 4.77)
3. **Raveena Choudhary**, O.P. Pandey, Loveleen K. Brar, Soy flour based biochars for enhanced removal of anionic and cationic dyes, *Biomass conversion and biorefinery* (2022) https://doi.org/10.1007/s13399-022-03371-7 (IF- 4.05)
4. **Raveena Choudhary**, O.P. Pandey, Loveleen K. Brar, Low temperature chemical activation of soy flour based N-doped carbons for adsorption of emerging pollutants, **(communicated)**

Other publications:

1. **Raveena Choudhary**, O.P. Pandey, Loveleen K. Brar, Novel ultrasonic pretreatment for HTC carbon nanosphere size control without yield compromise, *Journal of nanoparticle research*, 24 (2022) 75 https://doi.org/10.1007/s11051-022-05459-7 (IF- 2.53)
2. Shagun Kainth, **Raveena Choudhary**, Sanjay Upadhyay, Pankaj Bajaj, Piyush Sharma, Loveleen K. Brar, OP Pandey, Non-isothermal solid-state synthesis kinetics of the tetragonal barium titanate, *Journal of Solid State Chemistry*, 312 (2022) 123275, https://doi.org/10.1016/j.jssc.2022.123275 (IF- 3.65)
3. SK Arya, Manmeet K Chhina, **Raveena Choudhary**, Vimi Dua, Kulvir Singh, Growth of different nanocrystalline phases in ZnO–Li2O–B2O3–TiO2–V2O5 glass and their effect on photoluminescence and photocatalytic activity, *Ceramics International*, 48 (2022) 20619, https://doi.org/10.1016/j.ceramint.2022.04.030 (IF- 5.53)
4. Aashima Mahajan, **Raveena Choudhary,** Ashok Kumar, Manmohan Chhibber, Loveleen K. Brar, Facile immobilization of iron on carbon nanospheres using organometallic-complex for supercapacitor applications, *Particulate Science and Technology*, 40 (2021) 382, doi: 10.1080/02726351.2021.1979149 (IF- 2.35)
5. Runia Jana, Aayush Gupta, **Raveena Choudhary**, O.P. Pandey Influence of cationic doping at different sites in NaNbO3 on the photocatalytic degradation of methylene blue dye. *Journal of Sol-Gel Science and Technology*, 96 (2020) 405. https://doi.org/10.1007/s10971-020-05365-1 (IF-2.6)

Scopus publications:

1. **Raveena Choudhary**, Rajni Sharma, Loveleen K. Brar, ***Evolution of zirconyl-stearate Langmuir monolayers and the synthesized ZrO_2 thin films with pH,*** AIP Conference Proceedings (DAE-SSPS-2017)
2. MC Deepika Bhatnagar, Ashok Kumar, **Raveena Chaudhary**, Loveleen K. Brar ***A convenient method to aggregate CNS by tagging with diphenyl ether molecule***, AIP Conference Proceedings (DAE-SSPS-2018)

LIST OF CONFERENCES

1. **Raveena Choudhary,** O.P. Pandey, Loveleen K. Brar **Evolution of DEP removal capabilities of agro-waste soy flour derived N doped carbons with activation route**, 2nd international conference on materials for humanity, NUS, Singapore (**to be held on 19-21st sept. 2022).**
2. **Raveena Choudhary**, Aayush Gupta, O.P. Pandey, Loveleen K. Brar ***Soy flour ash for adsorption of cationic and anionic dyes from aqueous media***, 3rd international conference on Recent Advances in Materials, Manufacturing and Thermal Engineering (RAMMTE-2022), DTU, Delhi, India.
3. **Raveena Choudhary**, O.P. Pandey, Loveleen K. Brar ***High yield Facile hydrothermal CNSs synthesis for efficient cationic dye remova***l, International Conference on Electron Microscopy and Allied Analytical Techniques (EMAAT- 2019), Kufri, Himachal Pradesh, India.
4. **Raveena Choudhary**, Rajni Sharma, Loveleen K. Brar, ***Evolution of zirconyl-stearate Langmuir monolayers and the synthesized ZrO_2 thin films with pH,*** DAE-SSPS-2017, BARC Mumbai, India.

LIST OF FIGURES

Chapter 6

Chapter 7

LIST OF TABLES

Chapter 6

Chapter 7

Chapter 9

PREFACE

With increasing population, the requirement for pure water is increasing day by day. Moreover, to fulfill the demand of society, industrial growth is also essential. These industries also require pure water for developing their products. In turn, they discharge highly polluted water. Water containing pollutants when dumped into water bodies causes harm to aquatic animals and humans. Thus, the treatment of wastewater is the need of the hour. Among the available water treatment techniques, adsorption and photocatalysis are fast, efficient, easy to implement and cost effective. The most crucial factors in the adsorption of contaminants are porosity and surface chemistry. Out of different adsorbents, porous activated carbons are considered as the best for adsorption due to their porosity and surface area. Nitrogen doping in porous carbons has shown the improved adsorption capacity of carbons by increasing their basicity and selectivity. However, to dope nitrogen from green and clean synthesis methods using easily available precursors is a great challenge. Proteins in bio-based materials act as the main source for both nitrogen and carbons. Among different protein-containing agro-waste precursors, soy flour is cheap, abundant and has> 40% of protein content. The hydrothermal carbonization (HTC) approach, which is economical and environment friendly, can be used to synthesize N-doped porous carbons from protein-based precursors. This makes it feasible to clean the environment in two ways. Along the HTC sample, biochar is also considered to be a green alternate for energy and environment applications. In this N doped carbons were synthesized using HTC and pyrolysis method by soy flour as precursor. The entire work is presented in nine chapters which are as follows:

Chapter 1 introduces briefly the problem of wastewater containing dyes, phenols, pharmaceuticals, and phthalate esters wastes along with the discussion about different wastewater treatment methods. The role of adsorption in pollutant removal has been discussed in detail. For N-doped carbons, different synthesis methods, the significance of HTC, and the pyrolysis approach have been explained. The importance of protein-based agro-waste precursors for both carbon and nitrogen source has also been described along with their use in the adsorption of various pollutants.

Chapter 2 describes the details of literature related to wastewater treatment for dyes, phenols, pharmaceutical and phthalate esters wastes using agrowaste synthesized porous activated carbons by adsorption and photodegradation. Different synthesis routes for the synthesis of carbons reported in the literature has been discussed briefly. The role of hydrothermal treatment, pyrolysis method and other methods in the synthesis of N-doped carbons has been

discussed. The importance of protein based precurosrs for the synthesis of N doped carbons has been described in details. Literature available on the use of soy flour as source of N and C to synthesize N doped carbons has been discussed in detail.

Chapter 3 presents the details of precursors, approach for sample synthesis and their characterization. All the characterization techniques used in the current work have been discussed in this chapter. This include electron microscopy, X-ray diffraction, surface area measurement, X-ray photoelectron spectroscopy, UV visible, FTIR, Raman spectroscopy, thermogravimetric analysis, adsorption studies, and photodegradation studies. The fundamental aspects of synthesis/characterizations, as well as the required test conditions, have been described.

Chapter 4 presents the results of the optimized conditions to get high yield of N doped carbons using hydrothermal method (HTC) where glucose as carbon source and protein-rich defatted soy flour as nitrogen and carbon source were used. The synthesized carbons (***GS1***) were found to be spherical in shape and show better adsorption efficiency than both glucose derived HTC spheres and HTC synthesized soy flour hydrochar. To understand the properties of synthesized samples, SEM, TEM, XRD, FTIR, UV-visible spectroscopy, N_2 adsorption-desorption isotherm, XPS were carried out. The molten salt technique was used to determine the point of zero charge (pH_{pzc}) of the samples. The as-synthesized N-doped carbons have been used for the treatment of wastewater containing cationic dyes MB and CV, anionic dye EBT, pharmaceutical waste CIP, phenol PNP and phthalate ester DEP by adsorption. For the best adsorption results, kinetic modeling and isotherm analysis has also been undertaken to determine the adsorption rate and adsorption mechanism.

Chapter 5 reports the N-doped carbon spheres synthesized using glucose and soy flour via the HTC method (***GS1***) and were heat-treated at 900 ºC in Ar and N_2 atmospheres separately to activate/modify the surface without additives. The effect of heating atmospheres on the sample properties has been studied using SEM, XRD, FTIR, UV–Visible, Raman, XPS, BET, and TG-DSC. The difference in surface chemistry was confirmed by XPS and the point of zero charge values of synthesized samples. Variation in results was explained on the basis of the diffusivity and density of the gases used and the corresponding mechanism has been proposed. The role of heat treatment atmosphere has been compared for the adsorption efficiency of synthesized samples for the chosen model pollutants: MB, CV, EBT, PNP, CIP and DEP. The adsorption rate and mechanism have been determined using kinetic model and isotherm analysis based on the best adsorption results.

Chapter 6 describes the chemical activation of N-doped carbon spheres synthesized using glucose and soy flour via the HTC method (***GS1***) explained in chapter 3 using KOH and $ZnCl_2$ in different impregnation ratios, separately. The effect of the chemical activating agent on the sample properties has been studied using FE-SEM, XRD, FTIR, UV–Visible, Raman, XPS, and BET. The difference in surface area and surface chemistry with impregnation ration as well as with activating agent was confirmed by BET, XPS and pH_{pzc} of samples. Variation in the results was explained on the basis of the reactivity of activating agents with the sample at low temperature and the corresponding activation mechanism has been proposed. The adsorption efficiency of the synthesized samples was carried out for cationic dyes MB and CV, anionic dye EBT, pharmaceutical waste ciprofloxacin, PNP and phthalate easter DEP. Based on the best adsorption data, the adsorption rate and the corresponding mechanism were determined using kinetic model and isotherm analysis.

Chapter 7 describes single-step synthesis of biochar by pyrolysis of defatted soy flour in argon atmospheres at various temperatures: 450, 650, and 750 ^{o}C. The pyrolysis temperatures were determined by TG/DTG/DTA analysis. The pyrolyzed sample was treated with HNO_3 for complete demineralization. Further, the variation in the samples characteristics with pyrolysis temperature and acid treatment was explained by FE-SEM, XRD, FTIR, UV-visible, FTIR, Raman, BET and XRD results. pH_{pzc} of the samples were also determined using the molten salt method. The synthesized samples were used for the adsorption of pollutants *viz* MB, CV, EBT, PNP, CIP, and DEP. The adsorption rate and mechanism were calculated using kinetic model and isotherm analysis based on the best adsorption data as done in the previous chapters.

Chapter 8 presents the the photo-induced activity studies for the samples which had the best adsorption chracteristics as observed and discussed in the previous chapters. These studies were done under UV irradiation and sunlight. The % decolorization efficiency of the chosen samples was tested for the pollutants viz. MB, EBT, PNP, CIP, and DEP. To determine the mechanism for decolorization enhancement, scavenger tests were carried out and explained with the help of valence band spectra and bandgap of the samples.

Chapter 9 summarizes the work done presented in this thesis. It also discusses the scope for future work.

Chapter 1
Introduction

Overview

The large quantities of pollutants such as pesticides, pharmaceutical wastes, phenolic compounds, dyes, and other chemicals that are discharged into water resources are cause of major concern. These make ground water toxic and are an important cause of concern for living organisms. To treat wastewater, numerous techniques have been developed. Among these, adsorption is considered as one of the most efficient, easy to implement, cost-effective, and environment-friendly. N doped activated carbons synthesized using protein-based agro-waste can be used as green adsorbents for a multitude of pollutants.

In this chapter, the problem of wastewater has been introduced along with a brief discussion about different wastewater treatment methods. The role of adsorption in pollutant removal has been discussed in detail. For N-doped carbons, different synthesis methods; the significance of HTC, and the pyrolysis approach have been explained. The importance of protein-based agro-waste precursors as both carbon and nitrogen source have also been described along with the applications of synthesized adsorbents in pollutant removal.

1.1 Background

Out of total water content available on the planet, only ~2.5 % is freshwater. From this freshwater content, only 0.007 % is accessible for the population of 6.8 billion people [1]. In the past 100 years due to the rapid growth of the world's population, the requirement of fresh and potable water has increased. According to a recent report from *United Nations*, 2.3 billion inhabitants are living in water-stressed countries, with 733 million people living in high and critically water-stressed countries [2]. A recent report from *UNICEF* stated that 1.42 billion people live in areas of high or extremely high water insecurity zone, including 450 million children [3]. Globally, 1.5 million children under the age of five die as a result of water-related diseases in a year. In India, 4,00,000 people die each year due to the consumption of untreated water as reported by the *World Economic Forum* [4]. Population growth has resulted in a large scale proliferation of various industries such as paper and pulp industries, dyeing of cloths, textiles, printing, food products, pesticides, pharmaceuticals, petrochemicals, etc. The wastewater from these industries is released as effluent and contains the used dyes, phenols, heavy metals, pharmaceuticals wastes etc. [5–13]. The pollutants dumped into water bodies cause harm to aquatic animals and humans by degrading the amount of dissolved oxygen in the water. These pollutants also result in hormonal disruptions, nervous system disorders and are carcinogenic in nature [14]. The river Ganga, which runs for 2601 km, is one of the most polluted rivers in the world, according to the Central Pollution Control Board (CPCB) of India [15].

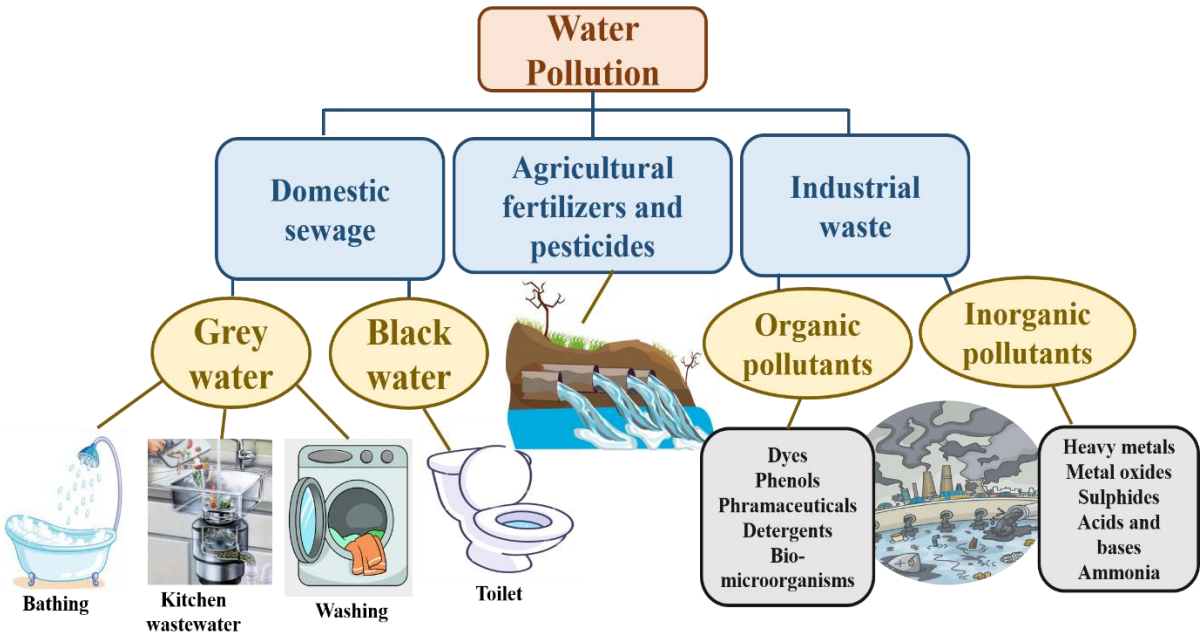

Fig. 1.1: Major sources of emerging water pollutants.

The effluents from textile, paper, rubber, jute and chemical industries contribute to Ganga River pollution as a result of untreated or partially treated trash dumping. Industrial waste accounts for approximately 12% of the total volume of effluents entering the river and is a major topic of concern as they are hazardous and non-biodegradable in nature [16]. Every day, nearly 40 million litres of wastewater enters waterways from various sources (Fig. 1.1), with only a small percentage appropriately treated. It is reported that approximately 70% of India's surface water is unsafe for consumption [4]. Thus, the treatment of wastewater is the need of the hour.

1.2 Adsorption and photodegradation for wastewater treatment

There are multiple stages involved in cleaning the wastewater *viz* preliminary treatment, primary treatment, secondary treatment, and tertiary treatment (Fig. 1.2). The preliminary, primary and secondary treatments include physical and mechanical treatments to remove the microorganisms and dissolved solids to get clean water. In preliminary treatment method, heavy materials, sand, stones etc. are separated from water by different methods *viz.* screening, grit removal, pre-aeration, flow metering and sampling. After preliminary treatment settleable organic solids are removed by primary treatment via sedimentation and floatation method. Secondary treatment is used to further break down organic matter and remove dissolved and colloidal solids via biological methods (aerobic and anaerobic microorganisms found in abundance in the ambient environment, such as lactic acid bacteria, photosynthetic bacteria, fungi, and a small number of actinomycetes which are environmentally benign). The final and most crucial phase involves an extensive tertiary treatment to clean the secondary treated water and make it suitable for drinking purpose [17,18].

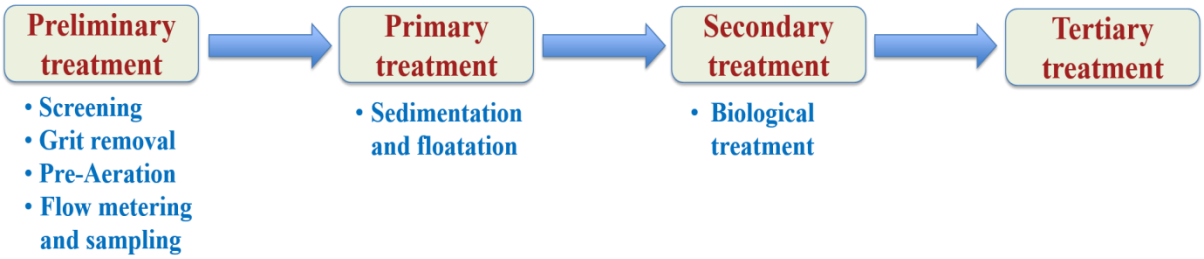

Fig. 1.2: Stages of wastewater treatment methods.

The tertiary treatment methods based on physical, chemical, and biological techniques are available to extract or degrade waste out of wastewater (Fig. 1.3). These techniques involve the processes such as precipitation, reverse osmosis, coagulation and flocculation, adsorption, ozonation, electrochemical techniques and fungal decolonization [19–25]. The conventional purification systems are either ineffective or too expensive for the tertiary treatment of

wastewater. In case of chemical methods, the drawback of chlorination is that it may form trihalomethane toxic disinfection by-product while in case of ozonation, its short life time and high cost makes it least effective method. The physical methods *viz.* reverse osmosis, is expensive and flocculation and filtration are inefficient methods to treat wastewater effectively [26]. In case of biological treatments, the handling of the system becomes very critical and also their dye removal efficiency is very less. Thus an efficient, cheap and easy to handle method for waste water treatment is still required.

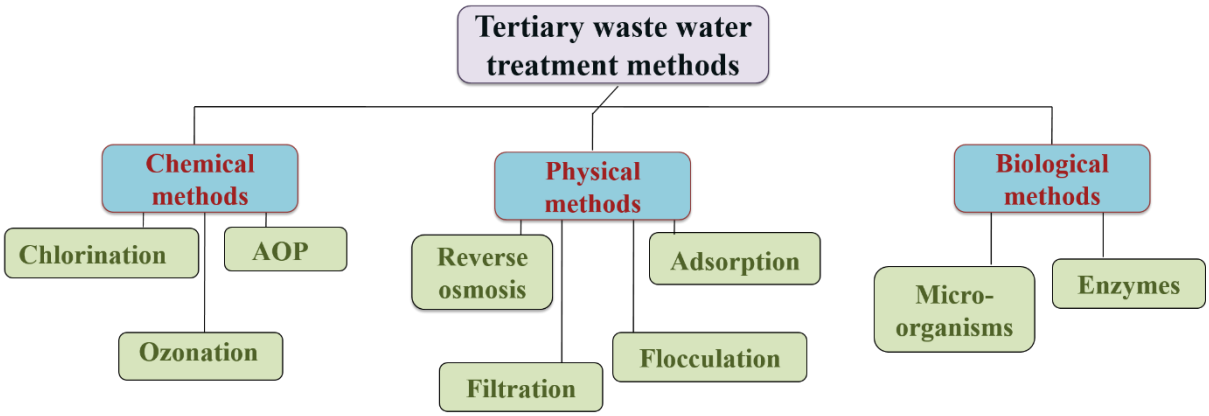

Fig. 1.3: Tertiary wastewater treatment methods.

Adsorption and advanced oxidation process (AOP) are fast, efficient and cost effective techniques in comparison with other techniques and are also able to remove snags such as toxic by-products, high cost and partial removal of pollutants. Adsorption is a surface phenomenon in which a pollutant gets attached to the surface of an adsorbent via physical or chemical bond. This process is called physisorption or chemisorption, respectively [27]. Physical adsorption (physisorption) is caused by attractive intermolecular interactions between molecules of the solid adsorbent and the material to be adsorbed, which is a reversible phenomenon. Chemisorption is the outcome of a chemical reaction between the solid adsorbent and the adsorbate (substance to be adsorbed) to form strong chemical bond. In certain adsorbents both processes can occur at the same time or alternatively, dependent on the favourable conditions. The pollutant can also enter the appropriate sized pores on the adsorbent surface and get adsorbed (Fig. 1.4).

Adsorbate migration onto/into the solid adsorbent occurs in multiple stages: (1) Migration of the adsorbate from the bulk fluid phase to a thin volume surrounding the particle/solid and further diffuse through this boundary layer. This step is called film diffusion or boundary layer diffusion; (2) Mass transfer of the adsorbate onto the particle surface as well as recepient pores via intraparticle diffusion process. (3) Interaction with the adsorbate surface

sites, either by physical or chemical mechanisms. These mechanisms are in general reversible so the adsorption and desorption of the adsorbate species onto and from the active sites takes place continuously. The rate of all of these processes is determined by the properties of the adsorbate, adsorbent, and their matrix. Adsorption isotherms are used to calculate the maximum adsorption capacity for the given adsorbent [28]. There are numerous parameters which affect the adsorption capacity of the adsorbents. An increase in adsorbent porosity results in more surface area being available for the adsorption [29]. Also it is important that size of pores (diameter) should be greater than average molecular size of the pollutant for efficient adsorption inside the pores. Other parameters that affect the process of adsorption are the pH of solution, type of adsorbate and adsorbent, concentration of adsorbent and adsorbate, temperature of adsorbate, adsorption time etc. [30]. Along with the surface porosity, surface chemical groups are also key parameters for adsorption process and affect the acidic or basic nature of adsorbent, interaction with certain specific compounds and improves their hydrophilicity [31,32].

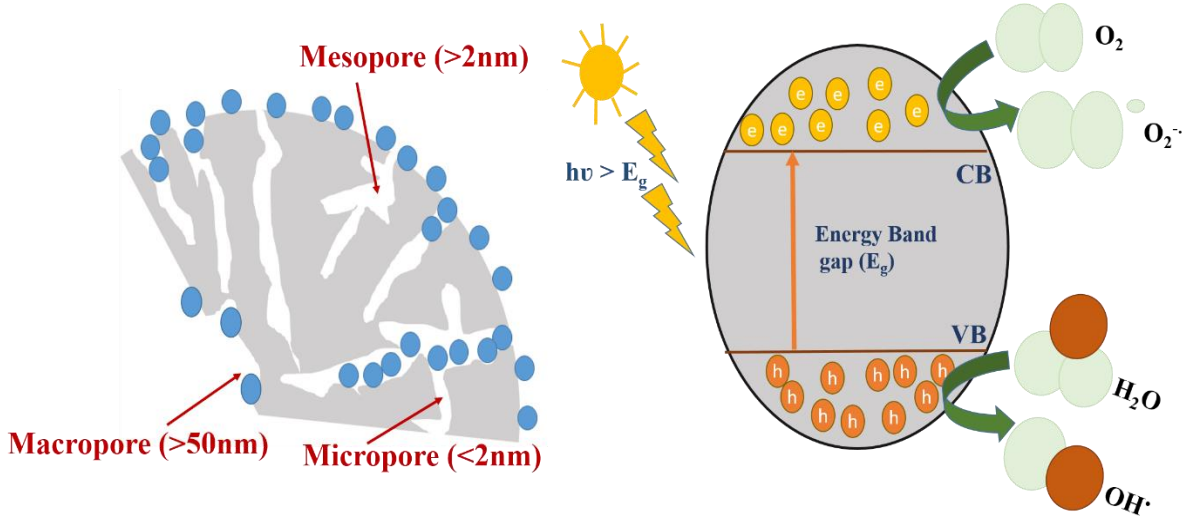

Fig. 1.4: Adsorption and photodegradation mechanism of pollutants.

In AOP's the pollutant adsorbed onto the surface of catalyst undergoes degradation by light irradiation with energy > band gap of catalyst. Semiconductor photo degradation is a green approach and most efficient process among all other AOPs. In this process, external and expensive oxidants are not required. Due to irradiation of light, light photons falling on the surface of sample generates electron-hole pair. The initially generated electron hole pair come across certain reactions with water and oxygen and generates highly reactive radicals (OH^- and O_2^-) which further oxidize the adsorbed pollutants on the surface of catalyst to form CO_2 and minerals (Fig. 1.4) [27].

1.3 N doped carbons for wastewater treatment

For wastewater treatment, adsorption method relies on a variety of materials as adsorbents. Generally used adsorbents are silica gel, agro wastes (sawdust, bark), activated carbons, chitosan, zeolites, clay minerals (bentonite, kaolinite, diatomite,), industrial wastes (fly ash, red mud, sludge) etc. [33–39]. Table 1.1 lists the advantages and disadvantages of most commonly used adsorbents.

Table 1.1: Advantages and disadvantages of different adsorbents.

Adsorbent	Advantages	Disadvantages	Ref.
Silica gel	It involves ion-exchange mechanism, very common adsorbent, found mainly in granular form	High-cost adsorbent, Less abundant	[40]
Chitosan	Abundant, renewable, biodegradable, and eco-friendly material	Non porous, high cost, low adsorption efficiency	[40]
Clay minerals	Low cost, abundant and natural adsorbent	Not effective for all pollutants Chemical modification or activation is required	[41]
Zeolites	Easily available and relatively cheap	adsorption properties depend on the different materials (type of zeolite)	[40]
Agro wastes	Cheap, abundant and fungi in agro waste lowers the contaminate concentrations to ppb level	Low adsorption efficiency and porosity	[41]
Industrial wastes	Low-cost materials and local availability	Adsorption properties strongly depend on the different materials, hazardous nature	[41]
Activated carbons	Most effective adsorbents in industry, cost effective, porous, versatile material, easy to prepare, environment friendly	Initial cost of the carbon precursor	[40]

Activated carbon has been found to be most efficient among other adsorbents in every aspect *viz.* low cost, abundance, environment friendly, easy preparation, porosity and high surface area etc. Also, these can adsorb diverse categories of pollutants from aqueous solution. Many reports are available on the adsorptive removal of major industrial pollutants *viz.* cationic dyes, anionic dyes, pharmaceutical wastes, plasticizers, pesticides, phenols and heavy metals by activated carbons [42–46]. Activated carbon, is a type of carbon that has been processed by chemical/physical treatment to have broad size range of pores that increase the available surface area for adsorption/chemical reactions. Immense amount of literature is available about the activation of carbons for increased surface area and thus their activity. Johann Lowitz, a Russian chemist, discovered the initial decoloration characteristics of charcoal in liquid in 1776. The activated charcoal water filters are still popular today. Carbon activation for the purpose of adsorption was first attempted in the early 1800s. Since then, significant work has

been done in tailoring the carbon surface to improve its properties and activity. Other than chemical and physical activations, the activity of carbon can also be improved by making composites, changing morphologies, doping, varying precursors, synthesis methods, synthesis conditions, etc.

The role of activated carbons in the photodegradation of contaminants in aqueous solutions has not been investigated thoroughly. Vast amount of literature is available for the synthesis of metal organic frameworks (MOFs) i.e. composite of activated carbon with any metallic oxide (ZnO, TiO_2 etc.) to enhance the photo degradation efficiency for water pollutants [47,48]. Only a few reports are available on the use of porous activated carbons for photodegradation of pollutants and the activated carbons synthesized using NaOH and H_3PO_4 or gamma radiation [49–51]. Apart from activated carbons, different carbon allotropes such as graphene, CNTs, carbon spheres also find applications in treatment of waste water both by photodegradation or adsorption mechanism due to their good electrical conductivity, high surface area and porosity. Moreover, nano regime of these materials leads to enhancement of the concentration of dangling bonds on the surface which enables them to be used in adsorption and photodegradation reactions [52–54].

1.3.1. Why N doped carbon-based adsorbents?

Nitrogen doping in the porous carbon materials have received a lot of interest in recent years because of their exceptional qualities such as superior electrical conductivity, enhanced hydrophilic characteristics, increased surface wettability, and ease of functionalization. Nitrogen atoms are more electronegative than carbon, resulting in charge delocalization in the carbon matrix. This results in more surface sites available for the adsorption [55]. The carbon atom close to the nitrogen atom will have a greater positive charge density due to relatively higher electron affinity of the nitrogen atom. This results in the good electrochemical and adsorption capabilities of N-doped activated carbons [56]. Due to the close size vicinity of the C and N atoms, N-doped porous carbon form active catalytic sites by the redistribution of atomic charge density or spin densities caused by the existence of N in the structure [57]. Furthermore, nitrogen doping has the potential to change carbon's electronic and crystalline structure which leads to an improvement in their chemical stability, surface polarity, and electron-donor characteristics [58]. Nitrogen doping in porous carbon adsorbents results in enhancement of their basic character with doping site acting as a Lewis basic site. This leads to enhancement in their adsorption capacity as well as the selectivity for certain specific materials [59,60]. N-doped carbons have recently gained popularity due to their superior

ability to adsorb dyes in the aqueous solution. Lian *et al.* [61] reported that for N-doped biochar synthesized by direct annealing of crop straws in NH_3, its dye adsorption capability enhanced by more than 15 times over the undoped biochar [62]. Sanchez *et al.* [63] reported that there is an enhancement in adsorption capacity of cationic and anionic dye by significant amount. N doping improves the adsorption capacity of carbons but it is still a challenge to dope nitrogen by green and clean method using natural precursors.

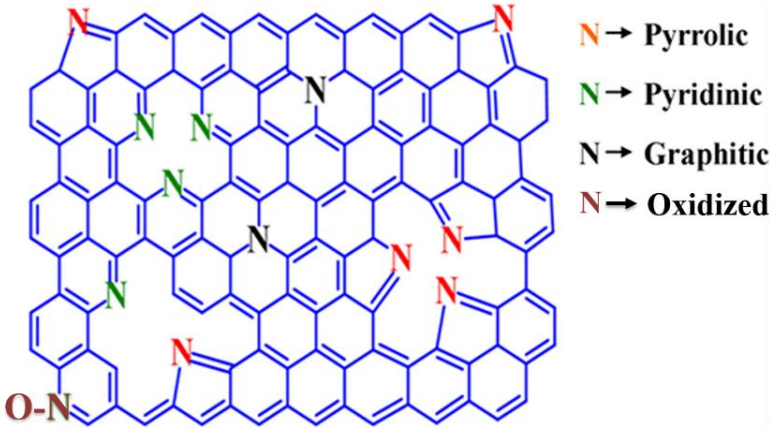

Fig. 1.5: Types of nitrogen functionalities in the carbons.

Fig. 1.5 shows the different types of N functionalities which exist in N doped carbons. These N-doped species are of four types *viz.* pyrrolic-N (edge nitrogen in five membered ring), pyridinic-N (edge nitrogen in six-membered ring), graphitic-N (present in bulk inbetween six membered three rings) and oxidized-N (edge oxidized nitrogen in six-membered ring). The individual N functionalities play important role in the adsorption process and surface chemistry of the sample. The presence of pyrrolic-N (NH functional group) functionality improves the CO_2 adsorption on the surface of N doped carbon by interaction with N and H atoms functional groups [64]. The availability of pyrrolic-N and graphitic-N in the carbons skeleton improves the wettability, resulting in increased dyes adsorption onto carbon surfaces via H-bonding and Van der Waals interactions [65]. Ko *et al.* [66] reported that pyrrolic monomer improves the Cr adsorption capability by reduction of hexavalent Cr ion to trivalent Cr ion. The pyridinic N, on the other hand contains high electron density and acts more basic than pyrollic-N. At high temeperature heating (above 500 °C), pyrrolic-N transforms to form pyridinic-N. The pyridinic N combines with two adjacent sp^2 hybridised carbon atoms at the edge of the carbons, and it can give one p electron to the π system, allowing the pyridinic N's lonely pair electron to be unconfined. As a result, pyridinic N can improve the hydrophilicity of N doped carbons and boost the adsorption process. Reports are available on the role of pyridinic-N showing an enhanced adsorption of P-nitrophenol, P-chlorophenol, pharamaceutical compounds and

CO_2 [66–69]. Pyrrolic and pyridinic-N being basic and hydrophilic in nature, adsorb acidic pollutants (CO_2, various dyes, phthalates, phenols etc.) better.

With heating of N doped carbons above 800 °C , most of pyrrole and pyridine-N converts to form graphitic-N making it most stable N species. Graphitic-N is reported to be best for the adsorption of metal ions among other N species. The lone electron pair in graphitic N atoms may give additional adsorption sites for heavy metals to adsorb. Also, It makes the carbon surface more hydrophilic and tend to make better contact between metal ions and adsorbent. The positive surface charge of graphitic-N makes it a suitable adsorbent for anionic pollutants [60]. The oxidized nitrogen is induced on the surface due to chemisorbed oxygen by the pyridinic-N while heating. It is also a stable species than pyrrole and pyridinic-N [70]. Balog *et al.* [71] reported that the adsorption of Ni(II) on the oxidized-N site of N- CNTs takes place via ion exchange with the release of H^+ ions. The role of oxidized-N in the adsorption is not much studied. This is because it is a neutral site and enhancemed of adsorption capacity was found to be insignificant in several reports [72,73].

In order to synthesise N-doped carbon via eco friendly methods for wastewater treatment, waste resources that are green and inexpensive must be used. This helps to clean the environment in two ways. Abundant agrowastes with insignificant economic value can be used as potential raw material for the synthesis of N doped carbon i.e. to convert waste to value added products.

1.4 Synthesis methods and precursors for N doped carbons

1.4.1 Synthesis methods: Substitutional doping of nitrogen to numerous carbon materials, including graphene, biochar, CNTs, carbon nanofibers, fullerenes, and carbon spheres, has been done in the past three decades for various environmental applications. The spherically shaped carbon materials have a long history of investigation and the spherical shape is acquired by materials during synthesis via nucleation and growth of graphene flakes. Among other N doped carbons, spherical carbons have piqued the interest of researchers due to their uniform size, large surface area, and physicochemical features.

Multiple methods are in use for the synthesis of N doped carbon spheres *viz.* arc discharge [74], chemical vapor deposition (CVD) [75], sol-gel [76], pyrolysis [77], solvothermal [78], hydrothermal carbonization (HTC) [79] etc. For the arc discharge method, low yield of carbon spheres are obtained, while CVD, sol-gel and pyrolysis routes require high temperature and inert atmosphere. These methods also require specialized equipment which are cost intensive and are also not eco-friendly due to use of harsh chemicals. Except for the

solvent employed in the reaction, the solvothermal and HTC techniques are very similar. Organic solvents such as ethanol, acetone, etc. are utilised as solvents in the solvothermal approach, whereas water is used as a solvent in the HTC method. Both methods entail the synthesis of sample in a closed autoclave at high pressure and low temperature (150-250 °C), with the solvothermal technique requiring higher temperatures than the HTC method.

Among all these methods, the HTC method is found to be most suitable because it is a low temperature, inexpensive and green process. It is a wet method which also possesses the potential of converting waste (bio/agro) into value enriched products. In this method, the size of the particles, yield and surface area can be tailored easily by changing the precursor concentration, temperature or by adding templates etc. Hydrothermal carbonization of biomass containing lignin, hemicellulose, and cellulose leads to formation of HTC sample via hydrolysis, dehydration, polymerization and aromatization followed by interamolecular condensation to form aromatic carbon network below 200 °C [80]. For HTC sample to be of spherical shape, it is needed that precursors contain ring structure to avail nucleation sites [81]. Most of the agrowastes consists of long organic polymeric chains and thus require an additional precursor such as saccharides, graphene oxide etc. for assistance to avail nucleation sites.

1.4.2 Precursors for N doped carbon spheres: Waste biomasses have attracted increased attention due to their abundance, ease of availability and carbon neutrality. There is a need to develop efficient materials using waste biomass for energy and environment applications. Therefore, it becomes necessity in today's world to treat and convert biomasses into sustainable energy sources and usable commodities. For N doped carbon sphere synthesized via HTC method, nitrogen doping is usually done by using melamine [82], ammonia [83], ethylene diamine [84], thiourea [85] etc. Some studies based on bio-based precursors such as hair [86], cocoon silk [87], egg [88] etc. are also available in literature. But these in general have low yield and result in formation of N-carbon nanospheres of very small size which are difficult to handle.

1.4.3 Protein based biomass precursors: Protein-based biomasses have gained the interest of the research community as a source of both carbon and nitrogen. In HTC treatment, the Millard reactions between cellulose/hemicellulose and protein or their derivatives can considerably increase the retention of nitrogen in sample, resulting in high yield with enriched N-containing functional groups [89]. The direct carbonization of protein leads to the formation of N doped carbons by retaining high content of oxygen as well as nitrogen compared to HTC sample. Ma *et al.* [90] compared HTC of egg and egg mixed with graphene oxide and concluded that

carbonization occurred with graphene oxide mixed egg as GO acts as a catalyst for carbonization to occur and template for self-assembled carbons as discussed above. Alatalo *et al.* [91] reported the use of soy protein as nitrogen and carbon assisted by H_2SO_4 and glucose for HTC to give self-assembled N doped graphitic structure. Falco *et al.* [92] reported the synthesis of N doped spherical carbons using microalgae supported by glucose. In a study by Ren *et al.* [93], only microalgae was used to synthesize N doped carbons via HTC method and no spherical morphology was observed in resulting sample.

Table 1.2: % amount of protein present in the different biomasses and their price per kg.

Biomass	Egg	Microalgae	Hairs	Prawn shells	Silkworm cocoon	Milk powder	Corn stalk
% Protein	47	43-50	90	22	7 (extractable)	26	6
Min. Price (Rs/Kg)	100	50	800	400	750	500	120
Biomass	Chicken bone	Sunflower meal	Fish scale	Mung bean	Cottonseed meal	Wheat flour	Soy flour
% Protein	19	37	21	24	43	36	47
Min. Price (Rs/Kg)	150	50	150	60	32	35	39

1.4.4 Soy flour as precursor: There are a variety of protein containing biomasses available for the synthesis of N doped carbons (Table 1.2). The protein content of some important biomasses is given in Table 1.2. The amount of protein in biomass is directly related to amount of nitrogen doped in the synthesized carbons. It is evident from Table 1.2 that eggs, microalgae, hairs, cottonseed meal and soy flour contain a good amount of protein (>40%). Hairs, microalgae and eggs need pretreatment such as heating, drying and grinding before HTC. The cottonseed meal is available in dry state but is less abundant than soy flour. Soy flour is a byproduct of soybean oil extraction, with global production currently exceeding one hundred million tons. Because of its high protein content, this soybean meal has traditionally been utilised in animal feed. In India, the production of cottonseed meal and soy meal were 4.5 and 8.1 million tons, respectively, in the year 2021. Therefore, among these biomasses, soy flour is considered to be the best for N doping as soy flour is easily available and also easy to handle as it is already available in a powdered and dry state. The cost of soy flour is also very low among other protein containing biomasses (Table 1.2). Reports are available in literature showing the conversion of soy flour to form potential N doped carbons. The synthesis methods includes high temperature carbonization with chemical/physical activation [94–99]. Only a

few reports are available in which soy flour was converted to N doped carbons using a "green" approach like hydrothermal carbonization [91,100].

1.5 N doped biochar by pyrolysis of agrowaste

Alongwith the HTC sample, biochar is also considered to be a green alternate for energy and environment applications. Protein based biomasses have been found to produce the most effective biochars. Pyrolysis of protein-rich biomass leads to the formation of nitrogen (N) containing biochar. Biochar is generally synthesized by the carbonization of biomass at high temperature (400-900 °C) in an inert atmosphere. The properties of biochar completely depends upon the type of biomass and its constituents.

Protein based biomass have been found to produce the most effective biochars. Pyrolysis of protein-rich biomass leads to the formation of N containing biochar. The content and functionalities of nitrogen in biochar depend upon the type of biomass and pyrolysis temperature [101]. Different types of feedstocks show thermal stability at different temperatures. The temperature for the pyrolysis of biomass can be determined from the thermal analysis of biomass [100]. The presence of N functionalities in the biochar plays an important role in adsorption of pollutants from aqueous solutions [63,103]. The electronegativity difference between N and C atoms results in N-doped carbon material providing a significant number of anchoring sites for the adsorption of positively charged ions [104].

1.6 Activation of N-doped carbons

Unless the HTC sample is synthesized in the presence of additives/activating agents, it does not have a high surface area and porosity. To improve the surface area, porosity and activity of the synthesized HTC sample, several post-processing methods are in use including thermal activation, physical activation and chemical activation. The thermal activation is carried out by heating the synthesized HTC sample at high temperature (500-1000 °C) in an inert atmosphere (argon, nitrogen). The thermal treatment of HTC sample leads to the material with enhanced physical-chemical characteristics. It results in changing surface area and porosity, structure, chemical composition for a better adsorption efficiency of the HTC sample. The temperature and atmosphere of thermal treatment plays an important role in the properties of the synthesized materials. Some studies demonstrate the role of treatment temperature on the properties of the HTC sample. However, there have been no systematic research on the characteristics of HTC sample after thermal treatment under different atmospheres. There are

reports available showing that thermally treated HTC sample has been useful as an electrode material in metal ion batteries, supercapacitors, solar cells, and catalytic templates [105].

Physical activation comprises of pyrolysis/HTC of biomass followed by activation of product obtained in steam or carbon dioxide. While chemical activation is activation of biochar/ HTC sample by adding chemical agents (strong acids and bases) such as KOH, $ZnCl_2$, NaOH, H_3PO_4, H_2SO_4, HCl, HNO_3 etc. and heating in an activation kiln at 400-700 °C [106]. Chemical activation is recommended over physical activation because it requires less energy and has better carbon yields and surface areas [107]. Among the several chemical activation agents, $ZnCl_2$ and KOH are the most commonly utilized because they produce high surface area as well as yield [108,109]. The type of the activation agent, the impregnation ratios, activation temperature and time plays a vital role in determining the surface area, pore size, and pore volume. This is because the mechanism of the reaction of biochar/ HTC sample is different for various activating agents [109,110].

Considering all the above aspects, the present work has been undertaken where the role of N doped carbon spheres synthesized from soy flour and modified under different conditions to adsorb different pollutants has been demonstrated in a systematic way.

Chapter 2

Literature Survey

Overview

Present chapter describes the details of the literature related to wastewater treatment for dyes, phenols, pharmaceutical wastes, and phthalate esters using agro-waste synthesized porous activated carbons by adsorption and photodegradation. Various synthesis routes for the synthesis of carbons reported in the literature have been discussed briefly. The role of hydrothermal treatment, pyrolysis method, and other methods in the synthesis of N-doped carbons has been discussed. The role of protein-based agro/bio-based precursors has been described from available literature for N doped carbons synthesis. The use of soy flour as protein containing precursor for both N and C source has been explained thoroughly.

2.1 Introduction

Good water quality is crucial for ecological health, social and economic advancement, and human health. Nearly 80% of wastewater is not treated or recycled before it is released back into the environment leading to destruction of the human health and aquatic life. In the previous chapter, it is discussed that adsorption and AOP are the best tertiary wastewater treatment methods. The adsorption using agro waste precursors to form porous carbons has been considered to be efficient, economic, and eco-friendly via cleaning waste from the environment. Among agro-waste precursors, proteins are considered to be best to form N doped carbons to treat wastewater. On the basis of literature survey, the different synthesis techniques adopted so far and their related results are presented

2.2 Adsorption based wastewater treatment with porous carbons from agro-waste

2.2.1 Adsorption of dyes

Babaei *et al.* [111] in 2016, prepared activated carbon biochar having surface area 245.7 m^2/g using oak wood agro-waste via pyrolysis method in an inert atmosphere at temperatures 450–600 °C. The sample was used for MB adsorption with maximum adsorption capacity of 97.55 mg/g. From the kinetics and isotherm modeling, the adsorption process was found to follow pseudo second order (PSO) kinetics and Langmuir adsorption isotherm.

Charola *et al.* [112] in 2018, utilized empty cotton flower as an agro waste precursor to produce activated carbons. The sample was synthesized by pyrolysis assisted by KOH activation in N_2 atmosphere at 600 °C with surface area 1058 m^2/g and pore volume 0.69 cm^3/g. The activated carbon was used to adsorb reactive orange 84 dye from aqueous solution with a maximum adsorption capacity of 154 mg/g.

Gupta *et al.* [113] in 2019, used bengal gram bean husk agro-waste to synthesize graphene-like porous carbons using pyrolysis method (at 400 °C, N_2 atm.) followed by chemical activation (KOH, 850 °C, N_2 atm.). Synthesized sample possesed high surface area and pore volume (1710 m^2/g, 0.834 cm^3/g). The sample was used to adsorb cationic dye MB and anionic dye MO and exhibited a maximum adsorption capacity of 469 and 418 mg/g, respectively.

Jasper *et al.* [114] in 2019, reported the carbonization of Millettia thonningii seed pods using H_3PO_4, in a muffle furnace at 400 °C for 30 minutes to form activated carbons. The study examined the adsorption kinetics and equilibrium of cationic dyes *viz.* CV and MB adsorption from aqueous media. The adsorption followed the Redlich-Peterson model closely followed by

the Freundlich isotherm model and PSO kinetic model for both dyes. The maximum adsorption capacity for CV and MB were 7.57 mg/g and 14.09 mg/g, respectively.

Zhu *et al.* [115] in 2021, derived the porous magnetic activated carbon using lignin (extracted from cornstalk). The sample was synthesized by making a composite of lignin@Fe_2O_3 via sonication and further carbonization at 400 °C in N_2 atmosphere followed by etching with H_2SO_4. The sample showed the maximum adsorption capacity of 420.40 mg/g for MB dye.

Yagmur *et al.* [116] in 2021, reported the synthesis of magnetic porous carbons by activating the coconut shell with $ZnCl_2$ and carbonization at 500 °C in N_2 atmosphere followed by Fe_3O_4 treatment. The sample was used for the adsorption of MB and showed 156.25 mg/g of maximum sorption capability. The Freundlich isotherm model and PSO kinetics produced the best fits to the equilibrium data.

Maheshwari *et al.* [117] in 2022, utilised waste walnut shell (WNS) to derive activated carbon by carbonization in muffle furnace at 350 °C for 3 hours. The synthesized sample showed a maximum adsorption efficiency of 140.84 mg/g for congo red dye. Further, the PSO kinetics and the Langmuir isotherm model provided the best fits to the equilibrium data.

Koli *et al.* [118] in 2022, synthesized N containing activated carbons by carbonization of sugarcane pith agro-waste in N_2 atmosphere at 500 °C with H_2SO_4 treatment. Surface area and pore volume for the synthesized samples were 725 m^2/g and 0.3377 cm^3/g, respectively. Further, the synthesized N doped activated carbon sample was used to efficiently capture CO_2 and anionic dye MO with maximum adsorption capacity- 527 mg/g.

2.2.2 Adsorption of phenols

Ahmaruzzaman *et al.* [119] in 2010, utilised tea waste to form activated carbons by treating it with H_3PO_4 and carbonizing further in muffle furnace at 500 °C in N_2 atmosphere. The study investigated the effects of pH, contact time. The sample showed maximum adsorption capacity of 142.85 mg/g via following Langmuir isotherm and PSO kinetic model.

Zhang *et al.* [120] in 2015, synthesized sunflower plates activated carbon by carbonization at 800 °C in N_2 atmosphere followed by activation in ammonia atmosphere. Further, for phenol, 4-chlorophenol, and p-nitrophenol (PNP), the synthesized sample showed adsorption capacities of 316.5 mg/g, 330.24 mg/g, and 387.62 mg/g, respectively. The Langmuir model is strongly supported by the adsorption isotherm data.

Chen *et al.* [121] in 2019, synthesized activated biochar using alfalfa by pyrolysis in two steps at 700 °C in N_2 atmosphere in muffle furnace. The sample showed a surface area of 119.98 m^2/g with a pore volume 0.068 cm^3/g. The sample was used for the adsorption of PNP and

showed maximum adsorption efficiency of 49.253 mg/g. The adsorption occurred via monolayer by following Langmuir adsorption isotherm.

Ma *et al.* [122] in 2019, used platanus orientalis L. leaves to synthesize biochar via activation using KOH followed by 3 stage carbonization in N_2 atmosphere at 450 °C, 650 °C for 30 minutes and finally at 800 °C for 1 hour. The prepared biochar showed 622.73 mg/g maximum adsorption capacity of PNP. The PSO model and the Langmuir adsorption isotherm model explained the experimental results better than other kinetic and isotherm models.

Hadi *et al.* [123] in 2020, prepared activated carbons using pomegranate husk agro-waste by first activating using $ZnCl_2$ followed by carbonization in N_2 atmosphere at 550 °C. The synthesized activated carbon was magnetized further using $FeCl_3$. The sample showed a surface area of 1168 m^2/g with total pore volume of 0.623 cm^3/g. The maximum adsorption capacity observed for p-chloropheol was 446.89 mg/g. Adsorption process followed Avrami model and Liu isotherm model.

Liu *et al.* [124] in 2020, used pine sawdust to synthesis biochar by pyrolysis method at temperatures 300-700 °C in N_2 atmosphere. The maximum surface area and pore volume were 397.864 m^2/g and 0.227 cm^3/g, respectively. The adsorption of PNP onto biochar included electrostatic interactions, H bonds, and π-π interactions. The maximum adsorption efficiency was 117 mg/g with adsorption process followed Elovich kinetic model and Freundlich isotherm model.

Talari *et al.* [125] in 2022, used bacterial cellulose to synthesize carbon fibre aerogel by hydrothermal treatment of precursor followed by pyrolysis under N_2 atmosphere at 800 °C. The synthesized aerogel was used for the adsorption of MB and PNP. The MB and PNP followed Langmuir and Freundlich isotherms and showed a maximum adsorption capacity of 106.3 and 60.2 mg/g, respectively.

2.2.3 Adsorption of pharmaceutical waste

Wang *et al.* [126] in 2015, prepared activated carbons by using bamboo raw materials via following steps: Agro-waste was impregnated with H_3PO_4 followed by treatment at 450 °C in N_2 atmosphere and further treated with K_2CO_3 and carbonized at 700-850 °C in N_2 atmosphere. The sample showed a maximum surface area and pore volume of 2237 m^2/g and 1.23 cm^3/g, respectively. The sample demonstrated a maximum ciprofloxacin adsorption of 613 mg/g, and the adsorption mechanism followed the PSO kinetics and the Langmuir isotherm.

Shang *et al.* [127] in 2016, prepared activated carbon from herbal residue (Astragalus mongholicus) agro-waste by thermal activation under oxygen-limited conditions at 200-800

°C followed by HCl treatment. The surface area and pore volume of best sample were 176.33 m^2/g and 0.044 cm^3/g, respectively. The sample was used to adsorb ciprofloxacin from aqueous solution with q_e= 42.9 mg/g (maximum adsorption efficiency). The adsorption process followed PSO kinetic model and Langmuir isotherm model.

Jang *et al.* [128] in 2019, used debarked loblolly pine chips agrowaste to synthesize activated biochar by pretreatment of precursor at 300 °C in N_2 atmosphere followed by NaOH activation and carbonization at 800 °C in N_2 atmosphere. The surface area and pore volume of the synthesized sample were 959.9 m^2/g and 0.4 cm^3/g, respectively. The sample was used to adsorb tetracycline with adsorption efficiency 274.8 mg/g and adsorption took place via following Elovich kinetic model and Freundlich isotherm model suggesting multilayer chemisorption.

Ai *et al.* [129] in 2020, used orange peel as agro-waste precursor to synthesize activated carbon for adsorption of ibuprofen and sulfamethoxazole from aqueous solution. The precarbonization of orange peel was carried out at 200 °C followed by carbonization at 200-600 °C in N_2 atmosphere. Further, the surface of sample was modified with CH_3OH and HCl. The modified biochar showed enhanced surface area (857.4 m^2/g) and pore volume (0.12 cm^3/g). The maximum adsorption efficiency for ibuprofen and sulfamethoxazole were 47.16 and 46.66 mg/g.

Wang *et al.* [130] in 2020, synthesized activated carbon using bagasse agro-waste by pre-carbonization treatment of precursor at 350 °C in N_2 atmosphere. Further sample was washed with acetone and pyrolysed at 950 °C in N_2 atmosphere. The surface area and pore volume of the prepared sample were 1119.53 m^2/g and 1.36 cm^3/g, respectively. The maximum adsorption capacity for sulfamethoxazole and tetracycline adsorption were 274.63 and 353.85 mg/g, respectively.

Liakos *et al.* [131] in 2021, synthesized activated carbon using plane tree leaves and tea leaves in 3 step. The synthesis involved carbonization at 650 °C in N_2 atmosphere followed by NaOH activation and again carbonization at 650 °C in N_2 atmosphere in final step. The activated tea char showed maximum surface area (1151 m^2/g) and pore volume (0.694 cm^3/g). The maximum adsorption capacity by this sample was observed to be 112 mg/g for pramipexole dihydrochloride pharmaceutical compound. The adsorption process followed Langmuir adsorption isotherm.

Al-Musawi *et al.* [132] in 2021, used azolla filiculoides fern to synthesize activated carbon to remove ampicillin from water via adsorption. The samples were synthesized by impregnation

of precursor with $ZnCl_2$ and carbonization at 450 °C in N_2 atmosphere followed by HCl washing. The sample showed specific surface area of 716.4 m^2/g and pore volume 0.621 cm^3/g. The maximum adsorption capacity for ampicillin was 114.3 mg/g.

2.2.4 Adsorption of phthalate esters

Wang *et al.* [133] in 2015, synthesized activated carbons using phoenix leaves to adsorb dibutyl phthalate. The samples were synthesized by carbonizing the precursor at 550 °C under N_2 atmosphere. The sample exhibited surface area 593.52 m^2/g with total pore volume 0.52 cm^3/g. The sample adsorbed a maximum 133.3 mg/g of pollutant and the adsorption process followed PSO kinetic model and Langmuir adsorption isotherm.

Jing *et al.* [134] in 2018, used peanut hull and wheat straw biomasses to prepare activated biochars by heating the biomasses in a muffle furnace at 450, 550, and 650 °C. The surface area and pore volume for the best sample were 474.9 m^2/g and 0.536 cm^3/g, respectively. The synthesized samples were used for the adsorption of dimethyl phthalate and diethyl phthalate with a maximum adsorption capacities of 1980 and 3588 mg/kg, respectively.

Guo *et al.* [135] in 2020, synthesized N, S co doped porous carbons using peanut shell via pyrolyzing in a muffle furnace at different temperatures *viz.* 200-800 °C under oxygen-limited conditions. The best sample exhibited maximum adsorption capacity of 14.34 mg/g for diethyl phthalate via following PSO kinetic model and Langmuir isotherm model.

Zhang *et al.* [136] in 2021, used the lotus stems agro-waste to synthesize activated carbon for the adsorption of phthalic acid ester from aqueous solution. The biochar was prepared by heating the agrowaste into muffle furnace at 600 °C under N_2 atmosphere prior of NaOH treatment. The surface area and pore volume for synthesized sample were 360.78 m^2/g and 0.29 cm^3/g, respectively. The maximum adsorption capacity for phthalic acid ester was 125 mg/g with adsorption took place through PSO kinetic model and Langmuir isotherm model.

Cheng *et al.* [137] in 2022, synthesized activated carbon by hydrothermal carbonization of cotton straw powder at 240 °C followed by thermal activation at 900 °C in N_2 atmosphere. The synthesized sample was used further for the adsorption of diethyl phthalate (DEP) with a maximum adsorption capacity of 657 mg/g. Lewis acid-based interactions, π-π stacking, and hydrogen bonding were responsible for the DEP's sorption rate control, while pore filling and partitioning processes were responsible for the DEP's sorption capacity onto synthesized samples.

Zhang *et al.* [138] in 2022, compared hydrochar, raw biomass (Pistia stratiotes) and pyrochar as precursors to synthesize porous activated carbon and their adsorption performance for

phthalate esters. The pyrochar and hydrochar from pistia stratiotes were synthesized at 800 °C under N_2 atmosphere and at 240 °C in an autoclave, respectively. Among these adsorbents, hydrochar was found to be the most effective with a maximum adsorption capacity of 595 mg/g for phthalate esters and exhibited a surface area of 2284.4 m^2/g and pore volume 0.68 cm^3/g.

Fan *et al.* [139] in 2022, synthesized biochar using nutshells (apricot, peanut, walnut and coconut shell) biomass by pyrolysis at different temperatures from 300-800 °C in N_2 atmosphere. The walnut shell biochar showed a maximum surface area (454.17 m^2/g) and pore volume (0.1114 cm^3/g). Among the four series of nutshell-derived biochar, peanut shell-derived biochar (PSBs) exhibited the best DEP sorption efficiency. The adsorption process followed Langmuir adsorption isotherm model.

2.3 Photocatalysis based wastewater treatment using porous carbons

Activated carbons have not been explored much for the photodegradation of pollutants in aqueous solutions. The fabrication of metal organic frameworks (MOFs), which are composites of activated carbon with any metallic oxide (eg. ZnO, TiO_2) to increase the photodegradation efficiency for water contaminants, is documented in a large amount of research [47,48,140–142]. There are very few papers on the use of porous activated carbon for photodegradation of contaminants.

Gala *et al.* [50] in 2013, purchased commercially available activated carbon from different companies. The availed activated carbons were treated with gamma radiations to reduce the band gap of the sample. This was done to make it suitable for photo degradation of model pollutant sodium diatrizoate. It was demonstrated that materials exposed to gamma radiation have a higher proportion of carbon atoms with sp^2 hybridization, which accounts for their normally superior DTZ photodegradation performance.

Mahajan *et al.* [78] in 2015, prepared CNSs of average size 40-50 nm by solvothermal route using acetone and Mg as a reducing agent at 600 °C in a sealed autoclave for 5 h. Photo catalytic activity was studied for the degradation of MB in UV light in the presence of CNSs. The band gap for direct transitions was calculated by UV-Vis spectra i.e. 3.54 eV.

Gala *et al.* [51] in 2017, availed commercially available activated carbon and treated with gamma radiations to study the effect of surface chemistry on the photo degradation of model pollutant sodium diatrizoate. It was observed that higher E_g values in activated carbons favour superoxide anion concentration whereas lower E_g values favour the production of hydroxyl radicals. Also, the availability of chemisorbed oxygen and the presence of dissolved oxygen in the solution is crucial for the photoactive behaviour of activated carbons and its removal from

the solution encourages the recombination of electron-hole pairs while inhibiting the formation of superoxide anions and, consequently, the production of hydroxyl radicals.

Ahmad *et al.* [49] in 2020, synthesized activated carbons by soaking of egg shells powder into NaOH solution and H_3PO_4 followed by carbonization at 550 °C for 3 hours. The photo degradation of MB under UV-Visible irradiation was carried out. Photo degradation of activated carbon achieved a maximum degradation efficiency of 83% after 2 hours.

2.4 Synthesis of N doped carbons

2.4.1 Hydrothermal carbonization (HTC) method

Wickramaratne *et al.* [143] in 2014, synthesized N containing carbon spheres via HTC method. In the typical experiment, ethanol and water were mixed and added with ethylenediamine, resorcinol and formaldehyde and subjected to HTC at 100 °C for 24 hours. The obtained HTC products were subjected to thermal treatment at 600 °C in N_2 atmosphere. The post synthesis activation was carried out at 850 °C in CO_2 atmosphere. The activated NCS were used for adsorption of CO_2 and supercapacitor electrodes.

Xu *et al.* [144] in 2015, used glucose as carbon source to form carbon spheres (CS) via HTC method. The CS were mixed with urea and pyrolyzed at 350 °C to form NCS and treated further with KOH and pyrolyzed at 650 °C. The activated NCS was further used for CO_2 adsorption.

Gu *et al.* [145] in 2017, synthesized N doped carbon spheres (NCS) by HTC method (at 180 °C for 8 hours) using glucose as carbon source and N doping was done by treating the spherical carbons in ammonia atmosphere. The NCS were further calcined in Ar atmosphere at 1000 °C for activation. The sample was used for electrocatalytic oxygen reduction.

Xu *et al.* [146] in 2019, added nickel nitrate hexahydrate, 1, 3, 5-benzenetricarboxylic acid, and polyvinylpyrrolidone to a mixed solution of water and DMF and subjected to HTC treatment at 150 °C for 10 hours. The final product was further annealed with melamine (for N doping) at 800 °C under Ar atmosphere. For high-performance sodium-ion batteries, the NCS served as the anode.

Huang *et al.* [147] in 2019, used glucose, Ni foam, dextrose solution as carbon precursor and subjected to HTC treatment at 180 °C for 8 hours. The HTC final product (CS/NF) was mixed with urea for N doping and again carbonized with HTC method at 180 °C for 8 hours. The obtained NCS/NF and CS/NF were heated at 800 °C in N_2 atmosphere. The synthesized samples were used as negative electrode in the super capacitance application.

Liang *et al.* [148] in 2019, mixed triblock copolymer pluronic F108 and ammonia solution and treated by HTC at 170 °C for 6 h and the products obtained were heated at 600 °C in N_2

atmosphere. The NCS obtained were treated with KOH and annealed at 700 °C in N_2 atmosphere. The obtained activated NCS were used in super capacitor application as an electrode.

Li *et al.* [149] in 2019, used phenol, bis-tris, and CTAB or OTAB and mixed them followed by stirring continuously. Further, formaldhyde was added and treated via two step HTC: 200 °C for 28 hours in thermostatic water bath and then at 200 °C for 6 hours in Teflon lined autoclave. The obtained NCS were annealed at 800 °C under N_2 atmosphere followed by KOH activation and heat treated at 850 °C. The obtained activated NCS was applied as an electrode material for super capacitance.

Zuo *et al.* [150] in 2020, derived N doped carbon spheres using dictyophora powder as precursor via HTC at 180 °C for 24 hours. The NCS were activated with KOH and calcined at 750 ℃ in nitrogen atmosphere. The activated NCS were further used as electrode material for high performance supercapacitor.

2.4.2 Pyrolysis method

Ren *et al.* [151] in 2017, synthesized N doped carbon nanospheres using 1,2-dichloroethane, indole, formaldehyde dimethyl acetal and ferric chloride anhydrous. The precursors were mixed and kept in microwave for 20 minutes at 45 °C and product was impregnated with KOH and pyrolyzed at 500-700 °C in N_2 atmosphere. The synthesized NCS were used for the capture of CO_2.

Zhang *et al.* [152] in 2017, used porphyra for the synthesis of hierarchical N doped porous carbons (NHPC) via KOH activation followed by pyrolysis at 800 °C in Ar atmosphere. Further, Hemin was adsorbed onto the NHPC to form Hemin/NHPC composite. The Hemin/NHPC composite was pyrolyzed at 800 °C in Ar atmosphere to form N-doped porous carbon supported single Fe atoms (SA-Fe/NHPC). The SA-Fe/NHPC was used further as electrocatalyst for oxygen reduction reaction.

Bi *et al.* [153] in 2018, used sodium citrate and melamine mixture to synthesize 3 dimensional N doped porous carbon by single step pyrolysis at 800 °C in Ar atmosphere followed by washing with HCl. The synthesized sample was used further as anode materials for microbial fuel cells.

Xue *et al.* [154] in 2020, synthesized N doped porous carbons (NPC) using mixture of rice husk and urea which was pyrolyzed at 800 °C in N_2 atmosphere. The pyrolysis product was soaked in HF solution to remove silica template and washed with DI water to obtain NPC.

Supercapacitors with great volumetric performance were made using the synthesised NPC as well.

Tang *et al.* [155] in 2020, prepared magnetic N doped porous carbons (MNPC) by mixing 2-methylimidazole, cobalt hydroxide, and ZnO nanoparticles and directly pyrolyzed at 600-900 °C in N_2 atmosphere. The synthesized sample showed exceptional ciprofloxacin adsorption capability and wide range of pH adaptability.

Gunasekaran *et al.* [156] in 2021, used dried bamboo woods to synthesize N doped activated carbon by carbonizing in air atmosphere at 300 °C followed by impregnation of the product with KOH and urea and pyrolyzed at 900 °C in an inert atmosphere. The obtained sample was used as electrode material for asymmetric supercapacitor with high energy density.

2.4.3 Other methods

Li *et al.* [157] in 2010, used arc discharge method to synthesize N doped graphene sheets by pure graphite rods. In a typical experiment, direct current arc discharge was done between graphite rod electrodes with current held at 120A. In a 760 Torr mixture of He and NH_3, the anode was converted to steam. The created soot was collected under ambient circumstances after the discharge was finished.

Parambhath *et al.* [158] in 2011, prepared N doped palladium decorated graphene by a combination of hummer method and nitrogen plasma treatment. After synthesising the graphene with hummer method, nitrogen plasma treatment of graphene (N-HEG) was carried out for N doping in a planar RF magnetron sputtering apparatus outfitted with a high-frequency generator operating at a frequency of 13.56 MHz. The synthesized sample was used for Hydrogen Storage.

Lu *et al.* [159] in 2013, created N doped graphene using low pressure 1,3,5-triazine chemical vapour deposition (CVD) on copper foils (1000 °C, 500 Torr). The tube was then heated to the necessary growth temperatures (900, 800, and 700 °C) under a 10 sccm H_2 flow and a 100 sccm Ar flow, while a total pressure of 5 Torr was maintained. The absorbed triazine molecules were split apart at high temperatures, and with the help of Cu, they were then brought back together to form N-doped graphene.

Tian *et al.* [160] in 2016, used Stober method (sol-gel method) to synthesize N doped carbon spheres. Prior to NCS synthesis, polymeric nanospheres were synthesized by mixing ethanol water and the 3-aminophenol and formaldehyde were added in the mixture (dropwise) and subjected to HTC treatment at 100 °C in an autoclave. The synthesizsed polymeric nanospheres

were heated in a furnace with N_2 flow up to 350 °C, dwelled for 2 hours, and then resumed upto 700 °C, dwelled for 4 hours, to produce the required N doped carbon spheres.

2.5 N doped porous carbons using protein based precursors

The HTC processes biomass in reaction solvents like water, is ideally suited for processing wet biomass, which mostly has a high protein or nitrogen content. The protein biomasses work as both carbon and nitrogen source during carbonization to form N doped carbons. In the recent years, many researchers have reported the use of protein biomass to synthesize N doped carbons with various methods. In 2016, Jia *et al.* [161] synthesized N doped carbons from milk proteins by KOH activation and heating of milk powder in between 500-800 °C in N_2 atmosphere. Gao *et al.* [162] in 2016, used prawn shells to synthesize N doped activated carbons by annealing at 600-800 °C in Ar atmosphere assisted by KOH activation. An *et al.* [163] studied the synthesis of N doped carbon using protein from tofu. The protein was first heated at 400 °C and then carbonized in N_2 atmosphere at 1100, 1200 and 1300 °C. The synthesized sample was used further for anode materials in Li ion batteries. In 2014, Song *et al.* [164] used chicken bones to produce N doped porous carbon materials by washing and pyrolysing the precursors at 800 °C in N_2 atmosphere. Other than these protein based N doped carbons, reports are available on the synthesis of N doped carbons using honey by Zhang *et al.* [165] in 2016, layer fish scale by Lu [166] in 2021, watermelon rind by Zhong *et al.* [167] in 2019, corn protein by Park *et al.* [168] in 2014. In the recent years, the conversion of soybean meal to potentially N-doped carbons has been documented in the literature.

Ferrero *et al.* [100] in 2015, used soybean meal and glucose to synthesize N doped carbons by HTC method at 200 °C for 15 hours. The synthesized sample was mixed with KOH and carbonized at 600, 650, 700 and 800 °C in N_2 atmosphere. The N content reduced from 4 to 1.6 at% with temperature increased from 600 to 800 °C. In high performance supercapacitor, the synthesised material was used as an electrode material.

Fang *et al.* [169] in 2016, synthesized C dots using soybean flour via HTC treatment at 200 °C for 3 hours and centrifuged at 10000 rpm to obtain the brown product. The HTC product was further put through dialysis membrane for purification of C dots. The maximum N content of the synthesized sample was 20.23 at%. The synthesized material was used further for Fe^{3+} detection.

Zhao *et al.* [97] in 2018, synthesized N,O doped carbon by impregnation of soybean meal with KOH and carbonizing at 600-900 °C in N_2 atmosphere. The final products were washed with HCl until neutral pH. The N content reduced from 5.64 to 1.34 at % with increasing

temperature from 600-900 °C. The synthesized material was used as electrode material in high-performance supercapacitor.

Li *et al.* [170] in 2019, synthesized N, O doped carbons using soybean dreg by HTC treatment at 180 °C for 24 hours. The obtained products were washed and impregnated with KOH and heat treated at 500, 650 and 800 °C in N_2 atmosphere. The content of N reduced to 1.8 to 4.2 at% with increasing temperature.

Shen *et al.* [95] in 2020, used soybean meal to prepare N doped carbons by impregnating the precursor with $ZnCl_2$ and calcined at 500-800 °C. The excess $ZnCl_2$ was removed by washing with HCl. The sample was used further as a catalyst for acetylene hydrochlorination.

Ding *et al.* [98] in 2021, synthesized N doped carbons using soybean meal by pyrolyzing at 700, 800 and 900 °C in CO_2 atmosphere. The N content was maximum for sample pyrolyzed at 700 °C (6.6 at%) and reduced with increasing temperature to 900 °C (5.24 at%). The sample showed good application in super capacitance.

Zhang *et al.* [94] in 2022, used soybean meal to synthesize N doped carbons via pyrolysis at 800 °C in N_2 atmosphere. The sample was further mixed with KOH and melamine and subjected to calcination at 800 °C in muffle furnace. The sample consisted of maximum 6.15 at% of nitrogen content. The synthesized sample was used further for CO_2 capture and DRM.

Tang *et al.* [96] in 2022, used molten salt method to synthesize N doped carbons using soybean meal. The soybean meal was first mixed with NaCl, KCl and $KHCO_3$ and heated in muffle furnace at 750 °C followed by HCl washing. The N content was 2.86 at% in the synthesized sample. The material was used further as electrode material in super capacitance application.

2.6 Gaps in the study

The detailed literature presented above gives insights about the various methods for the synthesis of porous carbons, wastewater treatment by adsorption and photocatalysis using porous carbons. Role of N-doping in enhancing the properties of the porous carbons and N-doping in carbons by various precursors has been studied but, there are few gaps found in the literature which are as follows:

1. There are reports available for the synthesis of N doped carbons using various nitrogen sources such as thioamine, melamine, triblock copolymers and various other chemicals which are exotic, expensive and require multistep synthesis involving highly toxic by-products. Use of agro by-product soy flour for synthesizing N-doped activated porous carbons especially with saccharides as source of carbon as well as catalyst/template has

not yet been systematically studied. A structured study on the adsorption and photocatalytic performance of these soy based porous carbons also needs to be undertaken.

2. Different studies show that by doping nitrogen in carbons, its applications in different areas such as electrocatalysis, super capacitance, sensing, ion batteries, oxygen reduction reaction (ORR) etc. are enhanced. The effect/role of nitrogen doping in porous carbons for adsorption/degradation of toxic waste in the industrial wastewater has not yet been studied systematically.

2.7 Objectives

On the basis of gaps in the literature, the following objectives are proposed in this work.

1. To synthesize and characterize N-doped porous carbons from saccharides (sucrose, glucose, xylose) and soy flour using hydrothermal and pyrolysis method.
2. To study the adsorption properties of synthesized material for dyes, phenols and pharmaceutical waste.
3. To analyze the effect of pH variation on adsorption capacity of the synthesized materials.

Chapter 3
Materials and Methods

Overview

The details of precursors and the approach for sample synthesis and their characterizations are described in this chapter. All characterizations used in the current work have been discussed in this chapter. This include electron microscopy, X-ray diffraction, surface area measurement, X-ray photoelectron spectroscopy, UV visible, FTIR, Raman spectroscopy, thermogravimetric analysis, adsorption studies, and decolorization studies under UV irradiation and sunlight. The fundamental aspects of synthesis/characterizations, as well as the required test conditions, have been defined.

3.1 Materials

3.1.1 Precursors

To synthesize N-doped carbons, defatted soy meal (soy flour) (99.0%, Loba Chemie) was used as nitrogen and carbon source, and saccharides viz. glucose ($C_6H_{12}O_6$, 99.0%; Loba Chemie), sucrose ($C_{12}H_{22}O_{11}$, 99.0%; Loba Chemie), and xylose ($C_5H_{10}O_5$, 99.0%; S D Fine-Chem. Limited) were used as carbon source, individually, without any pre-treatment or purification. All the precursors were received in powdered form as shown in Fig. 3.1. Properties of the precursors are given in Table 3.1 and Table 3.2 and their molecular structures are given in Fig. 3.2.

Fig. 3.1: Precursors obtained in powdered form.

Table 3.1: Properties of soy flour.

Colour	Protein content	Carbohydrate content	Crude fat	N%	C%	O%	H%	K%	Other elements
Light brown	~40%	~23%	~25%	~9	~47	~29	~10	~2.5	~2.5

Table 3.2: Properties of saccharides.

Property	Glucose	Sucrose	Xylose
Colour	White crystalline solid	White crystalline solid	White crystalline solid
Molecular formula	$C_6H_{12}O_6$	$C_{12}H_{22}O_{11}$	$C_5H_{10}O_5$
Molecular weight	180.16 g/mol	342.3 g/mol	150.13 g/mol
Density	1.54 g/cm^3	1.58 g/cm^3	1.52 g/cm^3
Melting point	146 °C	186 °C	153 °C
Type	monosaccharide	disaccharide	monosaccharide

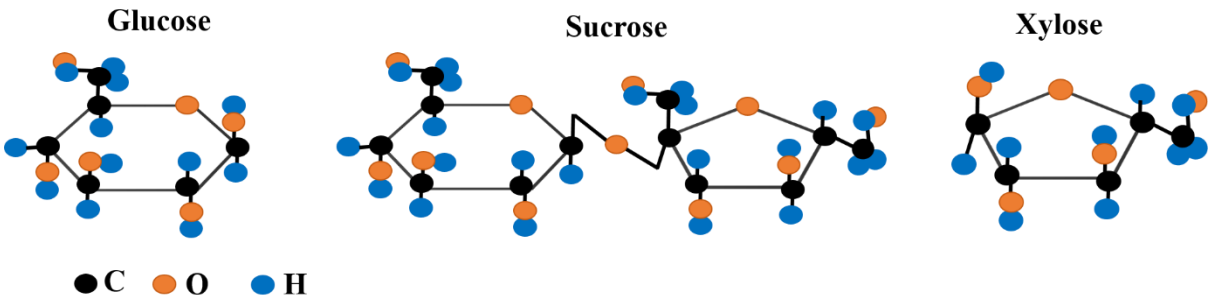

Fig. 3.2: Molecular structure of glucose, sucrose, and xylose.

3.1.2 Model pollutants

To carry out the adsorption/photo-induced decolorization experiments, cationic dyes methylene blue (MB) and crystal violet (CV), anionic dye eriochrome black-T (EBT), P-nitrophenol (PNP), ciprofloxacin (CIP) and diethyl phthalate (DEP) were used as model pollutants. The molecular structures of all the model pollutants are given in Fig. 3.3 and their properties are given in Table 3.3.

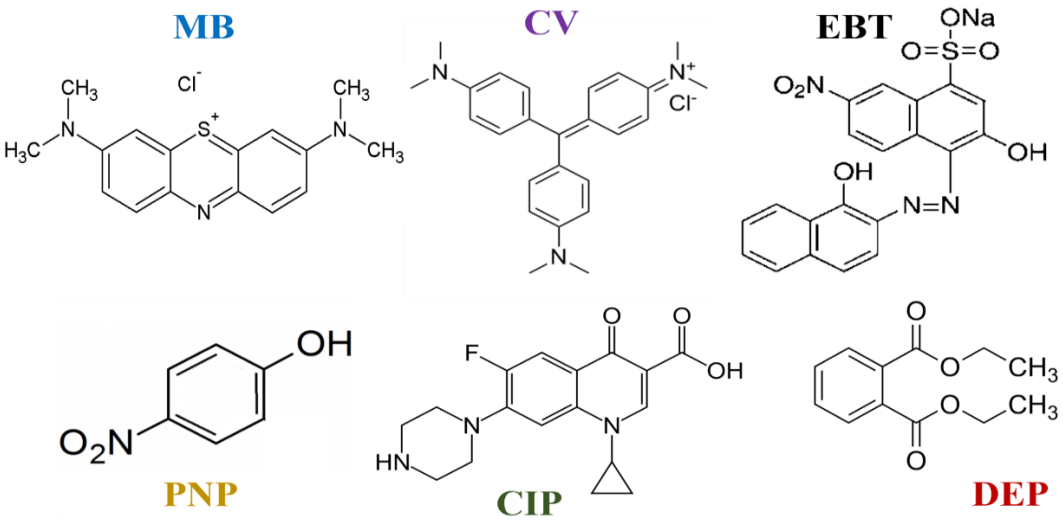

Fig. 3.3: The molecular structure of model pollutants used in this work.

All the model pollutants that were chosen in this work pose a special threat to the ecosystem. MB and EBT were chosen because both of them are sulphur-containing dyes and belongs to direct class dyes. Moreover, these dyes are inexpensive, therefore used extensively in textile industries [171]. CV has been identified as a refractory dye molecule that stays in the environment for an extended length of time and has hazardous consequences. In some fish species, it functions as a mitotic toxin, a carcinogen, and a clastogene, increasing tumour formation. As a result, CV is categorized as a biohazard material [172]. PNP is used in the production of pharmaceuticals, dyes, fungicides, insecticides, and in leather industries. PNP has minimal effects on human health but is found to have significant effects on the health of

animals when consumed directly [173]. CIP is a commonly used antibiotic, therefore its consumption is high. CIP contamination in water bodies disturbs human health causing diarrhoea, heartburn, nausea etc. Also, the continuous contamination may result in the growth of antibiotic-resistant microorganisms [174]. DEP is used in personal care products produced by pharmaceutical industries. DEP is easily bonded (non-covalent bond) with the products and gets separated from the product easily in water bodies. Its exposure may cause androgen-independent male reproductive toxicity alongwith developmental and hepatic toxicity, with a modest indication of female reproductive toxicity [175].

Table 3.3: Properties of model pollutants used in current work.

	MB	**CV**	**EBT**	**PNP**	**CIP**	**DEP**
Colour in aqueous solution	blue	violet	black with a violet tinge	yellow	colorless	colorless
Molecular formula	$C_{16}H_{18}ClN_3S$	$C_{25}N_3H_{30}Cl$	$C_{20}H_{12}N_3O_7SNa$	$C_6H_5NO_3$	$C_{17}H_{18}FN_3O_3$	$C_{12}H_{14}O_4$
Molecular weight	319.85 g/mol	407.98 g/mol	461.381 g/mol	139.11 g/mol	331.346 g/mol	222.24 g/mol
Minimum Molecular size	>1.2 nm	>1.2 nm	>1.3 nm	>0.8 nm	>1 nm	> 0.8 nm

3.2 Methodology

The schematic overview of the synthesised samples and characterizations in the present study is shown in Fig. 3.4.

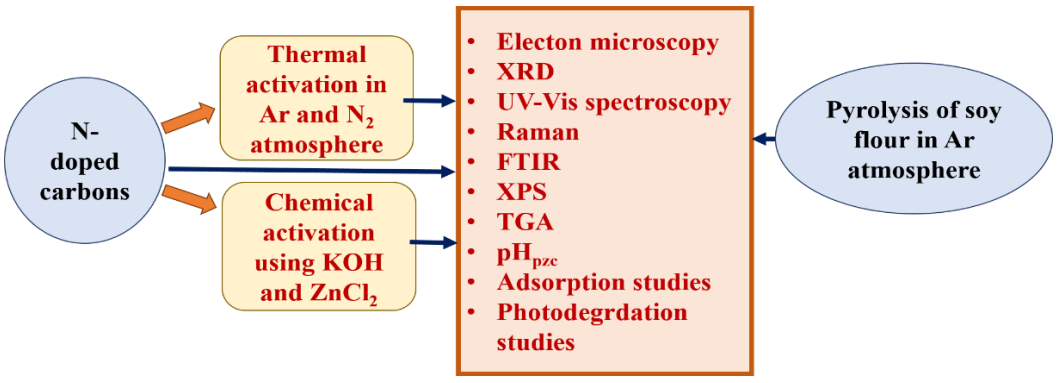

Fig. 3.4: Schematic representation of adopted methodology for synthesis and characterizations.

3.2.1 Synthesis of N-doped carbons

In a typical experiment, required amount of glucose/sucrose/xylose and soy flour in 1:0.3 w/w ratio were dispersed in 15 mL deionized water (resistivity- 18.2 MΩ-cm, Millipore Q3 system) by magnetic stirring. The solution was then transferred to a Teflon-lined stainless

steel autoclave and placed in an oven which was heated to and maintained at 180 °C for 8 hours. The resulting brown colored precipitates were separated by centrifuge and washed several times with deionized water and dried at 80 °C in a hot air oven for 24 hours. To optimize the synthesis conditions following batch experiments were also undertaken:

i) Varying the total precursor weight in the same water volume.

ii) Altering the glucose to soy flour ratio.

The details of exact parameter variations in these batch experiments are available in the Chapter 4. In another set of experiments, to understand the role of the simultaneous addition of soy flour and glucose, samples with only soy flour and glucose were also synthesized with the same total weight of the precursor (2.15 g). The schematic depiction of the approach used for the optimization to obtain the N doped carbon with appropriate morphology and yield is shown in Fig. 3.5.

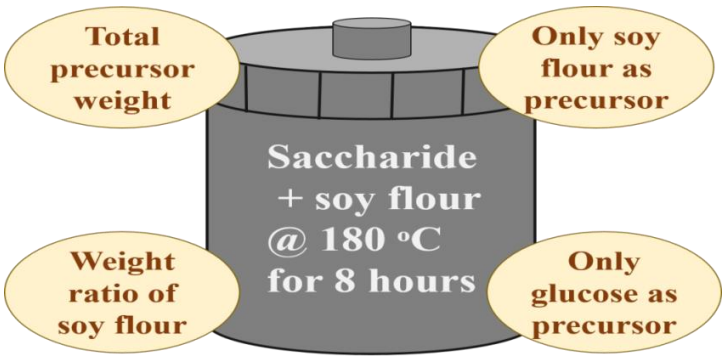

Fig. 3.5: Schematic depiction of the selected approach for N doped carbon sample synthesis optimization.

The optimized N-doped carbon sample, based on morphology and yield, was further used in synthesis of porous carbon samples using thermal and chemical activation.

3.2.2 Thermal activation of N-doped carbons

For thermal activation, the optimized sample was heat-treated in a tubular furnace in argon (Ar) and nitrogen (N_2) atmosphere, separately, at 900 °C for 4 hours at the heating rate of 10 °C/min. The obtained powder was used as such without further washing/modifications.

3.2.3 Chemical activation of N-doped carbons

The optimized sample synthesized via the hydrothermal method was activated by the chemical method using KOH or $ZnCl_2$ at low temperature and time. In a typical experiment, the optimized sample was mixed with KOH or $ZnCl_2$ powders in fixed ratios and kept for 24 hours. Further, the mixture was agitated for 4 hours after adding 10 ml water and afterwards dried at 100 °C for 12 hours. The dried mixture was placed in a muffle furnace and heated at

400 °C for 30 minutes. The resulting sample was washed three times with deionized water. HCl (3M, 20 ml) was added to the washed samples and mixture was agitated for 4 hours to remove any remaining K/Zn ions and/or any by-products. Finally the sample was centrifuged out and washed with deionized water to neutralize the sample pH. The neutralized samples were dried at 100 °C and used for characterizations and adsorption and photo-induced decolorization study.

3.2.4 Pyrolysis of soy flour

The biochar was prepared using soy flour. In a typical experiment, 4g of soy flour was placed in an alumina boat under Ar atmosphere in a tubular furnace and pyrolyzed at 450, 650, and 750 °C (heating rate = 10 °C /min.) for 2 hours. The synthesized samples were treated with HNO_3 for demineralization and then DI water until the neutral pH.

3.3 Characterization techniques

3.3.1 Scanning electron microscopy

Scanning electron microscopy (SEM) and Field emission scanning electron microscopy (FE-SEM) provide visual information on the topographical and morphological characteristics of the synthesized samples. In a typical experiment the electron beam is focused on a sample held in vacuum, resulting in inelastic and elastic scattering to eject secondary electrons and backscattered electrons, respectively. Secondary electrons provide topography, whereas backscattered electrons images reveal the contrast between particles of varying densities. The image is formed by raster scanning the electron beam on the sample surface and using the appropriate signal. The main difference between SEM and FE-SEM is electron generation source. In SEM, an electron beam is generated from W or LaB_6 electron gun. In FE-SEM, the electrons are ejected by a cold field emission source. The ejected electrons in FE-SEM are more focused than those ejected in SEM. Therefore high resolution images are generated in FE-SEM.

The SEM images of the synthesized samples were recorded using JSM-6510 SEM (at 15 kV). Elemental analysis of the samples was carried out using electron dispersive spectroscopy (EDS) using the Oxford INCAx-act detector attached with the SEM. The micrographs of the synthesized samples were recorded at Carl Zeiss Sigma 500 FE-SEM (at 20kV). The SEM/FE-SEM images were analyzed by Carl Zeiss Axio Vision 4 software.

3.3.2 High resolution transmission electron microscopy (HR-TEM)

In TEM electrons are transmitted through the sample to form image. HR-TEM relies on a phenomenon known as phase contrast (depending upon the sample density) for generating picture. Elastically scattered electrons leave the sample and pass through the microscope's lenses to generate the high-resolution image.

High resolution images of the samples were recorded on JEOL2100F TEM (HR-TEM) at 200 kV. These were used to explain the formation mechanism of N doped carbon spheres synthesized using HTC method (section 4.4).

3.3.3 X-ray diffraction (XRD)

XRD is a non-destructive technique and provides the details of the crystallographic phases present in the samples. The principle of XRD involves constructive interference of waves generated by elastic scattering of electrons to generate diffraction peaks via Bragg's law:

$$2d \sin\theta = n\lambda \qquad (3.1)$$

Where d is the distance between planes, θ is the angle of diffraction, n is diffraction order, and λ is the wavelength of X-ray.

In the current work, the XRD patterns were scanned using PANalytical Xpert-Pro diffractometer and Rigaku Xpert-Pro diffractometer. The XRD line profile of powdered sample was taken between 5-90° (2θ) with Cu Kα radiation (1.5406 Å; Ni filter), with a step size of 0.013° (2θ), and total scan time of 14 minutes.

3.3.4 Thermal analysis

Thermal analysis of the samples is carried out by thermogravimetric analysis (TGA), differential thermal analysis (DTA), and Differential Scanning Calorimetry (DSC). TGA is a thermal analysis method that measures the mass of a sample with time as the temperature varies. DTA compares the temperature of a sample to that of inert reference material during a controlled temperature change. DSC measures the variations in heat flow to and from a sample when the temperature is varied.

In current work, TG/DTA/DTG was carried out to determine the pyrolysis temperatures of soy flour at SII 6300 EXSTAR in Ar gas from room temperature to 800 °C at a heating rate of 5 °C /min. TG/DSC/DTG analysis of the synthesized carbon samples was undertaken from room temperature to 900 °C at a heating rate of 5 °C /min in the presence of Ar, N_2, and air

carrier gases using NETZSCH STA 449F3 to determine the thermal activation temperature of sample.

3.3.5 N_2 adsorption-desorption isotherms

N_2 adsorption-desorption isotherms help in the determination of specific surface area, pore-volume, pore size, and distribution. The porous structure of the adsorbent can be determined by comparing the obtained isotherms with IUPAC hysteresis loops of the gas adsorption-desorption curve.

In this study, Tristar 3000 (Micromeritics) was employed for N_2 adsorption-desorption analysis with a pretreatment temperature of 150 °C for 2 hours. To compute the specific surface area (SSA) using N_2 adsorption-desorption isotherms, the Brunauer-Emmett-Teller (BET) analysis were used and pore size distribution was determined by non-linear density functional theory (NLDFT) and Barrett-Joyner-Halenda (BJH) methods.

3.3.6 UV-Visible spectroscopy

UV-Vis spectroscopy gives the absorbance/reflectance behavior of the sample which is used to determine its bandgap. It is an analytical method that compares the quantity of wavelengths of UV or visible light absorbed/reflected/transmitted by a sample to a reference or blank sample.

In this work, the absorbance/reflectance spectra were recorded using Hitachi double beam UV-Visible Spectrophotometer U-3900H for liquid/solid samples. The bandgap from absorbance spectra was determined by Tauc's plot method:

$$\beta(E_g - h\nu)\ \alpha\ (\alpha * h\nu)^{1/n} \qquad (3.2)$$

Where α, β, E_g, h, and ν are absorption coefficient, constant, bandgap, Planck's constant, and frequency of photons, respectively.

The bandgap from the reflectance spectra was determined using Kubelka-Munk equation:

$$h\nu\ \alpha\ (F * h\nu)^{1/n} \qquad (3.3)$$

Where, 'F' is the Kubelka-Munk function related to the absorbance and can be given as:

$$F = \frac{(1-R)^2}{2R} \qquad (3.4)$$

R is the % reflectance of the sample. In both the methods, 'n' represents the type of transitions such as allowed direct (0.5), allowed indirect (2.0), forbidden indirect (1.5), and forbidden direct (3.0) transitions. In carbon samples, n = 0.5 for allowed direct transitions [50].

3.3.7 Fourier transform infrared spectroscopy (FTIR)

FTIR gives the information of available surface functional groups on the sample. When infrared radiation is passed through a sample, part of it is absorbed and some is transmitted. The resulting signal at the detector is a spectrum that represents the sample's molecular fingerprint.

In the current study, chemical bonds present in the samples were investigated using Agilent Cary 660 FTIR and Shimadzu IRTracer-100 (from 400 to 4000 cm^{-1}) by making a pellet with KBr powder. The available active functional groups and bonds on the surface of the sample determine the interaction of the adsorbent with the surface. For preliminary qualitative analysis of major functional groups present in the samples, FTIR was carried out.

3.3.8 Raman spectroscopy

Raman spectroscopy helps to investigate the structural perfection and defects in samples. This approach is based on the monochromatic radiation interaction with matter, which results in inelastic scattering of photons, generating a change in associated energy in terms of wavenumber.

In the present study, to examine the samples' graphitization level, Raman spectra were recorded using a LabRAM HR spectrometer and Renishaw spectrometer (spatial resolution of ~1 μm) with a 532 nm laser excitation source.

3.3.9 X-ray photoelectron spectroscopy (XPS)

XPS provides the details of elemental composition as well as chemical state and density of electronic states in the sample. XPS is a surface-sensitive quantitative technique and the working principle of XPS involves the photoelectric effect. Valence band (VB) spectra obtained from XPS provides the value/location of valence band edge of the sample. This, in conjuction with the band gap of the sample, is further used to calculate conduction band edge.

To determine the surface elemental composition and VB spectra of the synthesized samples, XPS was carried out using PHI 5000 Versa Prob II, FEI Inc. with Al αK radiation XPS (1486.7 eV, Ag standard). The obtained results have been analysed using XPSPEAK41 software.

3.3.10 Point of zero charge (pH_{pzc})

pH_{pzc} is the pH at which the surface of the sample has no net charge. The sample's surface has a net positive charge below pH_{pzc} and a net negative charge above pH_{pzc}. To determine pH_{pzc}, the salt addition method was used. In a typical experiment, 10 mL NaCl solution (0.005 M) having a pH value from 4 to 11 (adjusted by using HCl and NaOH) was prepared. 3 mg of the sample was added to this solution and agitated for 24 hours by magnetic stirring. The final pH of the solution was measured and the change in pH was calculated. The plot between the initial pH and the change in pH is used to determine pH_{pzc} for the given sample.

3.4 Adsorption study

Adsorption studies were carried out for the requisite concentration of pollutant solution (adsorbate) containing requisite concentration of synthesized sample (adsorbent), under continuous stirring in dark conditions. After a specific time period, required amount of pollutant solution was taken out. The adsorbents were separated by centrifugation and the dye concentration in solution was determined using UV-Visible spectrophotometer. The details for each individual sample are discussed in each chapter further.

The adsorption capacity of the synthesized samples has been studied by varying the pollutant solution pH from 2 to 10 using 0.1M HCl or 0.1M NaOH solution. The recyclability tests were carried out to test the reusability of synthesized samples. Recylability tests were done by regenerating the sample by centrifuging out the sample and washing it with water. The regenerated sample was used for further adsorption to check the recyclability of the sample for the requisite number of consecutive cycles.

3.4.1 Adsorption isotherm modeling

To determine the efficiency of adsorbent material and the nature of adsorption, fitting with adsorption isotherms was used [176]. Commonly used adsorption isotherm models *viz.* Langmuir and Freundlich isotherm models have been fitted to the experimental data obtained for adsorption of pollutants onto synthesized samples. There are various isotherms models categorized as one parameter, two parameter, three parameter, four parameter and five parameter isotherm models. Among them Langmuir and Freundlich isotherms belong to two parameter isotherms category [177]. For adsorption of pollutants using carbon based systems, these two models are commonly used [178].

3.4.1.1 Langmuir isotherm

The Langmuir isotherm is applicable for monolayer adsorption. The equation with which the experimentally obtained data for adsorption of pollutant onto sample was fitted is expressed as [42]:

$$\frac{C_e}{q_e} = \frac{1}{k_L q_0} + \frac{C_e}{q_0} \qquad (3.5)$$

Where C_e, q_e, and q_o represent the equilibrium concentration of pollutant (mg/L), amount of pollutant adsorbed at equilibrium (mg/g) and amount of pollutant adsorbed initially (mg/g), respectively. k_L (L/min) is Langmuir isotherm constant and is determined from the slope and intercept of the linear fitting of the graph between C_e/q_e and C_e.

R_L is separation constant, gives the details of separation of adsorbate and adsorbent and is given by:

$$R_L = \frac{1}{1+k_L C_0} \qquad (3.6)$$

Here, four possible cases can occur: $R_L=0$ (irreversible adsorption), $0<R_L<1$ (favorable), $R_L=1$ (linear) and $R_L>1$ (unfavorable) [42].

3.4.1.2 Freundlich isotherm

Freundlich isotherm is applicable in the case when multilayer adsorption takes place [179]. The linear equation representing the Freundlich isotherm can be represented as:

$$\log q_e = \log k_f + \frac{1}{n}\log C_e \qquad (3.7)$$

The parameters k_f (L/g) and n (g/L) represent the Freundlich constant and Freundlich exponent, respectively. The value of n between 1 and 10 represents that the adsorption process is favorable.

3.4.2 Adsorption kinetic modeling

To determine the rate and mechanism of adsorption process, it is important to study the adsorption kinetics. The kinetic data for the adsorption of pollutants onto synthesized samples were tested for well-known kinetic models, namely pseudo first order (PFO) model and pseudo second order (PSO) model and Elovich model. To study the diffusion mechanism involved in the adsorption, the data were fitted with intraparticle diffusion (IPD) model. All these models provided the information about adsorbate-adsorbent interaction [180].

Following equations were used to calculate the experimental values of the amount of pollutant adsorbed, q_t (mg/g) at any time t and the amount adsorbed at equilibrium, q_e (mg/g) [181]:

$$q_t = \frac{(C_0 - C_t)V}{m} \quad (3.8)$$

$$q_e = \frac{(C_0 - C_e)V}{m} \quad (3.9)$$

C_0, C_t, and C_e represent the initial concentration, concentration at any time t, and equilibrium concentration of pollutant (mg/L), while V and m are the solution volume in liters and adsorbent weight in grams, respectively. The details discussion of kinetic models is given below.

3.4.2.1 Pseudo First Order (PFO) model

Lagergren proposed PFO to study the adsorption kinetics. The basic equation involved in PFO can be expressed as [181]:

$$\ln \frac{q_e}{q_e - q_t} = k_1 t \quad (3.10)$$

Where k_1 is PFO rate constant. PFO model assumes that physisorption takes place during adsorption and the adsorption amount is directly related to the available active sites [181].

3.4.2.2 Pseudo Second Order (PSO) model

PSO model can be applied for the analysis of adsorption equilibrium. The equation involved in the PSO model can be presented as [180]:

$$\frac{t}{q_t} = \frac{1}{k_2 q_e^2} + \frac{t}{q_e} \quad (3.11)$$

Here, k_2 is the rate constant, and q_e is the equilibrium adsorbate amount on the adsorbent and was determined using slope and intercept of the linear fit, respectively. According to PSO, the adsorption mechanism takes place via chemisorption, where, adsorption from a solution occurs as a result of physicochemical interactions between the two phases.

3.4.2.3 Elovich model

The fitting of experimental data with the Elovich model can be expressed with the equation:

$$q_{t=} \left(\frac{1}{\beta}\right) \ln(\alpha\beta) + \left(\frac{1}{\beta}\right) \ln(t) \quad (3.12)$$

Here, α is the initial adsorption rate and β is the desorption constant and were determined using slope and intercept of straight-line fit, respectively. According to Elovich model, the multilayer adsorption process occurs through chemisorption. The Elovich model assumes that the adsorbent is heterogeneous in nature (contains more than one type of active site) [180].

3.4.2.4 Intraparticle diffusion (IPD) model

The IPD model depicts adsorption processes in which the rate of adsorption is determined by the rate at which adsorbate diffuses towards adsorbent (i.e., the process is diffusion-controlled). IPD is the rate-limiting step in the adsorption process and follows the equation [182]:

$$q_t = k_{idn}\sqrt{t} + C \qquad (3.13)$$

Here, k_{idn} are rate constants of multiple fits (1to n for n no. of fits) and were determined using slopes of the multiple linear fits. If the linear fit passes through the origin, it implies that the adsorption process was controlled by IPD [182]. A two-step linear fit indicates that the adsorption occurs initially through boundary layer diffusion and then via intraparticle diffusion [42].

3.5 Photo-induced decolorization studies

Photo-induced activity was tested for the samples which showed best adsorption efficiency. The batch experiments were carried out similarly to the adsorption study in the presence of UV irradiation/sunlight instead of dark. The experiments were conducted in the presence of UV irradiation (Philips, 125 W; Hg lamp; λ_{em}=250–400 nm; intensity=~14000 lx) and sunlight (intensity=~17500 lx) under continuous cooling by water circulation. The setup for decolorization study under UV irradiation is shown in Fig. 3.6. The decolorization mechanism under UV irradiation was explained by carrying out the scavenger tests. In this process, 0.5 mM each of isopropyl alcohol (IPA) ascorbic acid (AA), ammonium oxalate (AO), sodium sulphate (SS), were taken as scavenging agents respectively for hydroxyl free radical ($^{\cdot}OH$), superoxide free radical anion ($O_2^{\cdot -}$), holes (h^+), and electrons (e^-). These scavenging agents were mixed individually with dye solution during UV irradiation experiment.

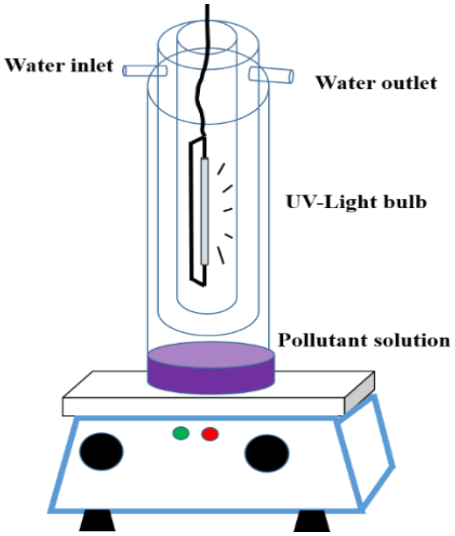

Fig. 3.6: Setup for photo decolorization study.

Chapter 4

N-doped soy based carbons

Overview

This chapter presents the results for the optimized high yield synthesis of N doped carbons. These were synthesized with hydrothermal method (HTC) using glucose as carbon source and protein-rich defatted soy flour as nitrogen and carbon source. The synthesized carbons were found to be spherical in shape and show better adsorption efficiency than both glucose derived HTC spheres and HTC synthesized soy flour hydrochar. To understand the properties of synthesized samples, SEM, TEM, XRD, FTIR, UV-visible spectroscopy, N_2 adsorption-desorption isotherm, XPS were carried out. The salt addition technique were used to determine the point of zero charge (pH_{pzc}) of the samples. The as-synthesized N-doped carbons have been used for the treatment of wastewater containing cationic dyes MB and CV, anionic dye EBT, pharmaceutical waste CIP, phenol PNP and phthalate ester DEP by their adsorption. For the best adsorption results, kinetic modeling and isotherm analysis has also been undertaken to determine the adsorption rate and adsorption mechanism.

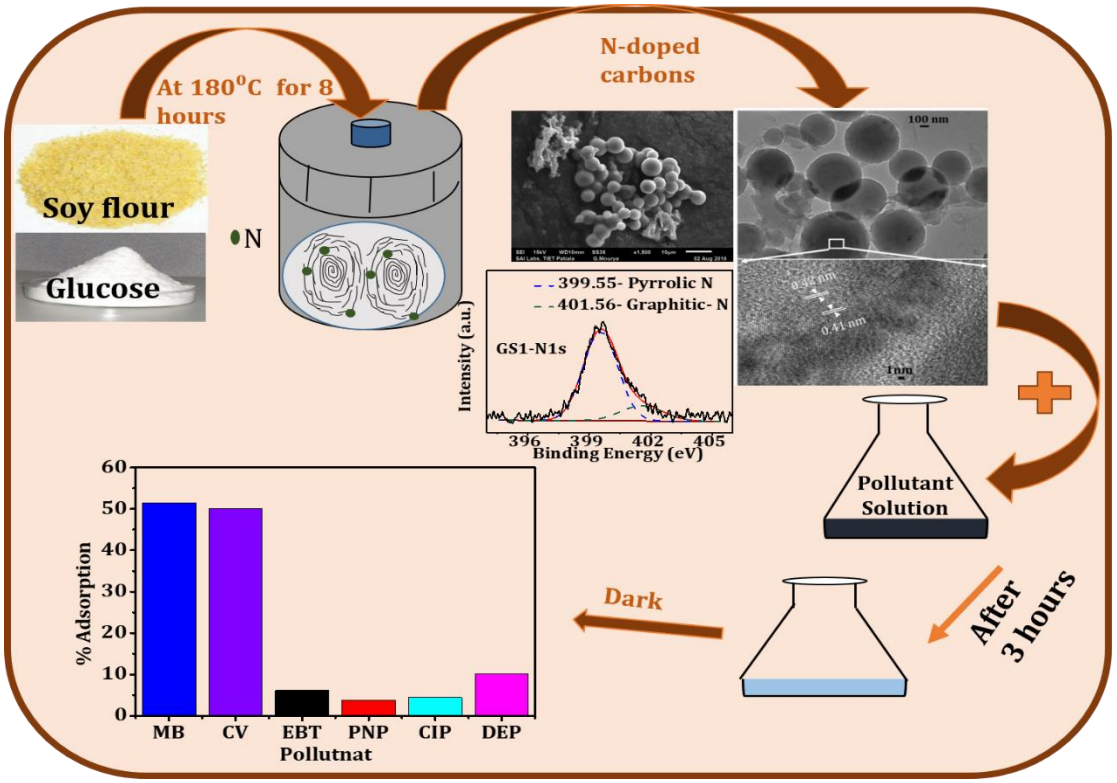

4.1 Introduction

Nitrogen (N) doping of carbon adsorbates enhances the basic character of porous carbons as N-doping sites act as lewis basic sites. This results in enhanced adsorption capacity as well as selectivity [103]. S´anchez-S´anchez *et al.* [63] reported that N-doping in carbon adsorbent results in an enhanced adsorption capacity for cationic as well as anionic dyes. The proteins in the precursor can act as the source for both nitrogen and carbons. Agro wastes rich in proteins can emerge as the cheapest source to synthesize N-doped carbons. Defatted soy meal contains 50.5% proteins, 34.2% carbohydrates and 15.3% fiber, ash and fat [183]. He *et al.* [184] reported that the standard chemical composition of defatted soy meal is crude protein, dietary fibre, amino acids and carbohydrate which makes soy flour a good source of carbon and nitrogen. Among different synthesis methods hydrothermal method was found to be most suitable because it is a low temperature green process.

The present chapter discusses in detail the synthesis parameter optimization and various characterizations of soy flour based N-doped carbons using saccharides.

Table 4.1: Details of the synthesized samples.

Sample ID	Precursor(s)	Precursor weight (g)	Precursors ratio (Saccharide: soy flour)	Yield (mg)	Average size (µm)	Bandgap (eV)
XS1	Xylose+soy flour	2.150	1:0.3	596	4.2	-
SS1	Surcose+soy flour	2.150	1:0.3	608	5.1	-
GSop1	Glucose+soy flour	2.150	1: 0.1	257	4.01	-
GSop2	Glucose+soy flour	2.150	1:0.2	390	4.42	-
GS1	Glucose+soy flour	2.150	1:0.3	600	4.96	4.5
GSop3	Glucose+soy flour	2.150	1:0.4	670	No	-
GS2	Glucose+soy flour	1.050	1:0.3	270	2.44	4.54
GS3	Glucose+soy flour	0.525	1:0.3	145	1.49	4.57
GS4	Glucose+soy flour	0.266	1:0.3	72	0.64	4.65
GS5	Glucose+soy flour	0.131	1:0.3	39	0.47	4.86
GS6	Glucose+soy flour	0.066	1:0.3	21	0.35	5
G	Glucose	2.150	1:0	13	0.64	3.38
S	Soy flour	2.150	0:1	350	No	5.5

4.2 Optimization of synthesis parameters for saccharide and soy-flour based N-doped carbons

The hydrothermal synthesis conditions are discussed in the previous chapter (section 3.2.1). The final optimized synthesis conditions were arrived by varying the initial conditions

such as precursor saccharide, precursors' weight ratio and total weight ratio. The different parameters taken into consideration before finalizing the parameters were: yield, cost, size, and adsorption characteristics. The optimized sample was further used for the removal of various pollutants from water via adsorption. Table 4.1 outlines the details of all synthesized samples.

4.2.1 Saccharide

The synthesis of N doped carbons was carried out using thee common saccharides viz. xylose, sucrose and glucose. Fig. 4.1 gives the representative SEM images of ***XS1***, ***SS1***, and ***GS1*** samples. Spheres were formed for all the samples and the image analysis brought to fore the log-normal distribution of the sphere size. It was observed that the size of spheres was smaller for xylose (XS1) while the addition of sucrose resulted in larger size (SS1). The glucose synthesized samples (GS1) are also nearly same size as SS1 (Table 4.1). The sample yield for the three precursors was equal (Table 4.1). Though the xylose samples having the smallest size spheres should be preferred, but considering the fact that xylose is much more expensive than the other two saccharides so it was eliminated for further use. The average price per kg for xylose (Rs 435/kg) is nearly 10 times the price of glucose (Rs 42/kg) and sucrose (Rs 45/kg). Among sucrose and glucose, sucrose is a disaccharide and contains glycosides linkage and the melting point of these linkages is above 260 °C. In the hydrothermal method, the maximum temperature was kept at 180 °C, so glucose is preferred.

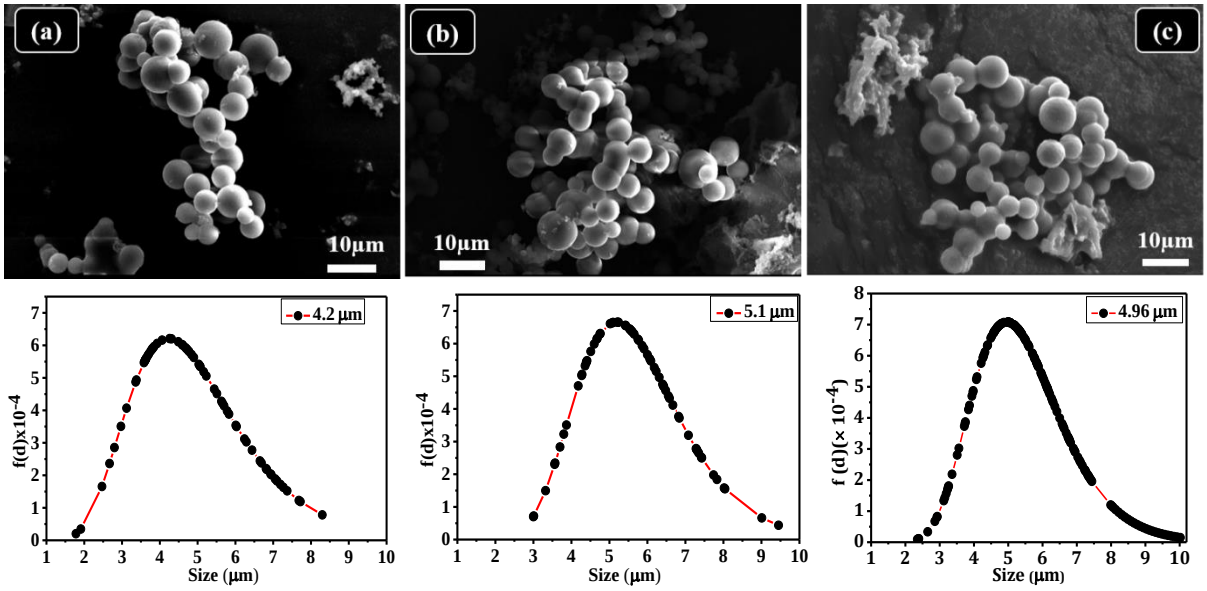

Fig. 4.1: SEM micrograph of (a) ***XS1*** (b) ***SS1*** and (c) ***GS1*** carbon spheres and their corresponding log- normal distribution of size.

Also as observed in the literature, the surface area and uniformity observed for the sample synthesized using glucose are higher than that of the sucrose [185,186]. Therefore

keeping these facts in mind and the fact that size was slightly lower for the glucose sample, glucose was used further for the synthesis of samples along with soy flour.

4.2.2 Glucose : soy flour ratio

To study the effect of variation of soy flour ratio on the morphology of samples, N-doped carbons were synthesized by varying the ratio of soy flour and glucose as mentioned in Table 4.1, and their SEM images are shown in Fig. 4.2. With the decrease in the ratio of soy flour to less than 0.3, the size of spheres reduced insignificantly but the yield reduced significantly (Table 4.1) than the ***GS1*** sample. When the ratio of soy flour was increased i.e. ***GSop3*** sample, no spherical structure was observed, as shown in SEM images. Therefore, by varying the ratios of soy flour and glucose, ***GS1*** with the glucose to soy flour ratio of 1:0.3 emerged to give the best results in terms of yield and average spheres size. Therefore, for the synthesis of N-doped carbons, the ratio of glucose and soy four was optimized to this value.

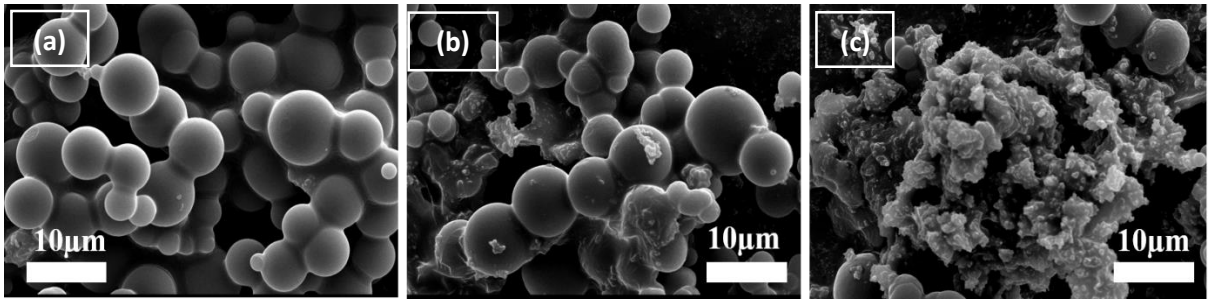

Fig. 4.2: SEM micrographs of samples synthesized for different ratio precursors: (a) ***GSop1*** (b) ***GSop2***, and (c) ***GSop3.***

4.2.3 Total precursor weight

To optimize the total weight of precursors in the starting solution, samples were synthesized with varying precursor concentrations while keeping the precursor's ratio constant (1:0.3) (Table 4.1). Fig. 4.3 gives the representative SEM micrographs of these samples. It indicated that both precursors (glucose and soy flour) still combined together to form spheres, but of different sizes. In certain areas, complete spherical features were observed, whereas in other areas flattened curve surface, an indication of the beginning of formation of spheres was observed. The spheres have smooth surfaces.

Fig. 4.4 (a) gives the variation of spheres size with initial precursor concentration. SEM images and the analyzed data clearly show that the sphere size of the synthesized samples decreases with decreasing precursor concentration in the initial dispersion. The effect of size of spheres was also tested on the adsorption efficiency of the samples for MB dye. It can be seen from Fig. 4.4 (b) (data was taken for 1 mg/L of MB adsorbed onto 4mg/L of synthesized

sample) that not much variation in the adsorption efficiency of the material with size variation occurs. Since, the yield obtained for ***GS1*** sample is nearly double even when compared with ***GS2*** sample, so, only ***GS1*** sample has been used for further studies.

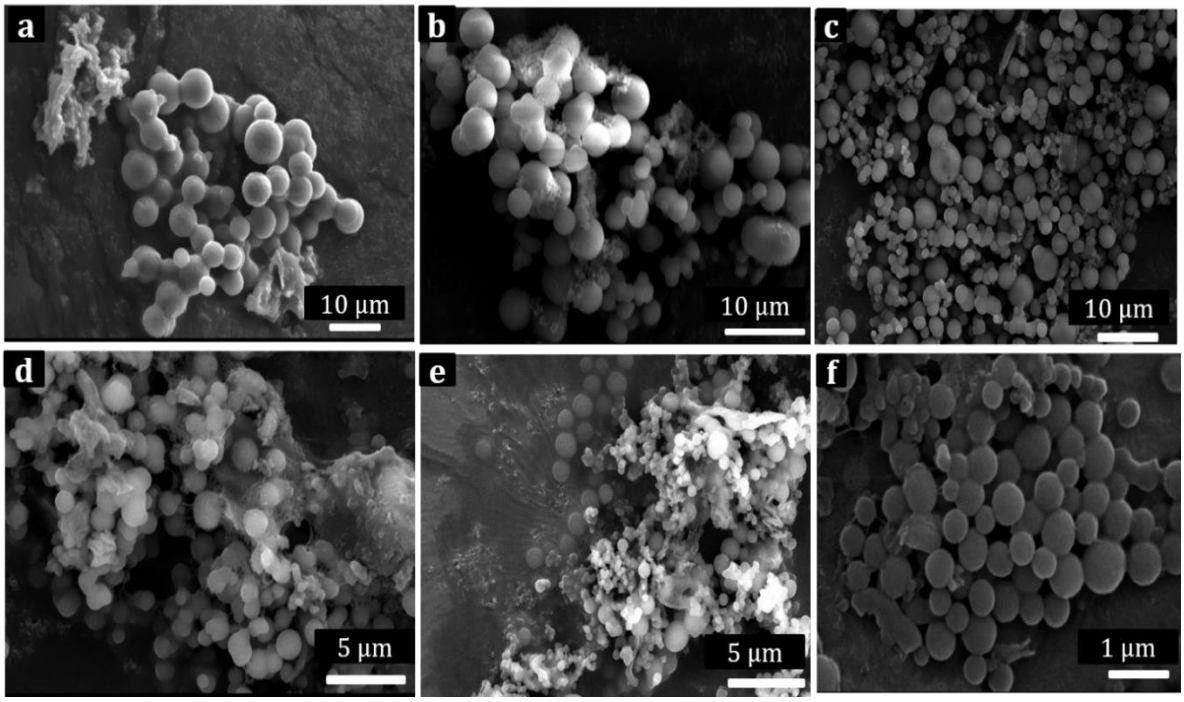

Fig. 4.3: SEM micrographs of samples synthesized for different initial concentrations of precursors: (a) ***GS1***, (b) ***GS2***, (c) ***GS3***, (d) ***GS4***, (e) ***GS5*** and (f) ***GS6.***

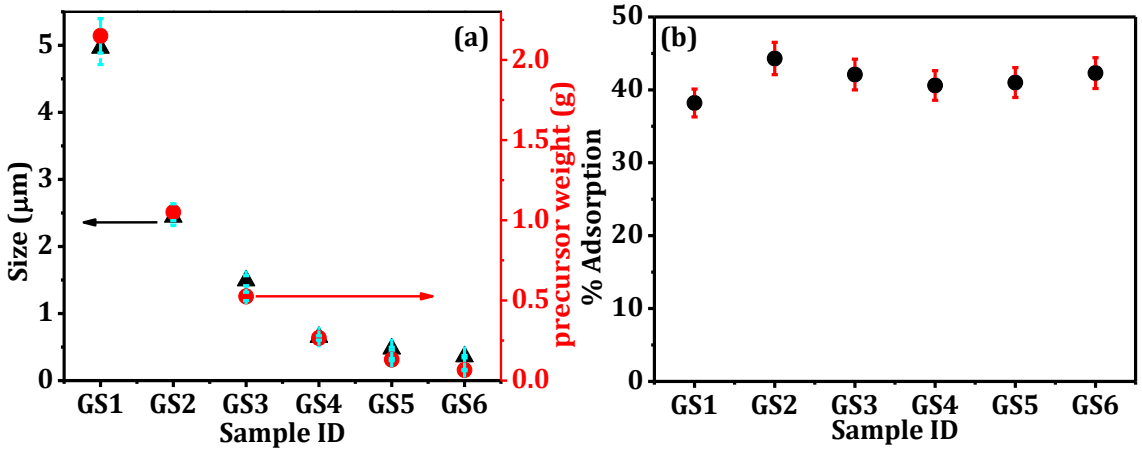

Fig. 4.4: (a) Variation in sphere size with precursor concentration in the initial solution and (b) % adsorption of MB onto the samples.

To compare the effect of mixing of glucose and soy flour, the samples were synthesized with only soy flour (***S***) and only glucose (***G***) by keeping precursor weight same (Table 4.1). Further characterizations were carried out for the optimized samples *viz.* ***S***, ***G*** and ***GS1*** sample.

4.3 Characterizations of optimized samples

4.3.1 SEM and EDS

SEM micrographs of samples synthesized using only soy flour (***S***) and glucose (***G***) samples (Fig. 4.5(a) and Fig. 4.5(b)) show that the hydrothermal treatment of soy flour alone does not lead to self-assembled structures/spheres. Also, it clearly emerged that the presence of soy flour in the initial dispersion has resulted in larger-sized spheres with non-uniform size distribution as compared with when only glucose was used (Table 4.1). Another important result emerged from the experiments was that the yield for the ***GS1*** sample (600 mg) is much higher as compared with samples ***S*** (350 mg) and ***G*** (13mg) with the starting precursor weight of 2.15g. In general, the yield from an HTC experiment depends on the amount of precursor and the reaction process. Thus combining the glucose (saccharide) and high protein precursors such as soy flour resulted in enhanced carbonization with self-assembled spheres and high yield.

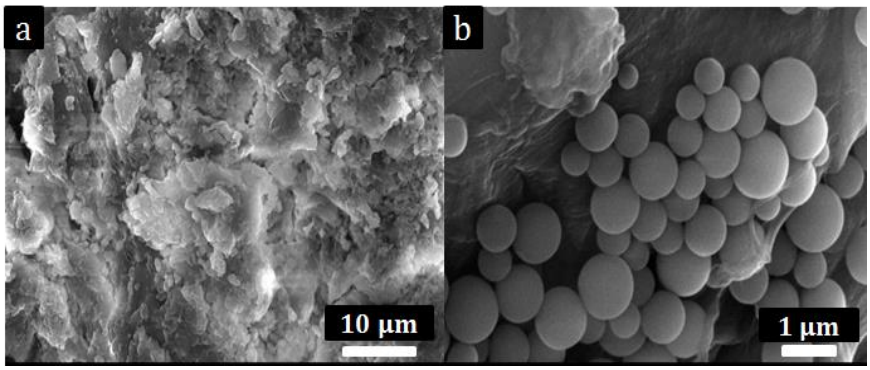

Fig. 4.5: SEM micrographs of (a) ***S*** and (b) ***G*** samples.

The elemental analysis of ***GS1***, ***S,*** and ***G*** samples using EDS is shown in Fig. 4.6. It can be seen that sample ***G*** carries peak of only carbon and oxygen, while, ***GS1*** and ***S*** have carbon, nitrogen and oxygen. The results of the EDS analysis are given in Table 4.2.

Table 4.2: Amount of C, N, and O present in the synthesized samples obtained from EDS.

Sample	Element	Weight %	Atomic %
GS1	C	64.04	69.83
	N	6.14	5.74
	O	29.83	24.43
S	C	61.45	67.13
	N	10.77	10.09
	O	27.78	22.78
G	C	67.21	73.20
	O	32.79	26.80

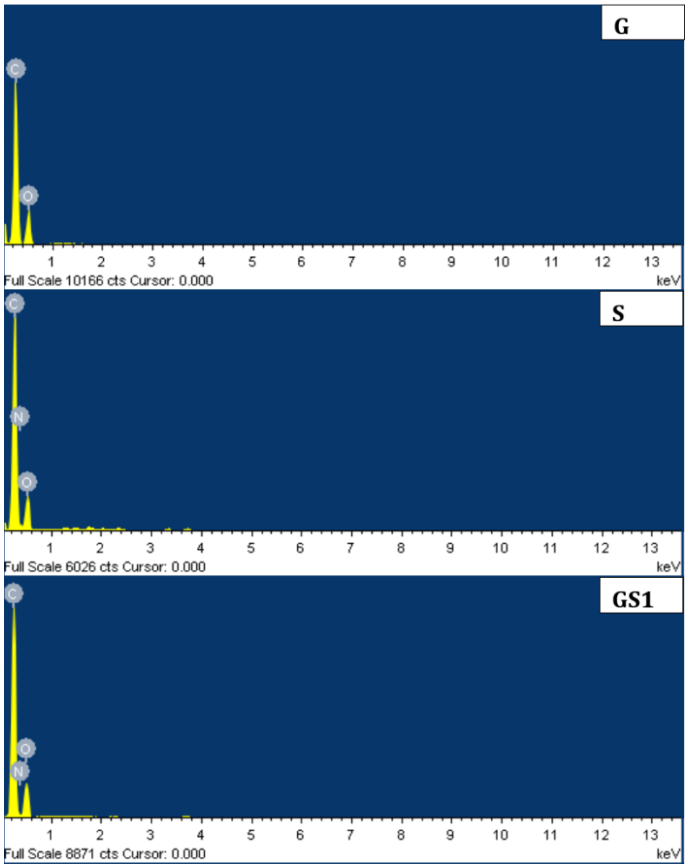

Fig. 4.6: EDS of ***G, S*** and ***GS1*** samples

4.3.2 XRD

The structural nature of the synthesized material was investigated using XRD. The XRD pattern for ***GS1*** sample (Fig. 4.7(a)) shows a broad hump at $2\theta \approx 21°$, and a peak at $2\theta \approx 26°$. The hump at 21° is a signature of carbon quantum dots (CQDs) and attributed to (002) lattice spacing of amorphous carbon material (indexed as (002)-CQD) [187]. For undoped carbon nanospheres (Sample **G** and literature [188]) the XRD line profile shows a hump at $2\theta \approx 24°$ that correspond with (002) plane of graphitic carbon (indexed as (002)-CNS). The XRD line profile for the **S** Sample revealed prominent peaks at $2\theta \approx 22°$ and 26°. The peak at 22° is attributed to the (002) plane in amorphous carbon having oxygen containing functional group (indexed as (002)-AO) [189]. The peak at 26° is attributed to (002) plane of graphitic carbon (indexed as (002)-g). Both these peaks confirm the hydrochar nature of the sample **S**. Presence of the peak at 26° in the ***GS1*** sample confirmed the presence of graphitic carbon in the sample along with the CQDs.

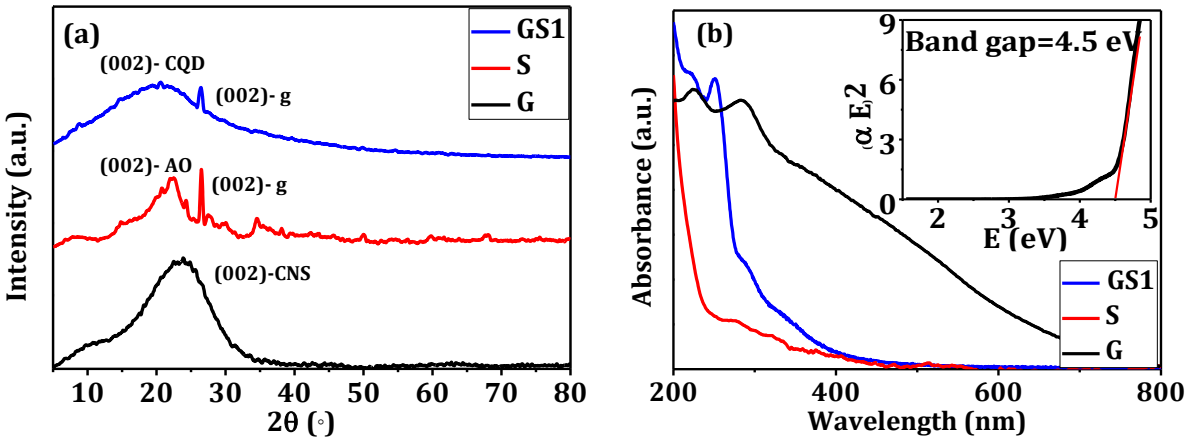

Fig. 4.7: (a) XRD and (b) absorbance spectra for ***G***, ***S,*** and ***GS1*** samples and inset (b) show Tauc-plot of ***GS1*** sample.

4.3.3 UV-Visible spectroscopy

Absorbance spectra from the UV-Visible spectroscopy measurement for the ***GS1***, ***S*** and ***G*** samples are shown in Fig. 4.7(b). It was observed that the main absorbance peak of ***S*** sample appears at nearly 200 nm in the UV region, which shows the π-π^* transition between the bands of graphitic carbon material. Two main absorbance peaks of ***G*** sample at nearly 280 nm and 224 nm indicated the n-π^* transition of C=O and π-π^* transition of the C=C bond [190]. ***GS1*** sample shows an absorption peak near 250nm, clearly indicating the π-π* transition between the domains of graphitic carbon, and this matches with data obtained for CQDs in literature [191]. This data supported the presence of a broad peak in the XRD line profile at ~21° for GS1 rather than at 22° (for **S**) or 24° (for **G**). The low-intensity peak/hump near 280 nm indicates the lowered concentration of C=O bonds in the sample. This indicated that the CQDs are not exposed to oxygen-rich environs after formation. The inset of Fig. 4.7(b) gives the Tauc's plot for the ***GS1*** sample. The band gaps for ***G***, ***S,*** and ***GS1*** to ***GS6*** samples were determined. The band gap increased from 4.5 to 5 eV with decrease in the size of the sample from ***GS1*** to ***GS6*** (Table 4.1).

4.3.4 HR-TEM

SEM micrographs of **GS1** sample show large spheres of average size 4.96 μm. This data is in contrast with the XRD line profile and UV-Vis data which indicated the presence of CQDs in the sample. It can be conjectured that the CQDs will not be visible in the magnifications of SEM. **GS1** samples are separated at the centrifuge speed of 4500 rpm. CQDs will not separate out of the solution at such low speeds. To understand the internal morphology of the carbon spheres and the TEM/HR-TEM studies were carried out. To ensure that the clear

picture emerges of the internal structure the **GS6** sample with average size of 350 nm was used for these studies. Fig. 4.8(a) gives the representative TEM image for the **GS6** sample clearly showing the nonuniform size distribution of solid spheres. The non speroidal material (also seen in SEM micrographs) under HR-TEM analysis emerged as graphitic carbon with interplaner spacing of ~0.33 nm, corresponding to $2\theta \approx 26°$ (Fig. 4.8(b)) [192]. HR-TEM of the spheres shows that the core of the spheres consists of CQDs with interplanar spacing of 0.41 nm corresponding to $2\theta \approx 21°$ (Fig. 4.8(c)) [193]. These results have been used to elucidate the synthesis mechanism of N doped carbon spheres using glucose and soy flour via HTC method (Section 4.4).

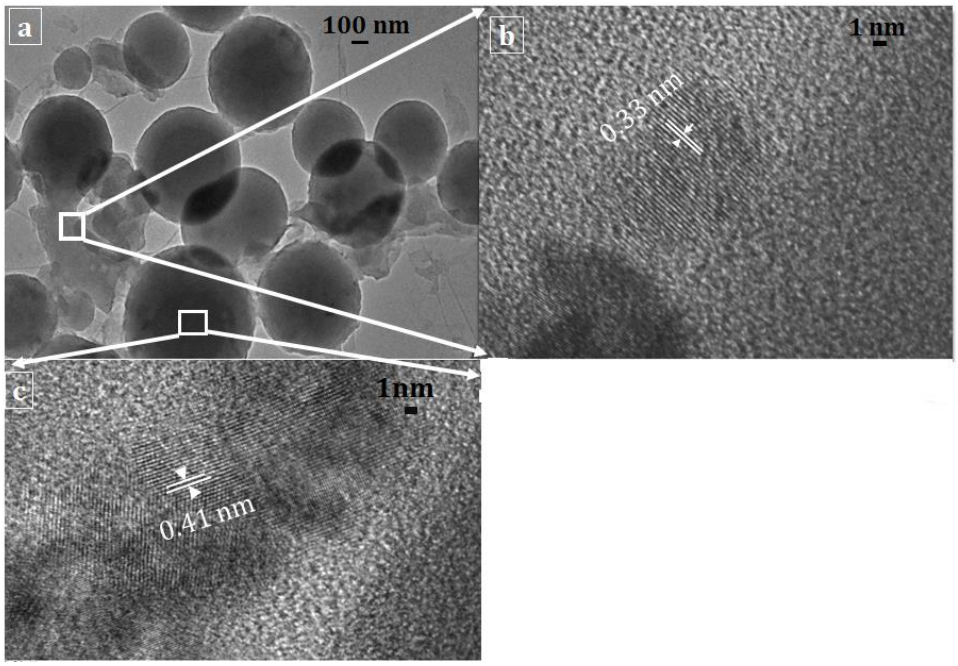

Fig. 4.8: (a) TEM images of ***GS6***, (b) HR-TEM of non-spheroid material indicating graphitic carbon (c) HR-TEM of the core of sphere showing carbon quantum dots.

4.3.5 FTIR spectroscopy

Fig. 4.9(a) shows the FTIR spectra for the ***GS1*** sample. The characteristic band for O-H is available around 3380 cm^{-1}. Various bonds of carbon with carbon, oxygen, hydrogen are visible and have been marked. C-H stretch band peak was observed around 2921 cm^{-1}. Another broad peak at ~ 1640 cm^{-1} represented the stretch vibration of C=C. Peak around 1460 cm^{-1} indicated the presence of aliphatic C-H bending group. Low intensity peaks around 1200 and 1500 cm^{-1} indicate the presence of C-N and C=N bond confirming the presence of nitrogen in the sample [84]. These FTIR results confirm the presence of adsorbed water and dangling bonds on the surface of the synthesized samples as well as N-doping. All three are indicators

for the synthesized samples to have good adsorption characteristics [188]. The exact nature of N-doping was examined in detail by XPS analysis (section 4.3.7).

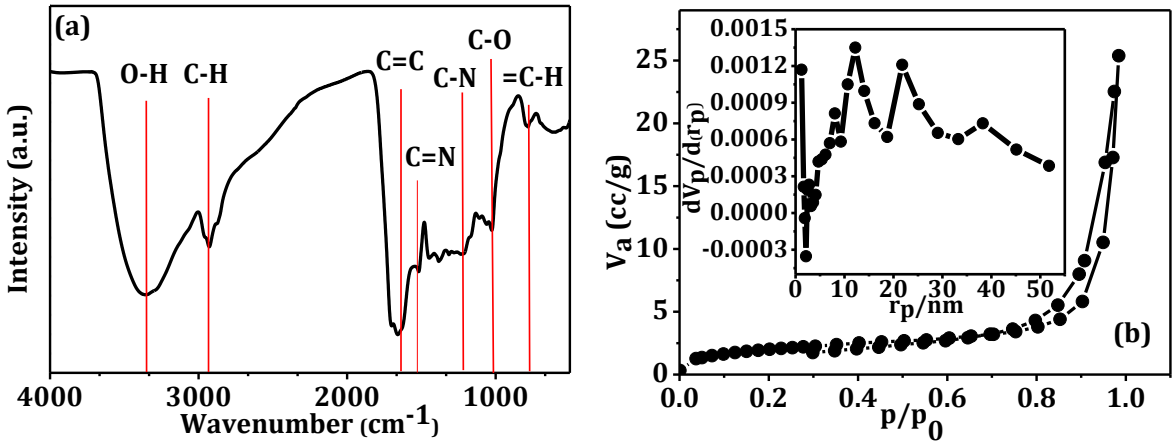

Fig. 4.9: (a) FTIR spectra of ***GS1*** sample and (b) N_2 adsorption-desorption isotherm and inset shows pore size distribution of ***GS1*** sample.

4.3.6 N_2 adsorption-desorption isotherm

Fig. 4.9(b) shows the N_2 adsorption-desorption isotherm and the pore size distribution (inset) for ***GS1*** sample. The BET isotherm displays type II IUPAC curve [194]. The H4 type adsorption hysteresis of the BET data indicated that the sample contains both micropores and mesopores. The calculated BET surface area was 7.43 m^2/g. Pore size distribution graph showed that pore size distribution is not uniform for the sample and ranged from micropore to mesopore region with a the total calculated pore volume of 0.0393 cm^3/g.. The pore size varies from 1.5 to 25 nm in mesopore region with a mean pore diameter of 21.1 nm. An important aspect of this data is that the microporous pores (pore size < 2 nm) were also substantial in number.

4.3.7 XPS

Comparison of XPS survey spectra of ***GS1***, ***S*** and ***G*** samples is shown in Fig. 4.10(a), with peaks at ~ 284.0 eV, 400.0 eV and 531.0 eV for C1s, N1s and O1s, respectively [82]. Absence of N1s peak for ***G*** sample clearly indicated that the incorporation of N in the synthesized samples occurred due to presence of soy flour in the initial precursor. The HR spectra of C1s for ***GS1*** sample deconvoluted into 3 peaks from 284 to 287 eV showing the presence of sp^2 hybridized carbon atoms, C-N and C-O bonds (Fig. 4.10(b)) [195]. The deconvolution of HR spectra of N1s for ***GS1*** sample indicated the presence of pyrrolic and graphitic N as indicated from peaks at 399.55 and 401.56 eV (Fig. 4.10(c)) [61,196]. Fig.

4.10(d) shows the N1s spectra of ***S*** sample and shows the presence of pyrrolic, oxidized and pyridinic nitrogen. From O1s HR spectra for ***GS1*** sample, it can be seen that the C=O bonds are present along with the C-O bonds (Fig. 4.10(e)). Table 4.3 and Table 4.4 give the parameters obtained from XPS analysis. It indicated the presence of 2.2% predominantly pyrrolic nitrogen in the samples. Different types of N bonding are shown in Fig. 4.10(f).

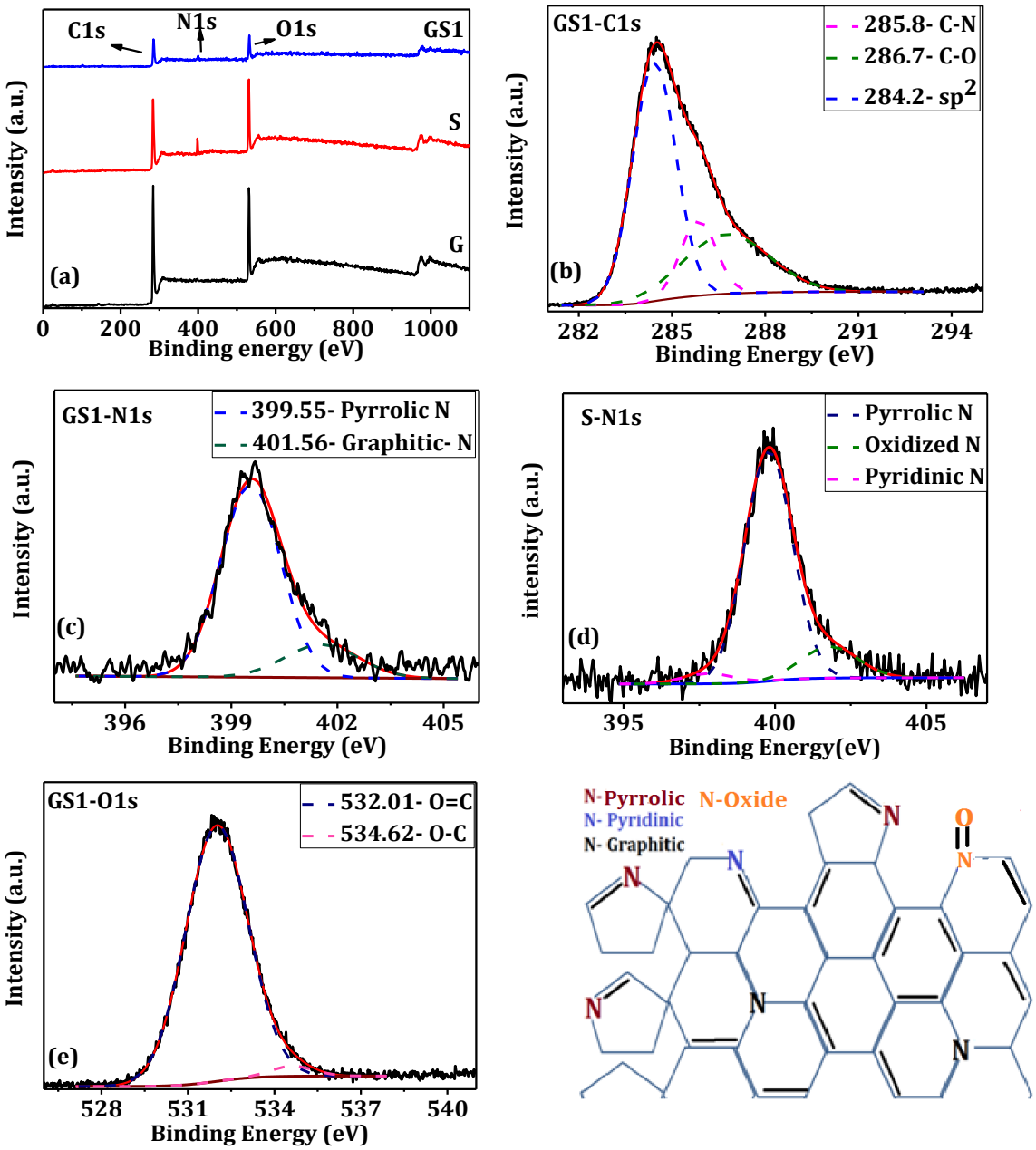

Fig. 4.10: (a) Comparison of the XPS survey spectrum of ***GS1***, ***S*** and ***G*** samples, deconvoluted peaks of (b) C1s of ***GS1*** (c) N1s of ***GS1*** (d) N1s of ***S*** (e) O1s of ***GS1*** and (f) types of N bonding.

Table 4.3: atomic percentage amount of C, N, and O present in the synthesized samples.

Sample ID	%C	%N	%O	pH_{pzc}
G	75.55	0	24.44	2.13
S	69.34	7.03	23.52	3.6
GS1	74.10	2.22	23.68	4.6

Table 4.4: XPS analysis parameters for ***GS1*.**

	Total %at.	Group	Position(eV)	FWHM	%at.
C1s	74.10	C sp^2	284.2	1.64	56.99
		C-N	285.8	1.36	14.8
		C-O	286.7	3.26	28.21
N1s	2.22	Pyrrolic-N	399.5	2.00	82.56
		Graphitic-N	401.5	2.46	17.44
O1s	23.68	C=O	532.0	2.55	97.36
		C-O	534.6	1.72	3.64

The % amount of nitrogen atoms present in the soy flour is about 8% [184]. For ***GS1*** sample, the amount of soy flour is ~ 25% of the total precursor content. XPS results shows that 2.2% nitrogen is present in the sample, which is nearly 2% (25% of 8%). Thus, almost all the nitrogen present in soy flour got doped in the synthesized samples.

4.3.8 Point of zero charge (pH_{pzc})

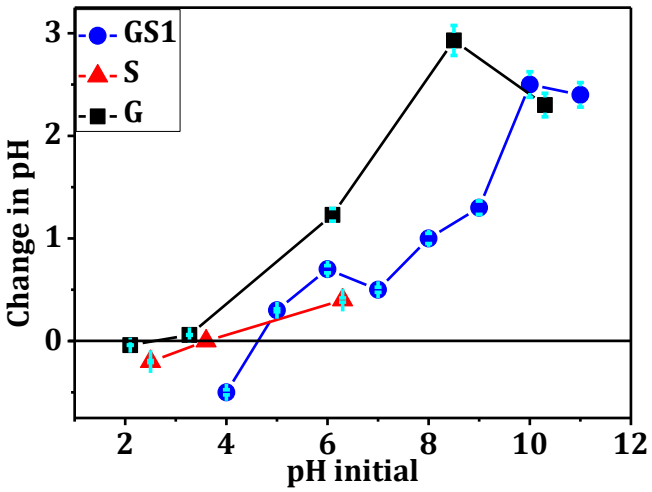

Fig. 4.11: Graph for point of zero charge (pH_{pzc}) determination for ***GS1***, ***S*** and ***G*** samples.

Surface charge plays a decisive role to determine the adsorption properties of a given material. Point of zero charge (pH_{pzc}) is the value of pH at which the net charge on the surface of the material is zero and is used to determine the surface charge characteristics of the given sample. Fig. 4.11 gives the salt addition method analysis for the ***GS1***, ***S*** and ***G*** samples with

the pH_{pzc} values coming out to be 4.6, 3.6 and 2.13, respectively (Table 4.3). Larger pH_{pzc} value for sample ***S*** in comparison with sample ***G*** is due to the enhanced basicity of the surface as a result of nitrogen presence. The highest pH_{pzc} value at 4.6 is obtained for ***GS1*** inspite of having lower amount of nitrogen as compared with the ***S*** sample. This is because the nitrogen in ***S*** sample is partially oxidized as confirmed by N1s XPS spectra of sample ***S*** [197].

4.4 Formation mechanism of N-doped carbon spheres from glucose and soy flour

The formation mechanism of the spherical shaped carbons using saccharides via HTC is well documented [189,198]. Under hydrothermal conditions the saccharides undergo dehydration and fragmentation to form phenols, aldehydes and furfural like molecules. These water soluble molecules further polymerize via condensation reactions resulting in aromatization of these polymeric chains through dehydration to form graphene flakes at temperature greater than 160 °C. These graphene flakes act as nuclei and curve around each other during carbonization to form spherical carbons [189,199].

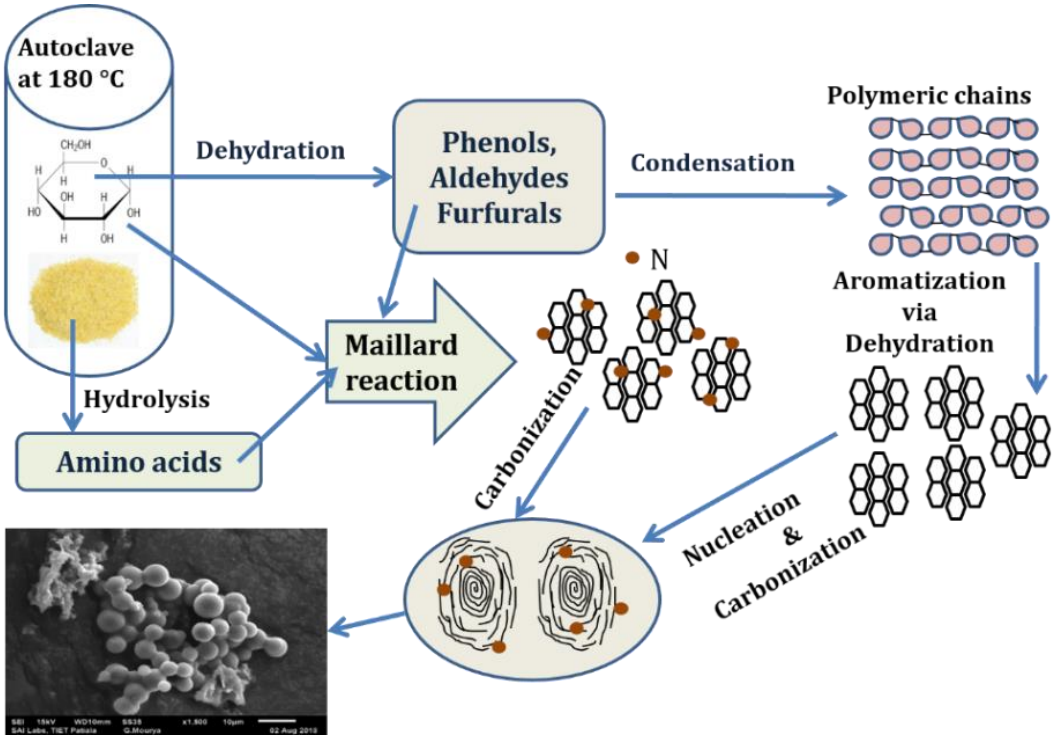

Fig. 4.12: Formation mechanism of ***GS1*** spheres.

For the protein-rich biomaterials, under the HTC conditions the lower content of hydrocarbons in comparison with proteins results in formation of hydrochar/biochar [199]. The small fraction of carbohydrates present undergo a series of reactions such as hydrolysis, dehydration, polymerization and aggregation to form coke. Simultaneously, the excess amount

of proteins undergo hydrolysis to form amino acids which undergo the Maillard reaction with the degradation products of carbohydrates to form N containing ring compounds. These compounds finally combine with the coke to form hydrochar of undetermined structure. The complexity of reaction mechanism followed by proteins interactions hinders the nucleation. This lack of available nucleation sites prevent the formation of the spherical structures [90,200,201].

In the present work, glucose has been added in addition to soy flour as a precursor to provide nucleation sites and assist in carbonization. When taken into consideration various characterization results (XRD, UV-Vis, TEM, HR TEM, SEM) for the N-doped spheres, the following formation mechanism has been proposed (Fig. 4.12). The glucose molecules undergo simultaneous dehydration-hydrolysis and then polymerize to form long chains. After that, through aromatization, pentagonal, hexagonal and heptagonal graphitic rings are formed. Here, partial carbonization led to form carbon dots prior to the process of nucleation. The formation of carbon dots and their presence in the core of the carbon spheres is confirmed by UV-Visible spectroscopy, XRD and HR-TEM for ***GS1*** sample. These carbon dots provide the nucleation sites for the spherical structures to be formed around them. The carbonized soy flour with N containing ring compounds and aromatized glucose curves around the nucleus to form a sphere. Due to involvement of bigger polymeric chains of soy flour, the size of the spheres formed is multiple times more than that of ***G*** sample spheres [91,200].

This synthesis mechanism brings together the characterization results for the present samples and the available literature in the field of high protein carbonization [199]. The role of carbon rich saccharide (glucose) in providing the nucleation sites in the form of CQDs which facilitate the carbonization of the protein and spheres formation is confirmed.

4.5 Adsorption studies

4.5.1 Optimization of adsorbate and adsorbent concentrations for adsorption studies

To determine the optimum concentration of pollutants and adsorbent, the adsorption tests were conducted using varying concentration of pollutants (1, 5, 10, 20, 50 mg/L) and ***GS1*** sample (20, 40, 60, 80, 100 mg/L). The % adsorption after 3 hours with varying aforementioned parameters is shown in Fig. 4.13. It was observed that for MB and EBT dye, the maximum % adsorption was observed for 1 mg/L of dyes. With variation in the ***GS1*** concentration at 1mg/L of dye, no difference in the % adsorption was observed. Therefore, the amount of dyes (MB and EBT) for further studies were taken as 1 mg/L with 20 mg/L of adsorbent. The variation in % adsorption was not much with the dye and adsorbent concentration variation for PNP, CIP

and DEP. But for 20mg/L of PNP, CIP and DEP, maximum % adsorption was observed for 100 mg/L of adsorbent. Therefore for further studies, 20 mg/L of PNP, CIP and DEP with 100 mg/L of adsorbent amount were used.

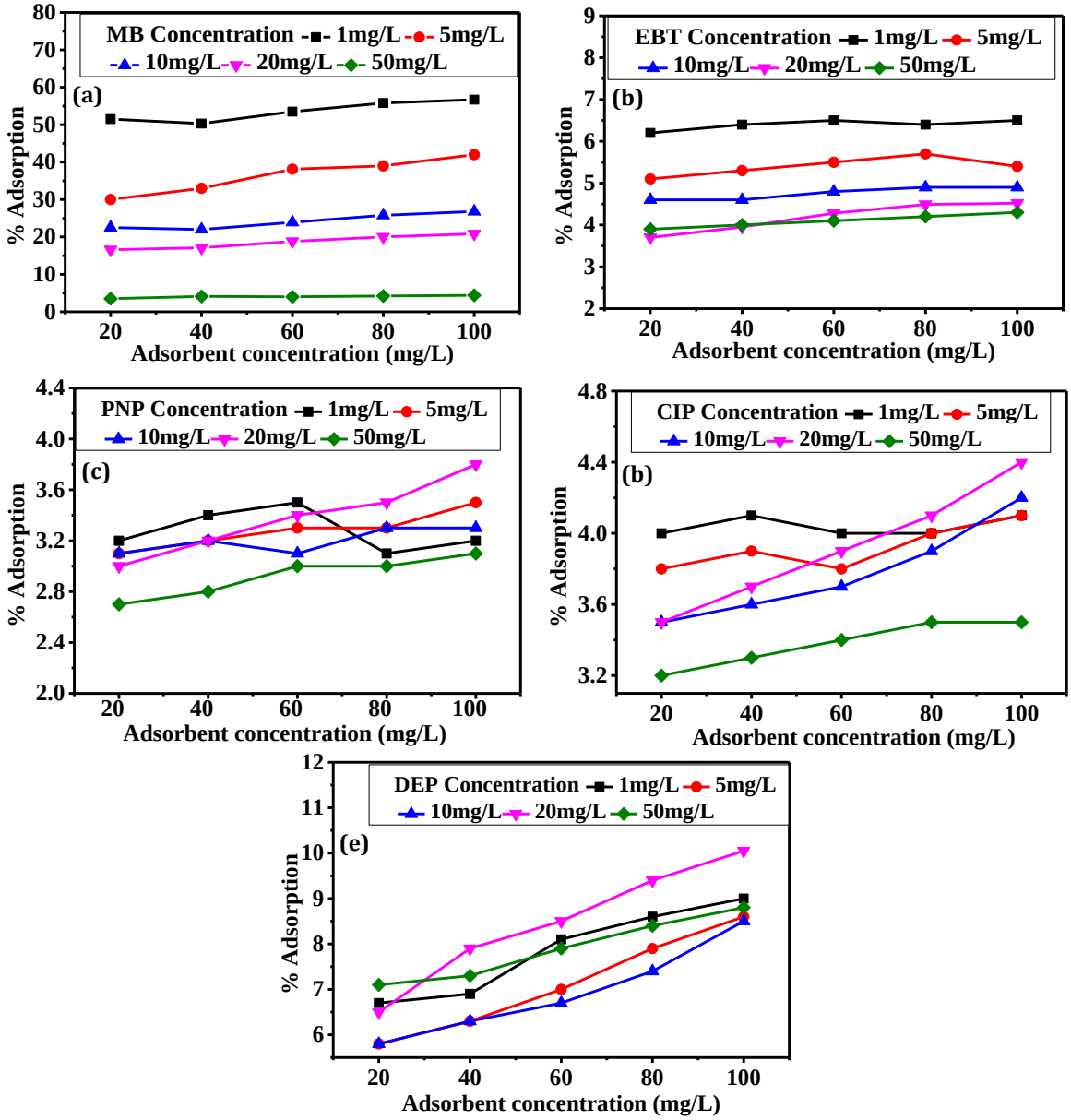

Fig. 4.13: % Adsorption with change in ***GS1*** concentration (20, 40, 60, 80 100 mg/L) and adsorbate concentration (1, 5, 10, 20, 50 mg/L) with (a) MB, (b) EBT, (c) PNP, (d) CIP and, (e) DEP.

4.5.2 Adsorption study of N-doped carbons for model pollutants

From pH_{pzc} of samples, ***GS1*** sample was found to be more suitable to adsorb both cationic and anionic pollutants at natural water conditions. While the other two samples are more likely to adsorb cationic pollutants because above the pH_{pzc} value the surface has a net negative charge.

The adsorption studies were carried out for the removal of MB, CV, EBT, PNP, CIP, and DEP using ***GS1*** sample. For adsorption of dyes, the amount of adsorbate and adsorbent were taken as 1 mg/L and 20 mg/L, respectively. After 3 hours, the amount of MB and CV adsorbed on the surface of sample ***GS1*** are 51.5% and 50%, respectively. For anionic dye EBT, the % adsorption was decreased to 6.1%. The adsorption study for PNP, CIP and DEP were conducted in dark for 20 mg/L of pollutant and 100 mg/L of ***GS1*** sample. It was observed that after 3 hours of agitation, the % adsorption for PNP, CIP and DEP were 3.8%, 4.4% and 10.05%, respectively. The maximum adsorption was observed for cationic dyes only (Fig 4.14 (a)). Fig. 4.14(b) shows the evolution of MB dye adsorption onto sample ***GS1*** with time.

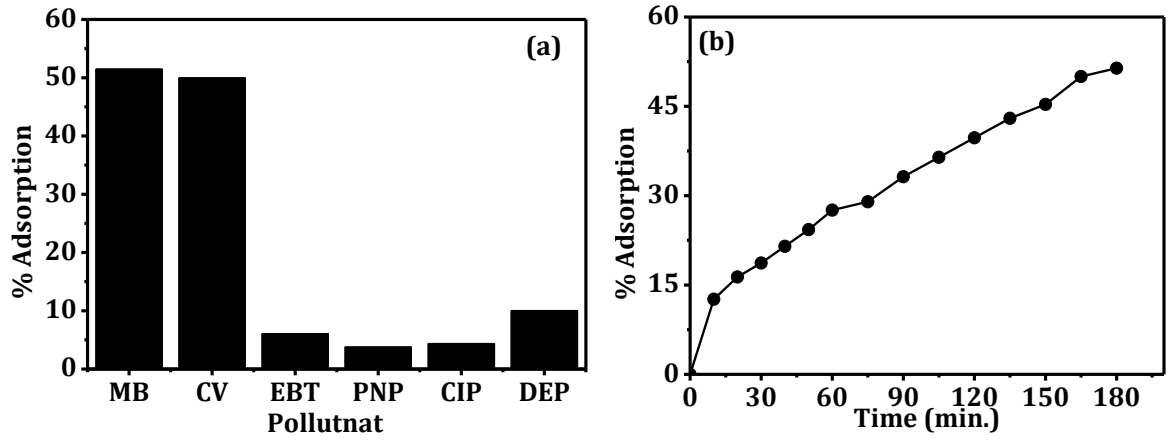

Fig. 4.14: The % adsorption of (a) pollutants, (b) MB in dark onto ***GS1*** sample with time.

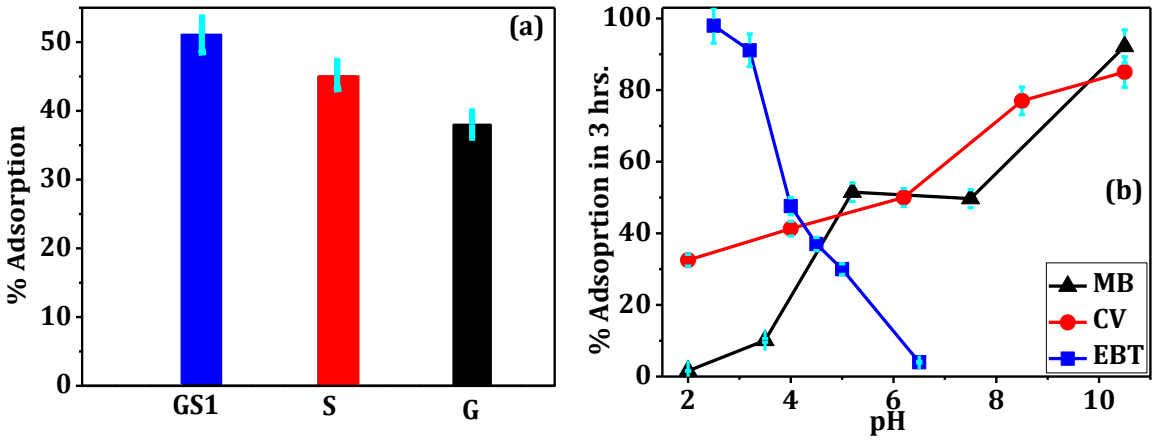

Fig. 4.15: (a) Comparison of % adsorption of MB dye (1mg/L) in dark for ***GS1***, ***S*** and ***G*** samples (20 mg/L), (b) % adsorption change with pH for MB, CV and EBT.

Fig. 4.15(a) compares the adsorption properties in dark (for cationic dye MB) of ***GS1*** sample with the ***S*** and ***G*** samples. The results clearly show that despite of the larger size (4.96 μm) the adsorption properties of the ***GS1*** sample (51%) are superior in comparison to the undoped ***G*** sample (640 nm, 38%). Moreover, despite the lesser content of nitrogen as compared to ***S*** sample the ***GS1*** has shown better adsorption. It is believed that this may be due

to partial oxidation of the nitrogen in the ***S*** sample (as indicated by the XPS results) which modified the surface charge and hence the adsorption.

4.5.3 Effect of pH on adsorption of cationic and anionic dyes

The pH of all the dye solutions (at the considered concentrations) lies between 5-6. The effect of pH on adsorption of cationic as well as anionic dyes was investigated and the results are shown in Fig. 4.15(b). The effect of pH was also observed for DEP, but no significant variation was observed (data not shown). At low pH the adsorption of the cationic dye onto the samples is hindered due to more positive charge on the surface of the carbon spheres. With increasing pH, the surface of carbon spheres becomes more and more negative and due to electrostatic attraction and/or hydrogen bonding, uptake of cationic dyes increases on the surface of synthesized sample [176]. It can be observed from Fig. 4.15(b), that the % adsorption of the cationic dyes (MB and CV) reaches the value of 92.2% (MB) and 84.9% (CV) at pH 10. The effect of pH on adsorption was reversed for anionic dye (EBT). It is clear from Fig. 4.15(b) that for EBT, adsorption of about 98% took place at pH 2.4 but with an increase in pH, there is a decrease in the adsorption and it reaches a value of 6% at pH 6.5. The adsorption results are in line with the pH_{pzc} value of 4.5 for ***GS1***. Above this pH the cationic dyes were adsorbed more and below it the anionic dyes adsorption increases.

4.5.4 Recyclability of *GS1*

The ***GS1*** was also checked for reusability. This was done by regenerating the sample by centrifuging and washing with water. The regenerated sample was used for further adsorption to check the recyclability of the sample for 14 consecutive cycles for MB dye (100 mg/L of ***GS1*** sample). The small decrease of 6% was observed in the adsorption capacity after 14 cycles. This shows the recyclability of the sample as shown in Fig. 4.16.

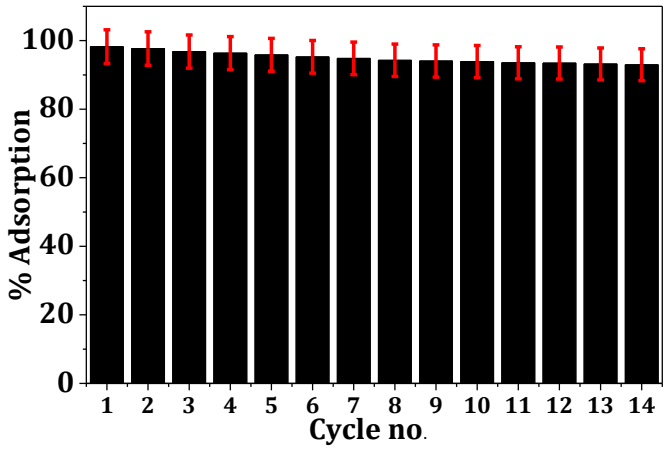

Fig. 4.16: Recyclability of ***GS1*** (100 mg/L) in dark for MB dye (1 mg/L).

The small amount of decrease in % adsorption observed with increase in number of cycle was due to loss of sample during washing. Here it is important to note that ***GS1*** sample consisted of large spheres so it was easy to centrifuge them out of the solution even at low speed of 4500 rpm rather than needing high speed centrifuge or other specialized techniques such as dialysis etc.

4.5.5 Adsorption Isotherm modeling

The adsorption isotherms for MB and EBT dyes (Fig. 4.17(a) and Fig. 4.17(b)) are obtained for change in % adsorption with change in dye (adsorbate) concentrations (1-50 mg/L) for a constant amount of adsorbent (100 mg/L). The increase in the dye amount increases the mass transfer force. This resulted in a higher amount of dye absorbed onto the surface of ***GS1*** sample [9]. It is clear from the Fig. 4.17(a) that the amount of MB adsorbed has a maximum value q_e ~ 52 mg/g at C_e ~ 20 mg/L. A further increase in the dye concentration (50mg/L) results in a slight decrease which may be due to stearic hindrance offered by already adsorbed dye to further adsorption on the surface. For the EBT since the overall adsorption is less so no saturation is observed. The ***GS1*** sample shows q_e ~ 31.5 mg/g of EBT for C_e ~ 50 mg/L.

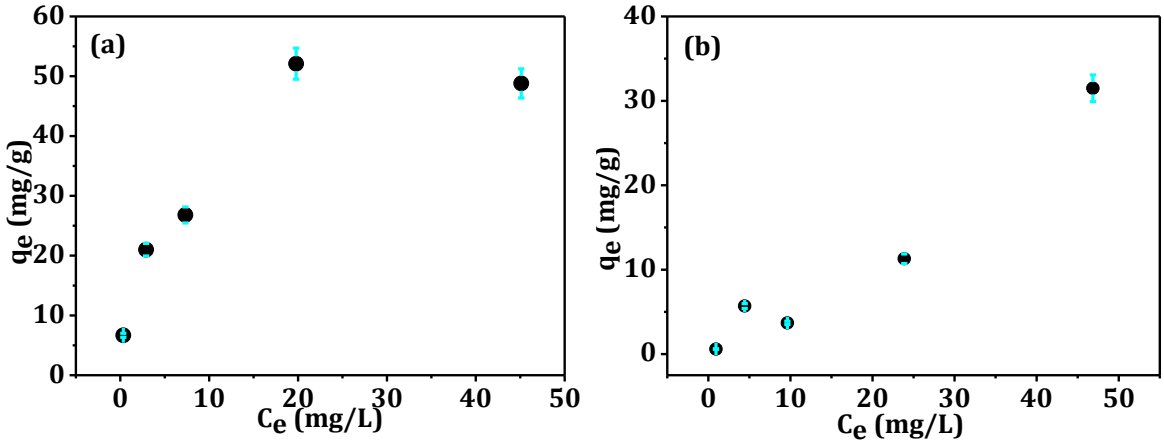

Fig. 4.17: Adsorption isotherm obtained for adsorption of (a) MB and (b) EBT dye with change in adsorbate amount.

Adsorption isotherms help with the adsorbent materials efficiency interpretation and the theoretical model fits to the data provide information about the nature of the adsorption [176]. Two adsorption isotherm models, namely Langmuir and Freundlich isotherm models have been fitted to the experimental data obtained for adsorption of MB and EBT dyes onto ***GS1*** sample. Fig. 4.18 and Fig. 4.19 give the graphs for isotherm fitting for MB and EBT dye, respectively.

The experimentally calculated values of amount of dye adsorbed at time *t*, q_t (mg/g) and amount of dye adsorbed at equilibrium, q_e (mg/g), for MB and EBT adsorbed at any time t onto ***GS1*** sample are obtained using equation 3.5 and 3.6 as explained in chapter 3 (section 3.4.2).

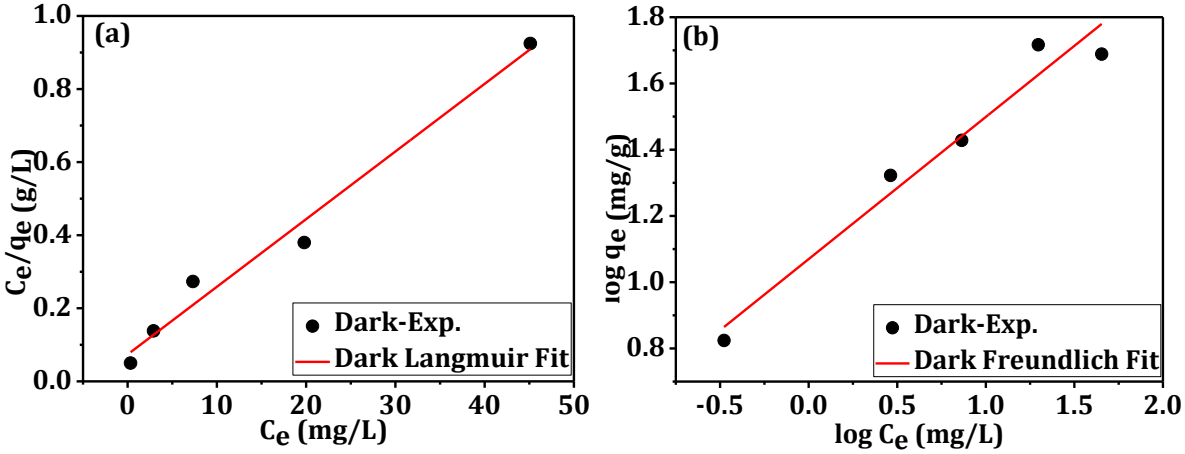

Fig. 4.18: Isotherm fitting for MB (1mg/L) adsorbed on ***GS1*** using (a) Langmuir and (b) Freundlich models.

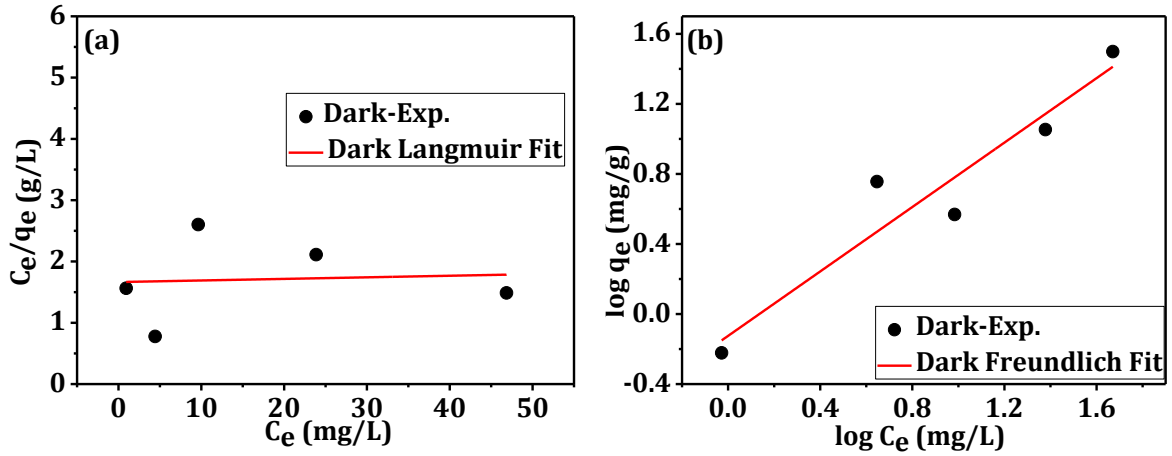

Fig. 4.19: Isotherm fitting for EBT (1mg/L) adsorbed on ***GS1*** using (a) Langmuir and (b) Freundlich models.

4.5.5.1 Langmuir isotherm

k_L and q_e for MB and EBT are determined from the linear fit of plots in Fig. 4.18(a) and Fig. 4.19(a) (Table 4.5). The value of R_L for MB and EBT is 0.8 and 0.98, respectively. It indicated favourable adsorption for both the dyes. The values of regression coefficient for MB and EBT are 0.981 and 0.0049, respectively. The very small regression coefficient value for EBT dye adsorption data clearly indicates the non-adherence to Langmuir model adsorption model for this dye.

4.5.5.2 Freundlich isotherm

The experimentally obtained data for MB and EBT dyes were fitted with Freundlich isotherm equation and are shown in Fig. 4.18(b) and Fig. 4.19(b), respectively. The parameters obtained from the Freundlich fitting are given in Table 4.5. The value of n between 1 to 10 indicates that adsorption processes are favorable. The values of n obtained are 2.330 and 1.087 for MB and EBT, respectively, indicating that the adsorption is favorable in both cases. The values of regression coefficients for MB and EBT are 0.9591 and 0.9095, respectively.

The comparison of regression coefficient values for both models discerned that the MB dye adsorbs onto ***GS1*** sample by monolayer formation [202]. The emergence of Freundlich model is a better fit for EBT indicating that the adsorption occurred via multilayer adsorption [179].

Table 4.5: Parameters obtained from Langmuir and Freudlich isotherm models obtained for adsorption of MB with 100 mg/L of ***GS1*.**

Adsorption isotherm	Dye Adsorbed	Parameter (units)	Value	R^2
Langmuir isotherm	MB	k_L (L/g)	0.251	**0.981**
		q_e (mg/g)	52.1	
		R_L	0.8	
	EBT	k_L (L/g)	0.0015	0.0049
		q_e (mg/g)	31.5	
		R_L	0.98	
Freundlich isotherm	MB	k_f (L/g)	2.907	0.9591
		n	2.330	
	EBT	k_f (L/g)	0.339	**0.9095**
		n	1.087	

4.5.6 Adsorption Kinetics modeling

To determine the rate and mechanism of adsorption process, it is important to study the adsorption kinetics. The kinetic data for the adsorption of cationic dye (MB) and anionic dye (EBT) onto ***GS1*** sample was tested for well-known kinetic models, namely pseudo first order (PFO) model and pseudo second order (PSO) model and Elovich model. To study the diffusion mechanism involved in the adsorption, the data were fitted with intraparticle diffusion (IPD) model. Fitting of models was done in the experiments in which 1 mg/L of the respective dye was used as adsorbate and 20 mg/L of ***GS1*** sample was used as adsorbent. The experimental obtained values of q_e using equation (ii) are 25.70 and 3.07 mg/g for MB and EBT, respectively.

Details of the experimental data fitted with PFO model are shown in Fig. 4.20(a) and Fig. 4.21(a) for MB and EBT, respectively. The parameters obtained from the PFO fitting are given in Table 4.6. The values of % Δq_e (the difference between experimental and theoretically calculated values of q_e) for MB and EBT are 9.6% and 1.2% respectively.

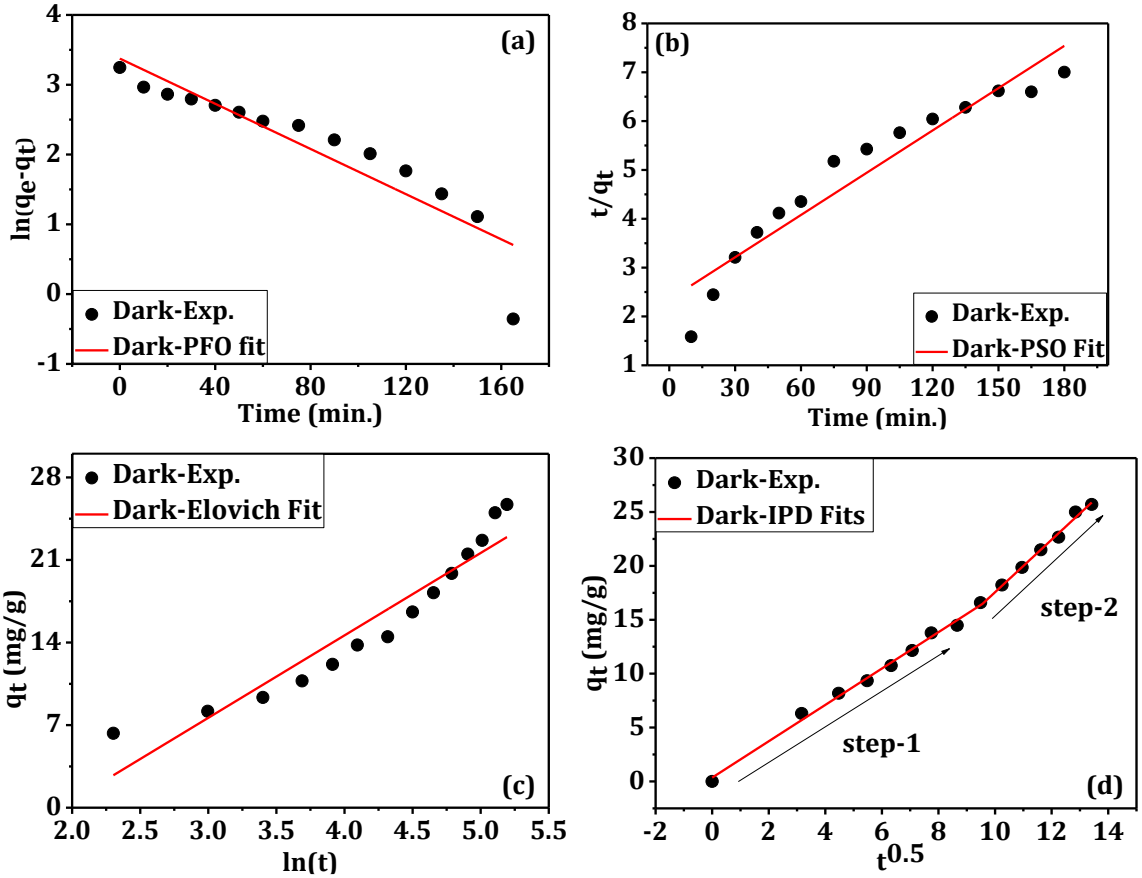

Fig. 4.20: Kinetic modeling of MB (1mg/L) adsorbed on ***GS1*** using (a) PFO, (b) PSO, (c) Elovich and (d) IPD model.

Fig. 4.20(b) and Fig. 4.21(b) show the fitting of experimental data with PSO model for MB and EBT dye, respectively and the parameters obtained are mentioned in Table 4.6 along with regression coefficients. The values of % Δq_e for MB and EBT are 25.8% and 25.7%, respectively. The fitting of experimental data with Elovich model is shown in Fig. 4.20(c) and Fig. 4.21(c) for MB and EBT dye, respectively. The kinetic parameters are given in Table 4.6. Based on the values of % Δq_e and regression coefficients, it emerged that the adsorption of EBT dye follows PFO adsorption kinetics more favorably than PSO and Elovich adsorption kinetics [42]. In case of MB dye while considering %Δq_e values the PFO model seems to be in better agreement with the experimental data among with the PFO and PSO model. But the value of regression coefficient indicates that Elovich model is more consistent for MB dye i.e. the adsorption is taking place via chemisorption. Fig. 4.20 (d) and Fig. 4.21(d) give the fitting

of experimental data with IPD model for MB and EBT dye, respectively. The parameters obtained from fitting of IPD model are given in Table 4.7. For both the dyes the regression coefficient values are high (>0.99) for the IPD fits to the adsorption data. So, it can be concluded that in both the cases, adsorption is taking place by intrapaticle diffusion [203]. The linear fits pass through origin indicating that the mechanism is completely IPD controlled for both MB and EBT [182].

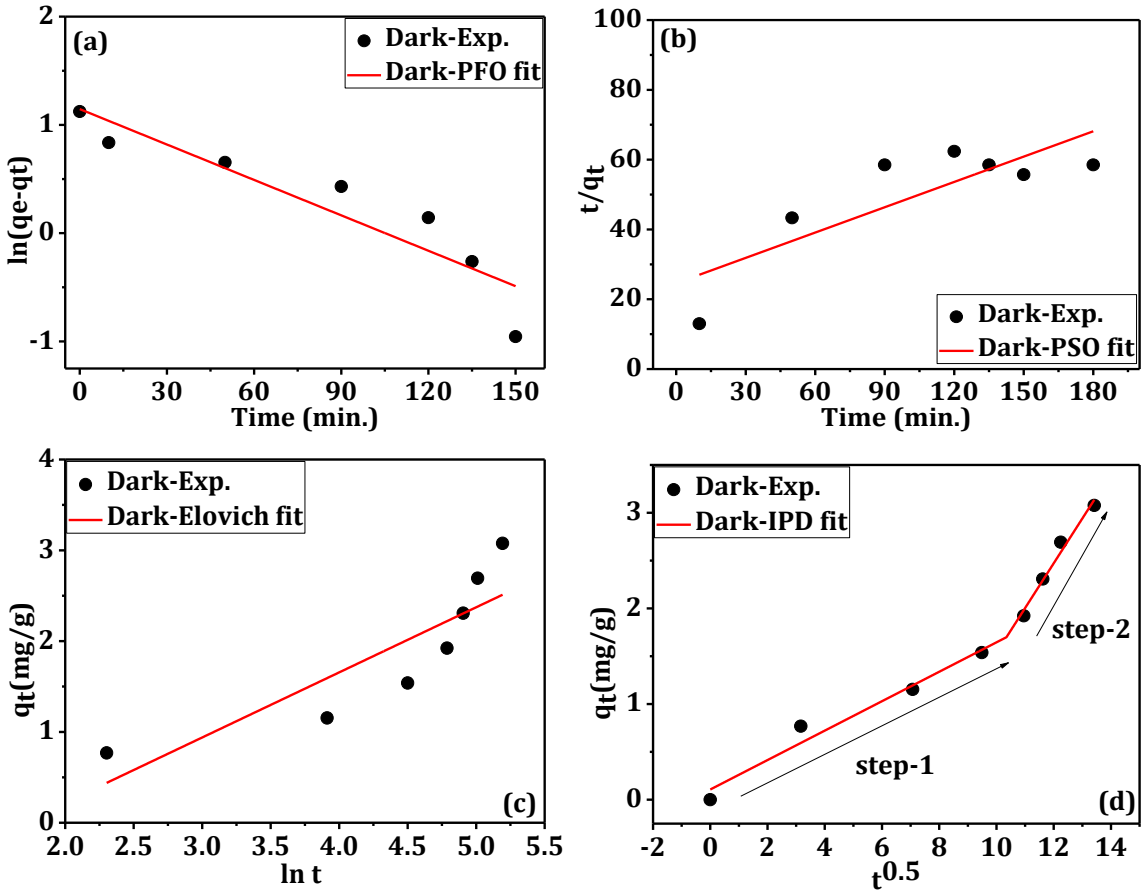

Fig. 4.21: Kinetic modeling of EBT (1mg/L) adsorbed on ***GS1*** using (a) PFO, (b) PSO, (c) Elovich and (d) IPD model.

Table 4.6: Parameters of kinetic modeling of MB and EBT adsorbed at ***GS1*** sample. (q_e (MB) = 25.70 mg/g and q_e (EBT) = 3.07 mg/g).

Kinetic model	Dye Adsorbed	Parameter (unit)	Value	R^2
PFO	MB	k_1 (1/min)	0.01619	0.8510
		q_e (mg/g)	28.4400	
	EBT	k_1 (1/min)	0.0109	**0.85014**
		q_e(mg/g)	3.11	
PSO	MB	k_2 (g/mg min.)	0.0003547	**0.9185**
		q_e(mg/g)	34.662	
	EBT	k_2 (g/mg min.)	0.00237	0.6774
		q_e(mg/g)	4.135	
Elovich model	MB	α (mg/g min.)	1.0340	0.90872
		β	0.1431	
	EBT	α(mg/g min.)	2.392	0.75038
		β	1.395	

Table 4.7: Parameters of diffusion model (IPD) of MB and EBT adsorbed at ***GS1*** sample.

Dye Adsorbed	Parameter (unit)	Value	R^2
MB	k_{id1} (mg/g $min^{1/2}$)	1.68707	0.997
	k_{id2}(mg/g $min^{1/2}$)	2.43091	
EBT	k_{id1} (mg/g $min^{1/2}$)	0.15387	0.991
	k_{id2}(mg/g $min^{1/2}$)	0.46821	

4.5.7 Adsorption mechanism

For both MB and EBT the adsorption onto the ***GS1*** sample is initially fast and saturates to a final value at a later stage (>150 min) as shown in Fig. 4.17(a). Table 4.8 lists the results obtained from different model fittings to various isotherm and kinetics data.

Table 4.8: Results of different adsorption isotherm and kinetics modeling.

Dye Adsorbed	Isotherm model	Kinetics Model	IPD
MB	Langmuir	Elovich	2 step
EBT	Freundlich	PFO	2 step

For MB: Langmuir nature of the isotherm indicated that for MB the reversible adsorption at multiple equivalent sites leading to monolayer formation on the surface of ***GS1.*** The monolayer nature of the adsorption is also confirmed by the saturation of the % Adsorption in Fig. 4.17(a) with the increase in dye concentration in the solution. Elovich kinetic fit

indicated that the MB strongly adsorbs on to ***GS1*** via chemisorption. This is in accordance with the opposite charge of the dye and ***GS1*** at the relevant pH (section 4.5.3). Two step fit of IPD indicated that initially adsorption takes place through boundary layer diffusion and then by intraparticle diffusion beyond ~ 91 min [42].

For EBT: Freundlich nature of the isotherm indicated that for EBT ***GS1*** is a heterogeneous adsorbent with the sites of N-doping (Lewis-Acid sites) behaving as favourable adsorption sites. This information in conjuntion with the PFO kinetics model emerging as the most favourable model clearly indicated that adsorption occurs by multilayer physisorption. The multilayer nature of the adsorption is also confirmed by the non-saturation of the % Adsorption in Fig. 4.17(b) with the increase in dye concentration in the solution. Two step fit of IPD indicated that initially adsorption takes place through boundary layer diffusion and then by intraparticle diffusion beyond ~ 109 min [42].

The value of kinetics rate constants is higher for MB as compared with those for EBT. This is because the MB is a basic dye and the adsorbent is acidic (pH_{pzc}=4.6) so the MB dye uptake on the adsorbent is faster than that of anionic EBT. EBT contain acidic functional group on its surface and hence the same nature of adsorbate adsorbent makes the adsorption slower. This difference in interaction mechanism of the two dyes is also clear from the rate constants values of the two dyes with k_{id1} value of EBT (0.153) is an order of magnitude smaller than that for MB (1.687). After diffusive mass transefer, intrapaticle diffusion occurs in both the cases as shown by second linear curve. The rate constants for interaparticle diffusion are higher compared with that for the initial boundary layer diffusion which indicated the enhancement of adsorption rates for both the dyes after the initial boundary layer diffusion.

Table 4.9 shows the conclusion of adsorption results obtained using the ***GS1*** sample for MB and EBT adsorption.

Table 4.9: Adsorption results for the best sample.

Sample ID	Pollutant	q_e (mg/g)	Kinetic model	Kinetic isotherm
GS1	MB	52.1	Elovich	Langmuir
	EBT	31.5	PFO	Freundlich

Chapter 5

Thermal activation of soy flour based N-doped carbons

Overview

In this chapter, the N-doped carbon spheres synthesized using glucose and soy flour via the HTC method (***GS1***) were heat-treated at 900 °C in Ar and N_2 atmospheres separately to activate/modify the surface without additives. The effect of heating atmospheres on the sample properties has been studied using SEM, XRD, FTIR, UV–Visible, Raman, XPS, BET, and TG-DSC. The difference in surface chemistry was confirmed by XPS and the point of zero charge values of synthesized samples. The variation in the results is explained on the basis of the diffusivity and density of the gases used and the corresponding mechanism has been proposed. The role of heat treatment atmosphere has been compared for the adsorption efficiency of synthesized samples for the chosen model pollutants: MB, CV, EBT, PNP, CIP and DEP. The adsorption rate and mechanism have been determined using kinetic modeling and isotherm analysis based on the best adsorption results obtained.

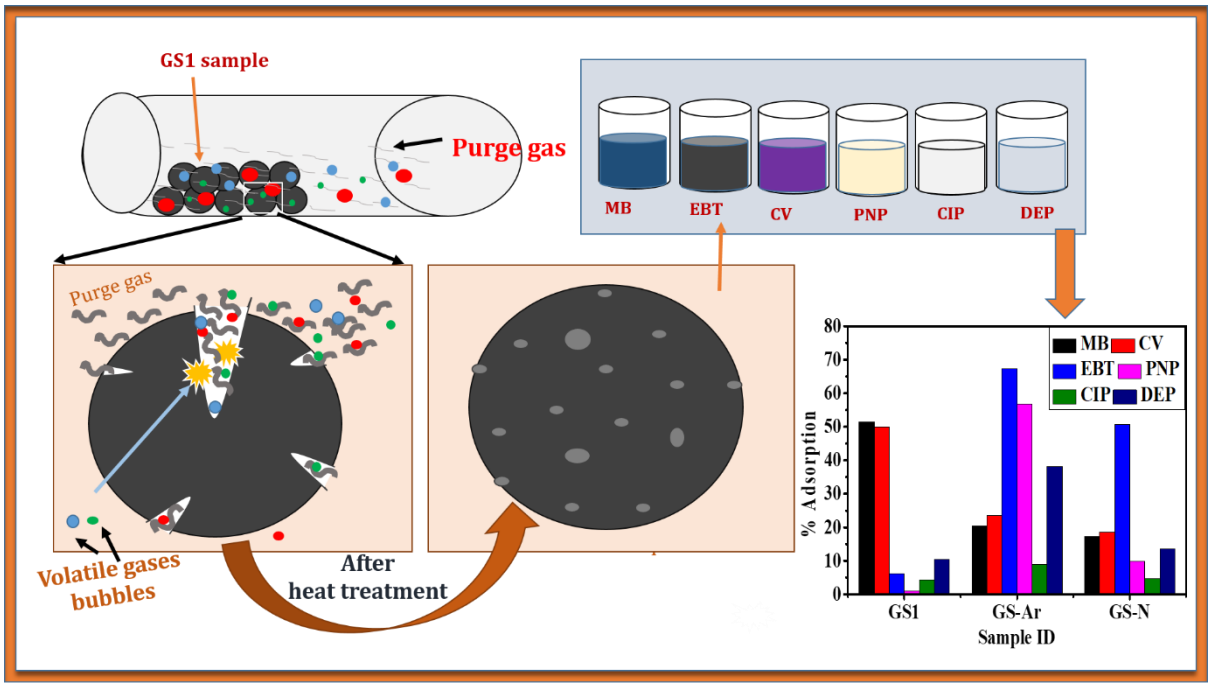

5.1 Introduction

The N-doped carbon spheres obtained from hydrothermal carbonization carry a lower specific surface area. Various techniques have been used to improve the surface properties of N-doped carbons, such as chemical activation, thermal activation, and both. There are various reports available on the comparison of various atmospheres for high-temperature thermal treatment of carbon materials such as CO_2 and nitrogen (N_2) [204], N_2 and H_2, [205], argon (Ar), CO_2 and water vapor [206] and CH_4 and H_2 [207] etc.

One of the simplest methods to activate N-doped carbon sphere for improvement of surface area and surface properties is thermal treatment at high temperatures in an inert atmosphere. Usually, N_2 or Ar gases are used for the thermal treatment process. Ar and N_2 are quite different from each other except for their non-reactivity. Ar has a higher density than N_2 gas and differs in other properties such as diffusivity, thermal conductivity, specific heat, etc. All these properties of carrier gas have a profound effect on the heat treatment of the sample. Hence it is expected that N_2 and Ar may differ in their effect on the sample being heat-treated. Thus it is essential to study the effect of Ar and N_2 heating atmosphere on the properties and applications of the heat-treated sample.

In this work, the ***GS1*** sample was heat-treated in Ar and N_2 atmospheres for thermal activation. These are the two most commonly used inert gases. In literature many times no distinction is made between the two. Therefore, to delineate the effect of the atmosphere, if any, during thermal treatment, heating was carried out under Ar and N_2 atmosphere.

5.2 Heat treatment temperature

The temperature for thermal activation was determined by TGA/DSC/DTG of the ***GS1*** sample. The TG/DSC curves were taken in the air, Ar, and N_2 at a heating rate of 5 °C/min as shown in Fig. 5.1.

Fig. 5.1 (a) clearly shows that when the ***GS1*** sample was heated with air as the carrier gas, a slow weight loss process occurred from room temperature to 100 °C and ~ 11% of mass loss occurred, which can be attributed to the evaporation of volatile substances and water content. On further increasing the temperature, the sample started to lose mass again at 212 °C, which continued till 510 °C when the sample got wholly burned. DTG and DSC curves clearly show that the mass loss in the sample was a two-step reaction. DSC data indicated that the reactions were exothermic in nature. The DTG/DSC peaks at 291 °C and 438 °C can be attributed to the decomposition of surface functional groups and oxidation of the sp^2 hybridized carbon skeleton of the flakes (which formed the microspheres) into CO_2, respectively [208].

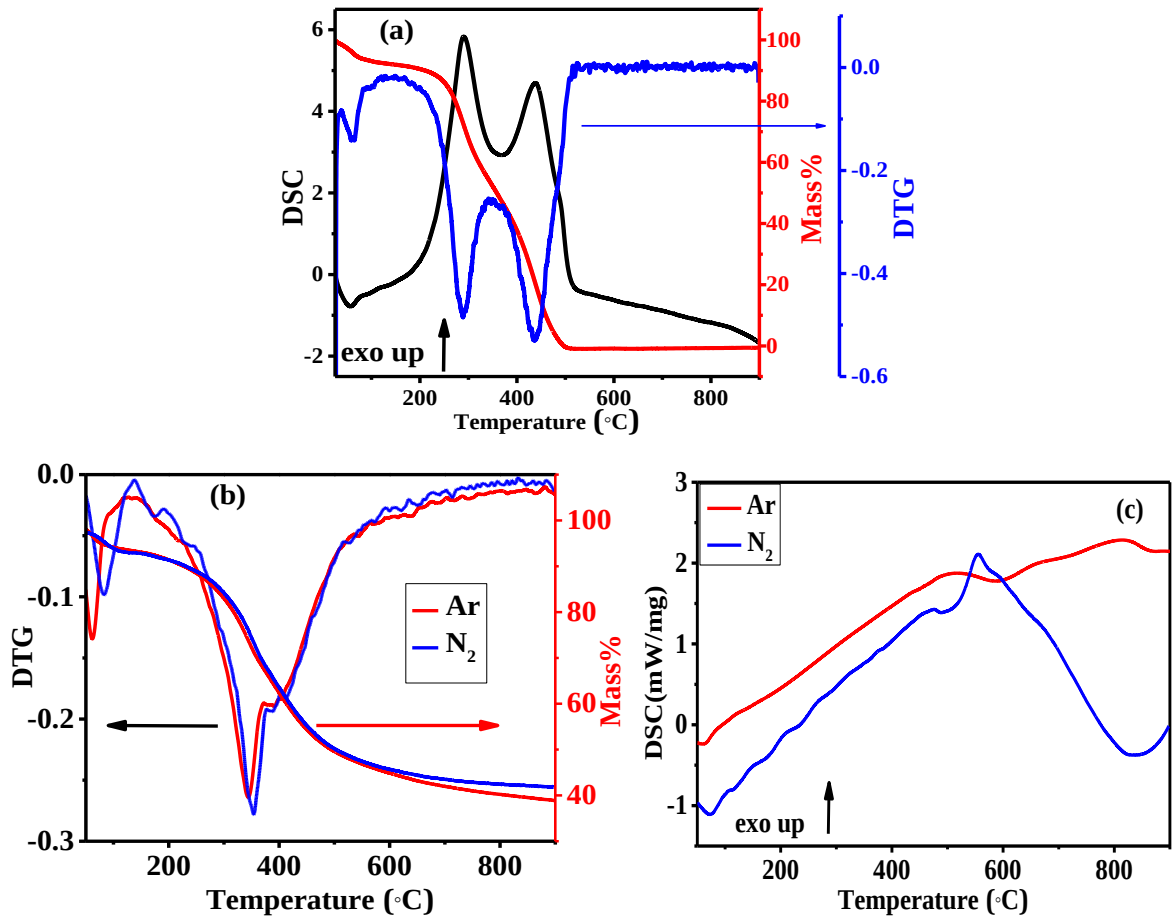

Fig. 5.1: Thermal analysis of ***GS1*** sample: (a) TGA/DSC/DTG in air, (b) TG/DTG in Ar and N_2 atmosphere, and (c) DSC in Ar and N_2 atmosphere.

Fig. 5.1(b) shows TG and DTG curves for Ar and N_2 carrier gases. From the TG data, it can be observed that slow mass loss occurred from room temperature to 150 °C, and all the adsorbed water content and volatile matter were lost by this temperature. On further heating, mass loss started to occur after 250 °C and continued till ~700 °C. Beyond ~ 700 °C, no more mass loss occurred up to 900 °C. The residual masses in the Ar and N_2 carrier gases at 900 °C were 39% and 42%, respectively. Observation of single peak in DTG data indicated that during heat treatment the removal of the volatile matters from the carbon sphere samples is a single step process. The single peak observed at 345 °C and 352 °C for Ar and N_2 carrier gases respectively in DTG, indicated that the decomposition started earlier in Ar. This can be attributed to higher density of Ar gas in comparison with the N_2 gases. Thus, the slow-moving volatile gases along with Ar gas caused localized heating and early onset of mass loss than N_2 gas. For both the carrier gases, sharp DSC peaks were not observed at all, while broad humps were observed at nearly 520 °C and 554 °C for Ar and N_2 carrier gas, respectively (Fig. 5.1(c)). These DSC humps indicated the exothermic process in the system during the mass loss. It has slowed down due to the graphitization of the sample in the inert atmosphere after the removal

of volatile substances. The DSC peak in the Ar atmosphere was observed earlier due to more localized heating, and hence earlier carbonization onset.

It was observed that all the reactions were completed before 900 °C, for both the carrier gases. Also, it has been reported that the temperature required for the thermal activation of carbon takes place generally between 800-1000°C [209,210]. Therefore, the ***GS1*** sample was heated in Ar and N_2 atmosphere at 900 °C, and the samples were named ***GS-Ar*** and ***GS-N***, respectively (Table 5.1).

Table 5.1: Properties of the synthesized samples.

	GS1	***GS-Ar***	***GS-N***
Precursors	Soy flour and Glucose	***GS1***	***GS1***
Carrier gas	-	Ar	N_2
Size of sphere (µm)	4.95	4	3.9
Nature of carbon (majority)	Amorphous C	Crystalline C	Crystalline C
Nature of Nitrogen (majority)	Pyrrolic N	Graphitic N	Graphitic N
Band gap (eV)	4.5	4.8	4.8
Surface area (m^2/g)	7.43	449	468.31
DFT mean pore diameter	14.86	1.1	0.8
DFT pore volume (cm^3/g)	0.029	0.261	0.270
pH_{pzc}	4.6	8.8	9.5

5.3 Characterizations of thermally activated soy flour based N doped carbons

5.3.1 SEM

The SEM micrographs of ***GS1, GS-Ar,*** and ***GS-N*** samples are shown in Fig. 5.2. Smooth spheres of average size 4.95 µm were clearly visible for the ***GS1*** sample (Fig. 5.2(a)) (size determined using Axio-vision software and fitted log normally with Origin™ Software and shown in the inset of Fig. 5.2). After heat treatment, the average size became 4 and 3.9 µm for ***GS-Ar*** and ***GS-N*** samples, respectively (Fig. 5.2(b) and (c)). As discussed in chapter 4 (section 4.4), N-doped carbon spheres derived from HTC of soy flour and sucrose consisted of the concentric accumulation of carbon nano flakes around the carbon quantum dot [211]. During heat treatment in an inert atmosphere at high temperature, the elimination of some of the outer graphene flakes may have reduced the size of spheres. It was observed from the SEM images that the sphere's surface was no longer smooth after thermal treatment (Fig. 5.2). This may be because of porous structure developed after high-temperature heat treatment in inert atmosphere. The extent of the porosity was probed further by the BET analysis of the samples.

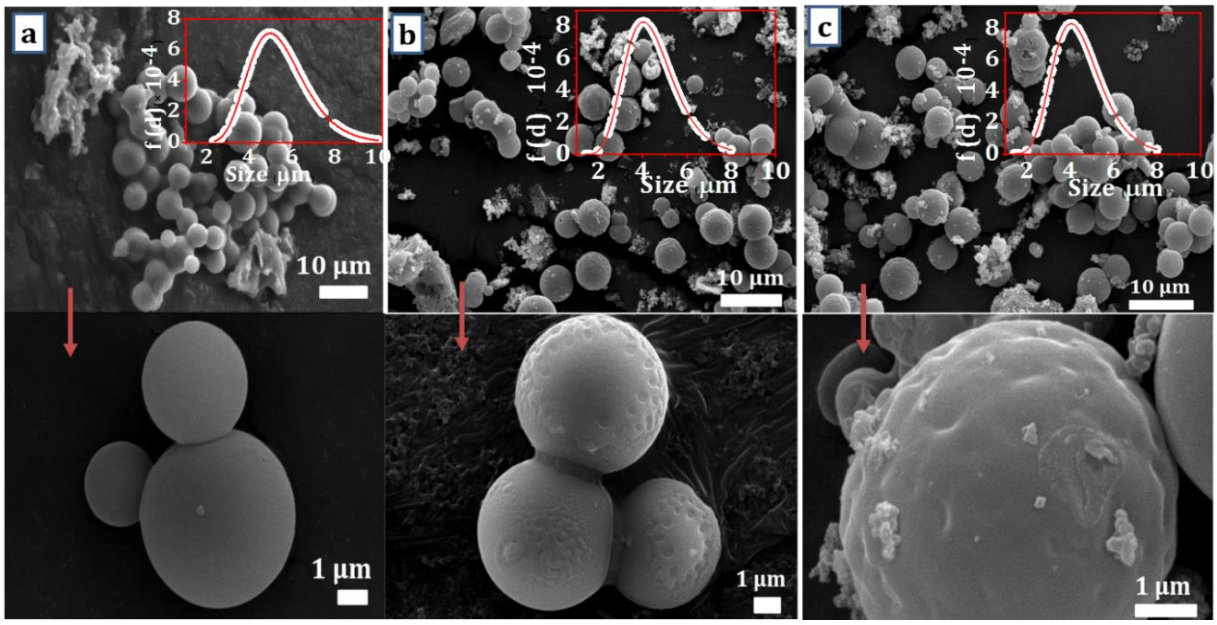

Fig. 5.2: SEM micrograph of (a) ***GS1,*** (b) ***GS-Ar,*** and (c) ***GS-N*** sample. The lower images show the enlarged detailing the surface morphology. Inset shows the log normal distribution of size for the carbon spheres.

5.3.2 XRD

The material's structural features were characterized using the XRD. A broad hump at $2\theta \approx 21°$ for the XRD pattern of the ***GS1*** sample (Fig. 5.3(a)), is a signature for the presence of carbon quantum dots in the core of the sphere [211]. It indicated (002) plane of amorphous carbon [212]. The appearance of a broad peak at $2\theta \approx 24°$ in ***GS-Ar*** and ***GS-N*** showed the presence of (002) plane of disordered graphitic carbon of carbon spheres [211]. The absence of 21° peak and the emergence of 24° peak for ***GS-N*** and ***GS-Ar*** samples (Fig. 5.3(a)), clearly indicated that even though the carbon sphere structure is persisting, it is now extensively porous with pores extending to the inner core of the sphere. The sharp peak at $2\theta \approx 26°$ which persisted for all the samples was for the (002) plane of graphitic carbon [197].

For the XRD line profiles of ***GS-N*** and ***GS-Ar,*** multiple sharp diffraction peaks not available in the XRD line spectra of the ***GS1*** sample were observed. The appearance of these sharp peaks indicated an increase in the degree of crystallization of the samples after heat treatment in the inert atmosphere [213]. The sharp peaks observed at 31.4° and 44.9° represented the presence of graphitic carbon [214] and (100) planes of graphite [84], respectively. The graphitization for samples occurred at high temperatures due to rearrangement and ordering of carbons with release of volatile components (such as H_2, CO_2, NH_3, CO, H_2O, and CH_4). This would have resulted in lowered oxygen and nitrogen content in these samples [215]. This conjecture was confirmed by further characterizations. The XRD

data of ***GS-Ar*** and ***GS-N*** samples are similar, indicating that no change in structural phase occurred due to change in heat treatment atmosphere.

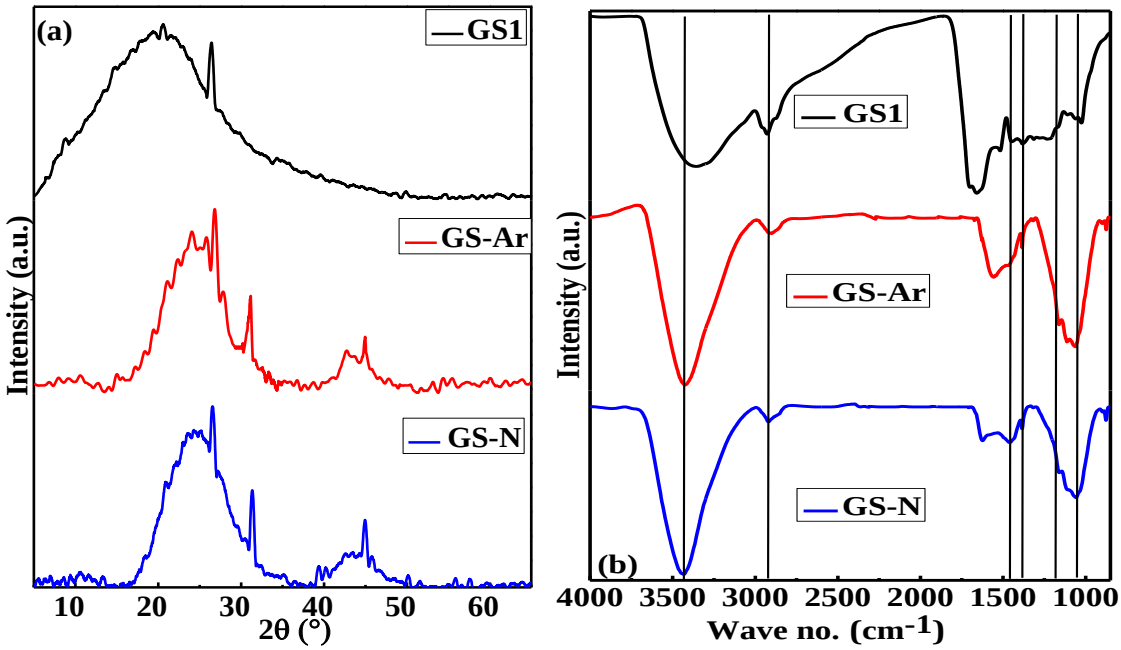

Fig. 5.3: (a) XRD, and (b) FTIR spectra of ***GS1, GS-Ar,*** and ***GS-N*** samples.

5.3.3 FTIR spectroscopy

To investigate the chemical bonds present in the samples, FTIR spectroscopy was carried out. Fig. 5.3 (b) shows the FT-IR spectra of ***GS1, GS-Ar,*** and ***GS-N***. The characteristic band available around 3436 cm^{-1} for all the samples indicated an oxygen-containing O-H functional group. This band was due to adsorbed water and was maximum for ***GS-Ar*** and ***GS-N*** samples, indicating enhanced surface area [216]. The firm C-H stretch band peaks were observed around 2921 cm^{-1} for all the samples. Another broad peak at ~ 1640 cm^{-1} represented the stretch vibration of C=C for ***GS1*** sample while for heat-treated samples C=C bond was observed ~1600 cm^{-1}. With heat treatment in inert atmosphere, the intensity of the C=C band decreased, indicating the breakage of some of the aromatic carbon chains [217]. Peaks around 1460 cm^{-1} and 1380 cm^{-1} for all the samples indicated the presence of aliphatic C-H bending group. At 1170 cm^{-1} and 1027 cm^{-1}, peaks of C-N and C-O stretching vibrations were observed, respectively. The ***GS1*** sample spectra has the characteristic peak of C=N at 1523 cm^{-1} not observed for the ***GS-N*** and ***GS-Ar*** samples. This supports the conjecture that heat treatment resulted in breakage/restructuring of bonds with release of volatile compounds. The bond restructuring will lead to significant changes in the surface chemistry of ***GS-N*** and ***GS-Ar*** samples.

5.3.4 UV-Visible spectroscopy

UV-Visible spectroscopy was performed for ***GS1, GS-Ar,*** and ***GS-N*** samples to obtain their reflectance spectra, as shown in Fig. 5.4(a). These samples showed a reflectance peak at ~ 250 nm, which indicated the π-π^* transition of sp^2 graphitic carbon [218]. The Kubelka-Munk model was used to calculate the bandgap of ***GS1, GS-Ar,*** and ***GS-N*** samples and the details of the analysis are given in chapter 3 (section 3.3.5).

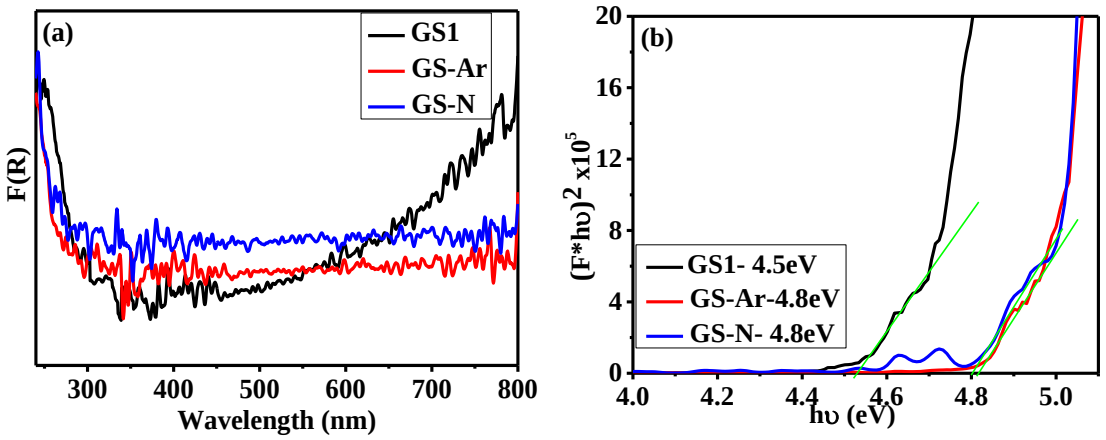

Fig. 5.4: (a) UV-Visible diffuse reflectance spectra, and (b) optical band gap energy curves of ***GS1, GS-Ar,*** and ***GS-N*** samples.

The allowed direct bandgap obtained for ***GS-Ar,*** and ***GS-N*** was 4.8 eV, (Fig. 5.4(b)). The variation in the heat treatment gas does not change the reflectance spectra and optical bandgap of samples. The increased bandgap of the thermally treated samples can be attributed to the lower surface oxygen and nitrogen content present in these samples [12, 13].

This conjecture of lower oxygen and nitrogen content with heat treatment in inert atmospheres emerging from XRD, FTIR and UV-Visible data need to be confirmed by XPS.

5.3.5 Raman spectroscopy

Fig. 5.5 (a) gives the Raman spectrum of ***GS1, GS-Ar,*** and ***GS-N*** samples, clearly showing peaks at ≈ 1350 and 1590 cm^{-1}. These peaks represent D and G bands, respectively. The D-band is attributed to disorder in graphitic carbon, and G-band exhibits the ordering in the carbon structure [221]. For the ***GS1*** sample, negligible peak intensities and broader bands were observed compared to ***GS-N*** and ***GS-Ar*** samples because the ***GS1*** sample has less amount of graphitization as confirmed by the XRD line profile comparisons (Fig. 5.3(a)) [213,221]. The ratio of D and G-band intensities (I_D/I_G) is a measure of the number of defects present in the material [222]. The values of I_D/I_G obtained for ***GS-N*** and ***GS-Ar*** were the same (=0.99). The band between 2500-3000 cm^{-1} for ***GS-Ar*** and ***GS-N*** samples represented the G" band, induced due to disorder, and was overtone of the D band [104]. This band confirmed the

graphitization of carbon in the heat-treated samples [221]. Thus Raman data add to XRD data results of intense graphitization peaks and the FTIR data indicating rearrangement of C=C and C=N bonds.

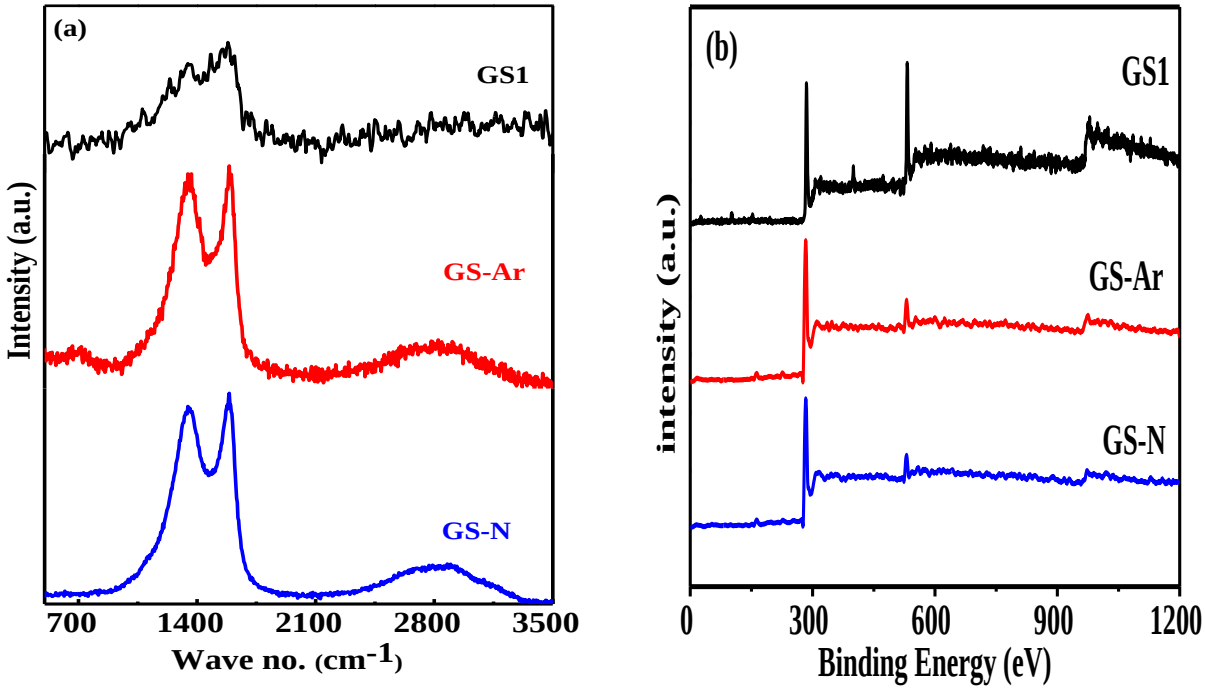

Fig. 5.5: (a) Raman spectra, and (b) XPS survey spectra of ***GS1, GS-Ar,*** and ***GS-N*** samples.

5.3.6. XPS

XPS measurements determined the elemental composition and various bonding configurations of ***GS1, GS-Ar,*** and ***GS-N*** samples. From survey spectra (Fig. 5.5(b)), peaks at ~ 284.0, 531.0, and 400.0 eV for C1s, O1s, and N1s, respectively, were visible for these samples [82]. The C, N, and O content in all the samples as obtained from the survey spectra are mentioned in Table 5.2. The data clearly shows that during the heat treatment in the inert atmosphere, %C content was enhanced significantly, with corresponding decrease in %O and %N content for both the gases. The observed change in C, N, and O content resulted from the formation and removal of oxygen and nitrogen containing volatile species at high temperatures [223]. The lowered O and N content for ***GS-Ar*** and ***GS-N*** samples also supports the earlier conjecture regarding graphitization as visible in XRD line profile [215], the C=N peak removal in FTIR spectra and enhanced band gap in UV-Visible data.

The deconvoluted HR spectra of C1s, N1s, and O1s for ***GS-Ar*** and ***GS-N*** samples are shown in Fig. 5.6. The parameters obtained from the deconvolution of C1s, O1s, and N1s HR spectra for all three samples are mentioned in Table 5.2. The peak at 284.2 eV corresponding

to sp^2 hybridized carbons dominates the C1s spectra of all the synthesized samples. The O1s spectra deconvoluted into O-C and O=C functionalities.

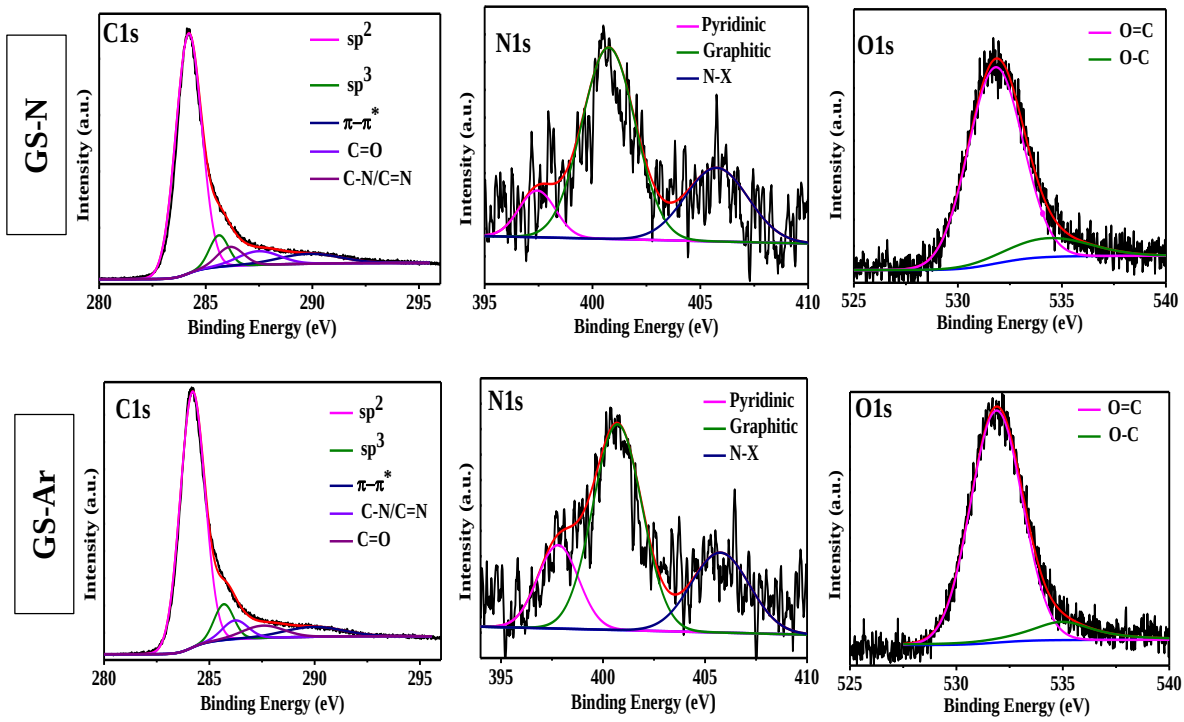

Fig. 5.6: HR-XPS spectra of C1s, N1s, and O1s of ***GS-N***, and ***GS-Ar*** samples (mentioned on top of the graph).

Table 5.2: The values of parameters obtained by fitting the XPS data.

	GS1			***GS-Ar***			***GS-N***		
	% Content	**Group**	**%at**	**% Content**	**Group**	**%at**	**% Content**	**Group**	**%at**
C1s	74.10	C sp^2	56.99	91.93	C sp^2	73.61	93.65	C sp^2	73.26
		C sp^3	-		C sp^3	8.13		C sp^3	7.07
		C-N/	14.8		C-N/	5.56		C-N/	5.87
		C=O	28.21		C=O	5.87		C=O	6.68
		π-π*	-		π-π*	6.79		π-π*	7.12
N1s	2.22	Pyridine	-	1.54	Pyridine	18.8	1.17	Pyridine	10.3
		Pyrrole	82.56		Pyrrole	-		Pyrrole	-
		Graphitic	17.44		Graphitic	55.5		Graphitic	61.7
		N-X	-		N-X	25.62		N-X	27.9
O1s	23.68	C=O	97.36	6.53	C=O	88.34	5.18	C=O	87.1
		C-O	3.64		C-O	11.66		C-O	12.9

In the deconvoluted N1s spectra of ***GS1,*** only pyrrolic and graphitic N were seen, having peaks at 399.55 and 401.56 eV [211]. The deconvoluted N1s spectra for ***GS-Ar*** and ***GS-N*** consisted of peaks of pyridinic (~397-398 eV) [224], graphitic (~400.7-402) [225], and

chemisorbed N-oxide (~405-406 eV) [224]. These results indicated that at temperatures above 500°C , the pyrrolic N transformed to form graphitic N [226] due to its higher theramal stability compared to other nitrogen functionalities [227]. With heat treatment, the oxidized nitrogen appeared as a result of pyrrolic N and pyridinic N oxidation during heat treatment. The availability of pyrrolic and pyridinic N functionalities leads to negatively charged surfaces, while the presence of graphitic and oxidized N results in a positively charged surface [224]. The net effect on surface charge of heat-treated samples needs to be verified by determination of pH_{pzc} for the samples.

5.3.7 N_2 adsorption-desorption isotherms

Fig. 5.7(a) and 5.7(b) show the N_2 adsorption-desorption isotherms and pore size distribution curves for ***GS1, GS-Ar,*** and ***GS-N*** samples. According to IUPAC classification, the adsorption isotherms were of H4 type and show type–II characteristics [194]. The BET surface area obtained for the ***GS1*** sample was 7.43 m^2/g. The BET surface area for ***GS-Ar*** and ***GS-N*** were 449 m^2/g and 468.31 m^2/g (Table 5.1), respectively. This manifold increase in the surface area indicated enhanced porosity in samples during heat treatment. The BET surface areas were similar for the ***GS-Ar*** and ***GS-N*** samples. The pore size distribution, calculated using NLDFT method is shown in Fig. 6(b). Availability of micropores in ***GS1*** sample was not observed and obtained mean pore diameter was 14.86 nm in mesopore region with the pore volume of 0.029 cm^3/g. The graph clearly showed that both ***GS-Ar*** and ***GS-N*** samples consisted of micropores only (diameter <2 nm). The mean pore diameter obtained for ***GS-Ar*** and ***GS-N*** samples was 1.1 nm and 0.8 nm, respectively. The mean pore volume for ***GS-Ar*** and ***GS-N*** samples obtained was nearly equal (Table 5.1). Since large micropores can allow for fast charge transport and entrance of pollutant molecules, the large micropore size (>1 nm) of ***GS-Ar*** sample may result in its enhanced applicability in various fields such as adsorption, photocatalysis, and electrocatalysis than ***GS-N*** sample.

The size and size distribution of pores in the heat-treated samples seemed to depend on the carrier gas. Carrier gases seemed to have played an important role in pore formation mechanism. The pore formation mechanism during heat treatment under Ar and N_2 carrier gas which provides insight into this apparent difference in porosity of the heat-treated samples has been proposed here.

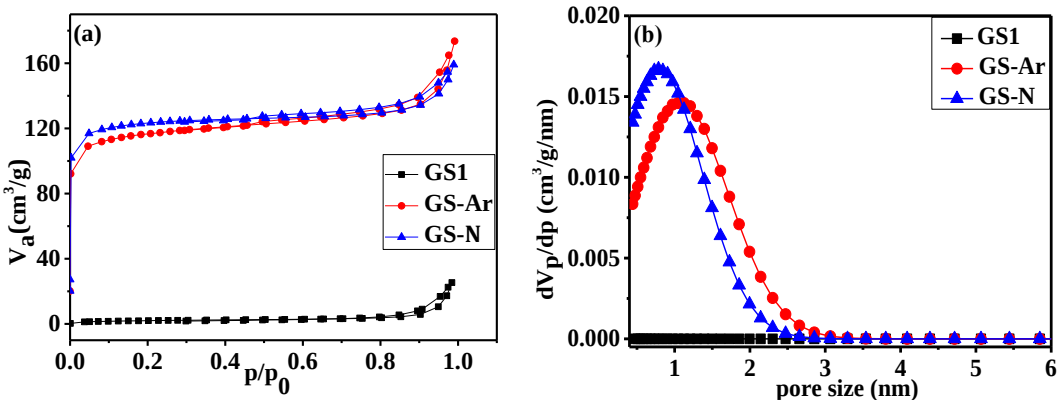

Fig. 5.7: (a) N_2 adsorption-desorption isotherm and (b) NLDFT pore size distribution for ***GS1, GS-Ar,*** and ***GS-N*** samples**.**

5.4 Mechanism of pore formation during heat treatment

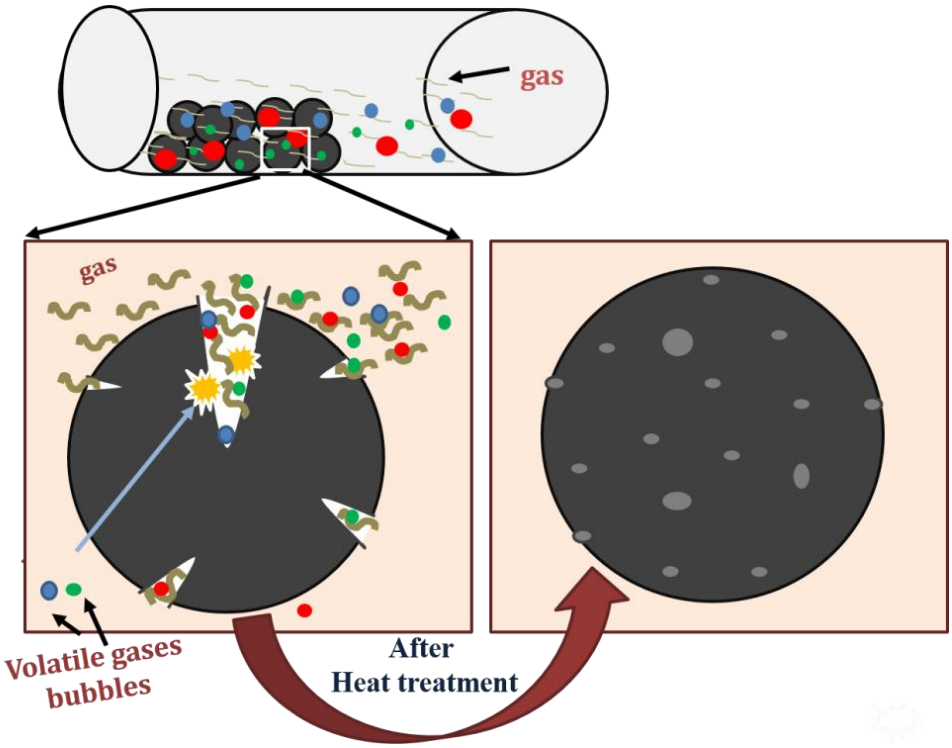

Fig. 5.8: Mechanism of pore formation during heat treatment in the inert carrier gas.

When the carbon spheres undergo heat treatment in presence of inert gas, volatile gases such as H_2, CO_2, NH_3, CO, H_2O, and CH_4 are produced. The volatile gas bubbles migrate with the carrier gas and perforate through the carbon spheres consisting of carbon nanosheets of N contained ring compounds and aromatized glucose to form pores [211,228]. For Ar, with higher density, the diffusivity was lower than the N_2. When the furnace was heated to a specific temperature, the produced volatile matter migrates slowly with Ar compared to N_2 due to its higher density and lower diffusivity [229]. Therefore, the bubbles nucleate and explode within the carbon sphere eventually to form micropores of large diameter compared to N_2 gas. The

penetration of the carrier gas with the volatile matter throughout the µm sized carbon sphere is supported by absence of carbon quantum dot signature which was present in the core of ***GS1*** sample as observed in the XRD line profile for the heat-treated samples. The mechanism of pore formation by heat treatment in an inert atmosphere is shown in Fig. 5.8.

5.5 Adsorption studies

5.5.1 Point of zero charge (pH_{pzc}) of samples

The pH_{pzc} for a sample is the pH at which the sample's surface has no net charge. The values of pH_{pzc} obtained for ***GS1, GS-Ar,*** and ***GS-N*** were 4.6, 8.8, and 9.5, respectively as shown in Fig. 5.9 (Table 5.1). Heating in Ar and N_2 increased the pH_{pzc} and was attributed to the change in surface functional groups. Increase in the pH_{pzc} of the sample is an indicator that the surface of the sample is having more positive surface groups [230]. The more positive surface of ***GS-N*** sample was due to availability of more graphitic N as indicated by XPS results [224].

Below the $pH_{pzc,}$ the sample's surface has a net positive charge, and above the pH_{pzc}, the sample's surface carries a net negative charge. Most dye solutions have pH of 5-6. The pH_{pzc} values of the heat-treated samples signal better performance for anionic dye adsorption in contrast with cationic dye adsorption on the ***GS1*** sample.

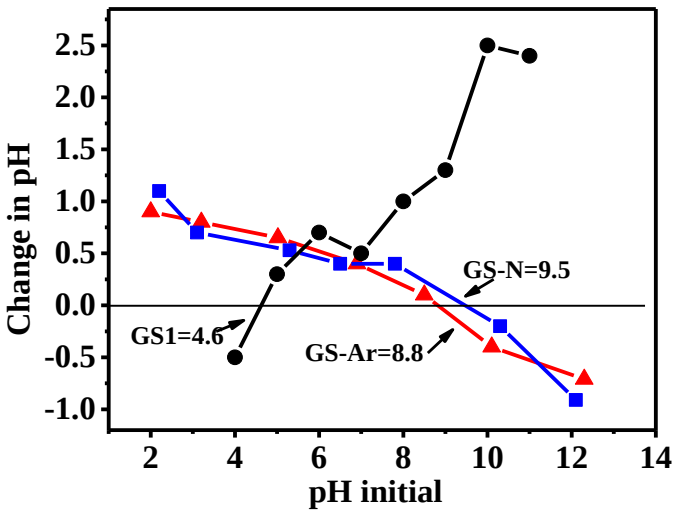

Fig. 5.9: Point of zero charge (pH_{pzc}) of ***GS1***, ***GS-Ar*** and ***GS-N*** sample.

5.5.2 Model Pollutants

MB and CV: The adsorption efficiencies of 20mg/L of ***GS1, GS-Ar,*** and ***GS-N*** samples for the adsorption of 1 mg/L of MB dye were 51.5, 20.4, and 17.3%. The % adsorption for CV dye for ***GS1, GS-Ar,*** and ***GS-N*** samples were 50, 23.5 and 18.6% (Fig. 5.10 and Table 5.3).

This is because the pH_{pzc} of ***GS-Ar*** and ***GS-N*** were higher than the ***GS1*** sample, and thus at normal pH of MB and CV solutions (~5.2), the ***GS1*** sample adsorbed the cationic dyes more efficiently. Compared to the ***GS-Ar*** sample, the ***GS-N*** sample's pH_{pzc} was higher and thus leading to a slightly lower adsorption efficiency. Also, the meanpore diameter of ***GS-Ar*** sample was higher than ***GS-N*** sample. It has led to more accessibility to the dye molecule on the surface as the MB and CV molecules possess diameter > 1nm. The adsorption studies of MB for ***GS1*** sample were carried out in detail in chapter 3 [211].

EBT: For 1mg/L of EBT dye, the observed adsorption efficiencies for ***GS1, GS-Ar,*** and ***GS-N*** samples were 6.1, 67.4, and 50.7% (Fig. 5.10 and Table 5.3). Normal pH of the anionic dye EBT solution was 6.6. For ***GS1*** sample, this pH was higher than its pH_{pzc} (4.6). Thus sample surface is negative and repels the dye resulting in lowered adsorption. The enhanced adsorption efficiency for heat-treated samples was because their pH_{pzc} were greater than the normal pH of EBT solution. The % adsorption for ***GS-N*** was lower than ***GS-Ar*** sample despite its high pH_{pzc}, because of the availability of micropores having size comparable to EBT molecule on the ***GS-Ar*** surface. Also, ***GS-Ar*** has more pyridinic N functionality resulting in enhanced adsorption [231].

PNP: PNP was used as a neutral model pollutant to study the effect of activation atmosphere on as-prepared samples' adsorption capacity. For PNP, sample ***GS1***'s adsorption capacity was negligible. The negligible adsorption capacity of PNP onto the ***GS1*** sample may be attributed to its lower surface area (7.43 m^2/g). There was a significant difference in the ***GS-N*** and ***GS-Ar*** adsorption efficiency i.e. 9.9% and 56.8%, respectively, (Fig. 5.10, Table 5.3). Despite nearly equal surface area, the low adsorption efficiency of the ***GS-N*** sample compared to the ***GS-Ar*** sample was due to following reasons. The content of pyridinic-N in ***GS-Ar*** sample was higher than that for ***GS-N*** sample. The pyridinic N has high electron density whereas the aromatic ring and the basal plane of PNP have delocalized π electrons. Therefore due to π-π dispersive interaction among adsorbate and adsorbent, more adsorption occurs on the surface of ***GS-Ar*** sample than for ***GS-N*** sample [66]. Also, the mean pore diameter obtained for ***GS-Ar*** sample (1.1 nm) was higher than that for the ***GS-N*** sample (0.8 nm). Therefore, for the PNP molecule having size >0.8 nm, the pores of ***GS-Ar*** were more accessible.

CIP and DEP: CIP was employed as a neutral pharmaceutical model pollutant to investigate the influence of activating atmosphere on the adsorption capacity of as-prepared samples. For CIP, sample ***GS1***'s adsorption capacity was negligible due to its lower surface

area. The adsorption efficiency of ***GS-Ar*** and ***GS-N*** does not change significantly and showed adsorption efficiency of 8.9% and 4.7 %, respectively, (Fig. 5.10, Table 5.3). Despite increased surface area, the low adsorption efficiency of the ***GS-N*** and ***GS-Ar*** samples for CIP was due to its molecular size being above 1 nm and therefore pores were not accessible to the CIP. Also due to higher pyridinic-N content in ***GS-Ar*** sample, it showed a little enhanced adsorption compared to the ***GS-N*** sample [66]. DEP being acidic in nature, it showed % adsorption of 10.5, 38.1, and 13.6% for ***GS1***, ***GS-Ar*** and ***GS-N*** sample, respectively (Fig. 5.10, Table 5.3). The molecular size of DEP being >0.8 nm and therefore it showed an insignificant increase in the % adsorption value for ***GS-N*** sample when compared with ***GS1***. The significant increase in the % adsorption for ***GS-Ar*** sample was due to accessibility of its pores by the DEP molecules. Also, the availability of graphitic-N in the ***GS-Ar*** contributes to enhanced adsorption of DEP onto its surface [135].

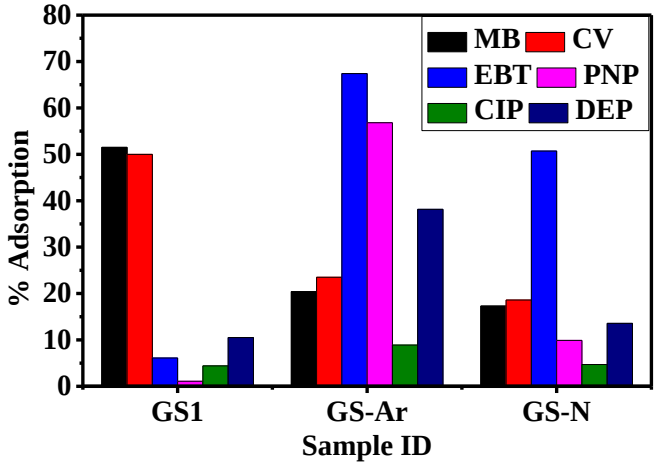

Fig. 5.10: %Adsorption of model pollutants using ***GS1***, ***GS-Ar*** and ***GS-N*** samples after 3 hours under dark conditions.

Table 5.3: %Adsorption of pollutants after 3 hours using ***GS1, GS-Ar*** and ***GS-N*** sample.

Pollutant	**Pollutant concentration (mg/L)**	**Sample Concentration (mg/L)**	**%Adsorption after 3 hours**		
			GS1	***GS-Ar***	***GS-N***
MB	1	20	51.5	20.4	17.3
CV	1	20	50	23.5	18.6
EBT	1	20	6.1	67.4	50.7
PNP	20	100	1.1	56.8	9.9
CIP	20	100	4.4	8.9	4.7
DEP	20	100	10.5	38.1	13.6

5.5.3 Effect of pH on the adsorption efficiency

PNP: To study the effect of pH variation on the adsorption efficiency of the ***GS-Ar*** sample, the solution pH of the PNP was varied from 2 to 12. The PNP in the aqueous solution exists in the form of following species: $C_6H_4(NO_2)OH$ and $C_6H_4(NO_2)O^-$. In acidic solutions, PNP exists in the form of neutral species: $C_6H_4(NO_3)$. In alkaline solution, PNP was present in the form of anionic species: $C_6H_4(NO_2)O^-$. Fig. 5.11 (a) shows the variation of % adsorption of PNP on ***GS-Ar*** sample with pH variation. The % adsorption of PNP first increased with increasing pH from 2 to 7.4. Further increase in the pH up to 12 showed a sharp decrease in the adsorption efficiency. The key processes which determine PNP adsorption on the ***GS-Ar*** surface include donor-acceptor interaction, π–π dispersion, and hydrogen bonding interactions [232]. The more positive charge on the sample surface will hinder the neutral phenol adsorption [9]. In an acidic medium, an increase in the adsorption efficiency with an increase in the pH from 2 to neutral can be attributed to the decreasing positive surface charge of the ***GS-Ar*** sample (pH_{pzc} =8.8). Increasing surface acidity of ***GS-Ar*** led to donor-acceptor interaction among electron and phenolic rings**,** hence increased removal efficiency. The maximum adsorption efficiency of ***GS-Ar*** was observed at the neutral pH, which was due to hydrogen bonding among the phenol molecule and adsorbed water molecule at the ***GS-Ar*** surface [232]. At pH above 8.8, the surface became negatively charged, and it interacted with the phenolate ions ($C_6H_4(NO_2)O^-$) to undergo electrostatic repulsion and showed a sharp decrease in the adsorption efficiency [9].

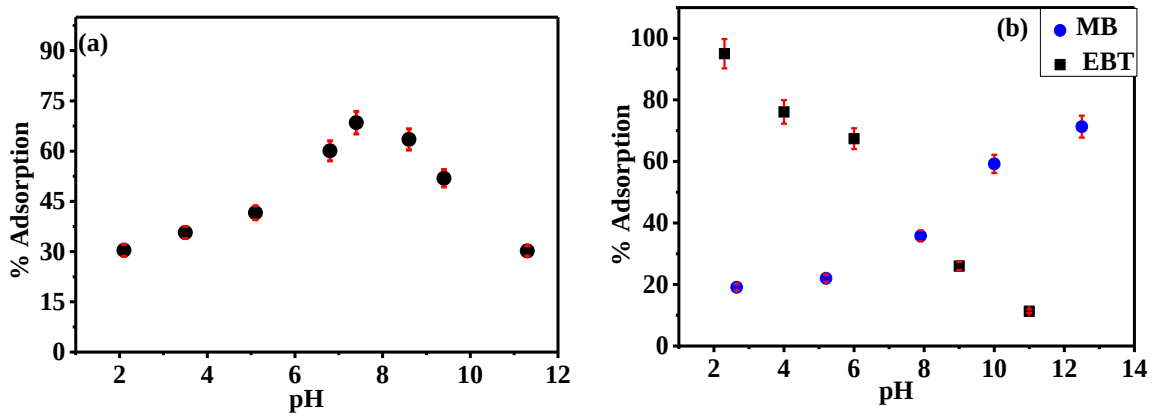

Fig. 5.11: %Adsorption with pH variation using ***GS-Ar*** for (a) PNP and (b) MB and EBT dye.

MB*:** The ***GS-Ar sample's adsorption efficiency for MB increased with an increase in the pH (Fig. 5.11 (b)). The sample's surface carried a net positive charge at lower pH values, thus restricting cationic dye adsorption on its surface. With the increase in the pH above the pH_{pzc} (8.8), the surface of the ***GS-Ar*** sample carried a net negative charge, and hence due to electrostatic interaction/hydrogen bonding, the surface adsorbed the MB dye more efficiently.

EBT: The adsorption capacity for the ***GS-Ar*** sample decreases with an increase in the EBT solution pH, as shown in Fig. 5.11 (b)**.** The sample's surface carried a net positive charge at lower pH and showed electrostatic interaction towards negatively charged anionic dye EBT. At higher pH i.e., above pH_{pzc} (8.8), the surface of the sample carried a net negative charge and repelled the negatively charged EBT dye and, hence, lower adsorption.

5.5.4. Recyclability test of *GS-Ar* for MB and PNP adsorption

Recyclability tests were conducted to check the recyclability of ***GS-Ar*** for the adsorption of PNP and MB dye (Fig. 5.12). PNP and MB were taken 20 mg/L and 1 mg/L for the recyclability test, respectively, with an adsorbent amount of 100 mg/L. The adsorption efficiency of the ***GS-Ar*** sample was tested for 14 consecutive cycles. The variation in %adsorption from the 1st to 14th cycle for PNP and MB dye were 3.7% and 4%, respectively. This small variation may be due to the loss of samples during the recycling experiments. Thus the sample was recyclable for both PNP and MB adsorption without any change of efficiency.

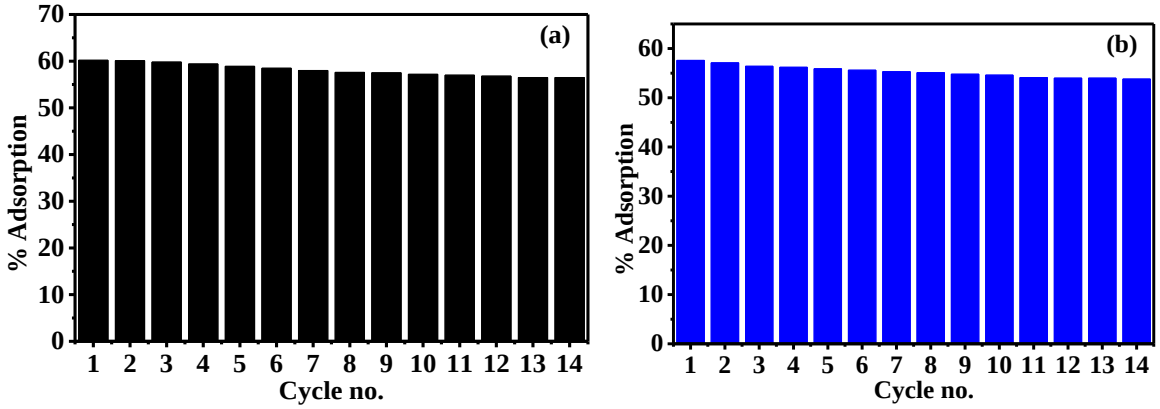

Fig. 5.12: Recyclability test of ***GS-Ar*** for the adsorption of (a) PNP and (b) MB dye.

5.5.5 Adsorption Isotherm Modeling

Langmuir and Freundlich isotherms were studied for PNP, EBT and DEP adsorption onto ***GS-Ar*** and ***GS-N*** samples. The calculation details for isotherm fitting are given in chapter 3 (section 3.4.1).

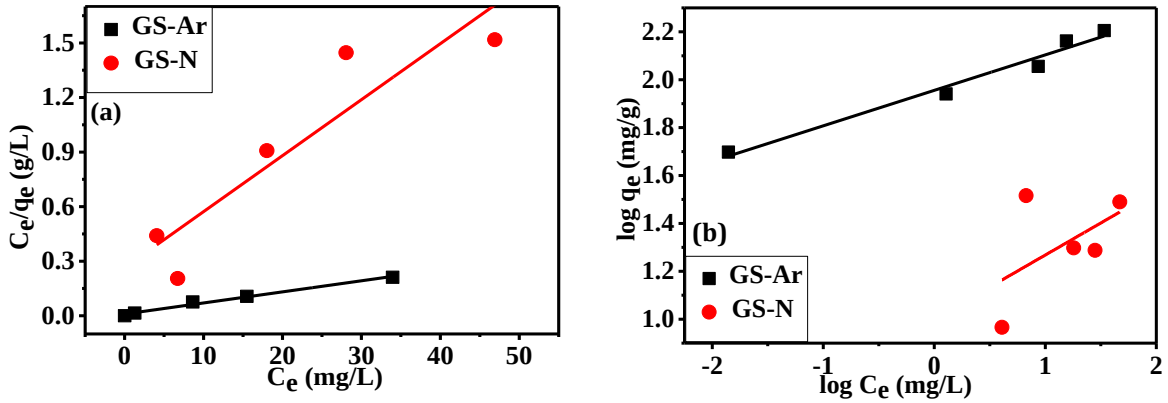

Fig. 5.13: Isotherm fitting for PNP adsorbed on ***GS-N*** and ***GS-Ar*** (100mg/L) using (a) Langmuir and (b) Freundlich model.

PNP: Langmuir and Freundlich adsorption isotherms for PNP were studied for change in PNP concentration from 1-50mg/L for a constant amount of ***GS-Ar*** and ***GS-N*** samples (100mg/L) and are shown in Fig. 5.13(a) and Fig. 5.13(b), respectively.

For Langmuir isotherm, the parameters obtained from the linear fit are given in Table 5.4. In both the samples, R_L value lies between 0 and 1, showing that adsorption was favorable. The parameters obtained from Freundlich fit are given in Table 5.4. The value of n was between 1 and 10 for both the samples representing favorable adsorption.

By comparing the regression coefficients of fitted isotherm models, one can conclude that Langmuir model was more satisfactory fit for ***GS-N*** indicating the monolayer adsorption of PNP onto the ***GS-N*** sample [202]. In the case of ***GS-Ar,*** Freundlich model fit was better, thus the adsorption process followed the multilayer adsorption.

Table 5.4: Parameters obtained from Langmuir and Freundlich isotherm models obtained for adsorption of PNP onto ***GS-N*** and ***GS-Ar*** (100 mg/L).

Adsorption isotherm	**Adsorbent**	**Parameter (units)**	**Value**	**R^2**
Langmuir isotherm	***GS-N***	k_L (L/g)	0.116	**0.787**
		q_e (mg/g)	19.844	
		R_L	0.632	
	GS-Ar	k_L (L/g)	0.640	0.985
		q_e (mg/g)	113.678	
		R_L	0.238	
Freundlich isotherm	***GS-N***	k_f (L/g)	2.719	0.044
		n	3.745	
	GS-Ar	k_f (L/g)	7.068	**0.996**
		n	6.756	

EBT: For isotherm studies of EBT adsorption onto the ***GS-Ar*** and ***GS-N*** samples the amount of adsorbent was constant (100 mg/L), and the amount of EBT was varied from 1-50 mg/L. The values obtained by fitting the isotherms in the experimental results are given in Table 5.5, and the fitted graphs are shown in Fig. 5.14. From Langmuir fitting, the value obtained for R_L is lying between 0 and 1, indicating favourable adsorption for both the adsorbents. From the Freundlich model, the obtained values of n for both samples were lying between 1 to 10, thus showed that adsorption was favorable. The Regression coefficient values in both cases show that the adsorption followed the Langmuir isotherm model, and hence the adsorption of EBT on ***GS-Ar*** occurred via monolayer adsorption.

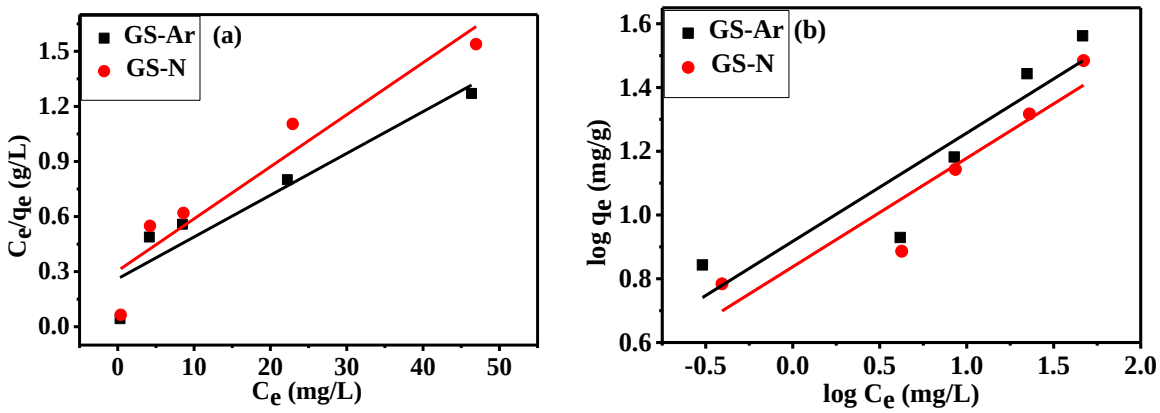

Fig. 5.14: Isotherm fitting EBT adsorbed on ***GS-Ar*** and ***GS-N*** samples (100 mg/L) using (a) Langmuir and (b) Freundlich model.

Table 5.5: Parameters obtained from Langmuir and Freundlich isotherm models obtained for EBT adsorption onto ***GS-Ar*** and ***GS-N*** samples (100 mg/L).

Adsorption isotherm	Adsorbent	Parameter (units)	Value	R^2
Langmuir isotherm	***GS-N***	k_L (L/g)	0.093	**0.878**
		q_e (mg/g)	25.378	
		R_L	0.914	
	GS-Ar	k_L (L/g)	0.087	**0.864**
		q_e (mg/g)	33.712	
		R_L	0.919	
Freundlich isotherm	***GS-N***	k_f (L/g)	2.275	0.840
		n	2.941	
	GS-Ar	k_f (L/g)	2.492	0.784
		n	2.949	

DEP: For isotherm studies of DEP adsorption the amount of ***GS-Ar*** and ***GS-N*** was constant (100 mg/L), and the amount of DEP was varied from 5-50 mg/L. Table 5.6 gives the values obtained by fitting the isotherms in the experimental results, and the fitted graphs are shown in

Fig. 5.15. The value for R_L obtained through Langmuir fitting is between 0 and 1, showing favourable adsorption for both adsorbents. The obtained values of n for both samples from the Freundlich model were in the range of 1 to 10, indicating that adsorption was favorable. The values of the regression coefficients in both situations indicate that the adsorption followed the Langmuir isotherm model, and as a result, DEP was adsorbed on ***GS-Ar*** via monolayer adsorption.

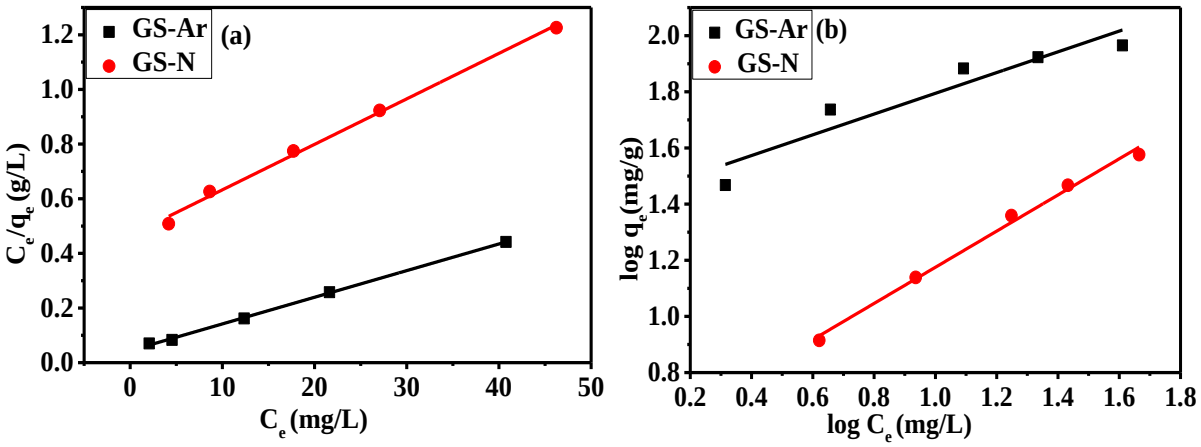

Fig. 5.15: Isotherm fitting DEP adsorbed on ***GS-Ar*** and ***GS-N*** samples (100 mg/L) using (a) Langmuir and (b) Freundlich model.

Table 5.6: Parameters obtained from Langmuir and Freundlich isotherm models obtained for DEP adsorption onto ***GS-Ar*** and ***GS-N*** samples (100 mg/L).

Adsorption isotherm	Sample	Parameter (units)	Value	R^2
Langmuir isotherm	***GS-N***	k_L (L/g)	0.035	**0.99**
		q_m (mg/g)	37.70	
		R_L	0.588	
	GS-Ar	k_L (L/g)	0.220	**0.99**
		q_m (mg/g)	92.29	
		R_L	0.18	
Freundlich isotherm	***GS-N***	k_f (L/g)	1.443	0.86
		n	1.55	
	GS-Ar	k_f (L/g)	3.873	0.99
		n	2.71	

5.5.6 Adsorption Kinetic Modeling

The understanding of adsorption kinetics is vital for determining the adsorption process's rate and mechanism. In the present work, the heat-treated samples showed better adsorption efficiency for EBT as compared with MB. So, the adsorption kinetics and isotherms of EBT adsorption for ***GS-Ar*** and ***GS-N*** samples has been studied. The kinetics of adsorption

of PNP, EBT and DEP onto ***GS-N*** and ***GS-Ar*** samples were studied using kinetic models as discussed in chapter 3 (section 3.4.2) *viz.* PFO model, PSO model, and Elovich model. The IPD model was applied to study the diffusion mechanism during the adsorption process.

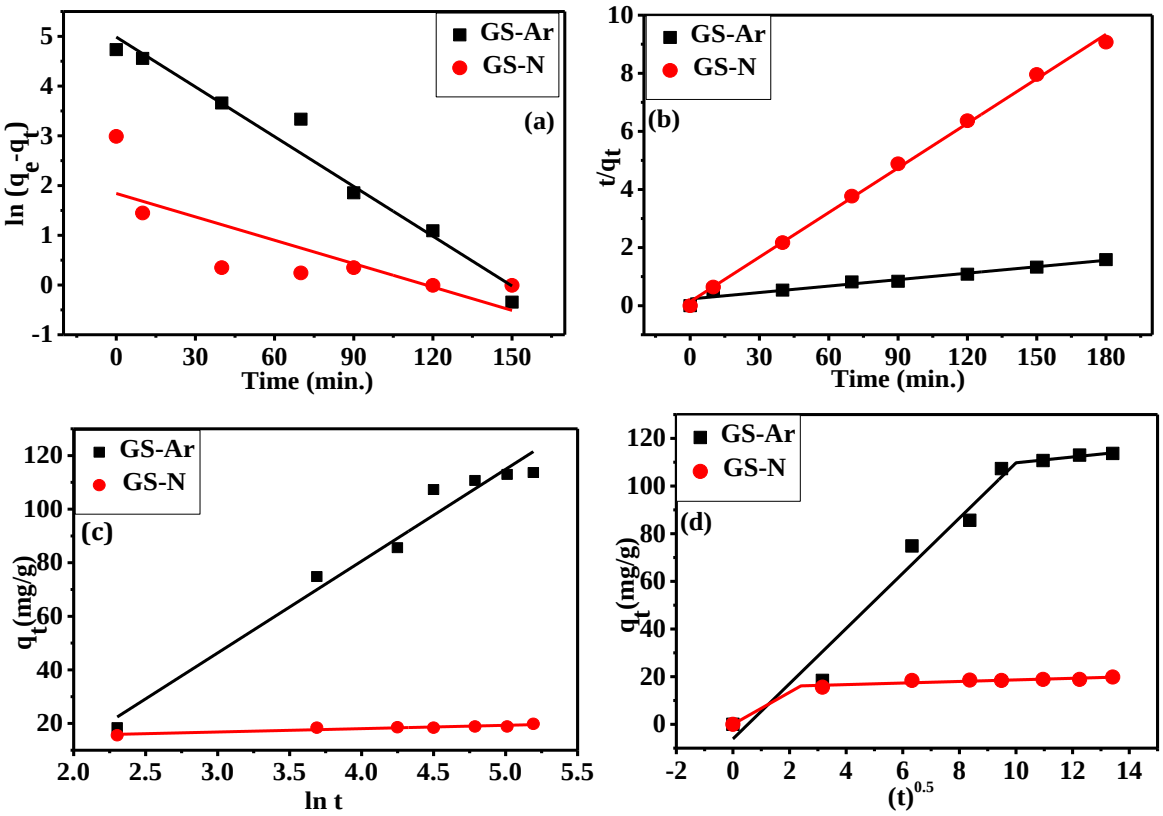

Fig. 5.16: Kinetic modeling of PNP (20mg/L) adsorbed on ***GS-N*** and ***GS-Ar*** (100mg/L) using (a) PFO, (b) PSO, (c) Elovich and (d) IPD model.

Table 5.7: Parameters of kinetic modeling of PNP adsorbed at ***GS-N*** and ***GS-Ar*** samples. (q_e (***GS-N***)= 19.844 mg/g and q_e (***GS-Ar***)= 113.678 mg/g).

Kinetic model	Adsorbent	Parameter (unit)	Value	R^2
PFO	***GS-N***	k_1 (1/min)	0.015	0.562
		q_e (mg/g)	6.299	
	GS-Ar	k_1 (1/min)	0.033	0.962
		q_e(mg/g)	146.29	
PSO	***GS-N***	k_2 (g/mg min.)	0.01880	**0.997**
		q_e(mg/g)	19.557	
	GS-Ar	k_2 (g/mg min.)	0.00023	0.919
		q_e(mg/g)	135.13	
Elovich model	***GS-N***	α (mg/g min.)	43095.2	0.868
		β	0.800	
	GS-Ar	α (mg/g min.)	178.219	**0.963**
		β	0.029	

PNP: Various models were fitted for 100 mg/L of adsorbent used in 20 mg/L of PNP solution. The experimentally calculated values of q_e (amount of adsorbate (in mg) adsorbed on per gram of adsorbent) for PNP adsorption on ***GS-Ar*** and ***GS-N*** samples were 113.678 mg/g and 19.844 mg/g.

For PFO, the linear fitted graphs between $\ln(q_e-q_t)$ and time are shown in Fig. 5.16(a). The parameters obtained from PFO fiiting are given Table 5.7. Here, the rate constant for PFO (k_1 (min^{-1})) was determined using linear fitting slope. The values of $\%\Delta q_e$ (the difference between experimental and theoretically calculated values of q_e) for ***GS-N*** and ***GS-Ar*** were 68.25% and 28.68%, respectively. The fitting of experimental data of adsorption of PNP with the PSO model is shown in Fig. 5.16(b) for ***GS-N*** and ***GS-Ar*** samples. The parameters obtained from PSO fit are mentioned in Table 5.7. For PSO, The values of $\%\Delta q_e$ for ***GS-N*** and ***GS-Ar*** samples were 1.4% and 16.3%, respectively. The fitting for adsorption of PNP using ***GS-N*** and ***GS-Ar*** with the Elovich model is shown in Fig. 5.16(c). The Elovich fit parameters are given in Table 5.7.

Table 5.8: Parameters of diffusion model (IPD) of PNP adsorbed at ***GS-N*** and ***GS-Ar*** samples.

Adsorbent	**Parameter (unit)**	**Value ($mg/g\ min^{1/2}$)**	**R^2**
GS-N	k_{id1}	6.719	0.975
	k_{id2}	0.331	
GS-Ar	k_{id1}	11.586	0.930
	k_{id2}	1.218	

For ***GS-Ar*** sample, $\%\Delta q_e$ values indicated that PSO is more suitable model as compared to PFO model indicating chemisorption nature of PNP adsorption. A comparison with the regression coefficient values of Elovich model indicated that adsorption was multilayer chemisorption [42].

Fig. 5.16(d) shows the IPD fit of the adsorption process of PNP onto ***GS-N*** and ***GS-Ar*** samples. The parameters obtained from fitting are given in Table 5.8. In both cases, two-step linear fits were obtained with a regression coefficient >0.9, showing that initially adsorption via boundary layer diffusion was taking place followed by intraparticle diffusion [203]. The linear fits in both cases were passing through the origin, which showed that adsorption process was IPD controlled. The rate constant obtained was higher for the ***GS-Ar*** sample, showing that adsorption occured at faster rate on this sample.

EBT: To study the adsorption kinetics for EBT, the adsorbent and adsorbate concentrations were taken as 20 mg/L and 1 mg/L, respectively. The experimentally calculated values of q_e were 33.71 mg/g and 25.38 mg/g for ***GS-Ar*** and ***GS-N*** samples, respectively. The values obtained by fitting the kinetic models are given in Table 5.9, and the fitted graphs are shown in Fig. 5.17.

The $\%\Delta q_e$ values for PFO and PSO models for the ***GS-Ar*** and ***GS-N*** samples were 71.8% and 66.9%, respectively. The $\%\Delta q_e$ values for PSO fit for ***GS-Ar*** and ***GS-N*** sample were 28.9% and 15.8%, respectively. Based on $\%\Delta q_e$ values and regression coefficient obtained by PFO, PSO and Elovich fit, adsorption of EBT onto both ***GS-Ar*** and ***GS-N*** followed the PSO model. This indicated that the adsorption was taking place via chemisorption.

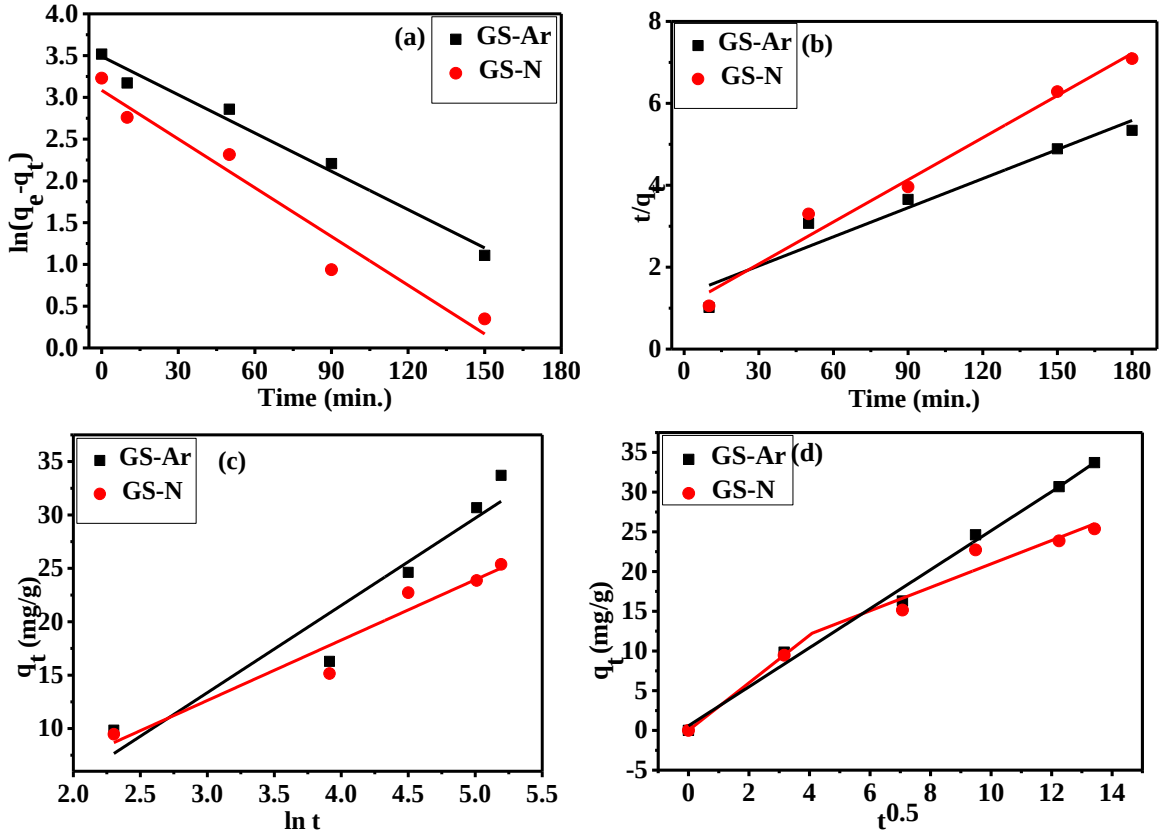

Fig. 5.17: Kinetic modeling of EBT (1mg/L) adsorbed on ***GS-Ar*** and ***GS-N*** samples (20 mg/L) using (a) PFO, (b) PSO, (c) Elovich and (d) IPD model.

To know the type of diffusion during adsorption mechanism, the IPD model was also fitted. Table 5.10 gives the parameters obtained from IPD fit. The regression coefficients obtained for the IPD mechanism were satisfactory (>0.9). In the case of the ***GS-Ar*** sample, the adsorption is single-step process indicating only IPD is controlling the process [233]. The adsorption takes place via two steps for ***GS-N*** sample, showing that the adsorption was first

via film diffusion and then via the IPD mechanism. It is clear from Fig. 5.17(d) that fitted lines pass through origin, showing that IPD mechanism controls the adsorption process.

Table 5.9: Parameters of kinetic modeling of EBT adsorbed at ***GS-Ar*** and ***GS-N*** samples. (q_e (***GS-Ar***)= 33.712 mg/g and q_e (***GS-N***)=25.378 mg/g).

Kinetic model	Adsorbent	Parameter (unit)	Value	R^2
PFO	***GS-N***	k_1 (1/min)	0.0194	0.940
		q_e (mg/g)	8.385	
	GS-Ar	k_1 (1/min)	0.0152	0.977
		q_e(mg/g)	9.485	
PSO	***GS-N***	k_2 (g/mg min)	0.0011	**0.973**
		q_e(mg/g)	29.41	
	GS-Ar	k_2 (g/mg min)	0.0004	**0.918**
		q_e(mg/g)	43.47	
Elovich model	***GS-N***	α (mg/g min)	11.035	0.925
		β	0.176	
	GS-Ar	α (mg/g min)	11.064	0.888
		β	0.122	

Table 5.10: Parameters of diffusion model (IPD) of EBT adsorbed at ***GS-N*** and ***GS-Ar*** samples.

Adsorbent	Parameter (unit)	Value (mg/g $min^{1/2}$)	R^2
GS-N	k_{id1}	2.456	0.982
	k_{id2}	2.592	
GS-Ar	k_{id1}	2.994	0.963

DEP: The $\%\Delta q_e$ values for PFO models using ***GS-Ar*** and ***GS-N*** sample were 84.3% and 61.4%, respectively. The $\%\Delta q_e$ values for PSO fit for the ***GS-Ar*** and ***GS-N*** sample were 38.8% and 17.6%, respectively. Adsorption of DEP onto ***GS-Ar*** and ***GS-N*** sample followed the PSO model, based on $\%\Delta q_e$ values and regression coefficient produced by PFO, PSO, and Elovich fit (Fig. 5.18 (a-c), Table 5.11). This demonstrated that chemisorption was involved in the adsorption process. For both samples, the adsorption process for DEP consists of two steps: initial adsorption via boundary layer diffusion, followed by intraparticle diffusion [42]. Boundary layer diffusion for adsorption using ***GS-Ar*** and ***GS-N*** sample occurs up to 118 and 60 minutes, respectively, while intraparticle diffusion occurs beyond these durations (Fig. 5.18(d)). The IPD fitting parameters obtained are given in Table 5.12.

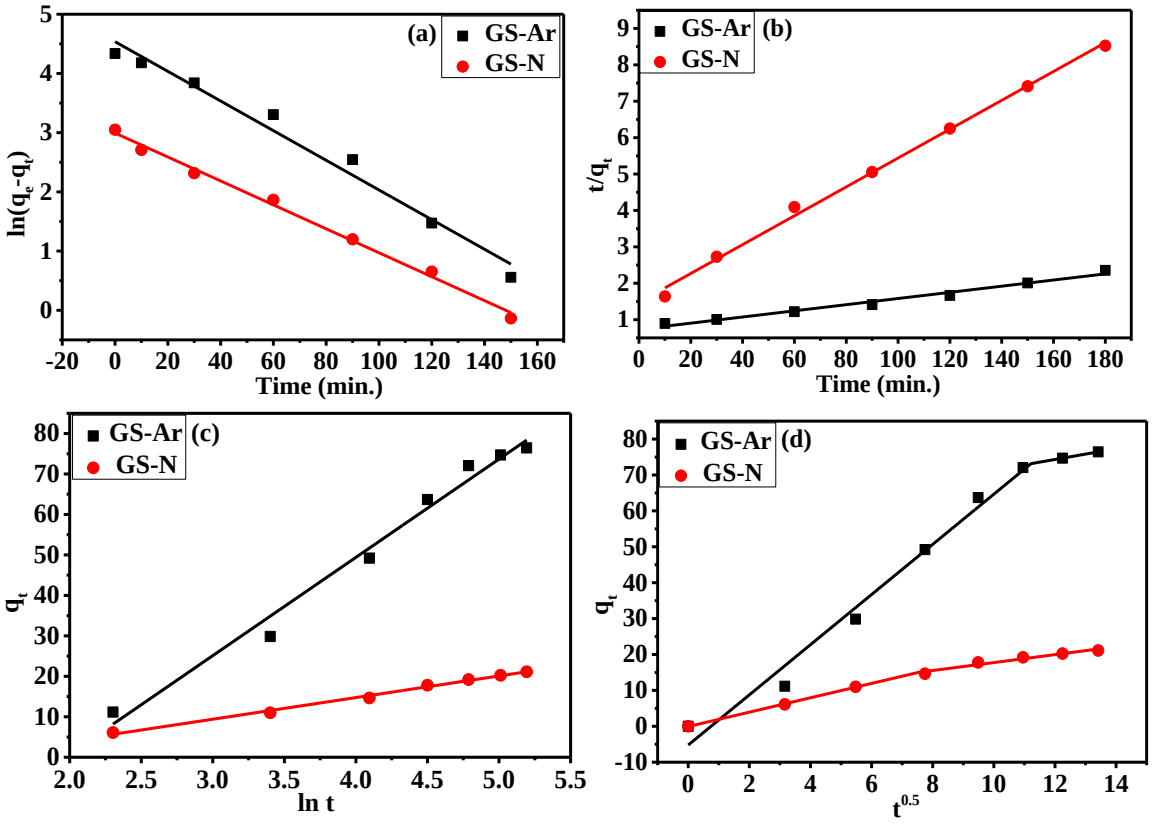

Fig. 5.18: Kinetic modeling of DEP (20mg/L) adsorbed on ***GS-Ar*** and ***GS-N*** samples (100 mg/L) using (a) PFO, (b) PSO, (c) Elovich and (d) IPD model

Table 5.11: Parameters of kinetic modeling of DEP adsorbed at ***GS-Ar*** and ***GS-N*** samples. (q_e (***GS-Ar***)= 76.43 mg/g and q_e (***GS-N***)=21.11 mg/g).

Kinetic model	Sample	Parameter (unit)	Value	R^2
PFO	***GS-N***	k_1 (1/min)	0.020	0.99
		q_e (mg/g)	8.13	
	GS-Ar	k_1 (1/min)	0.024	0.98
		q_e(mg/g)	12.01	
PSO	***GS-N***	k_2 (g/mg min)	0.0010	**0.99**
		q_e(mg/g)	25.64	
	GS-Ar	k_2 (g/mg min)	0.00009	**0.98**
		q_e(mg/g)	125.00	
Elovich model	***GS-N***	α (mg/g min)	18.041	0.99
		β	0.187	
	GS-Ar	α (mg/g min)	129.7	0.98
		β	0.041	

Table 5.12: Parameters of diffusion model (IPD) of DEP adsorbed at ***GS-N*** and ***GS-Ar*** samples.

Sample	Parameter	Value	R^2
GS-N	k_{id1}	2.002	0.99
	k_{id2}	1.106	
GS-Ar	k_{id1}	6.987	0.98
	k_{id2}	1.49	

From the kinetic model fitting, the results obtained shows that the adsorption was multilayer chemisorption and hence verifying the results obtained from isotherms modeling. The values of regression coefficient obtained for ***GS-Ar*** sample (>0.9) were better in comparison to ***GS-N*** (<0.9) sample validating the better adsorption efficiency of ***GS-Ar*** sample for PNP and DEP as discussed earlier under section 5.5.2.

5.5.7 Adsorption mechanism

On the basis of adsorption kinetic model and adsorption isotherms fitted for PNP, EBT and DEP adsorption onto ***GS-Ar***, the best fitted models are mentioned in Table 5.13. The adsorption mechanism can be explained as follows.

Table 5.13: Results of different adsorption kinetics and isotherm modeling for ***GS-Ar*** sample.

Pollutant adsorbed	Kinetic model	Isotherm model	IPD
PNP	PSO	Freundlich	2 step
EBT	PSO	Langmuir	1 step
DEP	PSO	Langmuir	2 step

For PNP: The Freundlich isotherm fit indicated the heterogeneous nature of ***GS-Ar*** sample for PNP adsorption with N-doping sites as favorable adsorption sites. The PSO kinetic model indicates the physicochemical interaction occurring between PNP and the sample via multilayer adsorption. Two step IPD fit indicated that initially adsorption takes place through boundary layer diffusion and beyond 91 minutes intraparticle diffusion occurred. This shows that initially, the external resistance to mass transfer occurred upto 91 minutes and thus slow adsorption took place via multilayer adsorption [233]. So for the ***GS-Ar*** sample the N-doped sites on the surface act as main adsorption sites for PNP with initial adsorption resulting in slow multilayer formation followed by fast intraparticle diffusion.

For EBT: For EBT, the reversible adsorption occurs at multiple equivalent sites leading to monolayer formation on the surface of ***GS-Ar*** as indicated by the Langmuir nature of the isotherm. PSO kinetic fit indicated that the EBT adsorbs strongly on to ***GS-Ar*** via chemisorption. This is in accordance with the opposite charge of the dye and ***GS-Ar*** at the relevant pH. Single step fit of IPD indicated that the adsorption takes place through intraparticle diffusion during the entire time period [233]. Thus the adsorption of EBT onto the ***GS-Ar*** sample takes place through the monolayer formation by multipoint adsorption as a result of electrostatic charge interaction.

For DEP: Isotherm's Langmuir nature showed that DEP undergo reversible adsorption at many equivalent sites, resulting in the formation of a monolayer on the adsorbent's surface. According to the PSO kinetic fit, the adsorption was by strong chemisorption. The strong interactions can be explained by acidic nature of DEP positively charged surface of the sample. Adsorption proceeds initially by boundary layer diffusion and then through intraparticle diffusion, according to a two-step fit of the IPD. For DEP adsorption onto ***GS-Ar*** and ***GS-N*** sample, boundary layer diffusion was followed by intraparticle diffusion after 118 and 60 minutes, respectively. The acidic nature of DEP (at the relevant pH) results in strong interactions with both the samples. This results in formation of monolayer on the sample surface by adsorption due to multipoint interaction. The formation of the monolayer proceeds initially by boundary layer diffusion and then by intraparticle diffusion.

Table 5.14 shows the conclusion of adsorption results obtained using the ***GS-Ar*** sample for EBT and PNP adsorption.

Table 5.14: Adsorption results for the best sample.

Sample ID	Pollutant	q_e (mg/g)	Kinetic model	Kinetic isotherm
GS-Ar	PNP	113.67	PSO	Freundlich
	EBT	25.37	PSO	Langmuir
	DEP	92.29	PSO	Langmuir

5.6 Summary

GS1 sample was heat-treated at 900°C in carrier gases Ar or N_2 for 4 h to test the effect of heating atmospheres on the properties of the resulting samples. SEM analysis indicated an increment in surface area. The XRD line profile, Raman spectroscopy, FTIR, UV–visible spectroscopy and XPS indicated that the amorphous ***GS1*** sample underwent graphitization and a decrease in the O and N content due to breakage/restructuring of bonds and release of volatile substances upon heating in the inert atmosphere. The results of a TG/DSC/DTG analysis of the sample revealed that inert atmospheres experienced simultaneous volatile release and graphitization, with Ar experiencing graphitization at a lower temperature (345 °C) than N_2 (352 °C). The bandgap increased for ***GS-Ar*** and ***GS-N*** samples to 4.8 eV from 4.5 eV of the ***GS1*** sample. From XPS the N content obtained in ***GS1, GS-Ar,*** and ***GS-N*** samples were 2.22, 1.54, and 1.17%, respectively. The pyrrolic and graphitic N functionalities in ***GS1*** sample changed to pyridinic, graphitic, and oxidized N upon heat treatment with graphitic N in highest

concentration due to its higher thermal stability. The BET surface area for ***GS1, GS-Ar,*** and ***GS-N*** samples were 7.43 m^2/g, 449 m^2/g, and 468.31 m^2/g, respectively. From the NLDFT analysis, the micropore size of ***GS-Ar,*** and ***GS-N*** samples were calculated as 1.1 nm and 0.8 nm with same pore volume. The mechanism of pore development in various atmospheres (N_2 and Ar) was thoroughly elucidated from the thermal treatment of ***GS1***. During heat treatment, the high density and low diffusivity of Ar resulted in the formation of micropores larger than 1 nm by the nucleation and explosion of volatile gases inside the carbon spheres.

The pH_{pzc} for ***GS1, GS-Ar*** and ***GS-N*** samples of 4.6, 8.8 and 9.6, respectively indicated drastic change in surface chemistry of heat-treated samples. The %adsorption in dark for PNP, EBT and DEP was observed maximum for the ***GS-Ar*** sample and were 56.8%, 67.4%, and 38.1%, respectively. The adsorption with pH variation of pollutants were also studied and explained in conjugation with surface chemistry. From the adsorption kinetics and adsorption isotherm studies of PNP for ***GS-Ar*** sample, it was emerged that the adsorption was taking place via chemisorption and the diffusion mechanism was controlled by boundary layer and IPD with multilayer adsorption. For EBT and DEP, adsorption was taking place via chemisorption with monolayer adsorption and diffusion was controlled by IPD. In conclusion, the sample prepared under Ar atmosphere has emerged as a good candidate for wastewater treatment with manifold efficiency.

Chapter 6

Chemical activation of soy flour based N doped carbons

Overview

This chapter describes the chemical activation of N-doped carbon spheres synthesized using glucose and soy flour via the HTC method explained in chapter 3 using KOH and $ZnCl_2$ in different impregnation ratios. The details of it has been presented in chapter 3. The effect of low temperature and time dependency on the sample properties has been studied using FE-SEM, XRD, FTIR, UV–Visible, Raman, XPS, and BET. The difference in surface area and surface chemistry with impregnation ration as well as with activating agent was confirmed by BET and XPS & pH_{pzc} of samples. The variation in the results has been explained on the basis of the reactivity of activating agent with the sample along with the corresponding mechanism. The adsorption efficiency of the synthesized samples was carried out for cationic dyes MB and CV, anionic dye EBT, pharmaceutical waste CIP, PNP and DEP as done in chapter 4. Based on the best adsorption data, the adsorption rate and mechanism were determined using kinetic modeling and isotherm analysis.

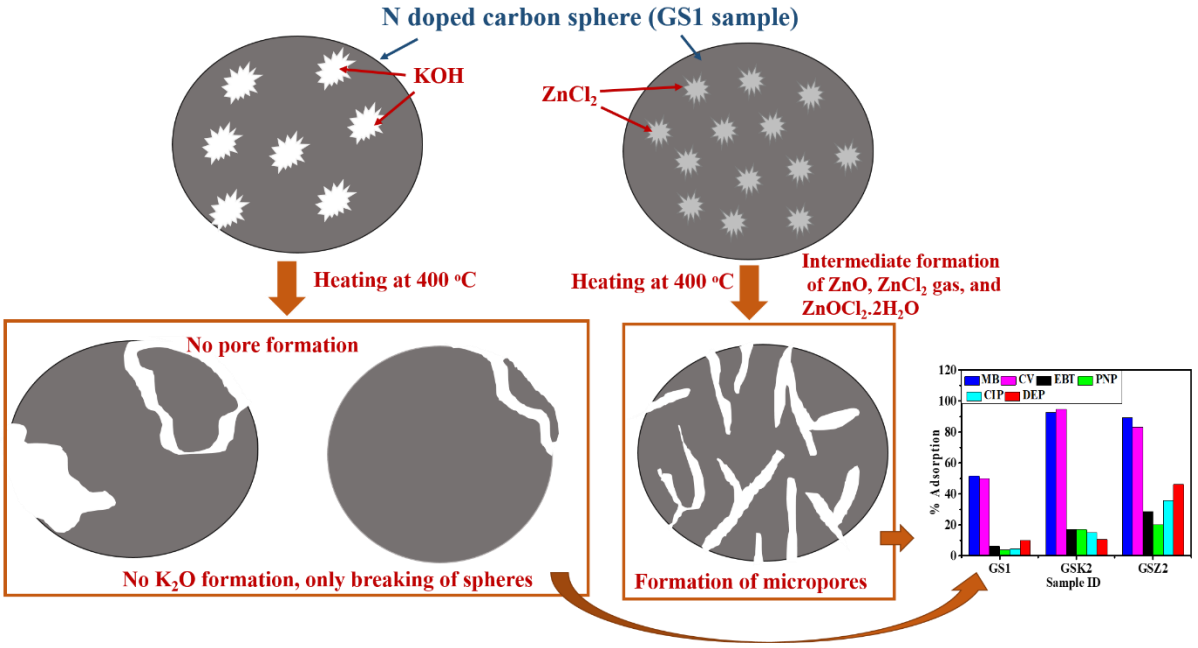

6.1 Introduction

These days, N-doped activated carbon is being employed as an effective adsorbent for wastewater treatment. The activation of HTC samples or biochar can be done either by physical or chemical activation. Chemical activation is recommended over physical activation since it requires less energy and has better yields and surface areas [107]. Chemical activation agent (AA) and its impregnation ratio along with activation temperature, atmosphere and time plays a vital role in determining the surface area, pore size, pore volume and surface chemistry [109,110].

In this chapter, chemical activation of ***GS1*** sample was done in a muffle furnace using KOH and $ZnCl_2$ as explained in chapter 3 (section 3.4.3). Activation agent and its impregnation ratios play an important role in determining the surface area and pore formation/distribution. The effect of chemical activation on the adsorption of MB, CV, EBT, PNP, CIP and DEP is explained in details. The properties of the synthesized samples are given in Table 6.1

Table 6.1: Properties of the synthesized samples.

Sample ID ⟶	***GS1***	***GSK0.5***	***GSK1***	***GSK1.5***	***GSK2***	***GSZ0.5***	***GSZ1***	***GSZ1.5***	***GSZ2***
Activation agent (AA)	-	KOH	KOH	KOH	KOH	$ZnCl_2$	$ZnCl_2$	$ZnCl_2$	$ZnCl_2$
Activation temperature (°C)	-	400	400	400	400	400	400	400	400
Ratio (GS1: AA)	-	1:0.5	1:1	1:1.5	1:2	1:0.5	1:1	1:1.5	1:2
%C	74.10	-	67.32	-	61.23	-	79.51	-	74.72
%N	2.22	-	2.67	-	3.22	-	2.91	-	3.72
%O	23.60	-	30.01	-	35.53	-	17.58	-	21.56
Nature of Nitrogen (major)	Pyrrolic	-	Pyrrolic	-	Graphitic	-	Graphitic	-	Graphitic
Band gap (eV)	4.50	-	4.82	-	4.79	-	4.77	-	4.75
I_D/I_G	-	-	0.8	-	0.7	-	0.7	-	0.7
Surface area (m^2/g)	7.43	5.40	5.12	6.45	7.60	58.51	232.39	226.47	110.93
Mean pore diameter(nm)	14.80	-	-	-	-	-	0.33	0.60	0.81
pH_{pzc}	4.6	6.2	6.8	7.1	7.2	7.3	7.3	7.8	8.0

6.2 Characterizations of chemically activated soy flour based N doped carbons

6.2.1 FE-SEM

Fig. 6.1 presents FE-SEM micrographs of all the synthesized samples. It can be observed that with the increase in the ratio of activators, no variation in the average size of the spheres was observed. The comparison of micrographs of ***GS1***, ***GSK2,*** and ***GSZ2*** samples is

shown in Fig. 6.2. Surface of the ***GS1*** sample was observed to be smooth without any pores as already discussed in previous chapter (chapter 4) [211,234]. For the ***GSK2*** sample, surface of spheres was uneven and shape had become distorted. Whereas for the ***GSZ2*** sample, the surface of the spheres was observed to be dappled without distortion in spherical shape. It shows that reaction of $ZnCl_2$ with the spheres took place evenly and followed a different mechanism than that for KOH. It can be observed in Fig. 6.1 that with increase in the KOH ratio, the distortion of surface increased. In the case of $ZnCl_2$ activated samples, the formation of the visible pores was not observed. The formation of nanosized pores may occur with an increasing $ZnCl_2$ ratio, which will need to be confirmed by the N_2 adsorption-desorption isotherms.

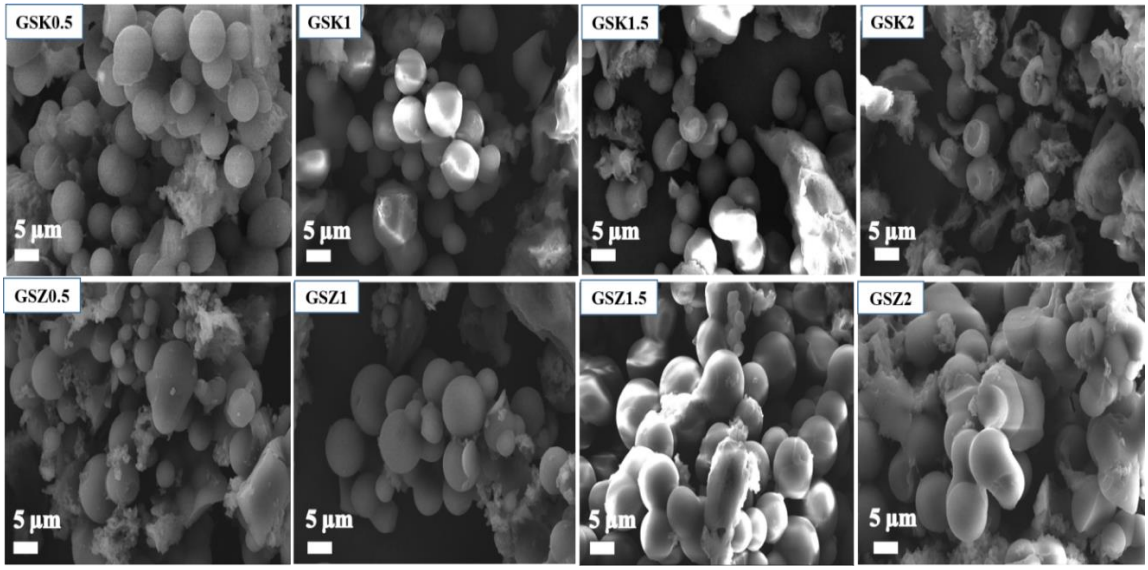

Fig. 6.1: FE-SEM micrographs of synthesized samples.

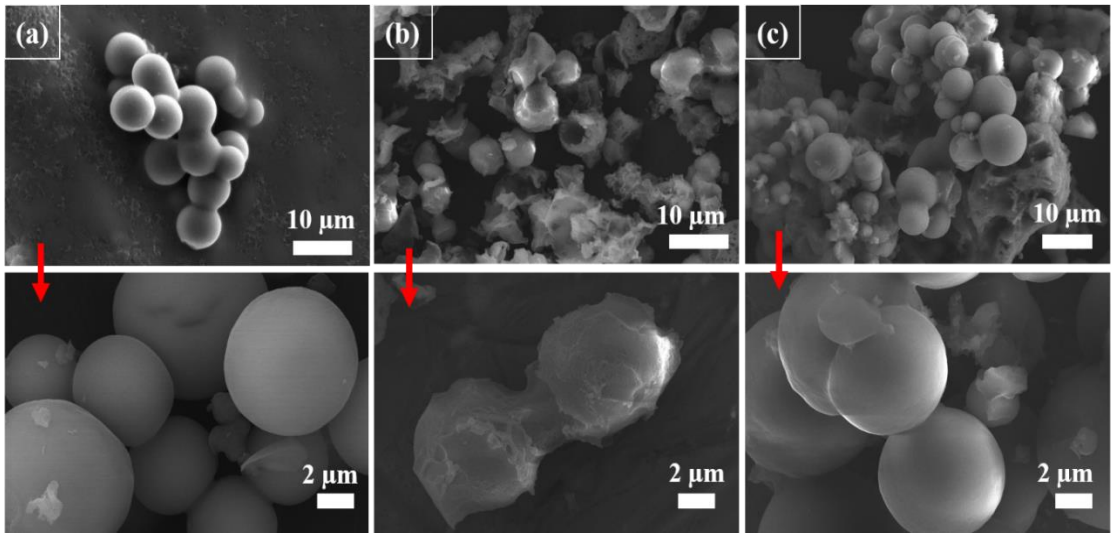

Fig. 6.2: FE-SEM images of (a) ***GS1***, (b) ***GSK2***, and (c) ***GSZ2.***

6.2.2 XRD

The X-ray diffraction pattern of all the synthesized samples are shown in Fig 6.3. The samples activated with KOH (Fig. 6.3(a)) showed amorphous peaks at 2θ ~21° and ~44°. While the samples activated with $ZnCl_2$ had diffraction peaks at 2θ ~26° and ~44° (Fig. 6.3(b)). Comparison of XRD pattern for ***GS1***, ***GSK2*** and ***GSZ2*** samples is shown in Fig. 6.4(a). For KOH activated samples, the first peak observed at 21°, was similar to as observed in the ***GS1*** sample (as reported in chapter 4). It signified carbon quantum dots in the sphere's centre and having (002) plane of amorphous carbon [211]. This suggested that the quantum dots present in the core of the ***GS1*** sample spheres remained intact when the activation of ***GS1*** was done by KOH. This was a clear indication that effects of KOH were limited to surface and it does not penetrate to the inner core of the ***GS1***. For the $ZnCl_2$ activated samples, a less broad peak observed at 2θ ~26° indicated (002) plane of the graphitic carbon and suggested that ***GSZ2*** samples had a more ordered structure than ***GSK2*** and ***GS1*** samples [234]. This variation in the XRD line profile of ***GSZ2*** sample indicated that the available quantum dots in the centre of ***GS1*** were restructured during activation with $ZnCl_2$. The peak at 2θ ~44° in both ***GSZ2*** and ***GSK2*** indicated the presence of (100) plane of graphitic carbon [235].

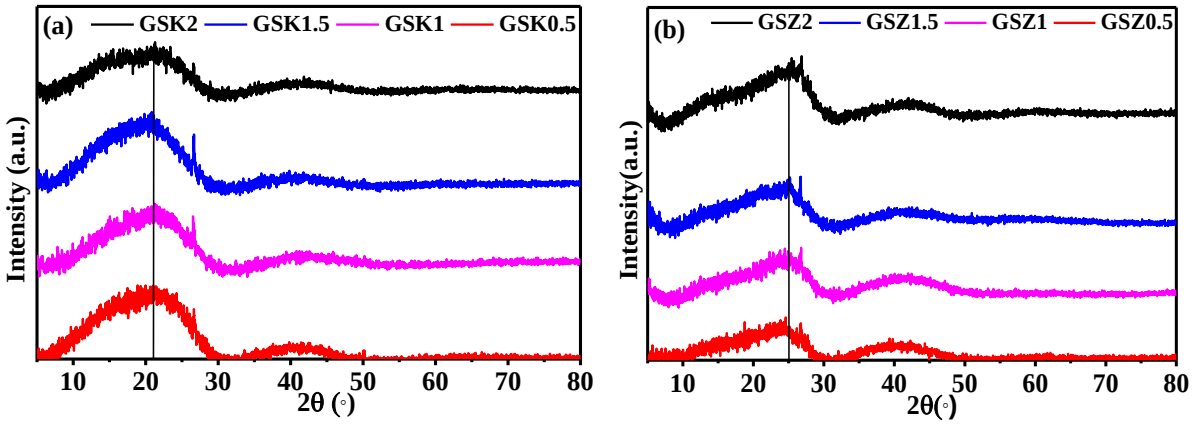

Fig. 6.3: XRD of samples activated by (a) KOH and (b) $ZnCl_2$.

6.2.3 N_2 adsorption-desorption isotherms

Fig. 6.5 shows the N_2 adsorption-desorption isotherms curves for KOH and $ZnCl_2$ activated samples, respectively. The comparison of N_2 adsorption-desorption isotherms of ***GS1***, ***GSK2*** and ***GSZ2*** is shown in Fig. 6.4(b). The adsorption isotherms exhibited type–II characteristics and were of the H4 type, according to IUPAC classification. [194]. From chapter 4, the BET surface area for the ***GS1*** sample was 7.43 m^2/g [211]. The BET surface area for samples activated with KOH has not changed (Table 6.1). The surface of the sample observed to be distorted in the FE-SEM images of KOH activated samples, which had no

significant impact on surface area. The sample's inner structure remained intact after KOH activation also as indicated by the XRD line profile.

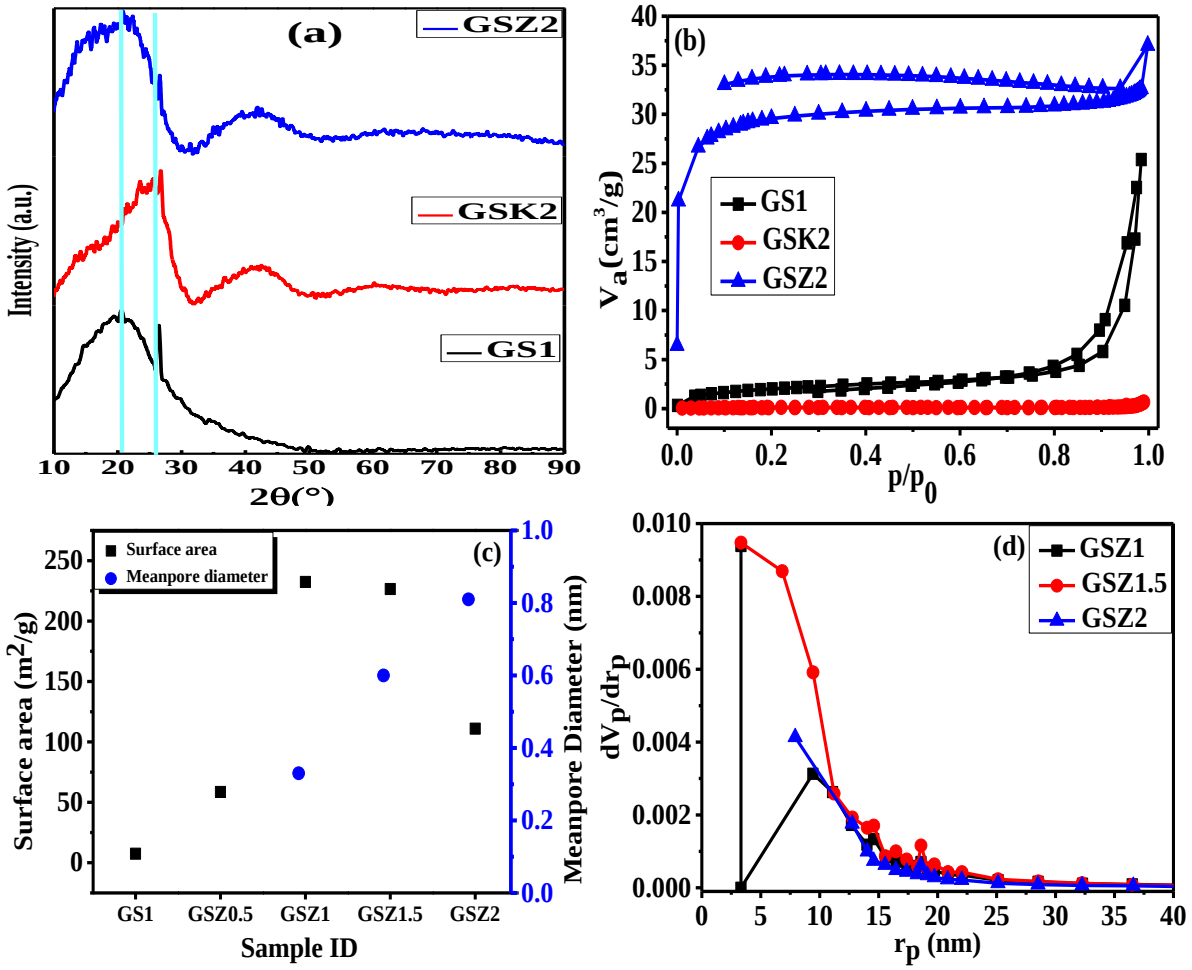

Fig. 6.4: (a) XRD, (b) N_2 adsorption-desorption isotherms of ***GS1***, ***GSK2*** and ***GSZ2***, (c) surface area and pore size of $ZnCl_2$ activated samples (d) pore size distribution of $ZnCl_2$ activated samples.

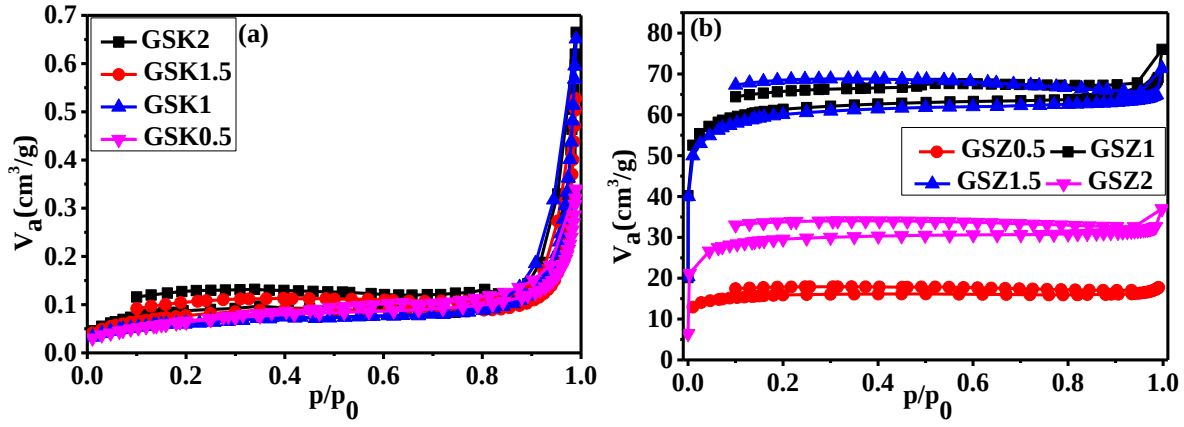

Fig. 6.5: N_2 adsorption-desorption isotherms of samples activated by (a) KOH and (b) $ZnCl_2$.

In the case of $ZnCl_2$ activated samples, the surface area changed significantly with impregnation ratio of $ZnCl_2$. Fig. 6.4(c) gives the variation of surface area with changing impregnation ratios. For ***GSZ0.5*** and ***GSZ1*** samples, the surface area increased but with further increase in the impregnation ratio the surface area starts to decrease. Further, for the ***GSZ2*** sample, surface area decreased to 110.93 m^2/g. This can be attributed to the reason that the formation of new micropores has been restricted and excess of $ZnCl_2$ resulted in widening of micropores developed. This is confirmed from the pore size distribution analysis using Horvath-Kawazoe method of $ZnCl_2$ samples (Fig. 6.4(c) and 6.4(d)) showing the increase in the average pore size with increased $ZnCl_2$ impregnation ratio (Table 6.1). The largest average pore size of 0.8 nm in the ***GSZ2*** sample is the best for adsorption as it will allow for volume within the pores to be available for the pollutants of larger size to be adsorbed. This fact will need to be confirmed further by adsorption study of the synthesized samples.

6.2.4 UV-Visible spectroscopy

UV-Visible spectroscopy was performed to get the reflectance spectra of synthesised samples, as shown in Fig. 6.6 (a) and 6.6 (b). A reflectance peak at 250 nm indicated π-π^* transition of sp^2 graphitic carbon [218]. The Kubelka-Munk model was used to evaluate the bandgap of synthesized samples (Fig. 6.6 (c) and 6.6(d)). The equation for the Kubelka Munk model is explained in chapter 3 (section 3.3.6)

The values of allowed direct bandgap calculated using the above equations for all the synthesized samples are given in Table 6.1. It can be observed that values of bandgaps increased for samples after activation and data of comparison of ***GS1*** with ***GSK2*** and ***GSZ2*** samples is shown in Fig. 6.7 (a) and 6.7 (b). The increased bandgap of chemically activated samples can be attributed to the reduced oxygen or nitrogen concentration in these samples [219,220]. Also, the value of band gap depends upon the % oxidation of sample during the activation [236]. These conjectures need to be probed further by XPS analysis of the samples. Further, the value obtained for the bandgap of activated samples did not significantly vary with variation in impregnation ratios of the activators.

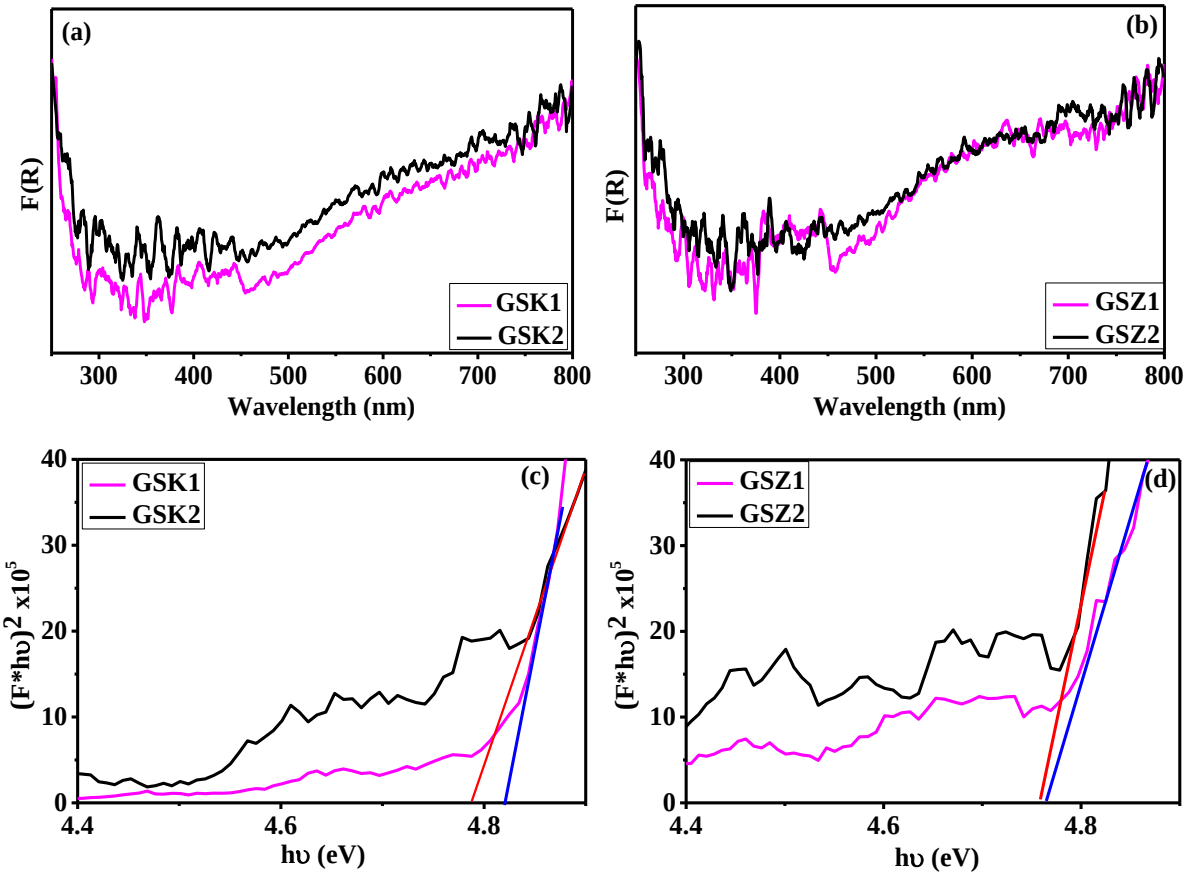

Fig. 6.6: Diffuse reflectance spectra and band gap of (a,c) ***GSK1*** and ***GSK2*** and (b,d) ***GSZ1*** and ***GSZ2*** samples.

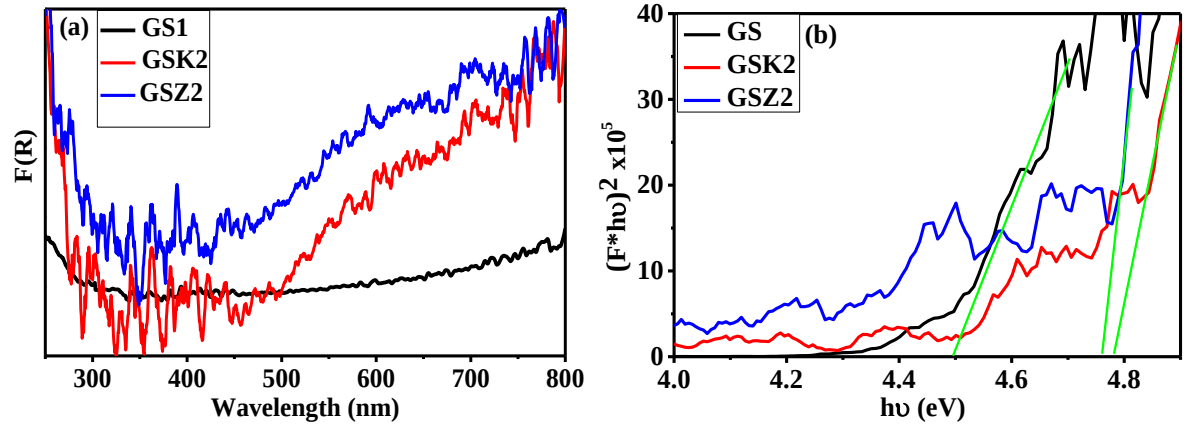

Fig. 6.7: (a) Diffuse reflectance spectra and (b) band gap of ***GS1***, ***GSK2*** and ***GSZ2.***

6.2.5 FTIR spectroscopy

Fig. 6.8 shows the FTIR spectra obtained for KOH and $ZnCl_2$ activated samples, respectively. Peaks in the spectra of KOH activated samples were determined at 3360, 2920, 2100, 1880, 1710, 1600, 1200, and 760 cm^{-1} indicating the presence of functional groups –OH (hydroxyl), –CH3 (alkane), C≡C (alkyne), C-H (aromatic), C=O (stretching), C=C (stretching), C-N (stretching) and C=C (bending), respectively. The spectra of $ZnCl_2$ activated samples

show peaks at 3300, 2070, 1870, 1600, 1200, 760 cm^{-1} indicating the presence of –OH (hydroxyl), C≡C (alkyne), C-H (aromatic), C=C (stretching), C-N (stretching) and C=C (bending) functional groups, respectively.

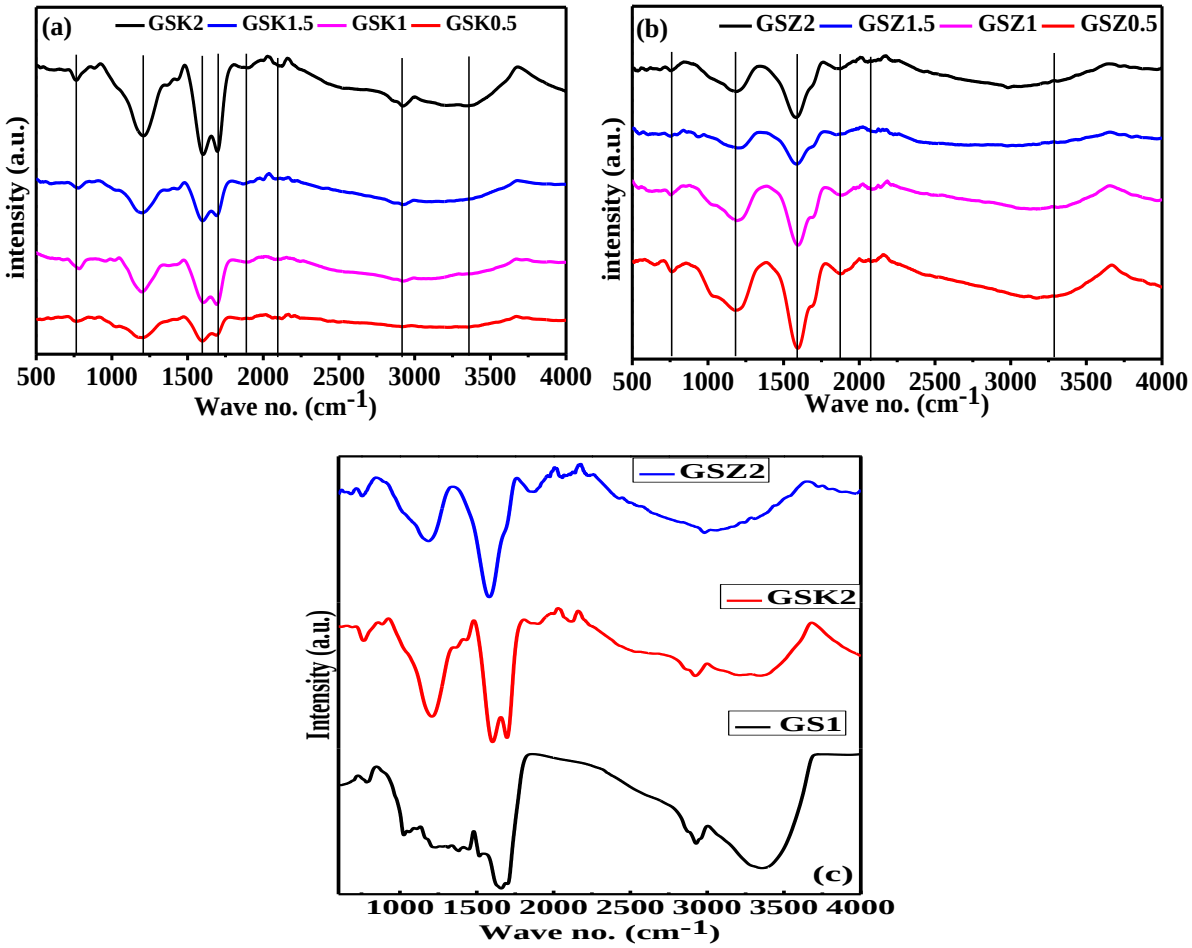

Fig. 6.8: FTIR of samples activated using (a) KOH and (b) $ZnCl_2$ and (c) comparison of ***GS1***, ***GSK2*** and ***GSZ2*** samples.

The comparison of FTIR spectra for ***GS1***, ***GSK2*** and ***GSZ2*** sample is shown in Fig. 6.8 (c). The results show that with the chemical activation of sample, the availability of surface functional groups remains consistent with ***GS1*** sample. For the ***GSK2*** sample, intense C=O band of carboxyl group was observed at 1710 cm^{-1} indicating the oxidation of sample after KOH activation [237]. Also, the intensity of C-N observed at 1200 cm^{-1} in ***GSK2*** was more than that in the ***GSZ2*** and ***GS1*** sample. The intensity of aromatic C=C at 1600 cm^{-1} in the ***GSZ2*** sample indicated a more evolved aromatic structure. This supports the conjecture obtained from XRD that ***GSZ2*** has a more ordered graphitic structure.

6.2.6 Raman spectroscopy

Raman spectroscopy is most extensively utilized in amorphous and nanocrystalline carbon materials to understand the degree of graphitization. Carbon compounds commonly exhibit broad bands in the range of 1300–1600 cm^{-1}. The D band available at nearly 1350 cm^{-1} is associated with the disordered graphitic carbon while the G band around 1590 cm^{-1} is associated with ordering in the amorphous carbon materials. The G band's position and the D to G bands intensity ratio (I_D/I_G ratio) are the most critical characteristics in identifying the nature of carbon in a material structure.

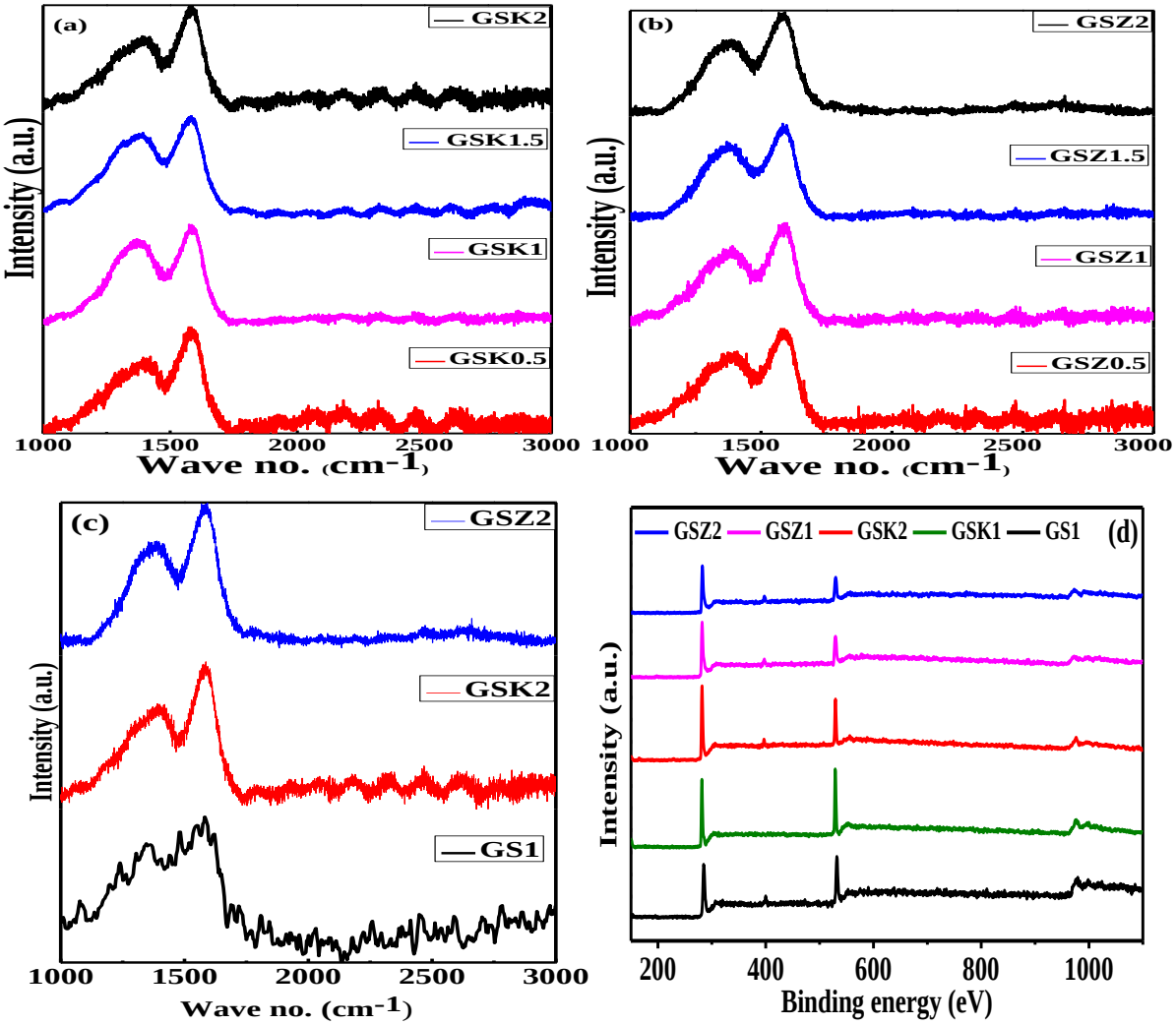

Fig. 6.9: Raman spectra of (a) KOH, (b) $ZnCl_2$ activated samples and (c) comparison of ***GS1***, ***GSK2*** and ***GSZ2*** samples and (d) XPS survey spectra of ***GS1***, ***GSK1***, ***GSK2, GSZ1,*** and ***GSZ2.***

Fig. 6.9 (a) and 6.9 (b) demonstrates the availability of D and G bands at 1380 and 1580 cm^{-1} in both ***GSK*** and ***GSZ*** samples. It can be observed that no changes in the positions of the D and G bands were detected. Furthermore, the I_D/I_G ratios were similar (Table 1) for the

synthesized samples and were below 1 indicating that ordered graphitic carbons dominates in the activated samples [234]. Fig 6.9 (c) exhibit the comparison of Raman spectra of ***GS1***, ***GSK2*** and ***GSZ2*** samples. ***GS1*** sample exhibits lower peak intensities and wider bands than the ***GSZ2*** and ***GSK2*** samples because of its low degree of graphitization as concluded from XRD line profile results.

6.2.7 XPS

The elemental composition and bonding configurations of ***GS1***, ***GSK1***, ***GSK2***, ***GSZ1*** and ***GSZ2*** samples were determined using XPS studies. Peaks at 284.0, 531.0, and 400.0 eV for C1s, O1s, and N1s, respectively, were apparent in survey spectra (Fig. 6.9(d)) [223]. Table 6.1 shows the %C, %N, and %O content of all samples based on the survey spectra. The data clearly reveals that as KOH concentration increased, the %C content dropped significantly, whereas the %O and % N contents increased. This indicated that during the KOH assisted activation of sample the carbon is removed by direct reaction of the sample with the reagent to form oxidized carbon on the surface. Therefore, with the increase in KOH concentration, the %O content increased with a lowering in %C content. With rising KOH concentration, the overall N content remained stable or seemed to increase insignificantly, presumably due to lower C content. While for the $ZnCl_2$ activation of ***GS1*** sample, with increasing concentration of $ZnCl_2$, the content of %C and %N increased while the %O content lowered significantly. This is because $ZnCl_2$ being a Lewis acid, acts as a dehydrating agent in the activation process. Therefore, it helps in aromatization of carbon structure without reacting directly with the carbon. Due to dehydration, the content of %O lowered and %C and %N increased [238].

Fig. 6.10 depicts the deconvoluted HR spectra of C1s, N1s, and O1s for for ***GSK1***, ***GSK2***, ***GSZ1*** and ***GSZ2*** samples. Table 6.2 lists the parameters obtained from deconvolution of C1s, O1s, and N1s HR spectra for all the samples. The peak at 284.2 eV, corresponding to sp^2 hybridised carbons, dominates all of the synthesised samples' C1s spectra. The remaining C1s peaks were deconvoluted as C-N/C=N, O-C=O for ***GSK1*** and ***GSK2*** samples, and C-N/C=N, C=O for ***GSZ1*** and ***GSZ2*** samples. The O1s spectra were deconvoluted into the functionality O-C, O=C, and O-C=O.

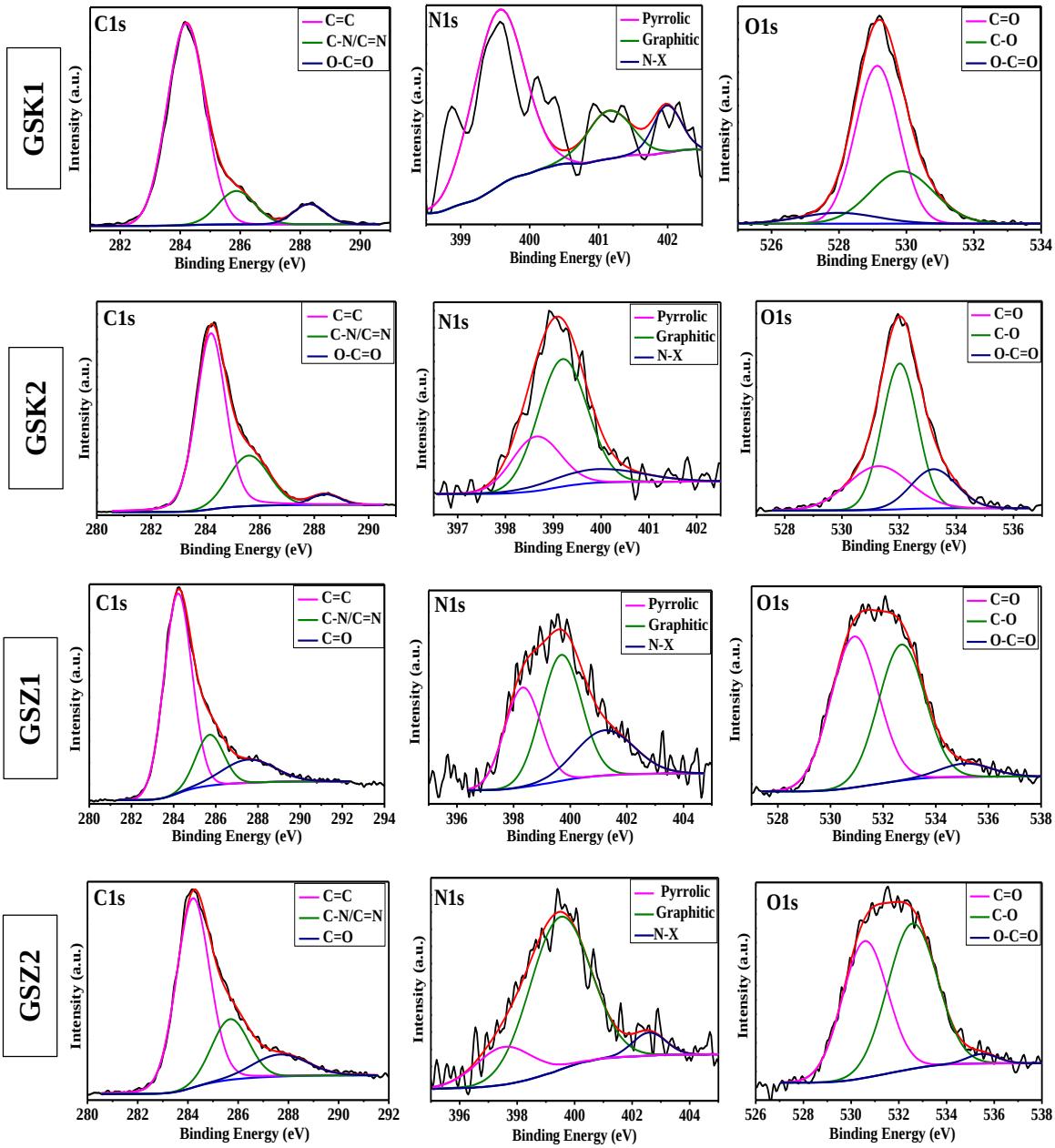

Fig. 6.10: HR-XPS spectra of C1s, N1s, and O1s of for ***GSK1***, ***GSK2***, ***GSZ1*** and ***GSZ2*** samples.

In the deconvoluted N1s spectra of ***GS1,*** only pyrrolic and graphitic N were seen, having peaks at 399.55 and 401.56 eV [211]. The deconvoluted N1s spectra for ***GSK1***, ***GSK2***, ***GSZ1,*** and ***GSZ2*** samples consisted of peaks of pyrrolic-N (~399-400 eV), graphitic-N (~400.5-401.5 eV) and oxidized nitrogen (~402-403 eV) [224,225]. These results indicated that with KOH activation, pyrrolic N content decreases and transformed to form graphitic-N and oxidized-N in case of ***GSK1*** sample and with further increase in KOH concentration i.e. for ***GSK2*** sample, the graphitic-N content increased significantly. Similarly, in the case of $ZnCl_2$ activation the pyrrolic-N transformed to form oxidized-N and graphitic–N content. In the ***GSZ2***

sample, the pyrrolic-N transforms to form the majority of graphitic-N functionality with a small amount of oxidized-N functionality. The enhanced graphitic-N was obtained for the activated samples due to thermal treatment at 400 °C during which the activation occured due to its thermal stability at higher temperature [239]. The availability of oxidized N was because of increased oxygen functionalities due to chemical activation. The KOH activated sample showed higher N-X concentration confirming the direct surface oxidation of these samples.

The presence of pyrrolic-N functionalities results in negatively charged surfaces, whereas the presence of graphitic-N and chemisorbed-N results in positively charged surfaces [224]. The net impact on surface charge of activated samples need to be validated by determining the sample's pH_{pzc}.

Table 6.2: Parameters obtained from XPS HR-spectra of C1s, N1s and O1s for ***GS1***, ***GSK1***, ***GSK2***, ***GSZ1*** and ***GSZ2*** samples.

Sample ID		**C1s**				**N1s**			**O1s**		
		C sp^2	C-N/ C=N	C=O	O-C=O	Pyrrole	Graphitic	N-X	C=O	C-O	O-C=O
GS1	**%at**	56.99	14.8	28.21	-	82.56	17.44		97.36	3.64	-
	% Content	74.10				2.22			23.60		
GSK1	**%at**	80.46	12.9	-	6.59	72.31	17.59	10.10	62.35	30.09	7.56
	% Content	67.32				2.67			30.01		
GSK2	**%at**	70.67	25.45	-	3.87	26.06	61.73	12.21	28.12	53.49	18.38
	% Content	61.23				3.22			35.53		
GSZ1	**%at**	67.98	17.20	14.80	-	32.03	44.73	23.23	50.78	44.47	4.74
	% Content	79.51				2.91			17.58		
GSZ2	**%at**	65.87	22.20	11.91	-	17.91	76.43	5.66	45.31	52.57	2.12
	% Content	74.72				3.72			21.56		

6.3 Activation mechanism using KOH and $ZnCl_2$

The characterization results revealed that activation with $ZnCl_2$ and KOH under same conditions resulted in considerable variations in the pore size and surface chemistry properties of the final activated carbons. The details of contrasting activation mechanisms of KOH and $ZnCl_2$ can be used to explain the results.

In general, for KOH activation, when the mixture of KOH and carbon sample is heated, three stage reaction takes place. At 200-300 ^{o}C, KOH becomes dehydrated and reacts with the oxygen containing functional groups of the sample (eq. (6.1) and (6.2)). Further, at 400-500 ^{o}C, oxidation of the carbon frame work takes pace through redox reactions of KOH or H_2O with the sample (eq. (6.3-6.6)). In the last stage, above 500 ^{o}C, the formation of K_2CO_3 and K_2O takes places resulting in the pore formation. So, in this work with the heat treatment limited to 400 ^{o}C, only the partial oxidation of the carbon framework at the carbon sphere surface will occur and the pore formation will not take place [240,241]. The oxygen containing functional group of sample (***GS1)*** reacted with dehydrated KOH and oxidized partially, thus enhancing the oxygen containing surface functional groups. The BET results for no significant enhancement in the surface area observed for KOH activation confirmed the negligible pore formation. The increase in amount of oxygen containing surface functional groups was confirmed by FTIR and XPS results [242]. XRD line profile results also confirmed that the KOH and ***GS1*** reaction does not penetrate the inner structure of the sample.

$$2KOH \xrightarrow{\Delta} K_2O + H_2O \quad (6.1)$$

$$\text{-COOH (}\boldsymbol{GS1}\text{)} + K_2O \xrightarrow{\Delta} \text{-COOK(}\boldsymbol{GS1}\text{)} + H_2O \quad (6.2)$$

$$\text{-COOK(}\boldsymbol{GS1}\text{)} + KOH \xrightarrow{\Delta} K_2CO_3(\boldsymbol{GS1}) + 1/2H_2 \quad (6.3)$$

$$\text{-}CH_2(\boldsymbol{GS1}) + 4KOH \xrightarrow{\Delta} K_2CO_3\ (\boldsymbol{GS1}) + K_2O + 3H_2 \quad (6.4)$$

$$H_2O + C(\boldsymbol{GS1}) \xrightarrow{\Delta} CO + H_2 \quad (6.5)$$

$$H_2O + CO \xrightarrow{\Delta} CO_2 + H_2 \quad (6.6)$$

The mechanism of activation by $ZnCl_2$ was fundamentally different from that of KOH activation. $ZnCl_2$ is a powerful dehydrating agent with a melting point of 290 ^{o}C. So it got fused at this temperature and thus was uniformly mixed with the ***GS1*** sample matrix [109]. Heat treatment enabled $ZnCl_2$ to react with the ***GS1*** sample, reducing the hydroxyl groups to generate zinc oxide chloride hydrate ($Zn_2OCl_2.2H_2O$). Heat treatment further decomposed $Zn_2OCl_2.2H_2O$ to generate $ZnCl_2$ gas and ZnO. The migration of $ZnCl_2$ gas resulted in formation of channel and hence the porous samples. The following chemical reactions explain the activation of ***GS1*** by $ZnCl_2$:

$$C\ (\boldsymbol{GS1}) + 2ZnCl_2 + 2H_2O \xrightarrow{\Delta} Zn_2OCl_2.2H_2O + 2HCl + C\ (\boldsymbol{GS1})\ \text{(dehydrated)} \quad (6.7)$$

$$C\ (\boldsymbol{GS1}) + Zn_2OCl_2.2H_2O \xrightarrow{\Delta} ZnCl_2 + ZnO + 2H_2O + \text{Activated C (}\boldsymbol{GS}\text{)} \quad (6.8)$$

From the XRD line spectra of ***GSZ2*** sample, it was observed that peak at 2θ ~21° for the quantum dot in the centre of the sphere was not observed. This confirmed that the formation of molten phase with $ZnCl_2$ resulted in restructured porous carbon spheres. Also, the BET results showed that higher impregnation ratios resulted in pores of larger radii due to higher emission of $ZnCl_2$.

6.4 Adsorption studies

6.4.1 Point of zero charge (pH_{pzc}) of samples

A sample's pH_{pzc} is the pH at which the surface of the sample has no net charge under specific conditions of temperature, pressure, and solution composition. This does not imply that the surface is chargeless at pH_{pzc}, but rather that the positive and negative charges are balanced. pH_{pzc} readings might aid in the selection of the best adsorbent for treating pollutants. Adsorbents with low pH_{pzc} values are excellent for treating cationic-contaminated effluents, whereas adsorbents with high pH_{pzc} values are better for capturing anions.

The graphs for initial pH vs change in pH are shown in Fig. 6.11 for all the synthesized samples. The pH_{pzc} values obtained for the synthesized samples are given in Table 6.1. It can be observed that with increase in the ratio of impregnation, the pH_{pzc} of the samples increased. The increase in the sample's pH_{pzc} indicated that the sample's surface has more positive surface groups. This conjecture was also supported using XPS results. The pH_{pzc} of ***GSZ2*** (8.0) was more than that of ***GSK2*** (7.2) and ***GS1*** (4.6) sample. This was due to availability of more graphitic N in the sample.

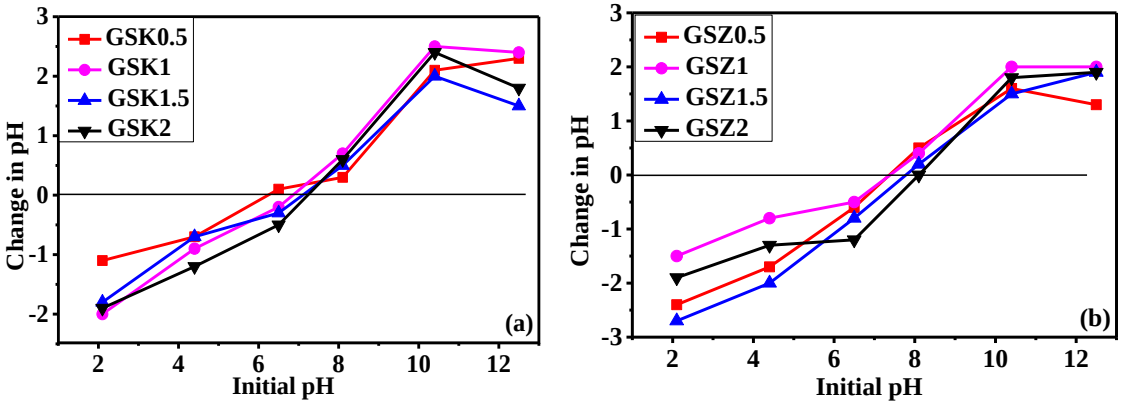

Fig. 6.11: pH_{pzc} of samples activated by (a) KOH and (b) $ZnCl_2$.

6.4.2 Model pollutants

The adsorption studies were carried out using all the synthesized samples for anionic dye EBT cationic dyes MB and CV, neutral PNP, phthalic ester DEP and pharmaceutical

compound CIP. For adsorption of dyes (MB, CV, and EBT), the amount of adsorbate and adsorbent were taken 1 mg/L and 20 mg/L, respectively. For PNP, DEP and CIP adsorption the adsorbate and adsorbent were 20 mg/L and 100 mg/L, respectively. The % adsorption of the various pollutants using KOH and $ZnCl_2$ activated samples is shown in Fig. 6.12 (a) and 6.12 (b), respectively.

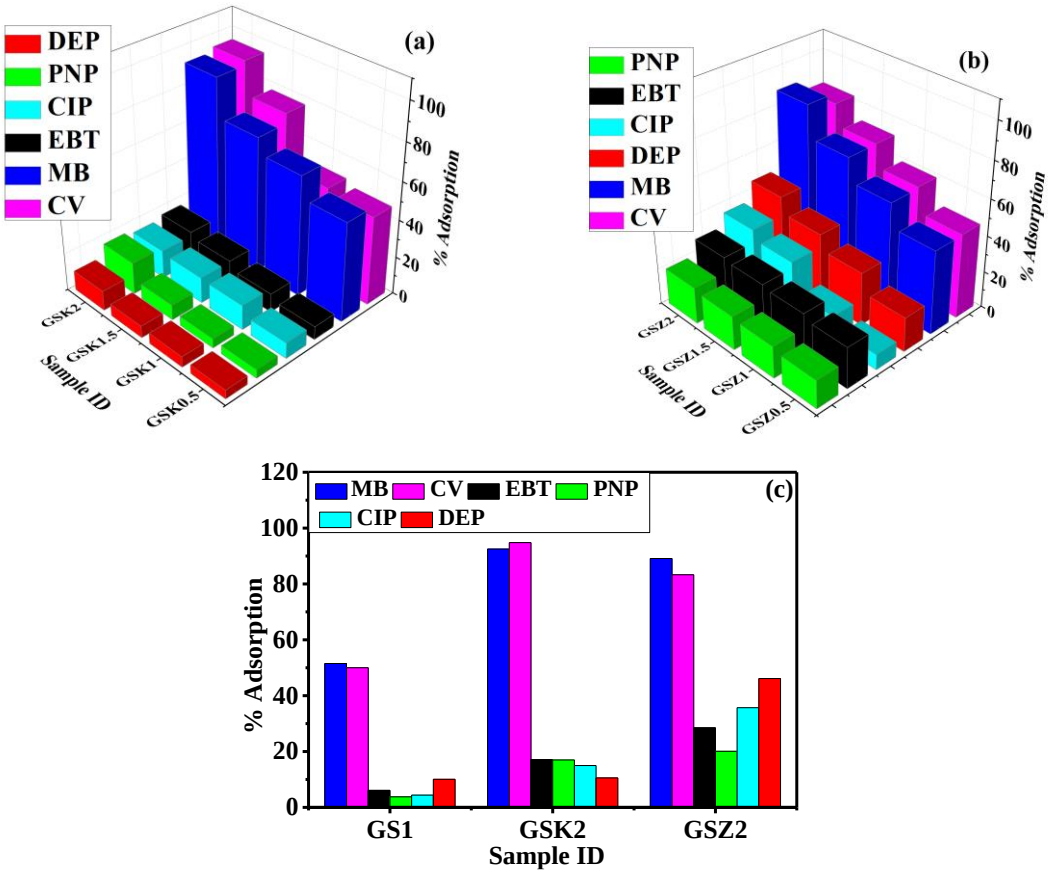

Fig. 6.12: % Adsorption of MB, CV, EBT, CIP, PNP and DEP onto (a) KOH activated and (b) $ZnCl_2$ activated samples after 3 hours.

The adsorption efficiency of ***GS1*** sample for the given pollutant was observed to be least among all the synthesized samples (Fig. 6.12(c)). The adsorption of pollutants onto the samples increased with increase in AA impregnation ratio due to increased surface area and hence availability of more adsorption sites. Thus, the maximum adsorption was observed for ***GSK2*** and ***GSZ2*** samples. ***GSK2*** sample showed significant adsorption of dyes in spite of very negligible surface area and porosity. This is attributed to the oxygen containing surface functional groups on the sample surface which interacted with dye species by hydrogen bonding and electrostatic interaction [237,243]. ***GSZ2*** showed better efficiency for the adsorption for all the pollutants due to its enhanced surface area. Also, the availability of more graphitic N in ***GSZ2*** sample compared to other samples makes its surface more positive and

led to electrostatic interaction between negatively charge pollutant and the sample showing enhanced adsorption. The surface area of ***GSZ1*** and ***GSZ1.5*** sample was more than ***GSZ2*** sample but both samples shows lower adsorption efficiency compared to ***GSZ2*** sample due to their lower pore size.

6.4.3 Effect of solution pH variation

From the adsorption study, it was concluded that ***GSK2*** and ***GSZ2*** samples showed better adsorption for all the pollutants. Therefore the effect of pH of pollutant solution on the adsorption efficiency of ***GSK2*** and ***GSZ2*** samples was studied. The pH of the solutions varied from 2 to 12 using HCl and NaOH. The % adsorption with the change in pH of MB, EBT, PNP, and CIP solution using ***GSK2*** and ***GSZ2*** samples is shown in Fig. 6.13 (a) and 6.13 (b), respectively.

MB: The adsorption efficiency for MB increased for both ***GSK2*** and ***GSZ2*** samples with an increase in the pH. At lower pH values, the sample's surface had a net positive charge, which prevented cationic dye adsorption. The surface of the adsorbents held a net negative charge when the pH increased beyond pH_{pzc} (7.2 for ***GSK2*** and 8.0 for ***GSZ2***), and hence adsorbed the MB dye more effectively owing to electrostatic interaction/hydrogen bonding [176].

EBT and DEP: EBT and DEP are both negatively charged species**.** With a rise in the EBT and DEP solution pH, the adsorption capacity of both ***GSK2*** and ***GSZ2*** samples decreases. At lower pH, the sample's surface had a net positive charge and electrostatic interaction occurs with the negatively charged anionic dye EBT and acidic DEP. The surface of the sample had a net negative charge at higher pH, i.e., above pH_{pzc}, which resisted the negatively charged EBT dye and acidic DEP and resulted in decreased adsorption.

PNP: In acidic and alkaline solutions, PNP exists in the form of neutral species: $C_6H_4(NO_3)$ and anionic species: $C_6H_4(NO_2)O^-$, respectively. When the pH was elevated from 2 to 7, the % adsorption of PNP increased. Further increase in pH up to 12 resulted in a significant decrease in adsorption efficiency. Donor-acceptor interactions, π–π dispersion, and hydrogen bonding interactions are all important factors in PNP adsorption on adsorbent's surfaces. The neutral phenol adsorption will be hampered by a higher positive charge on the sample surface. With increase in pH from 2 to neutral, positive surface charge of the ***GSK2*** and ***GSZ2*** samples decrease and hence improvement in adsorption efficiency occurred in an acidic medium. Increased removal efficiency was achieved by increasing the surface acidity of the adsorbents, which resulted in a donor-acceptor interaction between electron and phenolic rings.

At neutral pH, both adsorbents had the maximum adsorption efficiency, which was attributed to hydrogen bonding between the phenol molecule and the adsorbed water molecule on the sample surface. At pH beyond neutral for ***GSK2*** and ***GSZ2***, the surface became negatively charged, and it interacted with the phenolate ions ($C_6H_4(NO_2)O^-$) to undergo electrostatic repulsion, resulting in a significant reduction in adsorption efficiency [9,232].

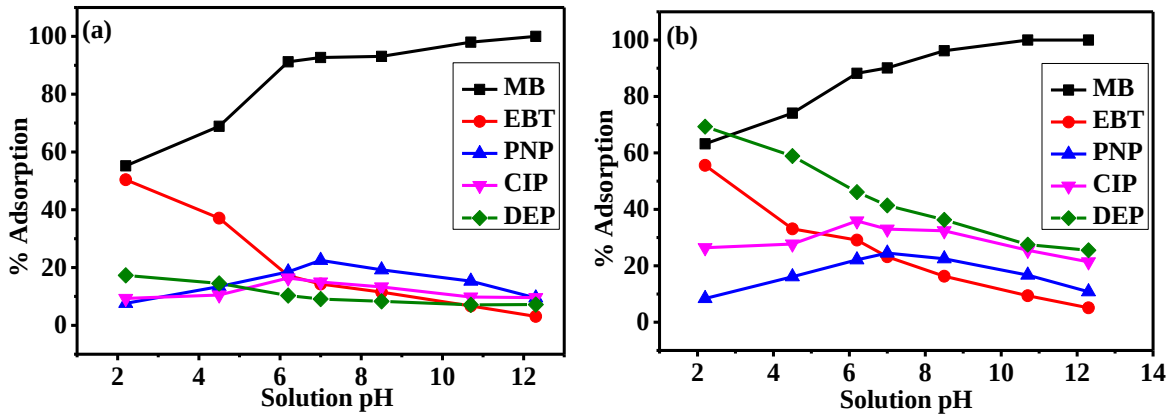

Fig. 6.13: % Adsorption of MB, EBT, CIP, and PNP with pH variation onto (a) ***GSK2*** and (b) ***GSZ2*** sample after 3 hours.

CIP: CIP is an ionizable chemical with variation in the solution. It exhibits pKa values of 5.9 and 8.9. Therefore, it exists in the cationic form CIP^+ below pH 5.9, in the anionic form CIP^- above pH 8.9, and as zwitterion $CIP^{\pm}$ between these pH values. The % adsorption of CIP on ***GSK2*** and ***GSZ2*** increased slowly from 2 to 4.5 and further a sharp increase in % adsorption was observed. The maximum % adsorption was observed at pH 6.1 for both the adsorbents. Beyond pH 8.9, the decrease in % adsorption was observed with increasing alkalinity. The results indicate that the predominant cationic form of CIP was responsible for the maximum amount of adsorption blow pH 6.1. Due to electrostatic interaction between the negative charge surface and cationic CIP, the adsorption increased. In the pH range 6.1–8.9, electrostatic interaction is believed to take place between the positively charged amine group in the CIP zwitterion and negatively charged carbon-oxygen groups on the adsorbent surface. However, a degree of repulsion between negatively charged carboxylate in the CIP zwitterion and the negatively charged surface probably takes place, leading to a slight decrease in CIP sorption above pH 6.1. When pH was increased above 8.9, the anionic form of CIP was the dominating species in aqueous solution. The oxygen-containing functional groups on the adsorbents, such as -OH and -COOH, are negatively charged and the electrostatic repulsion occurred between CIP and adsorbent thus reducing the CIP adsorption. As the pH moved toward high alkalinity, the adsorption affinity of adsorbents to CIP fell significantly [244,245].

6.4.4 Recyclability test

Recyclability experiments were carried out to investigate the recyclability of ***GSZ2*** sample for the adsorption of MB, EBT, PNP, CIP and DEP (Fig. 6.14). The concentration of MB and EBT dyes were 1 mg/L and PNP, CIP and DEP were 20 mg/L for the recyclability tests, with an adsorbent concentration of 100 mg/L. The adsorption efficiency of the ***GSZ2*** sample was measured 14 times in a row. The % adsorption of MB EBT, PNP, CIP and DEP reduced by 6, 8, 2.5, 5 and 6.3%, respectively, from the first to the fourteenth cycle. This minor variation could be attributed to sample loss during the recycling trials. As a result, the sample may be reused without reducing efficiency for the model pollutants adsorption.

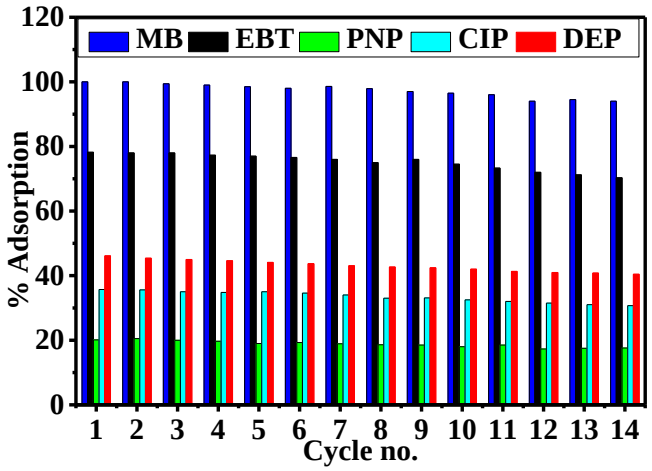

Fig. 6.14: Recyclability using ***GSZ2*** sample for MB, EBT, PNP, CIP and DEP.

6.4.5 Adsorption isotherm modeling

Langmuir and Freundlich isotherm models were investigated for MB, EBT, PNP, CIP adsorption onto ***GSZ2*** and MB, EBT adsorption onto ***GSK2*** sample. The amount of adsorbent was kept constant (100 mg/L) for all the cases with different concentrations of pollutants. The details and calculations for isotherm models are given in section 3.4.1 (chapter 3). The graphs obtained from the isotherms are shown in Fig. 6.15 and Fig. 6.16 for ***GSZ2*** and ***GSK2*** samples, respectively. The parameters obtained from isotherms are given in Table 6.3 and Table 6.4 for ***GSZ2*** and ***GSK2*** sample, respectively. In case of Langmuir model fit, the R_L value lies between 0 and 1 for all the pollutnats for both types of adsorbent. This shows that the process of adsorption was favorable. Also, from Freundlich fit, the obtained n values were between 1 and 10 for both the samples for all the pollutants showing favorable adsorption.

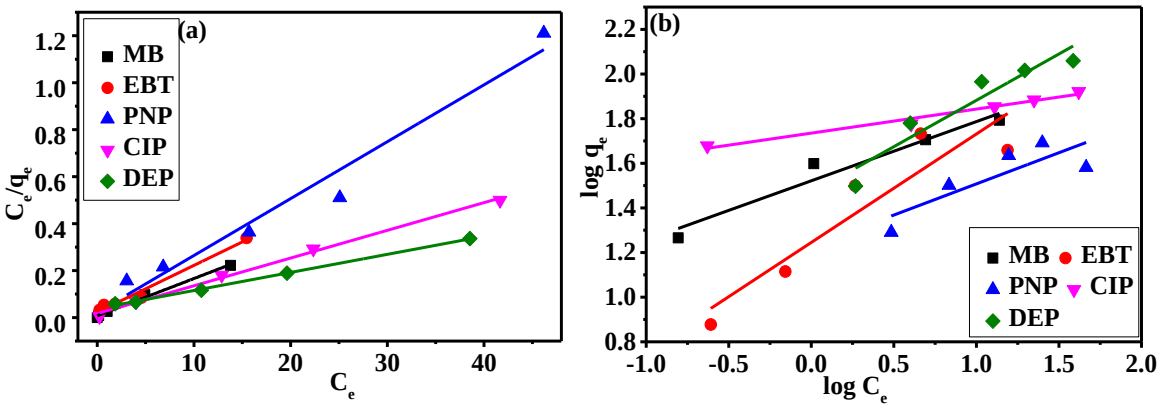

Fig. 6.15: Isotherm fitting of MB, EBT, PNP, CIP and DEP adsorbed on ***GSZ2*** sample (100 mg/L) using (a) Langmuir and (b) Freundlich models.

Table 6.3: Parameters obtained from Langmuir and Freundlich isotherm models obtained for adsorption of MB, EBT, PNP, CIP and DEP onto ***GSZ2*** sample (100 mg/L).

Adsorption	Pollutant	Parameter	Value	R^2
Langmuir isotherm	MB	k_L (L/g)	2.14	**0.99**
		q_m (mg/g)	62.09	
		R_L	0.32	
	EBT	k_L (L/g)	0.86	**0.97**
		q_m (mg/g)	54.03	
		R_L	0.536	
	PNP	k_L (L/g)	1.09	**0.95**
		q_m (mg/g)	49.17	
		R_L	0.48	
	CIP	k_L (L/g)	0.65	**0.99**
		q_m (mg/g)	84.10	
		R_L	0.61	
	DEP	k_L (L/g)	0.20	**0.99**
		q_m (mg/g)	114.59	
		R_L	0.19	
Freundlich isotherm	MB	k_f (L/g)	4.13	0.92
		n	3.77	
	EBT	k_f (L/g)	3.38	0.80
		n	2.06	
	PNP	k_f (L/g)	3.34	0.59
		n	3.58	
	CIP	k_f (L/g)	4.72	0.96
		n	9.28	
	DEP	k_f (L/g)	3.97	0.87
		n	2.44	

In case of ***GSZ2*** sample, from the regression coefficient values, it was concluded that all the pollutant adsorbed on the surface of adsorbent via following Langmuir isotherm model. This indicated that the adsorption of pollutants was taking place via monolayer adsorption onto

GSZ2 sample. In case of ***GSK2*** sample, the regression coefficient values indicated that MB was adsorbed on the sample's surface via monolayer adsorption following Langmuir isotherm model. While EBT followed Freundlich isotherm model to adsorb on ***GSK2*** sample via multilayer adsorption.

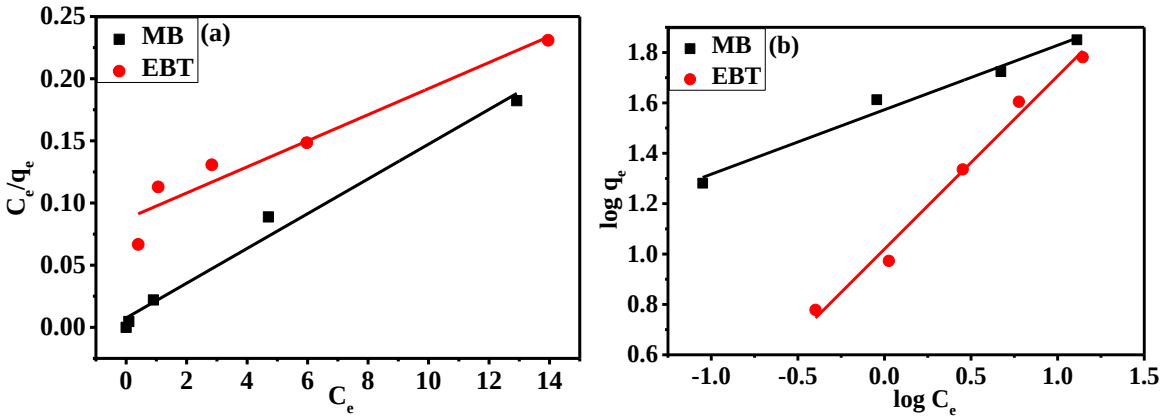

Fig. 6.16: Isotherm fitting of MB and EBT adsorbed on ***GSK2*** sample (100 mg/L) using (a) Langmuir and (b) Freundlich models.

Table 6.4: Parameters obtained from Langmuir and Freundlich isotherm models obtained for adsorption of MB and EBT onto ***GSK2*** sample (100 mg/L).

Adsorption isotherm	Pollutant	Parameter (units)	Value	R^2
Langmuir isotherm	MB	k_L (L/g)	1.85	**0.98**
		q_m (mg/g)	70.84	
		R_L	0.35	
	EBT	k_L (L/g)	0.12	0.90
		q_m (mg/g)	60.44	
		R_L	0.89	
Freundlich isotherm	MB	k_f (L/g)	4.27	0.96
		n	3.90	
	EBT	k_f (L/g)	2.77	**0.98**
		n	1.45	

6.4.6 Adsorption kinetics modeling

By fitting the adsorption kinetic models to the experimental data, the kinetic parameters were obtained to understand the adsorption processes and rate-limiting steps. Adsorption studies revealed that ***GSZ2*** had the highest adsorption efficiency for all the model pollutants. As a result, employing the ***GSZ2*** sample, kinetic modeling was performed for all four pollutants. MB and EBT were given at 1 mg/L with 20 mg/L of ***GSZ2***, whereas, PNP, CIP and DEP were taken at 5 mg/L with 100 mg/L of ***GSZ2***. The experimental data were fitted using the pseudo-first-order (PFO), pseudo-second-order (PSO), Elovich, and intraparticle diffusion

(IPD) models in this study. The fitted graphs are shown in Fig. 6.17 and Fig. 6.18 and the models are explained under section 3.4.2. (chapter 3). The parameters obtained from the fitting the models are given in Table 6.5 and Table 6.6. Also, ***GSK2*** sample was observed to be best for dye adsorption, therefore kinetic studies were also performed for 1mg/L of MB and EBT adsorption onto 20 mg/L of ***GSK2*** sample (Table 6.7 and Table 6.8).

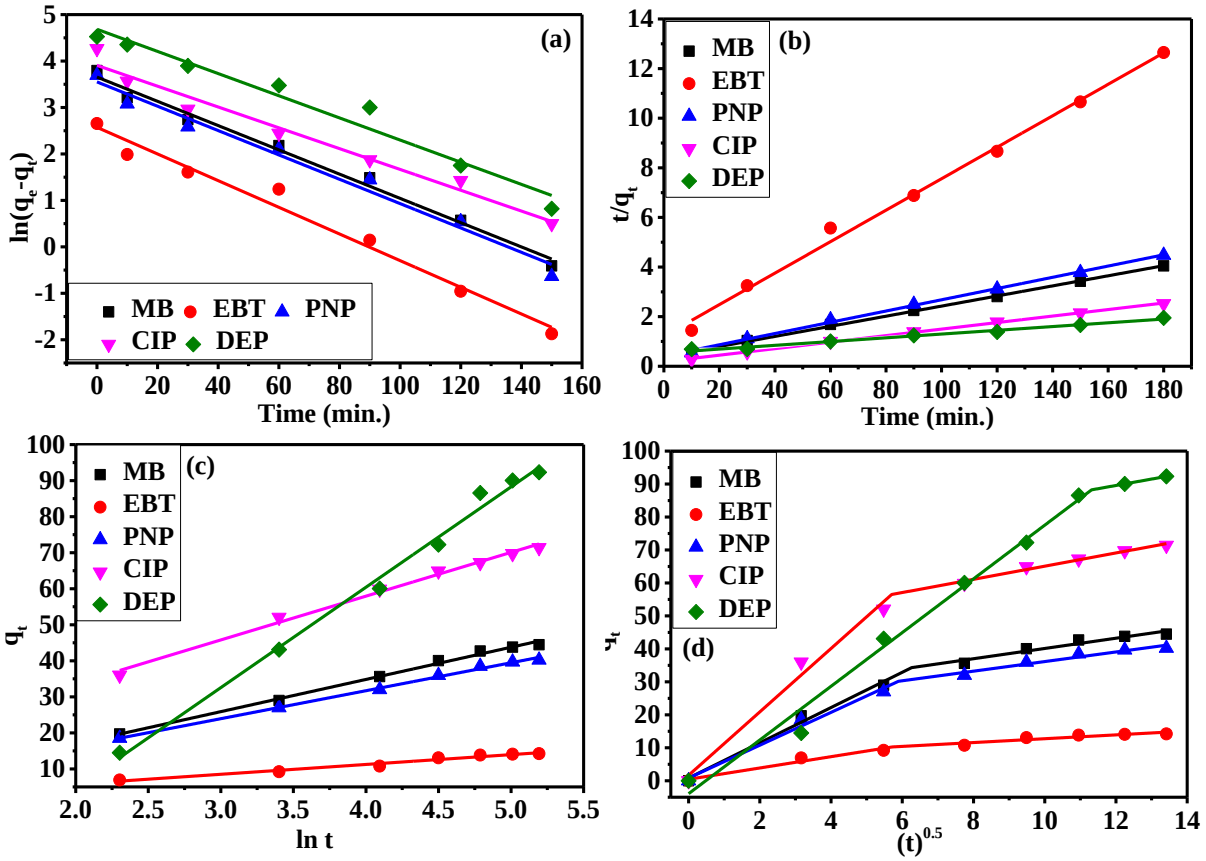

Fig. 6.17: Kinetic modeling of MB, EBT (1 mg/L with adsorbent 20 mg/L), PNP CIP and DEP (20 mg/L with adsorbent 100 mg/L) adsorbed on ***GSZ2*** sample (a) PFO, (b) PSO, (c) Elovich and (d) IPD model.

When using ***GSZ2*** as an adsorbent, all five pollutants were shown to follow the PSO kinetic model better than the PFO model. The conclusions was obtained using the Δq_e value (the difference in the amount of dye adsorbed on the surface of the sample obtained experimentally vs estimated through kinetic fitting) and the regression coefficient R^2. The Δq_e value for the PSO model was much lower than for the PFO model, and PSO fitting gave a higher R^2 value than PFO, indicating a stronger fit for all pollutants (Table 6.9). The adsorption, therefore, occurred via chemisorption for all the pollutants, as the value of R^2 obtained from Elovich fit was also comparable to PSO. The parameters derived from the IPD fit are shown in Table 6.6. The IPD mechanism's regression coefficients were adequate (> 0.9). Adsorption occurs in two stages for all four pollutants onto the ***GSZ2*** sample, indicating that adsorption

occurred first via film diffusion and subsequently via the IPD mechanism. The fitted lines in Fig. 6.17 (d) clearly pass through the origin, indicating that the IPD mechanism regulates the adsorption process.

Table 6.5: Parameters of kinetic modeling of MB, EBT, PNP, CIP adsorbed at ***GSZ2*** sample. (q_e (MB)= 44.46 mg/g, q_e (EBT)= 14.23 mg/g, q_e (PNP)= 40.21 mg/g, q_e (CIP)=71.40 mg/g and q_e (DEP)=92.32 mg/g).

Kinetic model	Pollutant	Parameter (unit)	Value	R^2
PFO	MB	k_1 (1/min)	0.0260	0.98
		q_e (mg/g)	9.9300	
	EBT	k_1 (1/min)	0.0280	0.97
		q_e(mg/g)	6.9900	
	PNP	k_1 (1/min)	0.0260	0.97
		q_e (mg/g)	9.6500	
	CIP	k_1 (1/min)	0.0220	0.96
		q_e(mg/g)	10.6100	
	DEP	k_1 (1/min)	0.0200	0.95
		q_e(mg/g)	12.7200	
PSO	MB	k_2 (g/mg min)	0.0010	**0.99**
		q_e(mg/g)	50.0000	
	EBT	k_2 (g/mg min)	0.0032	**0.99**
		q_e(mg/g)	15.8700	
	PNP	k_2 (g/mg min)	0.0011	**0.99**
		q_e(mg/g)	45.4500	
	CIP	k_2 (g/mg min)	0.0009	**0.99**
		q_e(mg/g)	76.9200	
	DEP	k_2 (g/mg min)	0.0002	**0.99**
		q_e(mg/g)	111.1100	
Elovich model	MB	α (mg/g min)	2.4950	0.99
		β	0.1110	
	EBT	α (mg/g min)	0.8830	0.96
		β	0.3660	
	PNP	α (mg/g min)	1.7650	0.99
		β	0.1280	
	CIP	α (mg/g min)	25.3800	0.99
		β	0.0820	
	DEP	α (mg/g min)	138.6200	0.99
		β	0.0350	

Table 6.6: Parameters of diffusion model (IPD) of MB, EBT, PNP and CIP adsorbed at ***GSZ2*** sample.

Pollutant	Parameter (unit)	Value	R^2
MB	k_{id1}	5.346	0.99
	k_{id2}	1.555	
EBT	k_{id1}	1.715	0.96
	k_{id2}	0.582	
PNP	k_{id1}	4.981	0.98
	k_{id2}	1.455	
CIP	k_{id1}	9.610	0.98
	k_{id2}	2.001	
DEP	k_{id1}	8.140	0.98
	k_{id2}	1.940	

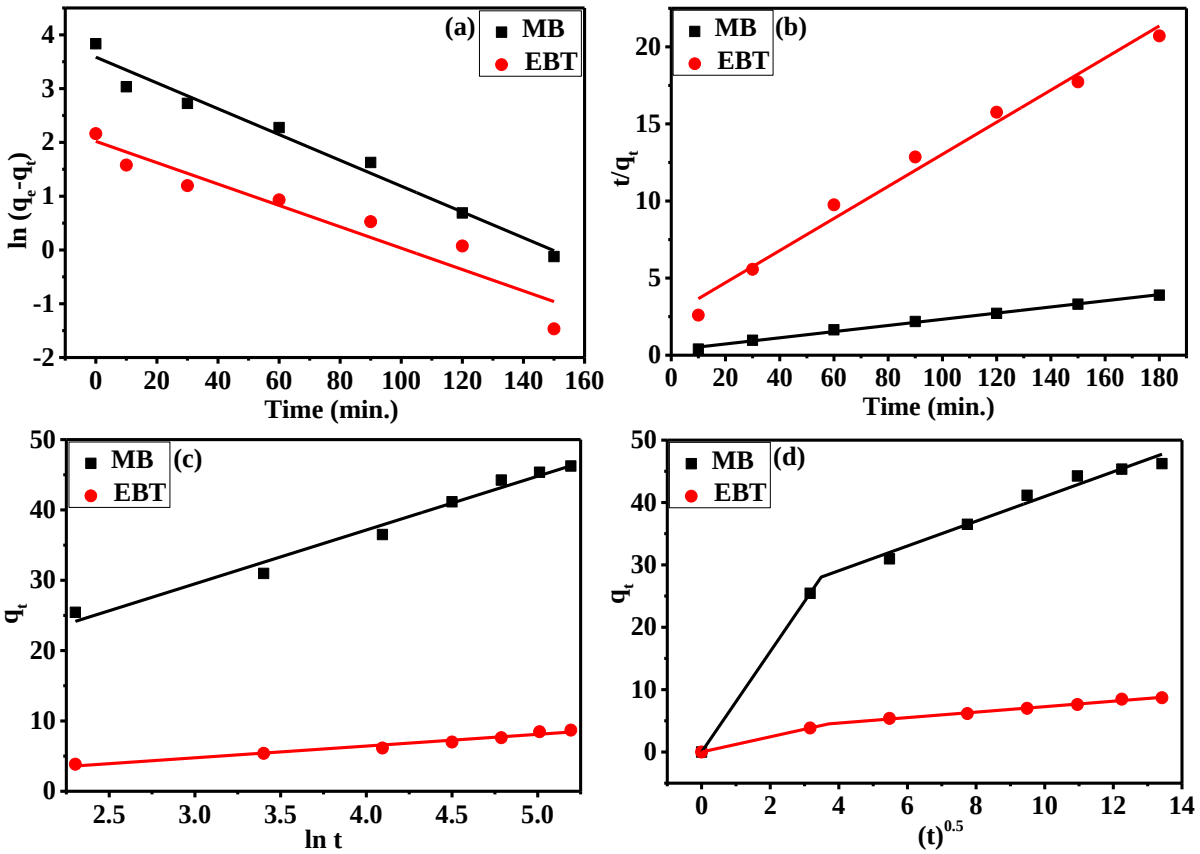

Fig. 6.18: Kinetic modeling of MB and EBT (1 mg/L with adsorbent 20 mg/L), adsorbed on ***GSK2*** sample (a) PFO, (b) PSO, (c) Elovich, and (d) IPD model

With ***GSK2*** adsorbent, similar to the ***GSZ2*** sample, MB and EBT both followed PSO kinetic model. The PSO fitting gave a higher R^2 value and lower Δq_e value than PFO thus showing better fit for all the pollutants (Table 6.9). Therefore, it can be concluded that adsorption occurring via chemisorption for both MB and EBT. With IPD fit, the R^2 values for both the dyes were satisfactory (> 0.9) and the adsorption was found to occur via two stages

for both the dyes. The two step IPD fit shows that adsorption proceeded first by film diffusion and then via the IPD process for both MB and EBT.

Table 6.7: Parameters of kinetic modeling of MB, EBT, PNP, CIP adsorbed at ***GSK2*** sample. (q_e (MB)= 46.23 mg/g, and q_e (EBT)= 8.69 mg/g).

Kinetic model	Pollutant	Parameter (unit)	Value	R^2
PFO	MB	k_1 (1/min)	0.023	0.97
		q_e (mg/g)	9.74	
	EBT	k_1 (1/min)	0.019	0.90
		q_e(mg/g)	5.49	
PSO	MB	k_2 (g/mg min)	0.0012	**0.99**
		q_e(mg/g)	50.00	
	EBT	k_2 (g/mg min)	0.0041	**0.98**
		q_e(mg/g)	9.61	
Elovich model	MB	α (mg/g min)	17.75	0.97
		β	0.130	
	EBT	α (mg/g min)	0.6768	0.96
		β	0.598	

Table 6.8: Parameters of diffusion model (IPD) of MB and EBT adsorbed at ***GSZK2*** sample.

Pollutant	Parameter	Value	R^2
MB	k_{id1}	8.045	0.99
	k_{id2}	1.983	
EBT	k_{id1}	1.216	
	k_{id2}	0.438	0.99

Table 6.9: q_e and Δq_e values for kinetic and isotherm models for both samples (***GSZ2*** and ***GSK2***).

Sample ID	Pollutant	q_e(mg/g)			Δq_e		Max.
		Exp.	PFO	PSO	PFO	PSO	Langmuir
GSZ2	MB	44.46	9.93	50.00	77.60	12.40	62.09
	EBT	14.23	6.99	15.87	50.87	11.52	54.03
	PNP	40.21	9.65	45.45	76.00	13.03	49.17
	CIP	71.40	10.61	76.92	86.09	7.73	84.10
	DEP	92.32	12.72	111.11	88.5	16.9	114.59
GSK2	MB	46.23	9.74	50.00	78.93	8.15	70.84
	EBT	8.69	5.49	9.61	36.82	10.58	60.44

6.4.7 Adsorption mechanism

Table 6.10 shows the list of kinetic model and isotherms followed during the adsorption of various pollutants onto ***GSZ2*** and ***GSK2*** samples. It was observed that MB adsorption onto ***GSZ2*** and ***GSK2*** and EBT, PNP, CIP, and DEP adsorption onto ***GSZ2*** followed the PSO model with 2-step IPD and Langmuir isotherm model.

For the ***GSZ2*** sample, the isotherm's Langmuir nature showed that pollutants undergo reversible adsorption at many equivalent sites, resulting in the formation of a monolayer on the adsorbent's surface. According to the PSO kinetic fit, the adsorption was by strong chemisorption. This was consistent with the pollutants and adsorbent having opposite charges at the optimum pH (Section 6.4.3). At optimum pH, strong interactions was observed between adsorbate (MB, EBT, PNP, CIP and DEP) and adsorbent (***GSZ2*** sample). This results in formation of monolayer on the sample surface by adsorption due to multipoint interaction. Adsorption proceeds initially by boundary layer diffusion and then through intraparticle diffusion, according to a two-step fit of the IPD. For MB, EBT, PNP, CIP and DEP onto ***GSZ2*** sample, boundary layer diffusion was followed by intraparticle diffusion after 40, 32, 34, 33 and 120 minutes. IPD occurs after 12 minutes for MB in the ***GSK2*** sample.

Table 6.10: Results of different adsorption isotherm and kinetics modeling.

Sample ID	Pollutant	Kinetic model	Isotherm	IPD
GSZ2	MB	PSO	Langmuir	2 Step
	EBT	PSO	Langmuir	2 Step
	PNP	PSO	Langmuir	2 Step
	CIP	PSO	Langmuir	2 Step
	DEP	PSO	Langmuir	2 Step
GSK2	MB	PSO	Langmuir	2 Step
	EBT	PSO	Freundlich	2 Step

The adsorption of EBT onto ***GSK2*** sample followed the Freundlich and PSO models. According to the Freundlich model, multilayer adsorption occurs when adsorption site is heterogeneous in nature. When n is less than one, the surface is heterogeneous, and when n is more than one, the surface becomes more homogeneous. The value of n found for EBT was 1.45. As a result, multilayer adsorption did not occur here. Adsorption on the surface of the sample occurs by chemisorption as per PSO model with a monolayer or bilayer. A two-step fit of IPD revealed that adsorption occurs first via boundary layer diffusion and subsequently via intraparticle diffusion after 14 minutes. Table 6.11 shows the adsorption results obtained using the ***GSZ2*** sample for MB, EBT, PNP, CIP and DEP adsorption.

Table 6.11: Adsorption results for the best sample.

Sample ID	Pollutant	q_e (mg/g)	Kinetic model	Kinetic isotherm
GSZ2	MB	62.09	PSO	Langmuir
	EBT	54.03	PSO	Langmuir
	PNP	49.17	PSO	Langmuir
	CIP	84.10	PSO	Langmuir
	DEP	114.59	PSO	Langmuir

6.5 Summary

In the present chapter, low temperature and time (400 °C and 30 min.) chemical activation was carried out for N-doped carbon spheres (***GS1***) using $ZnCl_2$ and KOH. The different impregnation ratios of AA with the sample were: ***GS1***: activating agent :: 1:0.5, 1:1, 1:1.5, and 1:2. SEM analysis showed that the shapes of the spheres distorted unevenly with increased KOH ratio and the dappled surface with no visible pores was seen in $ZnCl_2$ activated samples. XRD line profile and Raman spectra confirmed that $ZnCl_2$ activated samples show a more ordered structure. On the basis of activation parameters and available literature, it was proposed that activation of ***GS1*** with KOH results in the partial oxidation of the surface without development of pores and enhanced surface area. $ZnCl_2$ on the other hand resulted in completely restructured sample morphology at same activation parameters. The proposed mechanisms were validated by N_2 adsorption-desorption isotherms, FTIR and XPS results.

The adsorption efficiency of synthesized samples was studied for MB, CV, EBT, PNP, CIP and DEP as model pollutants. The sample activated with $ZnCl_2$ and having appropriate pore size (***GSZ2*** sample) showed the best adsorption efficiency towards all the pollutants. Despite having a low surface area and porosity, ***GSK2*** sample exhibited increased dye adsorption due to availability of abundant oxygen containing surface functional groups. The effect of solution pH on the adsorption efficiency of the pollutants has been explained on the basis of pH_{pzc}, nitrogen functionalities of the sample and chemical species of the model pollutants at given pH. From the adsorption kinetic modeling fitted for ***GSZ2*** and ***GSK2*** sample, the adsorption process followed PSO model with two step IPD model for all the pollutants and dye, respectively. The isotherm fit shows that Langmuir isotherm was found to follow during adsorption of all the pollutants onto the ***GSZ2*** sample. For ***GSK2*** sample adsorption of MB followed Langmuir isotherm while EBT adsorption takes place via Freundlich isotherm model. For ***GSZ2***, the obtained q_e values for MB, EBT, PNP, CIP and DEP were 62.09, 54.02, 49.16,

84.20 and 114.59 mg/g, respectively and for ***GSK2*** obtained q_e values for MB and EBT were 70.84 and 60.44 mg/g. In conclusion, for least possible conditions of activation i.e. temperature, time and atmosphere, $ZnCl_2$ activated samples showed enhanced results in terms of surface area, graphitic-N content and hence adsorption for a variety of pollutants. While, KOH activation resulted samples which showed significantly enhanced adsorption for dyes. When compared with the reports available in literature for similar materials, samples have enhanced adsorption properties.

Chapter 7

Pyrolysis of soy flour

Overview

This chapter describes the single-step synthesis of biochar from defatted soy flour by pyrolysis in Ar atmosphere at various temperatures: 450, 650, and 750 °C, determined by TG/DTG/DTA analysis. The pyrolyzed sample with the best adsorption characteristics was further treated with HNO_3 for complete demineralization. The variation in the properties of the synthesized samples with pyrolysis temperature and acid treatment were explained by characterizing the biochar using FE-SEM, XRD, FTIR, UV-visible, FTIR, Raman, BET and XRD. pH_{pzc} of the samples was determined using the salt addition method. The synthesized samples were used for the adsorption of pollutants *viz* MB, CV, EBT, PNP, CIP, and DEP. The adsorption rates and mechanisms were determined using kinetic modeling and isotherm analysis.

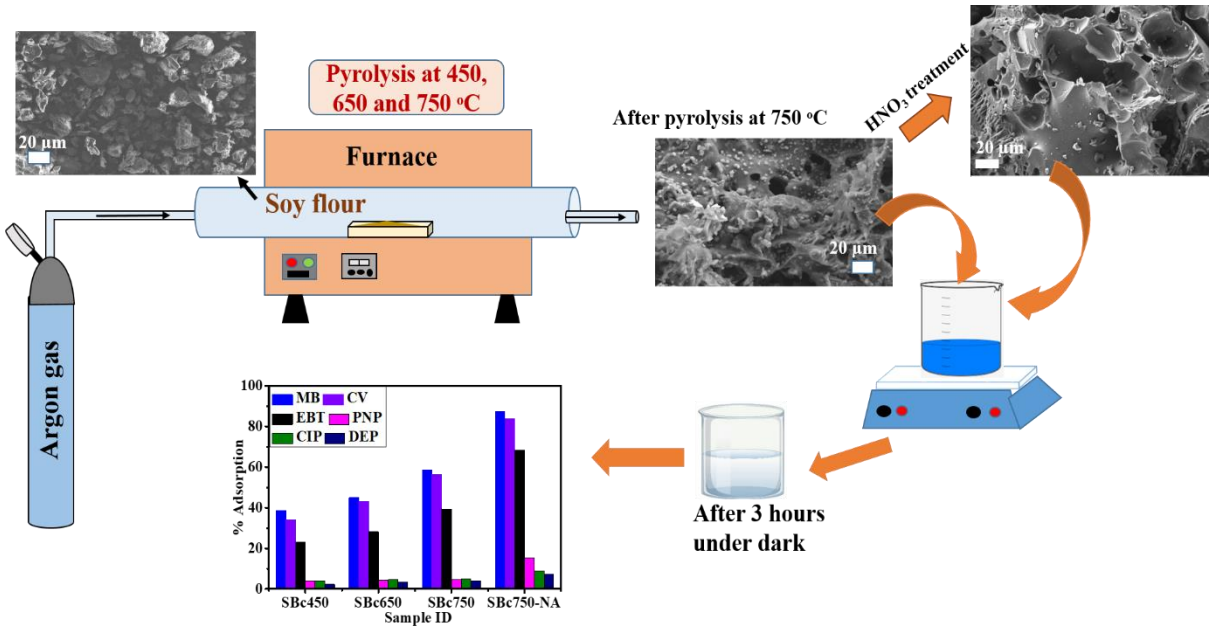

7.1 Introduction

Biochars are heterogeneous carbonaceous substances derived from the pyrolysis of animal and agricultural biomass. There are reports on the synthesis of biochar from various biomasses, including agricultural, marine, food, forest, and industrial biomass [244, 245]. Protein based biomasses have been found to produce the most effective biochars. Pyrolysis of protein-rich biomass leads to the formation of nitrogen (N) containing biochar. The content and functionalities of N in biochar depend upon the type of biomass and pyrolysis temperature [99, 246]. The presence of N functionalities in the biochar plays an important role in adsorption of pollutants from aqueous solutions [63,103]. Current chapter investigates the evolution of pollutant adsorption properties of protein-rich soy flour biomass converted to nitrogen-doped biochar. Biochars were synthesized from the single step pyrolysis of soy flour at different temperatures: 450, 650, and 750 °C, determined from the TG/DTA/DTG studies. The 750 °C pyrolyzed sample was further treated with HNO_3 for demineralization.

7.2. Soy flour thermal analysis

Fig. 7.1(a) gives the thermal analysis data for soy flour under argon atmosphere. Initially the TG shows a gradual weight loss process that occurred from room temperature to 110 °C, with ~9 % mass loss, which may be attributed to the evaporation of volatile chemicals and water content. On further heating, the sample started to lose mass at 160 °C which continued till ~418 °C. This mass loss was also confirmed from the DTG peak. The decomposition of cellulose, hemicellulose and lignin usually starts at 200 °C and completes below 400 °C [249]. In DTG data, a shoulder at 243 °C was followed by a single sharp peak at 294 °C indicating that the decomposition of cellulose, hemicellulose and lignin available in the soy flour occurred at these temperatures [250]. In DTA curve shoulder humps observed at 164 °C and 273 °C indicated the exothermic nature of decomposition process. From 350 °C to 500 °C the residual mass values decreased from 48 % to 38 % which further reduced to 30 % at 800 °C.

For the DTA data the broad exothermic peak was observed at ~418 °C with small gradual weight loss in TG data. This indicated the start of the final step of soy flour pyrolysis–residual carbon condensation into biochar, creating graphite-like rings [251]. Further a shoulder in DTA data ~750 °C was observed indicating the completion of biochar formation. Therefore, for biochar synthesis, the temperatures were fixed at 450 °C (start of biochar

formation), 650 °C (before completion of biochar formation) and 750 °C (beyond the end of biochar formation).

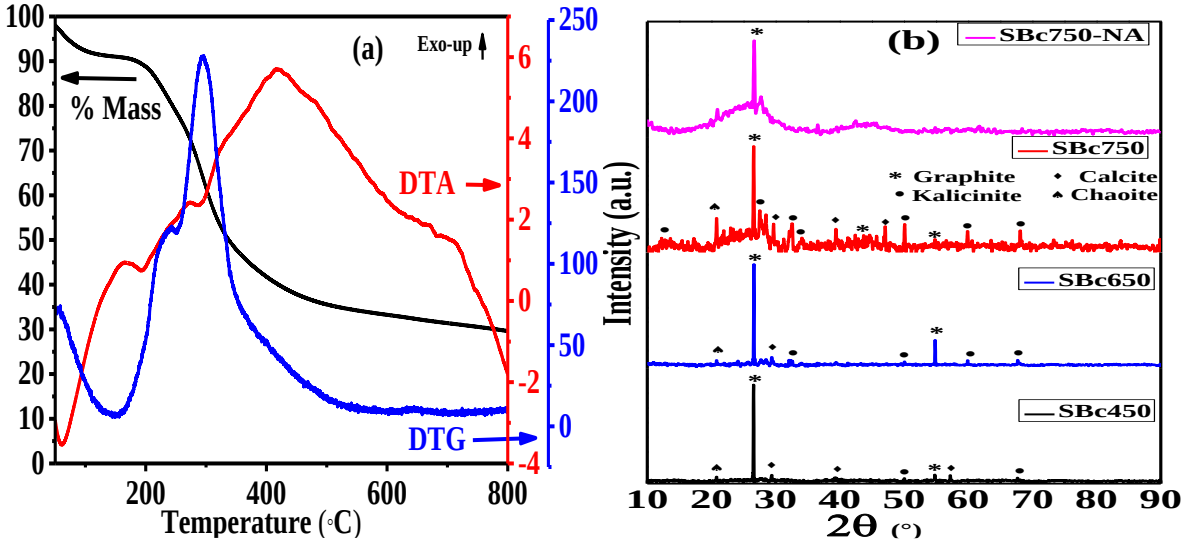

Fig. 7.1: (a) TG/DTA/DTG of soy flour in argon atmosphere at 5 °C/min. and (b) XRD line profiles of the synthesized samples.

Table 7.1: Properties of the synthesized biochar samples.

Sample ID	***SBc450***	***SBc650***	***SBc750***	***SBc750-NA***
Pyrolysis temperature (°C)	450	650	750	750
Treatment	-	-	-	HNO_3
%C	36.29	28.89	28.7	72.15
%N	10.8	4.9	4.6	7.31
%O	30.76	26.09	25.53	20.54
%Minerals	22.15	40.12	41.17	-
Nature of carbon (majority)	Graphitic C	Graphitic C	Amorphous graphitic C	Amorphous graphitic C
Nature of nitrogen (majority)	Pyrrolic and pyridinic N	Graphitic and pyridinic N	Graphitic and pyridinic N	Graphitic and pyridinic N
Band gap (eV)	4.70	4.78	4.81	4.83
I_D/I_G	0.91	1.01	1.04	0.98
Surface area (m^2/g)	0.82	0.60	0.50	94.09
Mean pore diameter (nm)	16.6	37.8	28.8	0.76
Pore volume (cm^3/g)	0.0034	0.0057	0.0036	0.043
pH_{pzc}	5.3	5.4	5.4	4.7

7.3 Characterization of pyrolyzed soy flour

7.3.1 XRD

The structure and phase identification of biochars were undertaken by employing XRD line profile analysis. X'Pert HighScore Plus software was used to locate and match the peaks present in XRD line profile data. The presence of a wide range of mineral crystals and other inorganic compounds was validated for the XRD line profiles of biochars synthesized at 450,

650, and 750 °C (Fig. 7.1 (b)). Peaks visible at various 2θ values for ***SBc450***, ***SBc650***, and ***SBc750*** samples indicated the existence of graphite (C, ICDD-03-065-6212), calcite ($CaCO_3$, ICDD-01-072-1937), kalicinite ($KHCO_3$, ICDD-01-074-1846), and chaoite (C, ICDD-00-022-1069), as shown in Fig. 7.1(b).

The availability of graphitic C confirmed the conjectures postulated from TG/DTG/DTA analysis. It can be seen that as the pyrolysis temperature was increased, more mineralization peaks appeared, marking an increase in the mineral content of the sample. The humps observed in the XRD pattern of ***SBc750*** at 2θ ∼26° and 44° could be due to amorphous graphitic carbon formed at higher temperature [252]. These results clearly indicated that pyrolysis of soy flour lead to formation of oxide ashes containing K and Ca, and the content of minerals increased with increasing temperature. Since soy flour was pyrolyzed in an inert atmosphere, so the carbon in the soy flour did not entirely burn off, and available carbon reacted with existing elements to generate the aforementioned ashes. In the case of ***SBc750-NA***, only two broad peaks at 2θ ∼26° and 44°, along with the peak for graphite, were observed. These peaks indicated the presence of amorphous carbon. In ***SBc750-NA*** sample, absence of sharp peaks for K and Ca based minerals indicated the complete demineralization after treatment with the HNO_3.

7.3.2 FE-SEM

The morphological details obtained for the soy flour, ***SBc450***, ***SBc650***, ***SBc750*** and ***SBc750-NA*** samples using FE-SEM are shown in Fig. 7.2. Fig. 7.2(a) shows that the soy flour consisted of particles with uneven morphologies. After pyrolysis these particles decomposed into powder with no distinct morphology or uniform pore size (Fig 7.2(b-d)).

Change in the morphology including the pore formation for biochar samples occurred due to release of volatiles during decomposition (decrease of mass in TG) and condensation of residual carbon [253]. The FE-SEM image of ***SBc750-NA*** sample shows the removal of small granular remains from the sample surface and also emergence of more/new type of pores (indicated by arrows) after the HNO_3 treatment (Fig. 7.2(e)). This may lead to increased surface area and needs to be probed further by using N_2 adsorption-desorption isotherm. The results about the porosity of the pyrolyzed samples will also have to be confirmed by BET analysis.

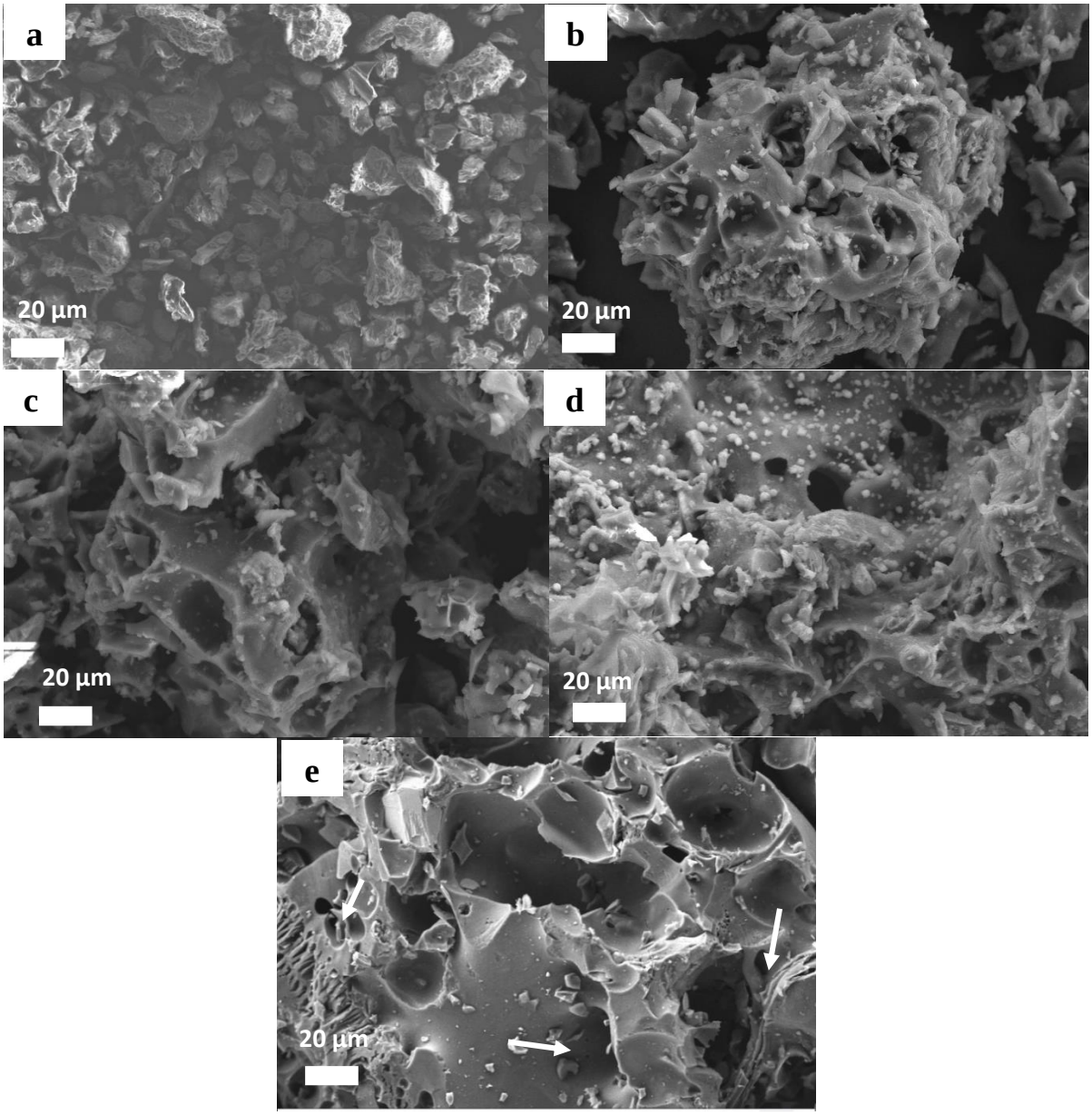

Fig. 7.2: FE-SEM image of (a) soy flour, (b) ***SBc450***, (c) ***SBc650***, (d) ***SBc750*** and (e) ***SBc750-NA*** sample (Arrows indicated the new type of pores which emerged after acid treatment).

7.3.3 Raman spectroscopy

Raman spectroscopy was carried out to investigate the structural perfection and defects in the synthesized samples. The obtained Raman spectra for ***SBc450***, ***SBc650***, ***SBc750***, and ***SBc750-NA*** samples are shown in Fig. 7.3. The spectra exhibit prominent peaks at 1350 cm^{-1}, 1590 $cm^{-1,}$ and 2900 cm^{-1}, designated as D, G, and G" bands, respectively. D-band is associated with the disorder in carbon, G-band with ordering in the carbon structure, and the G" band is induced due to disorder, and is an overtone of the D band. The ratio of the intensity of the D and G band was termed as I_D/I_G. The values of I_D/I_G for ***SBc450***, ***SBc650***, ***SBc750*** and ***SBc750-***

NA obtained were 0.91, 1.01, 1.04, and 0.98, respectively. With increasing pyrolysis temperature, the I_D/I_G ratio has increased, indicating that the structure of biochar becomes more disordered with increasing pyrolysis temperature [254]. This may also be attributed to the increased content of mineral ashes as confirmed from XRD. These results were in line with the XRD results which indicated that with increase in the pyrolysis temperature, the sample becomes amorphous and hence disordered. It was also observed that with increase in the pyrolysis temperature, the intensity of the G" band decreased indicating the decreased graphitization of carbon in the heat-treated samples [104,221]. For the ***SBc750-NA*** sample, the intensity of G band increased showing the increased content of ordered graphitic carbon for this sample.

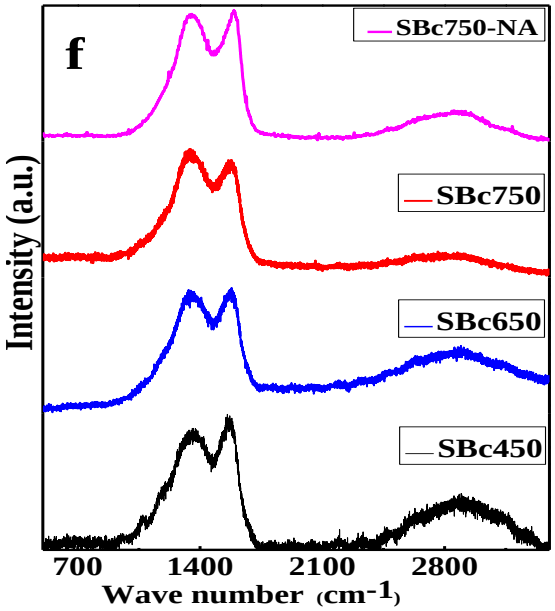

Fig. 7.3: Raman spectra of synthesized samples.

7.3.4 UV-Visible spectroscopy

Reflectance spectra of the synthesized samples were obtained using UV-Visible spectroscopy, as shown in Fig. 7.4(a). The π-π^* transition of sp^2 graphitic carbon was visible as a reflectance peak at 250 nm in these samples [218]. The bandgap of ***SBc750*** and ***SBc750-NA*** samples were calculated using the Kubelka-Munk model (Fig. 7.4(b)) as explained in chapter 3 (section- 3.3.6)

For ***SBc750*** and ***SBc750-NA*** samples, the calculated allowed direct bandgaps were 4.81 eV and 4.83 eV, respectively (Fig. 7.4(b)). The slight increase in bandgap with modification

with HNO_3 may be attributable to the reduced nitrogen content in these samples [219,220]. This conjecture needs to be confirmed further by XPS.

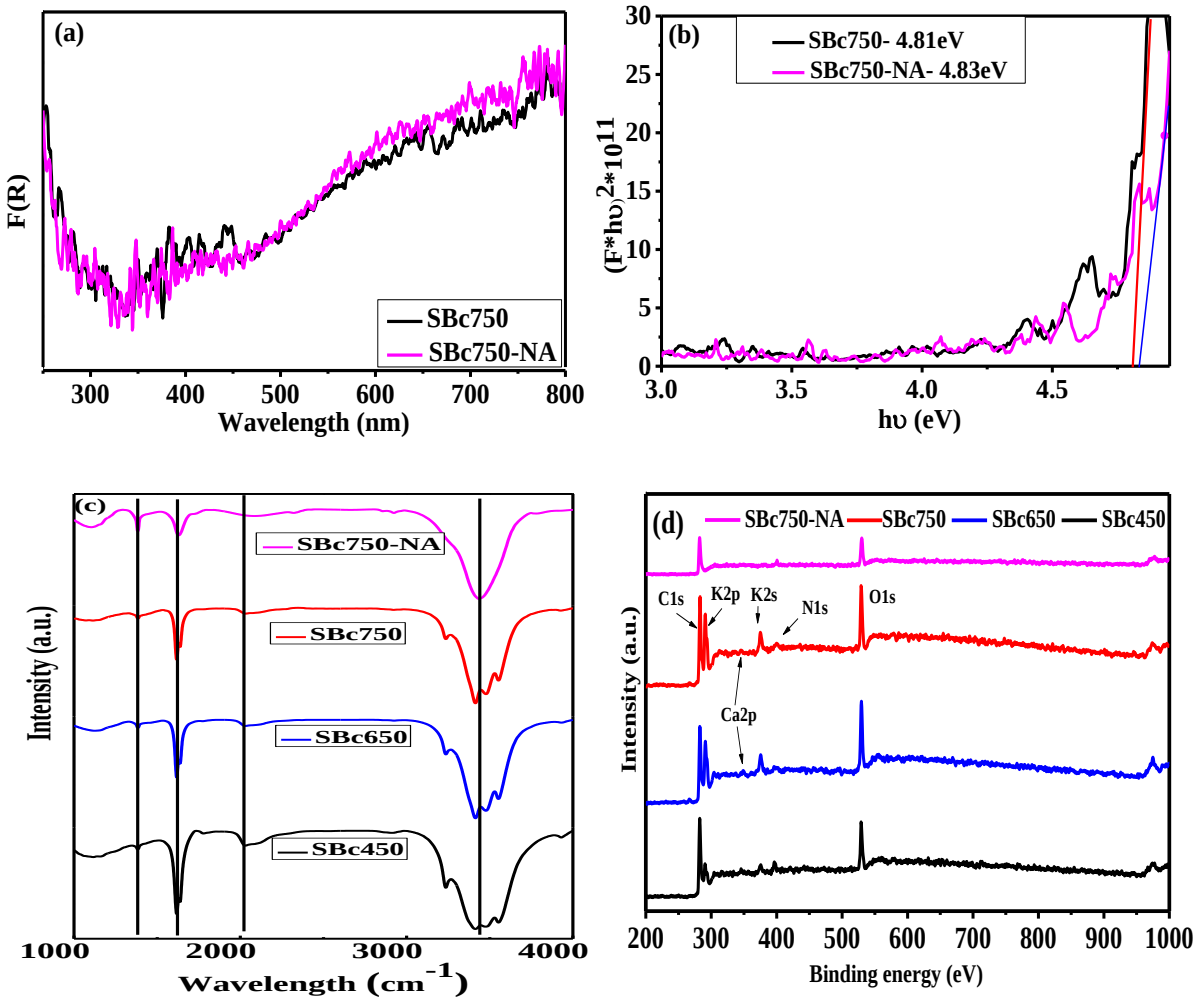

Fig. 7.4: (a) UV-Visible diffuse reflectance spectra, (b) band gap of ***SBc750*** and ***SBc750- NA*** samples (c) FTIR spectra and (d) XPS survey spectra of all the synthesized samples.

7.3.5 FTIR Spectroscopy

FTIR spectroscopy was used to study the chemical bonds present in the samples. The FTIR spectra of the synthesized samples are shown in Fig. 7.4(c). The characteristic band observed at ~ 3436 cm^{-1} indicated oxygen-containing O-H functional group for all four samples. This band was generated due to adsorbed water. Few shoulders were observed in non HNO_3 treated samples, which were not available in the ***SBc750-NA*** sample. These shoulders might have appeared due to adsorbed water on the various adsorption sites of minerals in the samples. The bands at ~1375 cm^{-1} and 1100 cm^{-1} were observed only in ***SBc750-NA*** sample and indicated the presence of oxygen containing nitrate group (NO_2) and strong C-O stretch. These bands appeared due to oxidation of the sample by HNO_3 [255]. For pyrolyzed samples, the wide peak at 1610 cm^{-1} indicated the stretch vibration of aliphatic –C=C-/C-C [102,256].

For increasing pyrolysis temperature and acid treatment, due of the availability of excess energy the breaking of aliphatic C=C/C-C band took place resulting in the decrease of its intensity [256]. The decreased intensity signalled that the biomass was transformed from aliphatic structure to aromatic structure [257]. All of the samples contained a small peak around 1380 cm^{-1}, indicating the existence of an aliphatic C-H bending group. A lower intensity band around 2030 cm^{-1} shows the presence of C≡C [258].

7.3.6 XPS

XPS was performed to characterize the surface elemental composition and chemical bonds of the synthesized samples. In the survey spectra of the samples as shown in Fig. 7.4(d), the distinct peaks at 285.8, 400.6, and 531.4 eV are assigned to C1s, N1s, and O1s, respectively. Along with C1s, N1s, and O1s, prominent peaks of K2p, K2s and Ca2p were also observed at 293 eV, 378 eV and 348 eV, respectively, in the pyrolyzed samples. In case of ***SBc750-NA*** sample, peaks of only C1s, N1s, and O1s were observed. The elemental content of all the samples is given in Table 7.1. The ratio of N/C in ***SBc450***, ***SBc650***, ***SBc750*** and ***SBc750-NA*** samples were 0.29, 0.17, 0.16 and 0.10, respectively. This confirms the conjecture from UV visible spectroscopy that the increased band gap was due to decreasing content of N and O in the samples. It can be observed that with increase in the pyrolysis temperature, the fractional content of C1s, N1s, and O1s decreased (Table 7.1) while that for K2p, K2s, and Ca2p increased. Soy flour consists of >50% protein resulting in ~7% nitrogen with C, H, O, N, K, Ca, S, P, and Mg as the primary elements [259]. The XPS survey spectra indicated that under pyrolysis the breakdown of S, P, and Mg compounds must have resulted in volatile products. These results also confirmed the XRD peak assignment for the presence of primarily Ca and K based minerals in the biochar (calcite and kalicinite). For ***SBc750-NA***, the presence of only C, N and O confirmed the results obtained from XRD line profile for complete demineralization.

HR XPS spectra of C1s, N1s, and O1s for the synthesized samples are shown in Fig. 7.5 and the parameters obtained from fitting are given in Table 7.2. For all the samples, C1s exhibited C=C peak at 284.2 eV. The % availability of C=C increased with an increase in the pyrolysis temperature and acid treatment. For ***SBc450*** and ***SBc650*** samples, the presence of C=N peak is observed which were not observed in ***SBc750*** and ***SBc750-NA*** samples indicating lowering N content with increasing pyrolysis temperature. The presence C=O peaks were observed in ***SBc750***, and ***SBc750-NA*** samples [260]. The increase in the sp^2 carbon content shows that the aliphatic structure is converting to aromatic structure with increasing temperature and acid treatment.

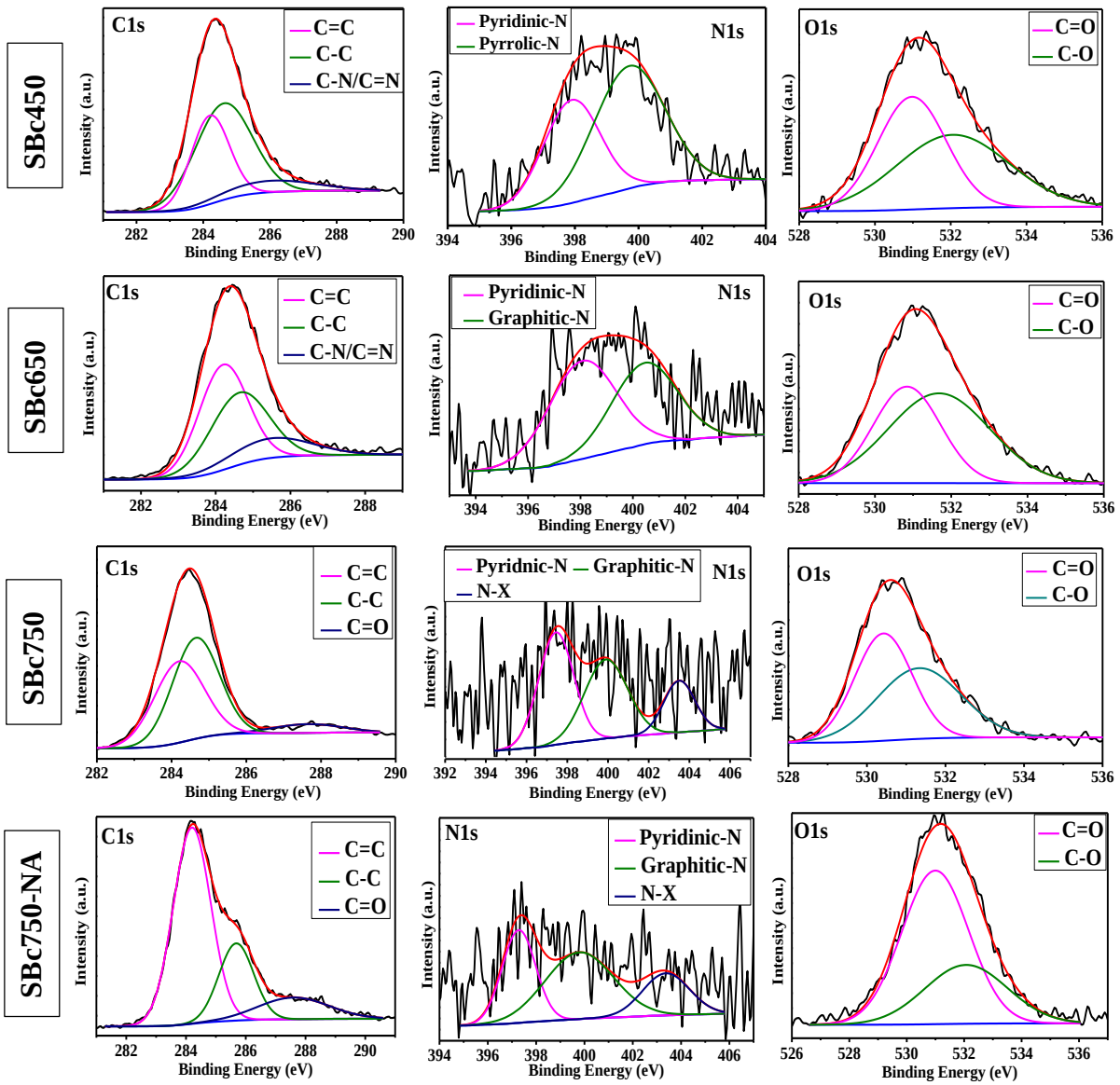

Fig. 7.5: HR-XPS spectra of C1s, N1s, and O1s of ***SBc450***, ***SBc650***, ***SBc750,*** and ***SBc750-NA*** samples.

From the high resolution N1s spectra of all the samples, it can be seen that the pyridinic-N content increased first with the increase in the pyrolysis temperature and decreased beyond 650 °C. Also, in ***SBc450*** sample, pyrrolic-N was present while in ***SBc650***, ***SBc750*** and ***SBc750-NA*** samples, graphitic-N was observed. This is because the pyridinic and graphitic-N are more stable functionalities than pyrrolic-N above 500 °C [227,261]. The presence of oxidized-N (N-X) in ***SBc750*** and ***SBc750-NA*** samples was observed due to the oxidation of pyrrolic-N and pyridinic-N with increase in pyrolysis tempaerature and further with acid treatment. From O1s spectra, the exhibition of C-O and C=O peaks were observed for all the samples. These results clearly show that even though the overall oxygen content of the samples

has decreased, the carbon as well as nitrogen were more oxidized for the ***SBc750*** and ***SBc750-NA*** samples.

Table 7.2: Parameters obtained from XPS peak fitting.

		%at			
	Group	**SBc450**	**SBc650**	**SBc750**	**SBc750-NA**
C1s	C sp^2	34.2	46.9	59.6	63.7
	C sp^3	55.3	38.3	32.0	23.1
	C-N/C=N	10.5	14.8	-	-
	C=O	-	-	8.4	13.2
N1s	pyridine	46.6	55.3	43.9	32.3
	Pyrrole	53.4	-	-	-
	Graphitic	-	44.7	38.2	47.2
	N-X	-	-	17.9	20.5
O1s	C=O	48.4	41.5	50.8	67.9
	C-O	51.6	58.5	49.2	32.1

7.3.7 N_2 adsorption-desorption isotherms

The N_2 adsorption-desorption isotherms and pore size distribution curves for all the synthesized samples are shown in Fig. 7.6(a) and 7.6(b). The BET surface areas obtained for only pyrolyzed samples were insignificant and below 1 m^2/g (Table 7.1). The BET surface area for ***SBc750-NA*** was observed to be enhanced multiple times (~100) and was 94.09 m^2/g. The adsorption behaviour of the ***SBc750-NA*** sample was similar to the type I and H4 adsorption classifications showing the adsorption amount increased sharply in the low relative pressure range due to the micropore filling effect [262].

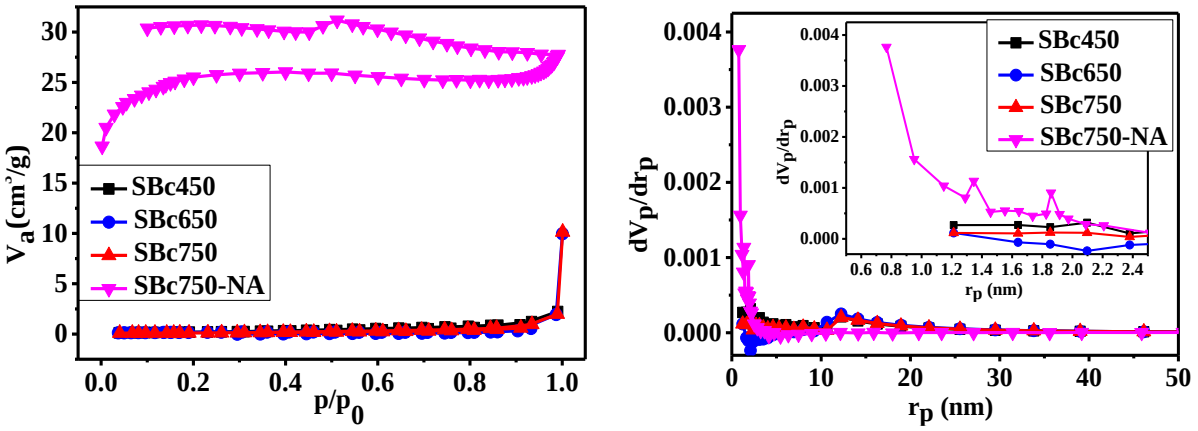

Fig. 7.6: (a) N_2 adsorption-desorption isotherm and (b) pore size distribution with inset showing the pore distribution in the microporous region for all the synthesized samples.

This significant increase in surface area post acid treatment indicated increased porosity. The pore size distribution, calculated using BJH (***SBc450***, ***SBc650***, ***SBc750***) and

Horvath-Kawazoe method (***SBc750-NA***) is shown in Fig. 7.6(b). The results clearly indicate that the lower surface area of ***SBc450***, ***SBc650***, ***SBc750*** samples was observed due to insignificant number of micropores available for the samples. For ***SBc750-NA*** sample there were significantly large number of pores observed in the microporous region (diameter < 2 nm) with average mean pore diameter of 0.8 nm. Pores resulted in enhanced surface area for the sample and might be helpful for the adsorption of lower molecular size pollutant molecules (< 0.8 nm).

7.3.8 Point of zero charge (pH_{pzc}) of samples

A pH_{pzc} is the pH at which the surface of the sample has no net charge. The sample's surface has a net positive charge below pH_{pzc} and a net negative charge above pH_{pzc}. As shown in Fig. 7.7, the pH_{pzc} values obtained for ***SBc450***, ***SBc650***, ***SBc750*** and ***SBc750-NA*** were 5.3, 5.4, 5.4, and 4.7, respectively. The decrease in the pH_{pzc} for ***SBc750-NA*** sample was due to acid treatment resulting in demineralization, thus reducing the ash content and also resulted in oxidation of sample making it acidic [260,263]. The pH of most dye solutions lies between 5-6 and pH_{pzc} obtained for the synthesized samples was in same range, therefore, all the samples will be able to show the better adsorption for both cationic and anionic dyes.

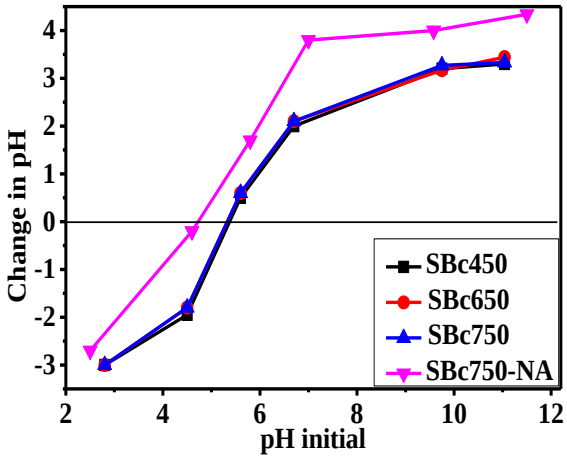

Fig. 7.7: pH_{pzc} of the synthesized samples.

7.4 Adsorption studies

7.4.1 Model Pollutants

The adsorption studies for MB, CV, EBT, PNP, CIP and DEP as model pollutants were carried out to study the effect of pyrolysis temperature and acid wash on the potential adsorption applications of synthesized biochar samples. The % adsorption of pollutants after 3 hours is shown in Fig. 7.8 (a). It was observed that all the samples show better adsorption for

dyes as compared with other pollutants (<10%). Therefore, further studies were carried out on cationic dye MB and anionic dye EBT. Fig. 7.8 (b) shows the % adsorption of MB and EBT with time on ***SBc750*** sample. It is clear from the data that with increase in pyrolysis temperature, the % adsorption increased for all the pollutants. For cationic dyes, the lower N functionality resulted in higher adsorption capacity. The higher N functionality in a sample leads to an enhancement in the basic nature of the sample and results in an electrostatic repulsion between N containing sample and cationic dyes. Thus, for the pyrolyzed samples the adsorption of cationic dyes MB and CV was maximum for the ***SBc750*** sample as the N-content was lowest in this sample [63]. In case of anionic dye EBT also the adsorption efficiency increased with the increasing pyrolysis temperature. This was due to enhanced Lewis basic nature as a result of higher pyridinic-N and graphitic-N content. The electrostatic interaction between Lewis basic sites and anionic surface of dye resulted in increased adsorption. The surface chemistry clearly played a vital role in the dye adsorption process and inspite of very low surface area of pyrolyzed samples, significant amount of adsorption was observed for the ***SBc750*** sample. For ***SBc750-NA*** sample, the enhanced % adsorption can be attributed to increased porosity and thus surface area. The enhanced surface area led to availability of more active sites for adsorption process. Also, the increased graphitic-N content in this sample enhanced positive surface which led to enhanced adsorption of EBT. The increased efficiency for cationic dye adsorption onto ***SBc750-NA*** sample was also attributed to the decreased pH_{pzc} of the sample due to enhanced N-X content. The adsorption of dyes onto ***SBc750-NA*** sample enhanced only by ~1.5 times in spite of having ~100 times of the surface area than ***SBc750*** sample. This is attributed to the lower average micropore size (0.8 nm) of ***SBc750-NA*** sample. The size of MB and EBT molecules are >0.8 nm and therefore the volume within the micropores was not accessible for adsorption.

For all the samples, cationic dyes adsorbed better than anionic dye. Since the point of zero charge of the samples was below the normal pH of EBT dye (6.6) so the sample possessed net negative charge on the surface. Therefore, due to electrostatic repulsion between negative surfaces of adsorbate and adsorbent, the adsorption of EBT was lower than cationic dyes for all the samples [264].

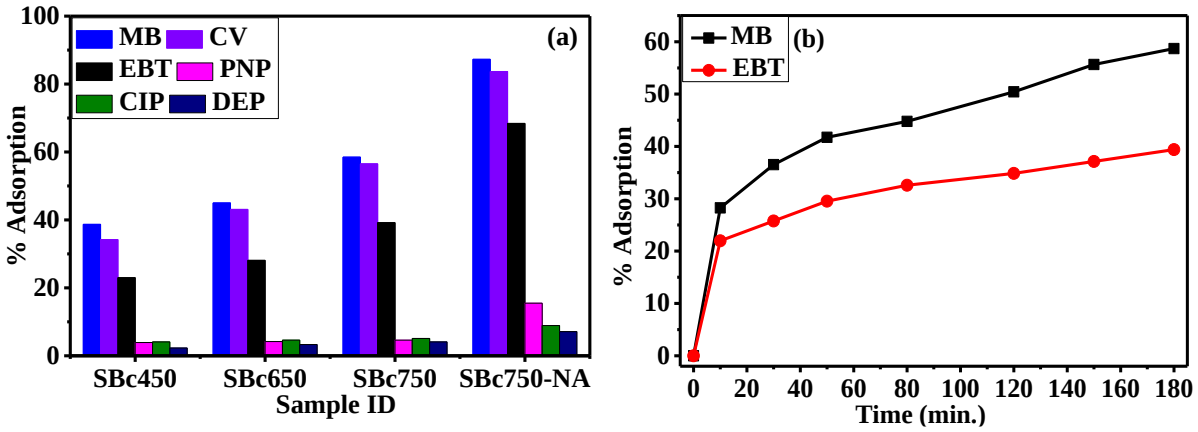

Fig. 7.8: % Adsorption of (a) MB, CV, EBT, PNP, CIP and DEP on ***SBc450***, ***SBc650***, ***SBc750*** and ***SBc750-NA*** samples after 3 hours and (b) MB and EBT with time on ***SBc750*** sample.

7.4.2 Effect of pH variation of dyes

The effect of pH variation was studied for ***SBc750*** sample with MB and EBT dyes using 1 mg/L of dye and 20 mg/L of adsorbent.

MB: The MB adsorption efficiency of the ***SBc750*** sample increased as the pH was elevated (Fig. 7.9 (a)). At lower pH values, the sample's surface had a net positive charge, which lowered the cationic dye adsorption. The surface of the ***SBc750*** sample had a more and more of net negative charge as the pH increased over pH_{pzc} (5.4), and therefore the sample absorbed the MB dye more efficiently due to electrostatic interaction/hydrogen bonding.

EBT: As demonstrated in Fig. 7.9(a), the adsorption capacity of the ***SBc750*** sample drops with the pH of the EBT solution. At lower pH, the sample's surface had a net positive charge, and an increased electrostatic interaction with the negatively charged anionic dye EBT was observed. The surface of the sample had a net negative charge at higher pH, i.e., above pH_{pzc} (5.4), which resisted the negatively charged EBT dye, resulting in decreased adsorption.

7.4.3 Recyclability test

To examine the recyclability of synthesized samples for adsorption of MB and EBT dye, recyclability studies were carried out (Fig. 7.9(b)). For the recyclability test, MB and EBT dyes were used at concentrations of 1mg/L, with an adsorbent concentration of 100 mg/L. The ***SBc750*** sample's adsorption efficiency was measured for 14 cycles in a row. From the first to the fourteenth cycle, the % adsorption of MB and EBT dye varied by 8.1% and 9.6%, respectively. This difference might be attributed to sample loss during the recycling studies. So, the sample is reusable for both MB and EBT dye adsorption without compromising efficiency.

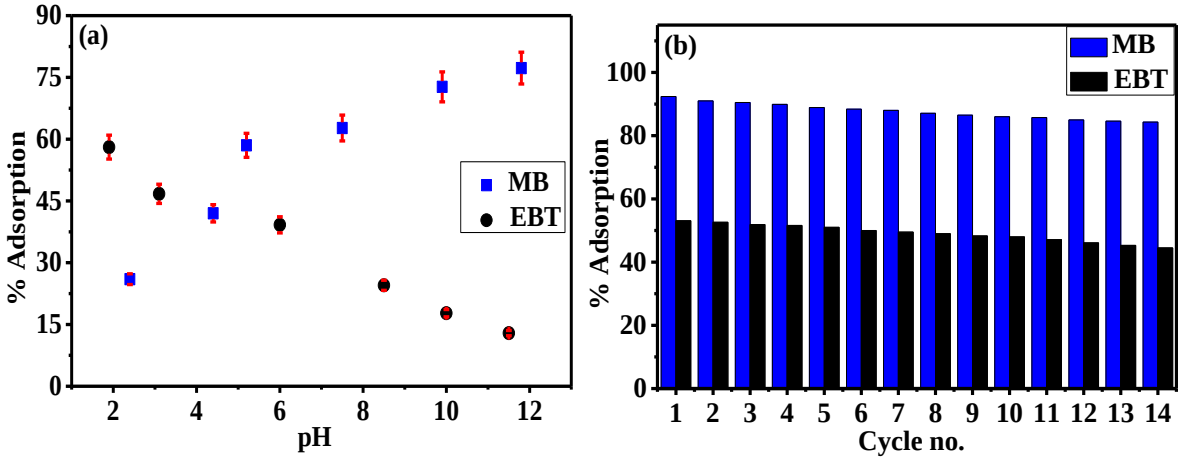

Fig. 7.9: % Adsorption of MB and EBT on ***SBc750*** sample (a) with variation in pH after 3 hours and (b) recyclability test for 14 cycles.

7.4.4 Adsorption isotherm modeling

Fitting with adsorption isotherms was utilized to estimate the effectiveness of adsorbent material and the type of adsorption [176]. Langmuir and Freundlich isotherm models were utilized to fit the experimental data for MB and EBT adsorption onto the ***SBc750*** and ***SBc750-NA*** sample (explained in chapter 3 (section 3.4.1)). The fitted graphs for the isotherms are shown in Fig. 7.10 and Fig. 7.11 and the parameters obtained from fitting both the isotherms are given in Table 7.3 and Table 7.4.

SBc750: The obtained n values for MB and EBT for the Freundlich fitting were 4.01 and 2.20, respectively, demonstrating that adsorption was favored in both instances. According to the regression coefficient values for both models, the MB dye adsorbs onto the ***SBc750*** sample through monolayer formation following Langmuir isotherm model. The emergence of Freundlich model as a better fit for EBT revealed that it forms multilayers on the surface of the ***SBc750*** sample [179].

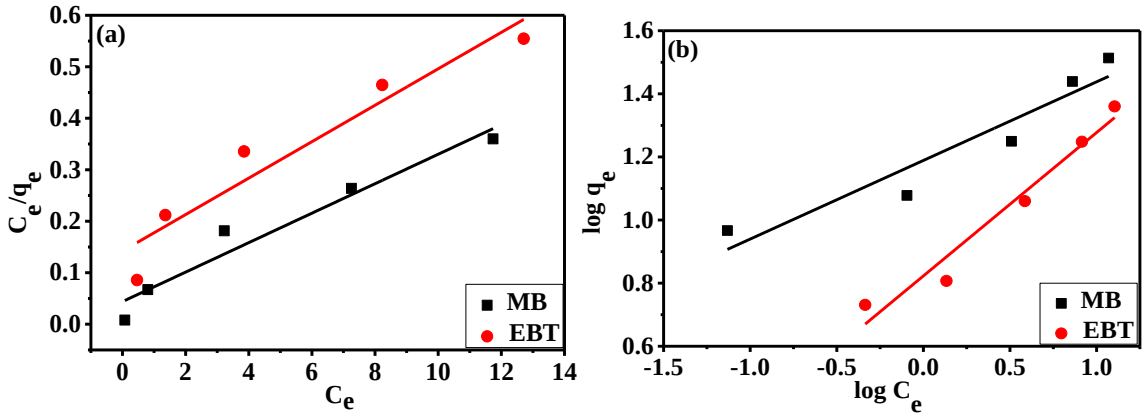

Fig. 7.10: Isotherm fitting for MB and EBT adsorbed on ***SBc750*** (100 mg/L) using (a) Langmuir and (b) Freundlich model.

Table 7.3: Parameters obtained from Langmuir and Freundlich isotherm models obtained for MB and EBT adsorption onto ***SBc750*** sample (100 mg/L).

Adsorption	Dye Adsorbed	Parameter	Value	R^2
Langmuir isotherm	MB	k_L (L/g)	0.65	**0.93**
		q_e (mg/g)	32.60	
		R_L	0.60	
	EBT	k_L (L/g)	0.24	0.89
		q_e (mg/g)	22.91	
		R_L	0.80	
Freundlich isotherm	MB	k_f (L/g)	3.23	0.87
		n	4.01	
	EBT	k_f (L/g)	2.23	**0.94**
		n	2.20	

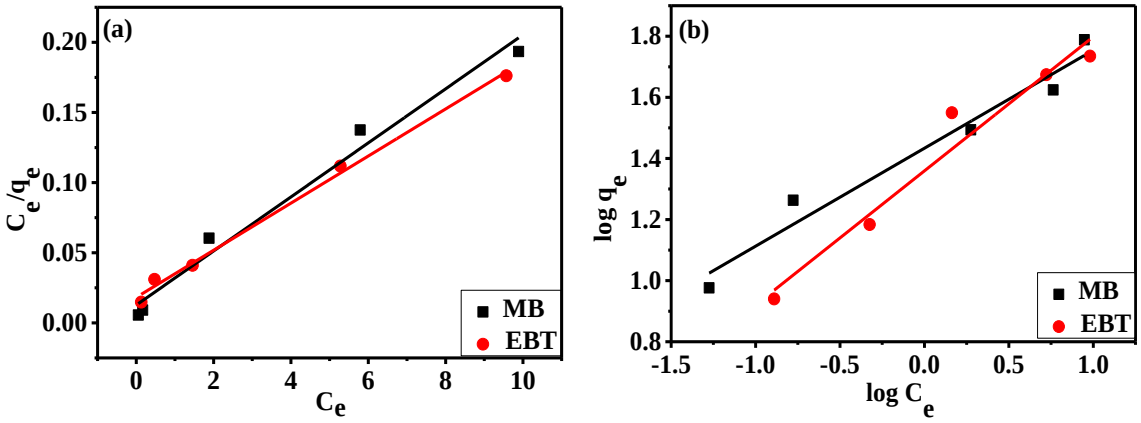

Fig. 7.11: Isotherm fitting for MB and EBT adsorbed on ***SBc750-NA*** (100 mg/L) using (a) Langmuir and (b) Freundlich model.

Table 7.4: Parameters obtained from Langmuir and Freundlich isotherm models obtained for MB and EBT adsorption onto ***SBc750-NA*** sample (100 mg/L).

Adsorption	Dye Adsorbed	Parameter	Value	R^2
Langmuir isotherm	MB	k_L (L/g)	1.52	0.974
		q_e (mg/g)	51.11	
		R_L	0.39	
	EBT	k_L (L/g)	0.92	**0.950**
		q_e (mg/g)	54.30	
		R_L	0.52	
Freundlich isotherm	MB	k_f (L/g)	3.89	**0.993**
		n	3.12	
	EBT	k_f (L/g)	3.69	0.945
		n	2.30	

SBc750-NA: The obtained n values for MB and EBT for the Freundlich fitting were 3.12 and 2.30, indicating that adsorption was favoured for both dyes. The Freundlich model's occurrence as a superior fit for MB revealed that it creates multilayers on the surface of the ***SBc750-NA*** sample. The EBT dye adsorbs onto the SBc750 sample via monolayer formation

using the Langmuir isotherm model, according to the regression coefficient values for both models.

7.4.5 Adsorption kinetic modeling

For estimating the adsorption rates of MB and EBT dyes (1mg/L) onto ***SBc750*** and ***SBc750-NA*** sample (20 mg/L), PFO, PSO and Elovich models were used to examine and evaluate the adsorption kinetics (explained in chapter 3 (section 3.4.2)). Simultaneously, the IPD model was used to investigate the diffusion process during adsorption. The fitted kinetic models curves for ***SBc750*** sample are shown in Fig. 7.12(a-d) and parameters obtained from the fittings are given in Table 7.5 and Table 7.6. The kinetic model fits for ***SBc750-NA*** sample are shown in Fig. 7.13(a-d) and parameters obtained from the fittings are given in Table 7.7 and Table 7.8. The experimental data of the amount of MB and EBT adsorbed, q_t (mg/g), at time t and the amount adsorbed at equilibrium, q_e (mg/g) were calculated using the equations as explained in chapter 3 (section 3.4.2).

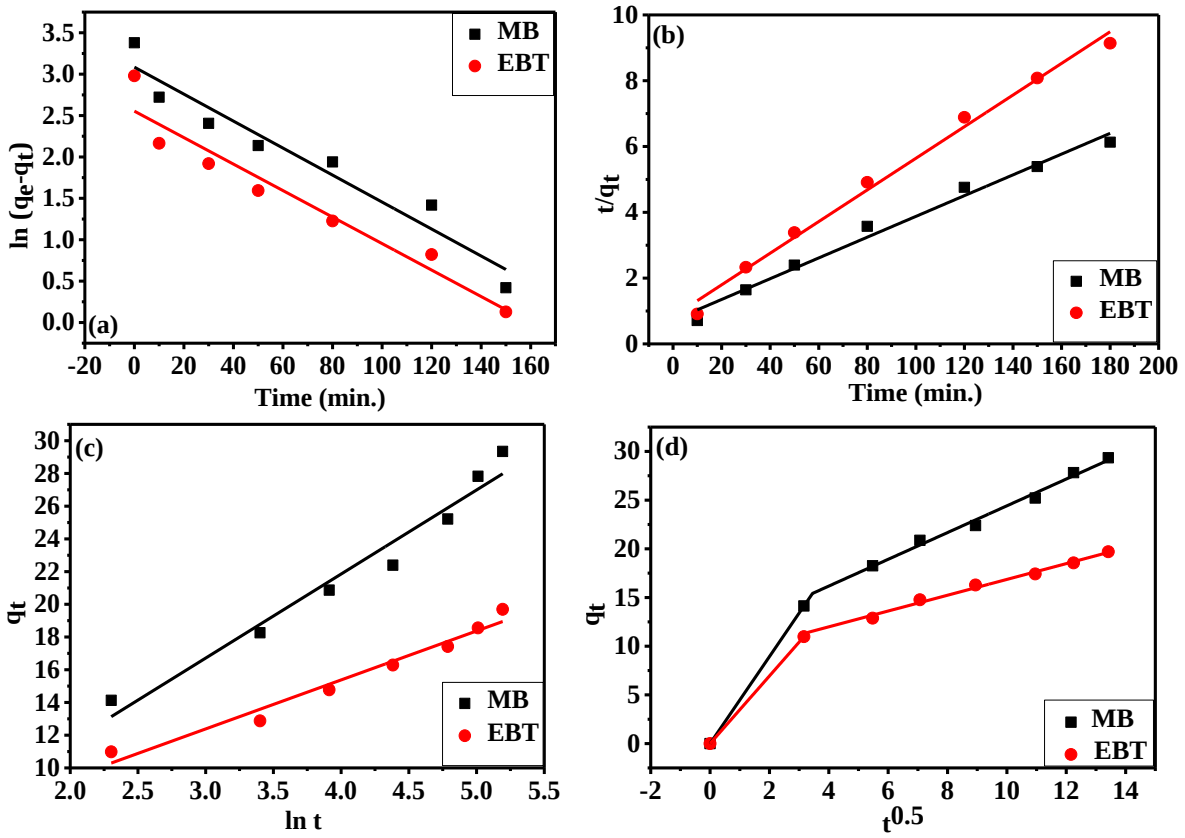

Fig. 7.12: Kinetic modeling of MB and EBT (1 mg/L) adsorbed on ***SBc750 (***20 mg/L) using (a) PFO, (b) PSO, (c) Elovich, and (d) IPD model.

The experimentally obtained q_e values for MB and EBT dye using ***SBc750*** sample were 29.34 and 19.69 mg/g, respectively. The experimentally obtained q_e values for MB and EBT

dye using ***SBc750-NA*** sample were 43.80 and 34.46 mg/g, respectively. The variation in the values of q_e was not much despite of higher surface area of ***SBc750-NA*** sample because of its lower average micropore size (0.8 nm). The size of MB and EBT molecules are above 0.8 nm and therefore could not enter in the pores <0.8 nm for adsorption.

Table 7.5: Parameters of kinetic modeling of MB and EBT adsorbed at ***SBc750*** sample. (q_e (**MB**) = 29.34 mg/g and q_e (**EBT**) = 19.69 mg/g).

Dye	Kinetic	Parameters	Value	R^2
MB	PFO	k_1 (1/min)	0.016	0.925
		q_e (mg/g)	8.385	
	PSO	k_2 (g/mg min.)	0.0013	**0.982**
		q_e (mg/g)	31.74	
	Elovich model	α (mg/g min.)	3.536	0.954
		β	0.194	
EBT	PFO	k_1 (1/min)	0.016	0.926
		q_e (mg/g)	6.939	
	PSO	k_2 (g/mg min.)	0.0027	**0.990**
		q_e (mg/g)	20.83	
	Elovich model	α (mg/g min.)	9.248	0.962
		β	0.334	

Table 7.6: Parameters of diffusion model (IPD) of MB and EBT adsorbed at ***SBc750*** sample.

Dye	Parameters	Value	R^2
MB	k_{id1}(mg/g $min^{1/2}$)	4.468	0.997
	k_{id2} (mg/g $min^{1/2}$)	1.373	
EBT	k_{id1}(mg/g $min^{1/2}$)	3.473	0.997
	k_{id2} (mg/g $min^{1/2}$)	0.811	

SBc750-NA: The $\%\Delta q_e$ values for the MB and EBT dyes were 76.3% and 73.6%, respectively. For the MB and EBT dyes, the $\%\Delta q_e$ values for PSO fit were 17.3% and 8.5%, respectively. Based on $\%\Delta q_e$ values and regression coefficients derived by PFO, PSO, and Elovich fits, adsorption of both MB and EBT onto ***SBc750-NA*** sample followed the PSO model (Table 7.7). This showed that chemisorption played a role in the adsorption process. The adsorption mechanism for both dyes in the ***SBc750-NA*** sample is divided into two steps: initial adsorption via boundary layer diffusion, followed by intraparticle diffusion [46]. For MB and EBT adsorption, boundary layer diffusion occurs up to 30 and 45 minutes, respectively, but intraparticle diffusion occurs beyond these times (Fig. 7.13(d)).

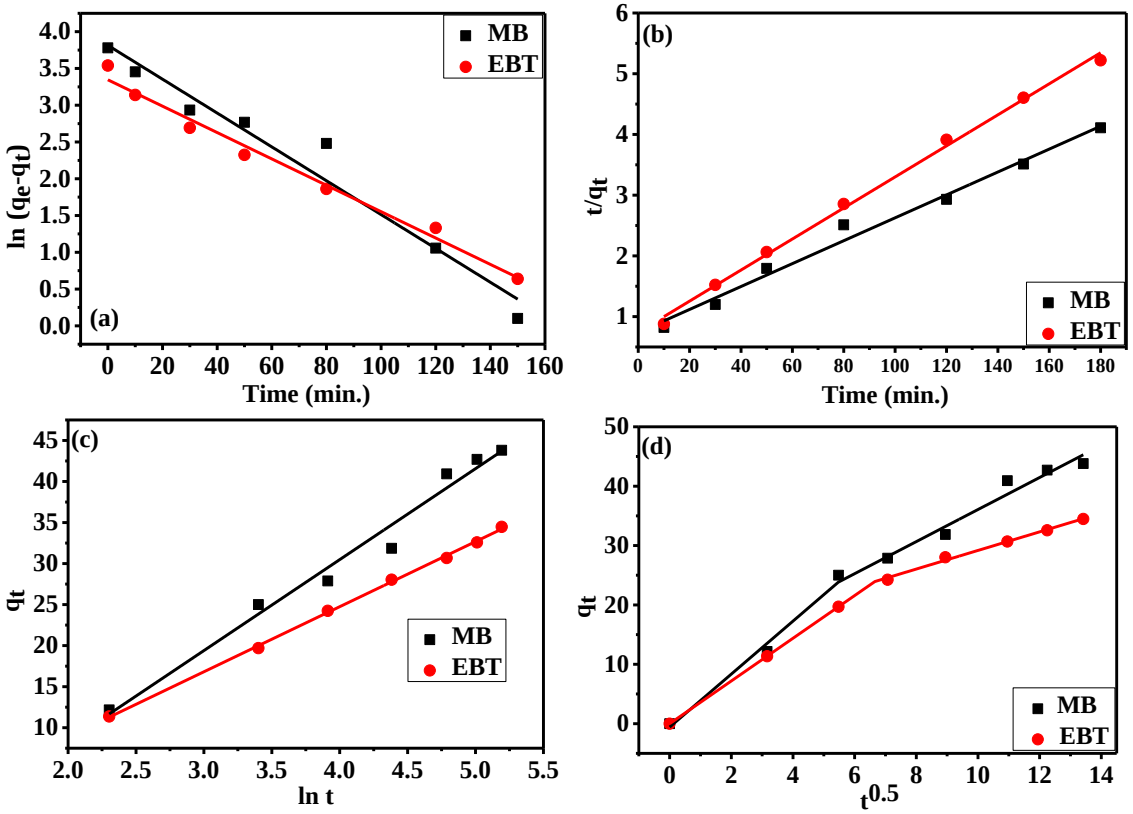

Fig. 7.13: Kinetic modeling of MB and EBT (1 mg/L) adsorbed on ***SBc750-NA*** **(**20 mg/L) using (a) PFO, (b) PSO, (c) Elovich, and (d) IPD model.

Table 7.7: Parameters of kinetic modeling of MB and EBT adsorbed at ***SBc750-NA*** sample. (q_e (***MB***) = 43.80 mg/g and q_e (***EBT***) = 34.46 mg/g).

Dye	Kinetic	Parameters	Value	R^2
MB	PFO	k_1 (1/min)	0.023	0.955
		q_e (mg/g)	10.36	
	PSO	k_2 (g/mg min.)	0.00048	**0.984**
		q_e (mg/g)	53.02	
	Elovich model	α (mg/g min.)	37.675	0.975
		β	0.0902	
EBT	PFO	k_1 (1/min)	0.017	0.982
		q_e (mg/g)	9.09	
	PSO	k_2 (g/mg min.)	0.00087	**0.996**
		q_e (mg/g)	39.12	
	Elovich model	α (mg/g min.)	18.978	0.998
		β	0.126	

Table 7.8: Parameters of diffusion model (IPD) of MB and EBT adsorbed at ***SBc750-NA*** sample.

Dye	Parameters	Value	R^2
MB	k_{id1}(mg/g $min^{1/2}$)	4.459	0.986
	k_{id2} (mg/g $min^{1/2}$)	2.701	
EBT	k_{id1}(mg/g $min^{1/2}$)	3.596	0.999
	k_{id2} (mg/g $min^{1/2}$)	1.567	

7.4.6 Adsorption Mechanism

The adsorption of both MB and EBT onto the ***SBc750*** sample was fast at first, but it saturated to the final value later (>120 min), as seen in Fig. 7.8 (b). Table 7.9 shows the results of different isotherm and kinetics fit with experimental data.

SBc750: For MB dye, the Langmuir nature of the isotherm suggested that MB undergoes reversible adsorption at several equivalent sites, resulting in the development of a monolayer on the surface of ***SBc750*** via chemisorption as confirmed by PSO model. A two-step fit of the IPD revealed that adsorption occurs first through boundary layer diffusion and subsequently through intraparticle diffusion after 12 minutes. For EBT dye, the adsorption followed Freundlich isotherm, the value of n obtained was 2.22 (>1) indicating the homogeneous nature of the surface for adsorption. Thus the adsorption on the surface of the sample takes place by chemisorption as it follows PSO model with a monolayer or may be by bilayer. The bilayer adsorption may occur due to strong electrostatic interaction of EBT and ***SBc750*** sample due to presence of Graphitic-N in the sample. Two step fit of IPD indicated that initially adsorption takes place through boundary layer diffusion and then by intraparticle diffusion beyond ~10 min.

SBc750-NA: The adsorption of MB followed Freundlich model and PSO model. In this case, value of n obtained for MB was 3.12. Therefore, the adsorption on the surface of the sample takes place by chemisorption as it follows PSO model with a monolayer or may be by bilayer. This was in agreement with opposite charge between the dye and ***SBc750-NA*** at the optimal pH. (Section 3.10.2). Two step fit of IPD indicated that initially adsorption takes place through boundary layer diffusion and then by intraparticle diffusion beyond ~30 min. For EBT dye, the isotherm's Langmuir nature revealed the formation of a monolayer on the surface of sample with chemisorption as confirmed by PSO. A two-step fit of the IPD revealed that adsorption occurs first by boundary layer diffusion and then after 45 minutes, occurs via intraparticle diffusion.

Table 7.9: Results of different adsorption isotherm and kinetic modeling.

Sample ID	Dye adsorbed	Isotherm	Kinetic model	IPD
SBc750	MB	Langmuir	PSO	2 step
	EBT	Freundlich	PSO	2 step
SBc750-NA	MB	Freundlich	PSO	2 step
	EBT	Langmuir	PSO	2 step

Table 7.10 shows the conclusion of adsorption results obtained using the ***SBc750-NA*** sample for MB and EBT adsorption.

Table 7.10: Adsorption results for the best sample.

Sample ID	Pollutant	q_e (mg/g)	Kinetic model	Kinetic
SBc750-NA	MB	51.11	PSO	Freundlich
	EBT	54.30	PSO	Langmuir

Chapter 8

Photo-induced decolorization studies

Overview

The present chapter describes the photo-induced activity studies for those samples which had the best adsorption chracteristics as described in the previous chapters by testing their properties under UV irradiation and sunlight. The % decolorization efficiency of the chosen samples was tested for the pollutants viz. MB, EBT, PNP, CIP, and DEP. To determine the mechanism for decolorization enhancement, scavenger tests were carried out and explained with the help of valence band spectra and bandgap of the samples.

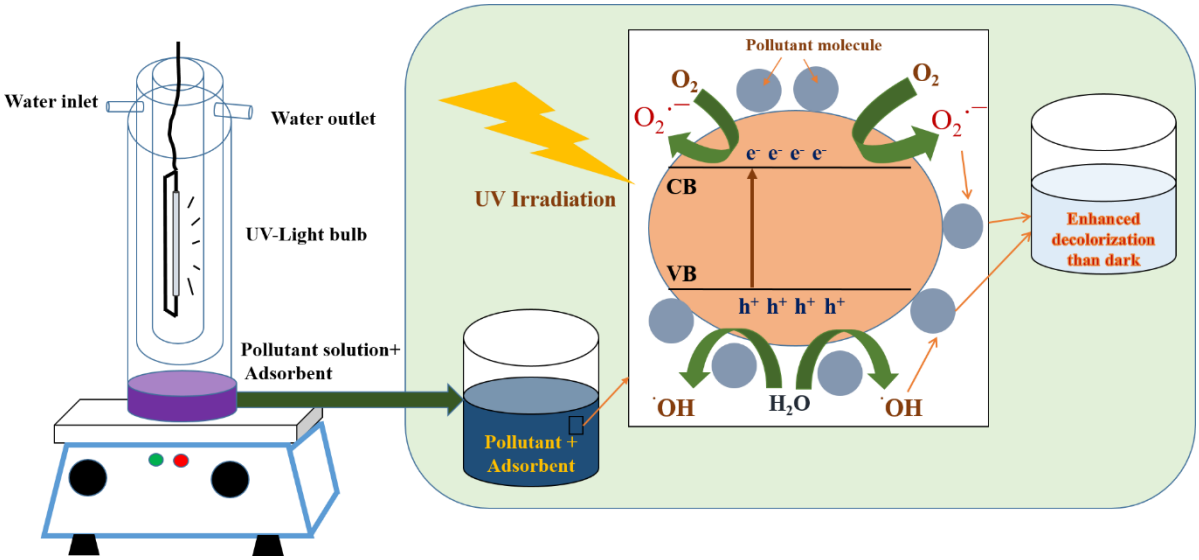

8.1 Introduction

It has been reported that carbon spheres show photodegradation of organic compounds [78,265]. The photodegradation ability of the material directly depends upon the band gap of the sample. There are few studies where the photodegradation of pollutants using porous/activated spherical carbons are reported. The photo-induced activity of the synthesized samples is discussed in this chapter. The samples were selected for these studies based on their adsorption results.

8.2 Selection of samples

On the basis of the results obtained for adsorption of various pollutants (discussed in chapter 4-7), selection of samples was done for the irradiation studies. From HTC synthesized samples, ***GS1*** sample was concluded to be the best sample for adsorption. Further from thermal and chemical activation of ***GS1*** sample, ***GS-Ar, GSK2*** and ***GSZ2*** samples were found to be better among other samples, respectively. From the pyrolysis of soy flour, the best sample for adsorption was ***SBc750-NA***. So, these 5 samples were selected to test their photo-induced activity, if any.

8.3 Photo-induced decolorization studies

8.3.1 *GS1* sample

GS1 sample was tested for pollutants *viz.* MB, EBT, PNP, CIP and DEP, under UV irradiation, and sunlight and the results are shown in Fig. 8.1(a). The data clearly showed that the % decolorization of MB and EBT dyes is enhanced under sunlight and UV irradiation in comparison with that for dark than other pollutants. The enhancement was maximum for sunlight containing mixture of UV and visible light having higher intensity (~17500 lx) as compared to UV lamp (~14000 lx). The further photo-induced activity studies have been undertaken only for UV irradiation (λ<400 nm). To test the recyclability of the sample under UV irradiation, it was tested for 5 consecutive cycles for MB % decolorization under UV irradiation. The sample shows similar % decolorization in all cases without any decrement (Fig. 8.1 (b)). Hence, the sample is completely recyclable for use under UV irradiation.

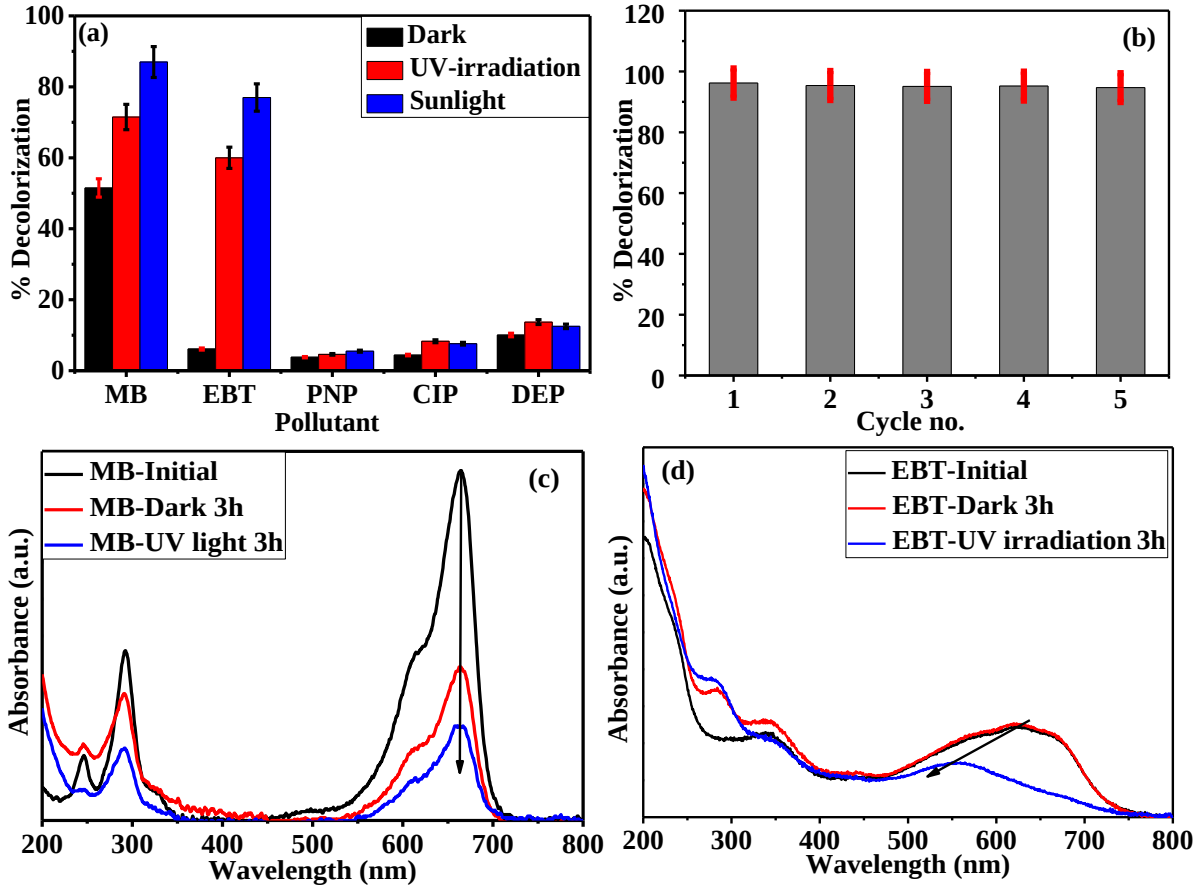

Fig. 8.1: Representing the % decolorization of (a) pollutants using ***GS1*** under dark, UV irradiation and sunlight (b) recyclability of ***GS1*** under UV irradiation for MB dye, UV-Vis absorbance spectra of (c) MB and (d) EBT under UV irradiation and in dark.

Fig. 8.1 (c) and (d) show the comparison of the UV-Vis absorbance spectra for dark and UV irradiation after 3 hours for both dyes. The data clearly showed that even though there was a decrease in intensity but no new peaks emerged. This indicated that though the % decolorization is increasing but this photo-induced activity may not have resulted in any significant degradation of dyes. The enhancement in % decolorization is ~20% for MB whereas for EBT it is 53 % after 3 hours. The possible reason for the stark contrast in the behavior of the MB and EBT can be explained by the adsorption isotherm fitting data for the two systems. The Langmuir model fit for MB dye adsorption already indicated a strong interaction between ***GS1*** sample and dye (section 4.5.5, chapter 4). Whereas for EBT, the % decolorization in dark is ~ 6.1 % and under irradiation, it is increasing manifolds indicating photo-induced enhancement of surface characteristics and hence adsorption.

The effect of concentration of the sample on % decolorization under UV irradiation was also studied for MB dye. From Fig. 8.2(a), it can be noted that with the increase in the sample concentration from 4 mg/L to 20 mg/L, % decolorization increases from 65 to 71.5% due to increased availability of surface sites.

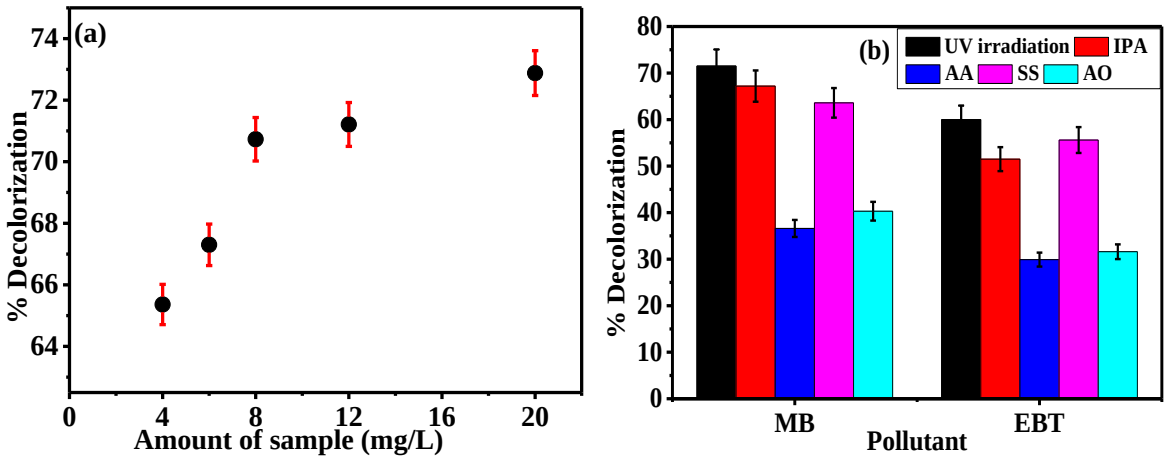

Fig. 8.2: (a) Variation in % decolorization of MB with increase in adsorbent amount and (b) % decolorization of MB and EBT (1 mg/L) for ***GS1*** sample (20 mg/L) under UV irradiation with and without scavengers after 3 hours.

The mechanism of enhanced photo-induced activity under UV irradiation was explained using a combination of scavenger tests and valence band spectra. In this process, 0.5 mM each of isopropyl alcohol (IPA) ascorbic acid (AA), ammonium oxalate (AO), sodium sulphate (SS), were taken as scavenging agents respectively for hydroxyl free radical ($^{\cdot}OH$), superoxide free radical anion ($O_2^{\cdot -}$), holes (h^+), and electrons (e^-). The % decolorization of MB and EBT in the presence of all the scavengers and without any scavenger under UV irradiation is shown in Fig. 8.2(b).

The retardation in the % photo-induced activity of MB using IPA AA, SS, and AO, were ~6%, 49%, 11%, and 44%, respectively. The retardation in the % photo-induced activity of EBT using IPA AA, SS, and AO, were nearly 14%, 52%, 7%, and 47%, respectively. It is clear from the results obtained that all the active species participated in the decolorization of MB and EBT but $O_2^{\cdot -}$and e^- were the predominant active species in the decolorization process while hydroxyl free radical and hole participated least. During the photo-induced activity process, the possible participation trend is: $O_2^{\cdot -} \sim e^- > h^+ \sim {}^{\cdot}OH$. The valence band spectra from the XPS data and band diagram obtained for the ***GS1*** sample in conjunction with the UV data are shown in Fig. 8.3(a). From VB spectra, the Valence Band Edge (VBE) is found to be lying at 0.5 eV. With the help of UV-Visible spectroscopy, the calculated band gap (E_g) of ***GS1*** is 4.5 eV. Hence, the value of conduction band edge (CBE) (Fig. 8.3(b).) came out to be -4 eV using formula:

$$\text{Bandgap} = |\text{CB-VB}| \qquad (8.1)$$

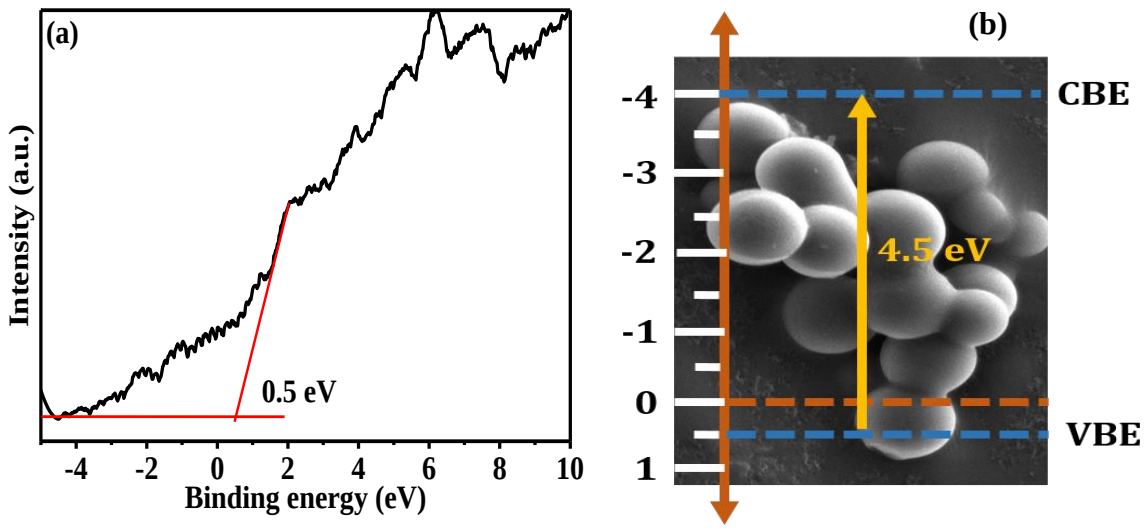

Fig. 8.3: (a) VB spectra and (b) band diagram for ***GS1*** sample.

The other pollutants showed negligible change in % decolorization under UV irradiation, so they were not tested further. The mechanism for the enhanced decolorization is discussed in section 8.4.

8.3.2 *GS-Ar* sample

The photo-induced activity studies were carried out with MB, EBT, PNP, CIP and DEP, under UV irradiation and sunlight for ***GS-Ar*** sample. The absorbance spectra of MB and EBT after 3 hours under dark and UV irradiation in the presence of ***GS-Ar*** sample are given in Fig. 8.4 (a) and (b), respectively. There was a clear shift in intensity but no new peaks emerged. The irradiation data for all the samples in comparison with dark is given in Fig. 8.4 (c). It was clear from the data that ***GS-Ar*** sample was not photoactive for PNP, CIP, and DEP. Therefore, further studies were carried out only for MB and EBT dye. The enhacement in % decolorization of MB and EBT obtained after 3 hours of exposure of UV irradiation were 62% and 14%, respectively. The adsorption isotherm fitting data for the two systems can be used to understand the potential cause of the major distinction in behaviour between the MB and EBT. A substantial interaction between the ***GS-Ar*** sample and EBT dye was evident from the Langmuir model fit for its adsorption (section 5.5.5, chapter 5). In contrast, for MB, the percentage of decolorization in the dark was only 20.4%, and when exposed to light, it multiplies, indicating photo-induced improvement of surface characteristics and consequently adsorption.

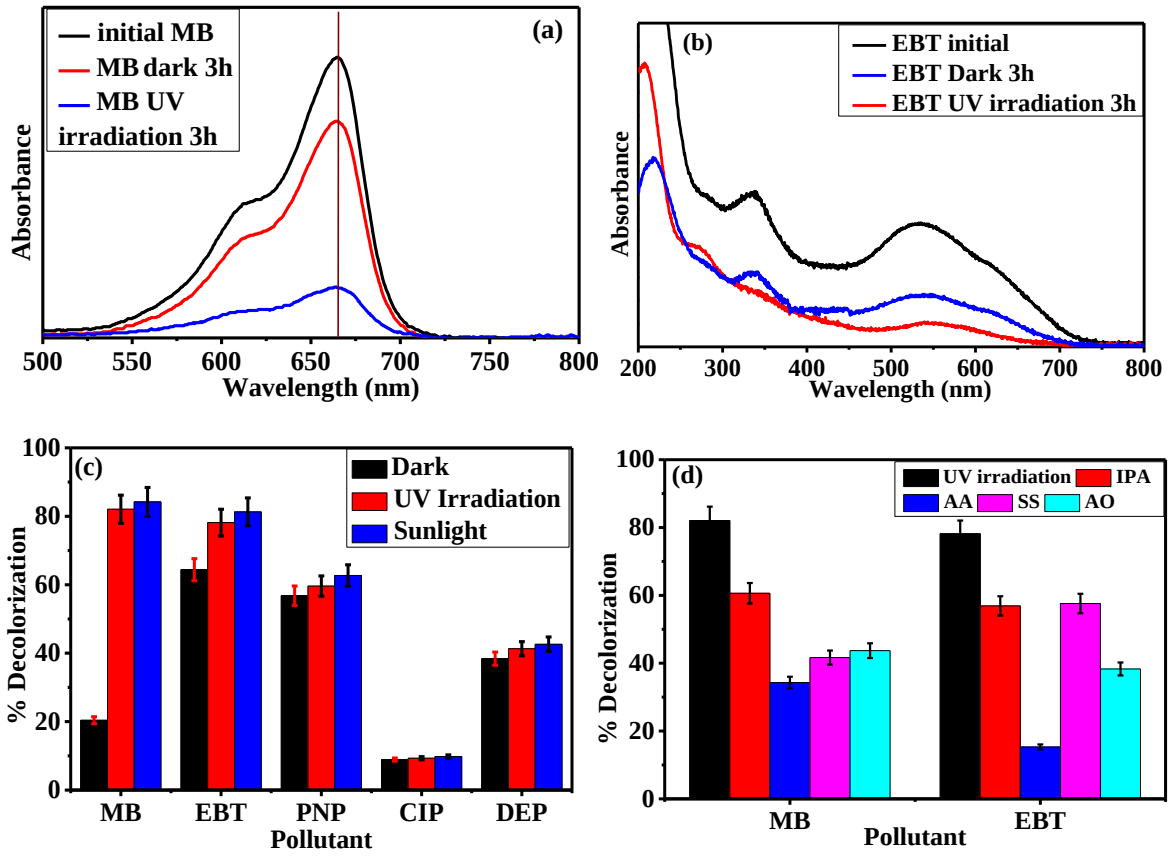

Fig. 8.4: Absorbance spectra of (a) MB and (b) EBT under UV irradiation, dark, using ***GS-Ar*** after 3 hours, % decolorization of (c) pollutants using ***GS-Ar*** sample under dark, UV irradiation and sunlight, and (d) MB, EBT using ***GS-Ar*** in presence of scavengers.

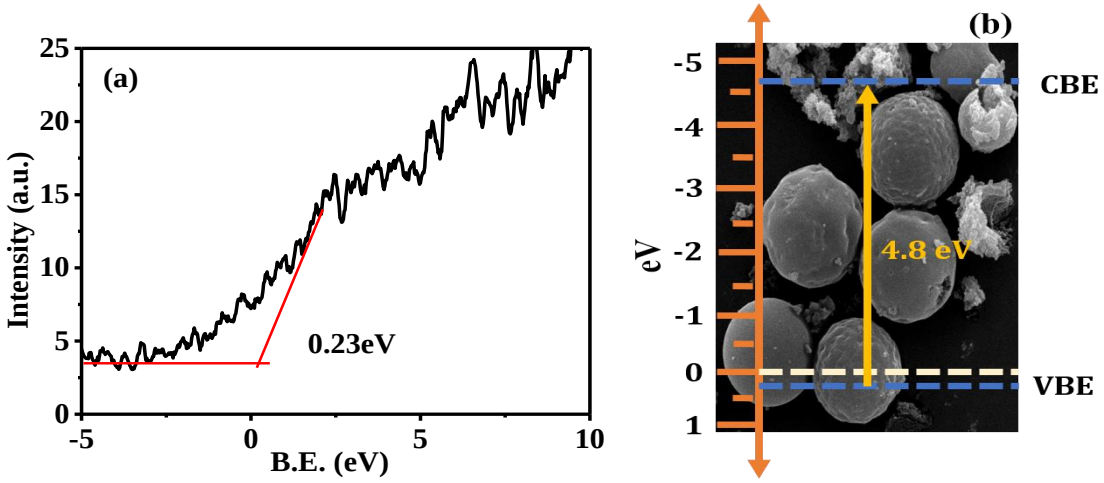

Fig. 8.5: (a) VB spectra and (b) band diagram of ***GS-Ar*** sample.

The results for the scavenger tests conducted for MB and EBT dyes are shown in Fig. 8.4(d). The retardation in the % photo-induced activity of MB using IPA AA, SS, and AO, were ~26%, 58%, 49%, and 47%, respectively. It is clear from the results obtained that all the active species participated in the decolorization of MB but $O_2^{\cdot -}$ was the predominant active

species in the decolorization process while hydroxyl free radical participated least. During the photo-induced decolorization process, the possible participation trend is: $O_2^{\cdot -} > e^- \sim h^+ > {}^{\cdot}OH$. The retardation in the % photo-induced activity of EBT using IPA, AA, SS, and AO, were ~27%, 80%, 26%, and 51%, respectively. The results clearly indicated that all the active species participated in the decolorization process but $O_2^{\cdot -}$was predominant active species for decolorization process followed by h^+, ${}^{\cdot}OH$ and e^-. For EBT dye, in presence of scavengers, the % decolorization was decreased below its adsorption efficiency in dark, strengthening the conjecture of photo-induced surface characteristics modification.

The band diagram of the ***GS-Ar*** sample was obtained using VB spectra (Fig. 8.5(a)) and UV-Visible spectra, as shown in Fig. 8.5(b). The position of VB was calculated to lie at 0.23 eV, and the position of CB was calculated at -4.57 eV.

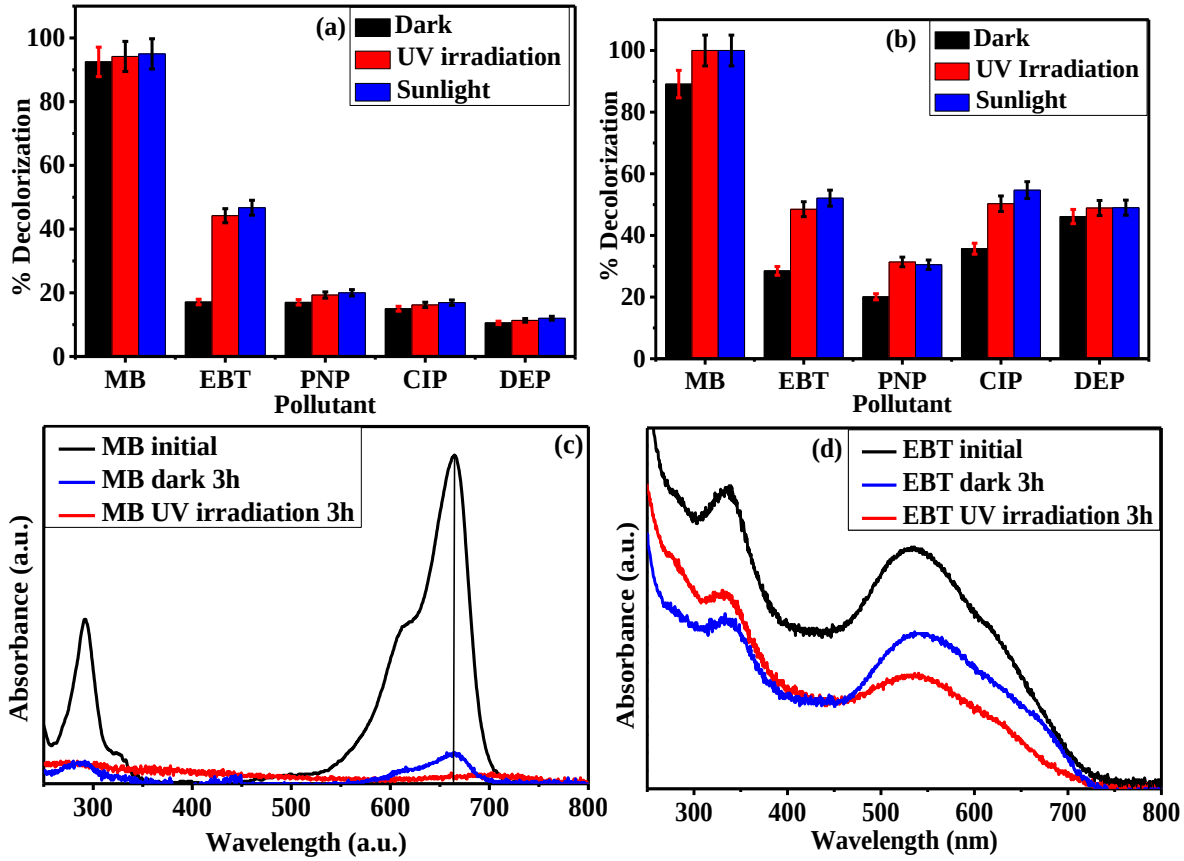

Fig. 8.6: % Decolorization of MB, EBT, PNP, CIP, and DEP in dark, UV irradiation and sunlight, using (a) ***GSK2*** and (b) ***GSZ2,*** absorbance spectra of (c) MB and (d) EBT under UV irradiation, dark, using ***GSZ2*** after 3 hours.

8.3.3 *GSK2* and *GSZ2* samples

For photo-induced activity study, ***GSK2*** and ***GSZ2*** samples were used for the pollutants including MB, EBT, PNP, CIP and DEP. Fig. 8.6(a) and 8.6(b) show the % decolorization of pollutants under dark, UV irradiation and sunlight using ***GSK2*** and ***GSZ2*** samples, respectively. It can be observed that ***GSK2*** sample showed enhanced decolorization under UV irradiation and sunlight for MB and EBT dyes. In case of PNP, CIP and DEP, no significant variation in the decolorization was observed under UV irradiation and sunlight. The change in % decolorization for MB and EBT using ***GSK2*** sample were 2% and 27%, respectively. The Langmuir model fit for MB dye adsorption showed that the ***GSK2*** sample and dye had a significant interaction (section 6.4.5, chapter 6). The percentage of decolorization for EBT, in comparison, is only 17.1% in the dark, and it increases when exposed to light, demonstrating the photo-induced enhancement of surface properties and thus adsorption. In the case of ***GSZ2*** sample, the decolorization was observed to be enhanced under UV irradiation and sunlight for MB, EBT, PNP, and CIP. The % adsorption under sunlight observed were nearly same as under UV irradiation indicating more dominating role of UV irradiation. For the ***GSZ2*** sample, the change in % decolorization for MB, EBT, PNP and CIP were ~11%, 20%, 11% and 15%, respectively. The Langmuir model fit for all the pollutants during adsorption showed that the ***GSZ2*** sample and pollutants had a significant interaction and therefore, the photo enhancement occurred was small but not insignificant (section 6.4.5, chapter 6). The UV visible absorbance spectra for MB and EBT under dark and UV irradiation using ***GSZ2*** sample are shown in Fig. 8.6 (c) and (d), respectively. Under UV irradiation for 3 hours, the initial peak diminished and no new peak emerged indicating that enhanced photo-induced adsorption rather than degradation occurred.

Fig. 8.7(a) shows the % decolorization of MB, EBT under UV irradiation and in presence of scavengers using ***GSK2*** samples. From scavenger tests, the retardation in the % photo-induced activity of MB using IPA AA, SS, and AO, were nearly 5.6%, 37.7%, 16.6%, and 24.7%, respectively. The following is a possible participation pattern throughout the photo-induced activity: $O_2^{\cdot -} > h^+ \sim e^- > {}^{\cdot}OH$. The retardation in the % photo-induced activity of EBT using IPA AA, SS, and AO, were 3.5%, 21.3%, 14.7%, and 11.6%, respectively. The possible participation pattern throughout the photo-induced activity is: $O_2^{\cdot -} > e^- \sim h^+ > {}^{\cdot}OH$. Data show that $O_2^{\cdot -}$ was the most participating active species and that ${}^{\cdot}OH$ was the least participating during the decolorization process of MB and EBT using ***GSK2*** sample. For MB dye using ***GSK2*** sample, in presence of scavengers, the % decolorization was decreased below its

adsorption efficiency in dark, strengthening the conjecture of photo-induced surface characteristics modification.

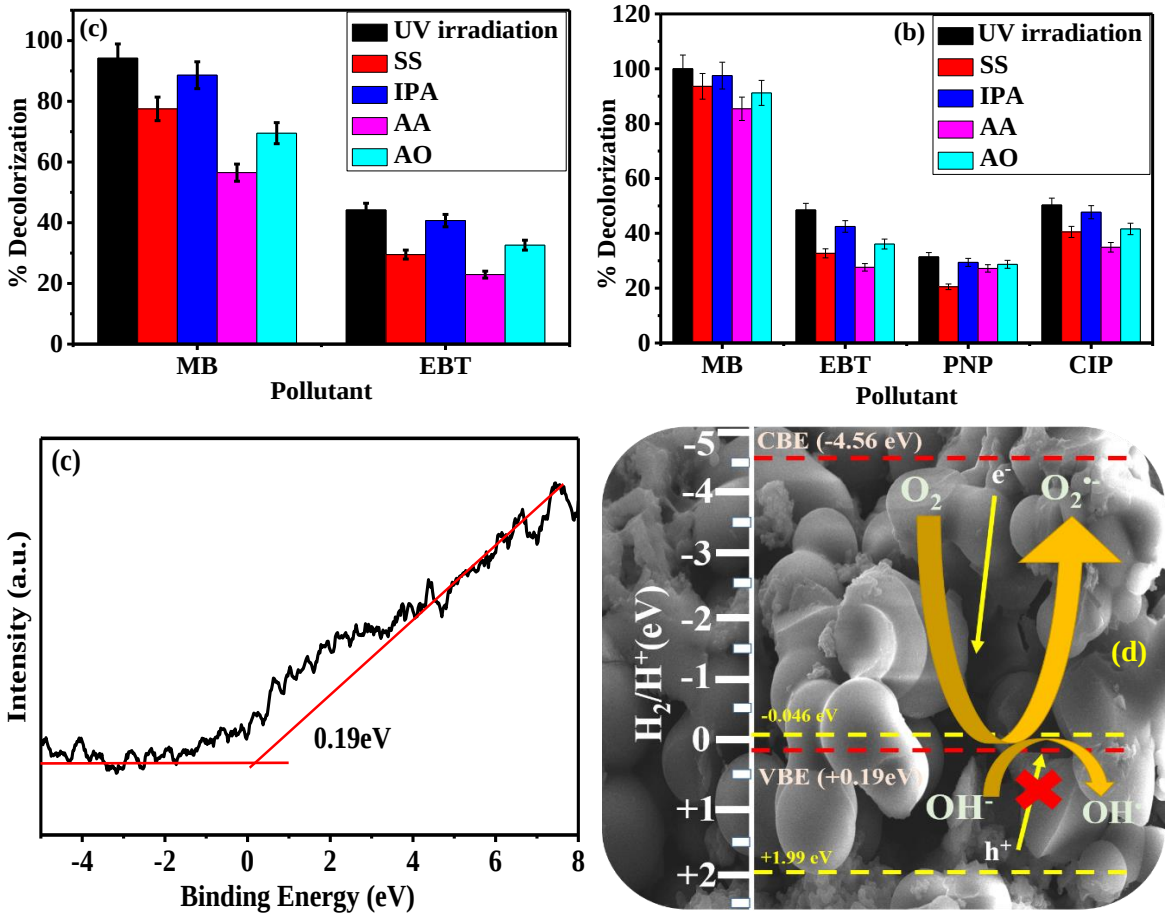

Fig. 8.7: % Decolorization of **(**a) MB, EBT using ***GSK2*** and (b) MB, EBT, PNP and CIP using ***GSZ2*** in presence of scavengers (c) VB spectra of ***GSZ2*** sample and (d) photo-induced decolorization mechanism of pollutants using ***GSZ2*** sample.

In case of ***GSZ2*** sample, Fig. 8.7(b) shows the % decolorization of MB, EBT, PNP and CIP under UV irradiation and in presence of scavengers. For MB dye, using IPA AA, SS, and AO, the % photo-induced activity was retarded by almost 2.5 %, 14.6 %, 6.4 %, and 8.8 %, respectively. The results show that while all active species contribute in the decolorization of MB, $O_2^{\cdot-}$ was the most prevalent active species in the decolorization process, while the hydroxyl free radical played the least important role. The following is a possible participation pattern throughout the photo-induced activity: $O_2^{\cdot-} > h^+ \sim e^- > {}^{\cdot}OH$. In the case of EBT dye, the % photo-induced activity was retarded by ~12%, 48%, 32%, and 25%, using IPA AA, SS, and AO, respectively. The results show that $O_2^{\cdot-}$ was the most prevalent active species and ${}^{\cdot}OH$ was least prevalent in the decolorization process. The following is a possible participation pattern throughout the photo-induced activity: $O_2^{\cdot-} > e^- > h^+ > {}^{\cdot}OH$. For PNP, the retardation in % decolorization was ~6, 13%, 34% and 8%, using IPA AA, SS, and AO, respectively. The

results showed that e^- participated most actively and $^{\cdot}OH$ participated least in the photo-induced activity and followed the trend: $e^- > h^+ \sim O_2^{\cdot -} > {}^{\cdot}OH$. IPA, AA, SS, and AO retarded the % photo-induced activity of CIP by almost 5.1 %, 30.6 %, 19.5%, and 17.3 %, respectively. The data demonstrate that $O_2^{\cdot -}$ was the most prevalent active species and $^{\cdot}OH$ was the least prevalent in the decolorization process. During the photo-induced activity, $O_2^{\cdot -} > e^- > h^+ > {}^{\cdot}OH$ is a possible participation pattern.

The VB spectra of ***GSZ2*** sample is shown in Fig. 8.7 (c). The position of VB edge was obtained at 0.19 eV, and the position of CB edge was obtained at -4.56 eV using band gap and VB spectra. The band diagram for ***GSZ2*** sample is shown in Fig. 8.7 (d).

Combination of scavenger tests and UV spectra clearly indicated that for all the synthesized samples, the photo-induced activity is the result of change in surface adsorption characteristics due to $O_2^{\cdot -}$ formation.

8.3.4 *SBc750-NA* sample

The photo-induced activity study using ***SBc750-NA*** sample for the pollutants including MB, EBT, PNP, CIP and DEP. The sample showed no significant variation in the % decolorization of pollutants under UV irradiation and sunlight as compared to dark. Therefore, further, photo induced decolorization studies were not carried out for this sample.

8.4 Mechanism of photo-induced activity

For all the four samples *viz.* ***GS1***, ***GS-Ar, GSK2*** and ***GSZ2***, the positioning of the CB edge has a higher negative value than the usual O_2/O_2^- redox potential (0.046 eV vs NHE), which aids in the reduction of dissolved O_2 in H_2O to create $O_2^{\cdot -}$. The VB edge of the $OH^-/{}^{\cdot}OH$ (+1.99 eV vs NHE) is greater than the VB edge of the samples. As a result, oxidation of OH^- to produce $^{\cdot}OH$ was prohibited [266,267]. The results were consistent with the scavenger tests for all the samples. The scavenger test results showed that $O_2^{\cdot -}$was maximum while OH^- was least responsible for the enhanced photoactivation of the synthesized samples. When the light of suitable energy (energy above the bandgap) falls on the sample surface, electron-hole pair is generated. These e^- react with the dissolved oxygen molecule (O_2) in water to form $O_2^{\cdot -}$ and the h^+ in the valence band react with the water to produce $^{\cdot}OH$ (limited in our samples). Presence of these ions may be responsible for modifying the adsorbate surface chemistry leading to enhanced adsorption and hence % decolorization.

The proposed mechanism for various pollutants based on the scavenger tests and VB spectra is shown in Fig. 8.8.

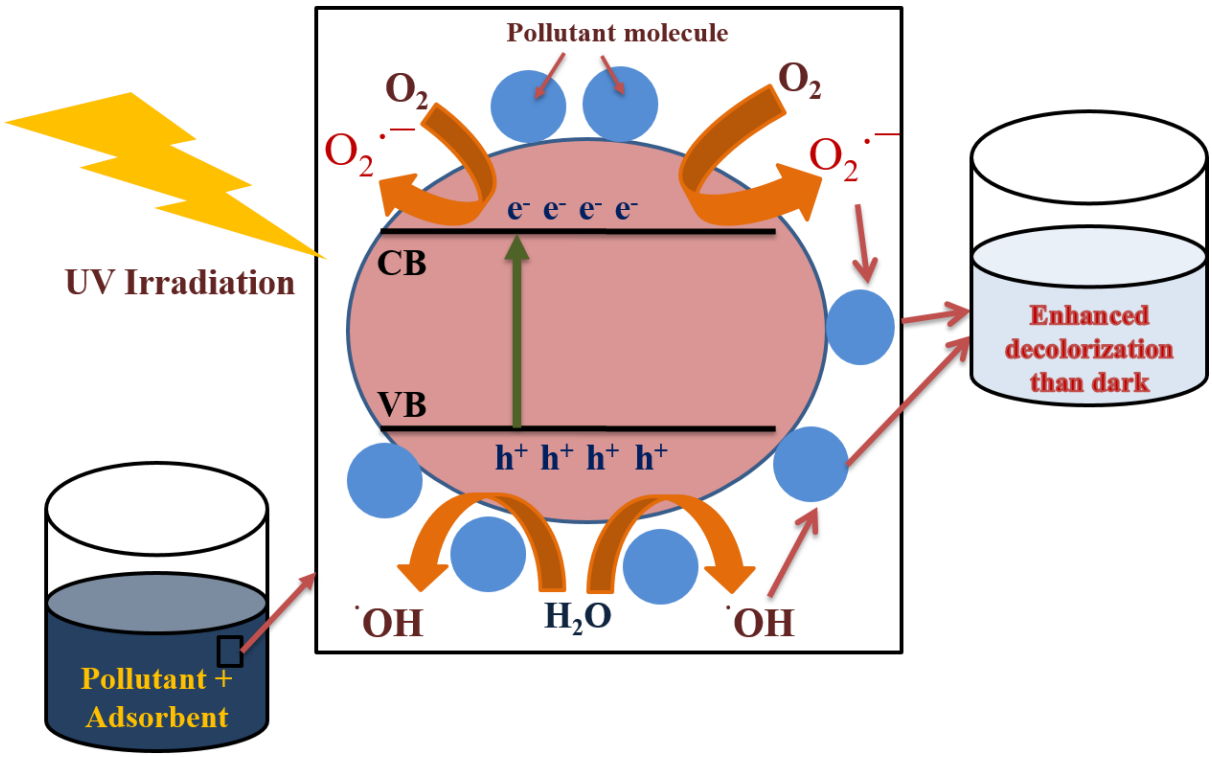

Fig. 8.8: Enhanced photo-induced decolorization mechanism of pollutants using ***GS1***, ***GS-Ar,*** ***GSK2*** and ***GSZ2*** sample.

Chapter 9

Conclusions and future scope

Overview

In this chapter, the conclusions obtained from the work undertaken for the synthesis of soy flour-based N doped carbons via the HTC method and their activation by thermal and chemical treatment, and also with the pyrolysis of soy flour, is discussed. The effect of N functionalities, surface area, and porosity on the adsorption and photo-induced activity of synthesized samples is also summarized. Suggestions for future work are also made based on the work accomplished.

9.1 Conclusions

N doped spherical carbons synthesized using a protein-containing bio/agro-based precursor via a green and low-cost approach with a high yield are believed to be strong candidates for treating wastewater containing various industrial contaminants such as dyes, phenols, pharmaceutical wastes, and plasticizers.

In the current work, N-doped high yield carbon spheroids were synthesized using agrowaste (soy flour) assisted by glucose via the simple HTC method (***GS1***). Further, the ***GS1*** sample was modified by thermal and chemical treatment to enhance the pollutant removal efficiency from the aqueous solution. During thermal treatment, ***GS1*** sample was heat-treated at 900 °C in carrier gases Ar or N_2 for 4 hours to test the effect of heating atmospheres on the properties of the resulting samples (***GS-Ar*** and ***GS-N***). For chemical treatment, low temperature and time (400 °C, 30 min.) chemical activation of ***GS1*** sample was carried out in closed muffle furnace using $ZnCl_2$ and KOH in varying ratios (the best samples: ***GSZ2*** and ***GSK2***). To compare the properties and efficiency of HTC synthesized samples with pyrolysis synthesized sample, pyrolysis of soy flour was carried out in a tube furnace under argon atmosphere at 450, 650, and 750 °C. The sample pyrolyzed at 750 °C ***SBc750*** sample was treated further with HNO_3 for demineralization (***SBc750-NA***). To understand the physicochemical properties of all the synthesized samples, characterization of all the samples was carried out using SEM, XRD, UV-Visible, XPS, FTIR, Raman, BET, Thermo gravimetric analysis, and pH_{pzc}. The samples synthesized were further used for adsorption and photo-induced decolorization (UV irradiation and sunlight) studies of MB, CV, EBT, PNP, CIP and DEP.

In this work, the HTC sphere (***GS1***) formation mechanism for protein-rich systems in the presence of the saccharides has been explained completely. Also, the activation mechanism for each activation route has also been delineated and discussed based on the characterization results.

- **Synthesis of HTC sample using soy flour and glucose**: The nucleation of the spheres starts with the derivatives of the glucose forming carbon quantum dots (CQDs). These CQDs are successively encapsulated by the N-doped graphene/graphene oxide platelets. The nitrogen and oxygen in the constituent platelets (formed from soy protein) ensures that the final structures formed are expanded/enlarged in morphology. This is especially useful for pollutant adsorbent application since these samples can be centrifuged out at low speeds at ambient temperature.

- **Thermal activation of HTC sample:** from thermal treatment of ***GS1*** the mechanism of pore formation in different atmospheres (N_2 and Ar) was explained in detail. High density and lower diffusivity of Ar led to the nucleation and explosion of volatile gases within the carbon spheres to form micropores of size > 1nm during heat treatment. TG/DSC/DTG study of the sample showed that the release of volatiles and graphitization occurred simultaneously in inert atmosphere and graphitization started earlier (345 °C) in Ar than N_2 (352 °C).
- **Chemical activation of HTC sample**: the chemical activation of ***GS1*** was carried at 400 °C for 30 min. in a closed air atmosphere. On the basis of activation parameters and available literature, it was proposed that activation of ***GS1*** with KOH results in the partial oxidation of the surface without the development of pores and surface area. While $ZnCl_2$ completely penetrated the ***GS1*** sample and restructured the morphology at given activation parameters. The proposed mechanisms were validated by N_2 adsorption-desorption isotherms, FTIR, and XPS results.
- **Pyrolysis of soy flour**: based on the TG/DTA/DTG results of soy flour under Ar atmosphere, the biomass sample was pyrolyzed in a tube furnace under argon atmosphere at 450, 650, and 750 °C. With pyrolysis in an inert atmosphere, the carbon in the soy flour did not entirely burn off, and available carbon reacted with existing elements to generate the ashes. Treatment of ***SBc750*** sample with HNO_3 results in complete removal of mineral content, the emergence of micropores, multifold increase in the surface area, higher oxidation of the surface, and lower pH_{pzc} (4.7).

The parameters that affected the adsorption of pollutants on the surface of synthesized samples were pH_{pzc}, N functionality, surface area, and pore size of the samples. Along with these parameters, the molecular size and surface charge of pollutants directly affected the interactions between adsorbate and adsorbent. The presence of various N type functionalities played a different role in the adsorption of different pollutants. The availability of pyrrolic-N and pyridinic-N makes the surface negative and help in the adsorption of positively charged pollutants. The modification of sample surface with temperature resulted in conversion to more stable graphitic-N functionality which makes the sample more positive and show enhanced adsorption for negatively charged pollutants. The sample with meanpore diameter equal to or greater than the molecular size of pollutant show enhanced adsorption for the particular pollutant. The variation in the adsorption efficiency with the pH variation of the adsorbate solution was thus explained on the basis of pH_{pzc} and the charge of the pollutants.

The comparison of the data obtained for the best samples synthesized using soy flour from various methods and treatments are given in Table 9.1.

Table 9.1: Comparative data of best samples obtained from soy flour by various methods.

Chapter and best sample		***Chapter4***	***Chapter5***	***Chapter6***		***Chapter7***
		GS1	***GS-Ar***	***GSK2***	***GSZ2***	***SBc750-NA***
Properties	**Nature of majority N**	Pyrrolic	Graphitic	Graphitic	Graphitic	Graphitic
	Band gap (eV)	4.50	4.80	4.80	4.70	4.80
	Surface area (m^2/g)	7.43	449.00	7.60	110.93	94.09
	Pore size (nm)	14.86	1.10	>10.00	0.81	0.76
	pH_{pzc}	4.60	8.80	7.20	8.00	4.70
q_e (mg/g)	**MB**	52.10	-	70.84	62.09	51.11
	EBT	31.50	25.37	60.44	54.03	54.30
	PNP	-	113.67	-	49.16	-
	CIP	-	-	-	84.10	-
	DEP	-	92.29	-	114.59	-
Kinetic model	**MB**	Elovich	-	PSO	PSO	PSO
	EBT	PFO	PSO	PSO	PSO	PSO
	PNP	-	PSO		PSO	-
	CIP	-	-	-	PSO	-
	DEP	-	PSO	-	PSO	-
Kinetic isotherm	**MB**	Langmuir	-	Langmuir	Langmuir	Freundlich
	EBT	Freundlich	Langmuir	Freundlich	Langmuir	Langmuir
	PNP	-	Freundlich	-	Langmuir	-
	CIP	-	-	-	Langmuir	-
	DEP	-	Langmuir	-	Langmuir	-
% Decolorization (Dark)	**MB**	51.50	20.40	-	89.10	-
	EBT	6.10	64.40	-	28.50	-
	PNP	-	-	-	20.10	-
	CIP	-	-	-	35.70	-
	DEP	-	-	-	46.13	-
% Decolorization (UV-irradiation)	**MB**	71.50	82.00	-	100.00	-
	EBT	60.00	78.10	-	48.5	-
	PNP	-	-	-	31.40	-
	CIP	-	-	-	50.30	-
	DEP	-	-	-	48.90	-
% Decolorization (Sunlight)	**MB**	87.00	84.20	-	100.00	-
	EBT	77.00	81.30	-	52.10	-
	PNP	-	-	-	30.50	-
	CIP	-	-	-	54.70	-
	DEP	-	-	-	49.00	-

From table, it was observed that ***GS-Ar***, ***GSZ2*** and ***SBc750-NA*** samples showed better adsorption efficiencies than ***GS1*** sample due to availabilities of graphitic-N, increased surface area and porosity. Despite having a low surface area and porosity, ***GSK2*** sample exhibited

increased dye adsorption due to availability of abundant oxygen containing surface functional groups. The presence of graphitic-N helped in the adsorption of pollutants via chemisorption and the adsorption process was found to follow PSO adsorption model. The adsorption of pollutants onto samples followed either Langmuir or Freundlich kinetic isotherm (Table 9.1). The ***GS1***, ***GS-Ar*** and ***GSZ2*** samples showed enhanced decolorization for pollutants in the presence of UV irradiation or sunlight. Based on the scavenger tests and VB spectra of sample, superoxide free radical anion ($O_2^{\cdot -}$) was found to play major role in the photo-induced decolorization process and mechanism was proposed.

In conclusion, comparing the availability and low cost of the precursors, followed by low temperature synthesis, high yield and ease of handling makes soy flour a very attractive candidate as a precursor for industrial pollutant removal adsorbents from aqueous solutions. The ***GS-Ar*** sample has emerged as a good candidate for wastewater treatment via adsorption and photo-induced decolorization. At least possible conditions for activation i.e. temperature, time and atmosphere, ***GSZ2*** sample showed enhanced results in terms of surface area, graphitic-N content and hence adsorption for variety of pollutants. While ***GSK2*** sample showed enhanced adsorption for dyes inspite of insignificant surface area. The sample synthesized using single step pyrolysis of soy flour to form N doped biochar (***SBc750***) showed better adsorption efficiency for all types of dyes despite its very low surface area (0.5 m^2/g). The ***SBc750-NA*** sample showed manifolds enhanced adsorption for the pollutants having molecular size equal to or below its meanpore diameter (0.8nm). When compared with the reports available in literature for similar materials, samples show enhanced adsorption properties. Further, the synthesized sample also shows photo-induced enhanced adsorption under UV irradiation and sunlight. Combination of scavenger tests and UV spectra clearly indicated that for all the synthesized samples, the photo-induced activity is the result of change in surface adsorption characteristics due to $O_2^{\cdot -}$ formation. This aspect of the synthesized samples opens new avenues and needs to be studied further to arrive at the mechanism of photo-induced decolorization.

9.2 Future scope

The present work reported the synthesis of high yield N doped carbon spheres using agro-based protein containing soy flour with cost-effective and green methods *viz.* HTC and pyrolysis method. Surface modification of HTC samples was done by thermal, and chemical activation. The samples showed good adsorption efficiencies for various pollutants. Some of the future possibilities are listed below:

- Role of saccharides in assisting other protein-containing biobased materials to form spherical N-doped carbons via HTC can be explored.
- Study the mechanism of pore formation during thermal treatment under gases such as ammonia, He, H_2, CO_2.
- The effect of other chemical activating agents (H_3PO_4, HCl, H_2SO_4, HNO_3, NaOH) on the porosity and surface area of carbon samples at low activation condition of temperature, time and atmosphere can be studied.
- Only a very few reports are available in literature showing the photodegradation efficiency of porous activated carbon after surface modification. The synthesized samples in the current work show photo-induced decolorization of pollutants under UV irradiation and sunlight. This aspect of the synthesized samples opens new avenues and needs to be studied further.

References

[1] M. of U. D. India, *Advisory on Conservation and Restoration of Water Bodies in Urban Areas* (2013).
[2] UN-Water, in *UN-Water Integrated Monitoring Initiative* (2021), pp. 1–58.
[3] In *Water Well Journal*, Vol. 56 (2021), p. 58.
[4] V. D. P. Hirani, in *World Economic Forum* (2019), pp. 1–13.
[5] X. Song, Y. Wang, K. Wang, and R. Xu, Ind. Eng. Chem. Res. **51**, 13438 (2012).
[6] J. Yin, M. Pei, Y. He, Y. Du, W. Guo, and L. Wang, RSC Adv. **5**, 89839 (2015).
[7] W. Konicki, K. Cendrowski, G. Bazarko, and E. Mijowska, Chem. Eng. Res. Des. **94**, 242 (2015).
[8] K. C. Bedin, A. C. Martins, A. L. Cazetta, O. Pezoti, and V. C. Almeida, Chem. Eng. J. **286**, 476 (2016).
[9] S. Kundu, I. H. Chowdhury, and M. K. Naskar, J. Chem. Eng. Data **63**, 559 (2018).
[10] J. C. Lazo-Cannata, A. Nieto-Márquez, A. Jacoby, A. L. Paredes-Doig, A. Romero, M. R. Sun-Kou, and J. L. Valverde, Sep. Purif. Technol. **80**, 217 (2011).
[11] A. Chen, Y. Li, Y. Yu, Y. Li, K. Xia, Y. Wang, S. Li, and L. Zhang, Carbon N. Y. **103**, 157 (2016).
[12] X. Song, P. Gunawan, R. Jiang, S. S. J. Leong, K. Wang, and R. Xu, J. Hazard. Mater. **194**, 162 (2011).
[13] J. Gong, T. Liu, X. Wang, X. Hu, and L. Zhang, Environ. Sci. Technol. **45**, 6181 (2011).
[14] A. K. Khambete, *Water Contamination and Pollution - A Growing Challenge for Health and Biodiversity* | (2021).
[15] P. R. Muduli, A. Kumar, V. V. Kanuri, D. R. Mishra, P. Acharya, R. Saha, M. K. Biswas, A. K. Vidyarthi, and A. Sudhakar, Int. J. Environ. Sci. Technol. **18**, 1645 (2021).
[16] M. Roy and F. Shamim, Int. J. Prev. Control Ind. Pollut. **6**, 1 (2020).
[17] J. Quach-Cu, B. Herrera-Lynch, C. Marciniak, S. Adams, A. Simmerman, and R. A. Reinke, Water **10**, 13 (2018).
[18] J. S. Jayalekshmi S J, Minnu Biju and D. S. Ajas, P E Muhammad, Int. J. Eng. Res. Technol. **1**, 3 (2021).
[19] M. Zhu, L. Lee, H. Wang, and Z. Wang, J. Hazard. Mater. **149**, 735 (2007).
[20] M. F. Abid, M. A. Zablouk, and A. M. Abid-Alameer, J. Environ. Heal. Sci. Eng. **9**, 1 (2012).
[21] C. Y. Teh, P. M. Budiman, K. P. Y. Shak, and T. Y. Wu, Ind. Eng. Chem. Res. **55**, 4363 (2016).
[22] S. Banerjee, G. C. Sharma, R. K. Gautam, M. C. Chattopadhyaya, S. N. Upadhyay, and Y. C. Sharma, J. Mol. Liq. **213**, 162 (2016).
[23] S. Atchariyawut, J. Phattaranawik, T. Leiknes, and R. Jiraratananon, Sep. Purif. Technol. **66**, 153 (2009).
[24] A. G. Vlyssides, M. Loizidou, P. K. Karlis, A. A. Zorpas, and D. Papaioannou, J. Hazard. Mater. **B70**, 41 (1999).
[25] Y. Qu, S. Shi, F. Ma, and B. Yan, Bioresour. Technol. **101**, 8016 (2010).
[26] M. Nageeb, in *Organic Pollutants - Monitoring, Risk and Treatment* (2013).
[27] H. Zhao, G. Zhang, and Q. Zhang, Ultrason. Sonochem. **21**, 991 (2014).
[28] R. Rashid, I. Shafiq, P. Akhter, M. J. Iqbal, and M. Hussain, Environ. Sci. Pollut. Res. **28**, 9050 (2021).
[29] A. Jain, R. Balasubramanian, and M. P. Srinivasan, Chem. Eng. J. **273**, 622 (2015).
[30] H. Li, Z. Sun, L. Zhang, Y. Tian, G. Cui, and S. Yan, Colloids Surfaces A Physicochem. Eng. Asp. **489**, 191 (2016).
[31] H. Li, N. An, G. Liu, J. Li, N. Liu, M. Jia, W. Zhang, and X. Yuan, J. Colloid Interface Sci. **466**, 343 (2016).
[32] X. Wang, H. Pan, Q. Lin, H. Wu, S. Jia, and Y. Shi, Nanoscale Res. Lett. **14**, (2019).
[33] S. Koner, A. Pal, and A. Adak, Desalination **276**, 142 (2011).
[34] S. Rangabhashiyam, N. Anu, and N. Selvaraju, J. Environ. Chem. Eng. **1**, 629 (2013).
[35] R. Guillossou, J. Le Roux, R. Mailler, E. Vulliet, C. Morlay, F. Nauleau, J. Gasperi, and V. Rocher, Chemosphere **218**, 1050 (2019).
[36] R. R. L. Vidal and J. S. Moraes, Int. J. Environ. Sci. Technol. **16**, 1741 (2019).
[37] E. Zanin, J. Scapinello, M. de Oliveira, C. L. Rambo, F. Franscescon, L. Freitas, J. M. M. de Mello, M. A. Fiori, J. V. Oliveira, and J. Dal Magro, Process Saf. Environ. Prot. **105**, 194 (2017).
[38] S. Barakan and V. Aghazadeh, Environ. Sci. Pollut. Res. **28**, 2572 (2021).
[39] M. Ahmaruzzaman, Adv. Colloid Interface Sci. **166**, 36 (2011).
[40] E. Laiq, S. Jabin, and P. Gupta, Orient. J. Chem. **37**, 868 (2021).
[41] G. Crini, E. Lichtfouse, L. D. Wilson, and N. Morin-Crini, Environ. Chem. Lett. **17**, 195 (2019).
[42] S. Nethaji, A. Sivasamy, and A. B. Mandal, Int. J. Environ. Sci. Technol. **10**, 231 (2013).
[43] R. Baccar, M. Sarrà, J. Bouzid, M. Feki, and P. Blánquez, Chem. Eng. J. **211**–**212**, 310 (2012).
[44] M. M. Abdel daiem, J. Rivera-Utrilla, M. Sánchez-Polo, and R. Ocampo-Pérez, Sci. Total Environ. **537**, 335 (2015).

[45] M. Kobya, E. Demirbas, E. Senturk, and M. Ince, Bioresour. Technol. **96**, 1518 (2005).
[46] N. Mojoudi, N. Mirghaffari, M. Soleimani, H. Shariatmadari, C. Belver, and J. Bedia, Sci. Rep. **9**, 1 (2019).
[47] D. Liu, W. Gu, L. Zhou, L. Wang, J. Zhang, Y. Liu, and J. Lei, Chem. Eng. J. **427**, 131503 (2022).
[48] M. Hao, M. Qiu, H. Yang, B. Hu, and X. Wang, Sci. Total Environ. **760**, 143333 (2021).
[49] A. Ahmad, D. Jini, M. Aravind, C. Parvathiraja, R. Ali, M. Z. Kiyani, and A. Alothman, Arab. J. Chem. **13**, 8717 (2020).
[50] I. Velo-Gala, J. J. López-Peñalver, M. Sánchez-Polo, and J. Rivera-Utrilla, Appl. Catal. B Environ. **142**–**143**, 694 (2013).
[51] I. Velo-Gala, J. J. López-Peñalver, M. Sánchez-Polo, and J. Rivera-Utrilla, Appl. Catal. B Environ. **207**, 412 (2017).
[52] M. Minale, Z. Gu, A. Guadie, D. M. Kabtamu, Y. Li, and X. Wang, J. Environ. Manage. **276**, 111310 (2020).
[53] A. K. Dutta, U. K. Ghorai, K. K. Chattopadhyay, and D. Banerjee, Phys. E Low-Dimensional Syst. Nanostructures **99**, 6 (2018).
[54] T. Xu, H. Ji, Y. Gu, T. Tong, Y. Xia, L. Zhang, and D. Zhao, Chem. Eng. J. **388**, (2020).
[55] G. Rekha Krishnan, K. Prabhakaran, and B. K. George, Microporous Mesoporous Mater. **315**, 110892 (2021).
[56] S. He, Q. Chen, G. Chen, G. Shi, C. Ruan, M. Feng, Y. Ma, X. Jin, X. Liu, C. Du, C. He, H. Dai, and C. Cao, Microporous Mesoporous Mater. **335**, 111848 (2022).
[57] K. C. Bedin, A. L. Cazetta, I. P. A. F. Souza, L. Spessato, T. Zhang, R. A. Araújo, R. Silva, T. Asefa, and V. C. Almeida, J. Environ. Chem. Eng. **10**, (2022).
[58] H. Chen, F. Sun, J. Wang, W. Li, W. Qiao, L. Ling, and D. Long, J. Phys. Chem. C **117**, 8318 (2013).
[59] M. Wang, J. Fu, J. Zhu, Y. Yan, and Q. Xu, RSC Adv. **5**, 28080 (2015).
[60] N. Kasera, P. Kolar, and S. G. Hall, Biochar **4**, (2022).
[61] F. Lian, G. Cui, Z. Liu, L. Duo, G. Zhang, and B. Xing, J. Environ. Manage. **176**, 61 (2016).
[62] L. Wang, W. Yan, C. He, H. Wen, Z. Cai, Z. Wang, Z. Chen, and W. Liu, Appl. Surf. Sci. **433**, 222 (2018).
[63] Sánchez-Sánchez, F. Suárez-García, A. Martínez-Alonso, and J. M. D. Tascón, J. Colloid Interface Sci. **450**, 91 (2015).
[64] A. Ekramipooya, F. M. Valadi, M. Latifi Pour, D. Rashtchian, and M. R. Gholami, Energy and Fuels **35**, 15918 (2021).
[65] Y. Liang, G. Huang, Q. Zhang, Y. Yang, J. Zhou, and J. Cai, J. Mol. Liq. **330**, 115580 (2021).
[66] G. Yang, H. Chen, H. Qin, and Y. Feng, Appl. Surf. Sci. **293**, 299 (2014).
[67] E. Lorenc-Grabowska, G. Gryglewicz, and J. Machnikowski, Appl. Surf. Sci. **256**, 4480 (2010).
[68] X. Niu, C. Liu, L. Li, X. Han, C. Chang, P. Li, and J. Chen, Water Sci. Technol. **85**, 2964 (2022).
[69] M. S. Khosrowshahi, M. A. Abdol, H. Mashhadimoslem, E. Khakpour, H. B. M. Emrooz, S. Sadeghzadeh, and A. Ghaemi, Sci. Rep. **12**, 1 (2022).
[70] Z. Zhang, L. Yu, Y. Tu, R. Chen, L. Wu, J. Zhu, and D. Deng, Cell Reports Phys. Sci. **1**, 100145 (2020).
[71] R. Balog, M. Manilo, L. Vanyorek, Z. Csoma, and S. Barany, RSC Adv. **10**, 3184 (2020).
[72] L. Vanyorek, G. Muránszky, B. Fiser, E. Sikora, Z. G. Hutkai, and B. Viskolcz, J. Dispers. Sci. Technol. **41**, 1879 (2020).
[73] D. Saha and M. J. Kienbaum, Microporous Mesoporous Mater. **287**, 29 (2019).
[74] X. Liu, X. Li, J. Yu, and Y. Sun, Mater. Lett. **223**, 203 (2018).
[75] X. Chen, K. Kierzek, Z. Jiang, H. Chen, T. Tang, M. Wojtoniszak, R. J. Kalenczuk, P. K. Chu, and E. Borowiak-palen, J. Phys. Chem. C 17717 (2011).
[76] A. Chen, Y. Li, L. Liu, Y. Yu, K. Xia, Y. Wang, and S. Li, Appl. Surf. Sci. **393**, 151 (2017).
[77] H. Kristianto, C. D. Putra, A. A. Arie, M. Halim, and J. K. Lee, Procedia Chem. **16**, 328 (2015).
[78] M. Mahajan, G. Singla, K. Singh, and O. P. Pandey, J. Solid State Chem. **232**, 108 (2015).
[79] S. Liu, X. Wang, H. Zhao, and W. Cai, Colloids Surfaces A Physicochem. Eng. Asp. **484**, 386 (2015).
[80] M. P. Maniscalco, M. Volpe, and A. Messineo, Energies **13**, (2020).
[81] S. A. Nicolae, H. Au, P. Modugno, H. Luo, A. E. Szego, M. Qiao, L. Li, W. Yin, H. J. Heeres, N. Berge, and M. M. Titirici, Green Chem. **22**, 4747 (2020).
[82] W. Zhang, Z. Ren, Z. Ying, X. Liu, and H. Wan, J. Alloys Compd. **743**, 44 (2018).
[83] T. Zhou, R. Ma, Y. Zhou, R. Xing, Q. Liu, Y. Zhu, and J. Wang, Microporous Mesoporous Mater. **261**, 88 (2018).
[84] K. Xiang, S. Cai, X. Wang, M. Chen, and S. Jiang, J. Alloys Compd. **740**, 687 (2018).
[85] H. W. Zhang, J. M. Lu, L. Yang, M. X. Hu, Z. H. Huang, R. T. Lu, and F. Y. Kang, New Carbon Mater. **32**, 517 (2017).
[86] J. Hou, J. Li, J. Sun, S. Ai, and M. Wang, RSC Adv. **4**, 37342 (2014).

[87] W. Li, Z. Zhang, B. Kong, S. Feng, J. Wang, L. Wang, J. Yang, F. Zhang, P. Wu, and D. Zhao, Angew. Chemie - Int. Ed. **52**, 8151 (2013).
[88] Z. Li, Z. Xu, H. Wang, J. Ding, B. Zahiri, C. M. B. Holt, X. Tan, and D. Mitlin, Energy Environ. Sci. **7**, 1708 (2014).
[89] L. Leng, L. Yang, S. Leng, W. Zhang, Y. Zhou, H. Peng, H. Li, Y. Hu, S. Jiang, and H. Li, Sci. Total Environ. **756**, 143679 (2021).
[90] H. Ma, C. Li, M. Zhang, J. D. Hong, and G. Shi, J. Mater. Chem. A **5**, 17040 (2017).
[91] S. M. Alatalo, K. Qiu, K. Preuss, A. Marinovic, M. Sevilla, M. Sillanpää, X. Guo, and M. M. Titirici, Carbon N. Y. **96**, 622 (2016).
[92] C. Falco, M. Sevilla, R. J. White, R. Rothe, and M. M. Titirici, ChemSusChem **5**, 1834 (2012).
[93] M. Ren, T. Zhang, Y. Wang, Z. Jia, and J. Cai, J. Mater. Sci. **54**, 1606 (2019).
[94] X. Zhang, Y. Xu, G. Zhang, C. Wu, J. Liu, and Y. Lv, Int. J. Hydrogen Energy 1 (2022).
[95] Z. Shen, Y. Liu, Y. Han, Y. Qin, J. Li, P. Xing, and B. Jiang, RSC Adv. **10**, 14556 (2020).
[96] J. Tang, Z. Guo, X. Kong, S. I. Wong, N. H. Wong, J. Sunarso, W. Xing, J. Zhou, Y. Zhao, and S. Zhuo, Mater. Chem. Phys. **284**, 126055 (2022).
[97] H. Zhao, B. Xing, C. Zhang, G. Huang, Q. Liu, G. Yi, J. Jia, M. Ma, Z. Chen, and C. Zhang, J. Alloys Compd. **766**, 705 (2018).
[98] Y. Ding, Y. Li, L. Wang, X. Han, L. Zhu, and S. Wang, Fuel **304**, 121449 (2021).
[99] J. Yu, X. Li, Z. Cui, D. Chen, X. Pang, Q. Zhang, F. Shao, H. Dong, L. Yu, and L. Dong, Renew. Energy **163**, 375 (2021).
[100] G. A. Ferrero, A. B. Fuertes, and M. Sevilla, Sci. Rep. **5**, 1 (2015).
[101] S. Xu, J. Chen, H. Peng, S. Leng, H. Li, W. Qu, Y. Hu, H. Li, S. Jiang, W. Zhou, and L. Leng, Fuel **291**, 120128 (2021).
[102] A. Tomczyk, Z. Sokołowska, and P. Boguta, Rev. Environ. Sci. Biotechnol. **19**, 191 (2020).
[103] I. Hussain, Y. Li, J. Qi, J. Li, and L. Wang, J. Environ. Manage. **215**, 123 (2018).
[104] S. Kundu, I. H. Chowdhury, and M. K. Naskar, ACS Omega **3**, 9888 (2018).
[105] M. Wortmann, W. Keil, B. Brockhagen, J. Biedinger, M. Westphal, C. Weinberger, E. Diestelhorst, W. Hachmann, Y. Zhao, M. Tiemann, G. Reiss, B. Hüsgen, C. Schmidt, K. Sattler, and N. Frese, J. Anal. Appl. Pyrolysis **161**, 105404 (2022).
[106] B. R. Patra, A. Mukherjee, S. Nanda, and A. K. Dalai, Environ. Chem. Lett. **19**, 2237 (2021).
[107] D. Bergna, T. Varila, H. Romar, and U. Lassi, J. Carbon Res. **4**, 41 (2018).
[108] E. Yagmur, Y. Gokce, S. Tekin, N. I. Semerci, and Z. Aktas, Fuel **267**, 117232 (2020).
[109] Y. Ma, Waste and Biomass Valorization **8**, 549 (2017).
[110] A. Ahmadpour and D. D. Do, Carbon N. Y. **34**, 471 (1996).
[111] A. A. Babaei, S. N. Alavi, M. Akbarifar, K. Ahmadi, A. Ramazanpour Esfahani, and B. Kakavandi, Desalin. Water Treat. **57**, 27199 (2016).
[112] S. Charola, R. Yadav, P. Das, and S. Maiti, Sustain. Environ. Res. **28**, 298 (2018).
[113] K. Gupta, D. Gupta, and O. P. Khatri, Appl. Surf. Sci. **476**, 647 (2019).
[114] E. E. Jasper, V. O. Ajibola, and J. C. Onwuka, Appl. Water Sci. **10**, 1 (2020).
[115] S. Zhu, J. Xu, Y. Kuang, Z. Cheng, Q. Wu, J. Xie, B. Wang, W. Gao, J. Zeng, J. Li, and K. Chen, Ind. Crops Prod. **159**, 113071 (2021).
[116] H. K. Yağmur and İ. Kaya, J. Mol. Struct. **1232**, (2021).
[117] K. Maheshwari, M. Agarwal, and A. B. Gupta, Chem. Pap. **76**, 3119 (2022).
[118] A. Koli, A. K. Battu, R. Kishan, and M. Sandip, Biomass Convers. Biorefinery **93**, (2022).
[119] M. Ahmaruzzaman and S. L. Gayatri, J. Chem. Eng. Data **55**, 4614 (2010).
[120] Z. Zhang, X. Feng, X. X. Yue, F. Q. An, W. X. Zhou, J. F. Gao, T. P. Hu, and C. C. Wei, Korean J. Chem. Eng. **32**, 1564 (2015).
[121] H. Chen, Y. Zhang, J. Li, P. Zhang, and N. Liu, Environ. Sci. Pollut. Res. 15300 (2019).
[122] H. Ma, Z. Xu, W. Wang, X. Gao, and H. Ma, RSC Adv. **9**, 39282 (2019).
[123] S. Hadi, E. Taheri, M. M. Amin, A. Fatehizadeh, and T. M. Aminabhavi, Chemosphere **270**, 128623 (2021).
[124] L. Liu, G. Deng, and X. Shi, Sci. Rep. **10**, 1 (2020).
[125] M. Hosseini Talari, N. S. Tabrizi, V. Babaeipour, and F. Halek, J. Sol-Gel Sci. Technol. **101**, 345 (2022).
[126] Y. X. Wang, H. H. Ngo, and W. S. Guo, Sci. Total Environ. **533**, 32 (2015).
[127] J. G. Shang, X. R. Kong, L. L. He, W. H. Li, and Q. J. H. Liao, Int. J. Environ. Sci. Technol. **13**, 2449 (2016).
[128] H. M. Jang, S. Yoo, Y. K. Choi, S. Park, and E. Kan, Bioresour. Technol. **259**, 24 (2018).
[129] T. Ai, X. Jiang, Z. Zhong, D. Li, and S. Dai, Adsorpt. Sci. Technol. **38**, 304 (2020).
[130] W. Wang, R. Kang, Y. Yin, S. Tu, and L. Ye, Chemosphere **292**, 133454 (2022).

[131] E. V. Liakos, K. Rekos, D. A. Giannakoudakis, A. C. Mitropoulos, J. Fu, and G. Z. Kyzas, Antibiotics **10**, 1 (2021).
[132] T. J. Al-Musawi, N. Mengelizadeh, M. Taghavi, S. Mohebi, and D. Balarak, Biomass Convers. Biorefinery **767**, (2021).
[133] Z. Wang, Int. J. Environ. Sci. Technol. **12**, 1923 (2015).
[134] F. Jing, M. Pan, and J. Chen, Environ. Sci. Pollut. Res. **25**, 11493 (2018).
[135] R. Guo, L. Yan, P. Rao, R. Wang, and X. Guo, Environ. Pollut. **258**, 113674 (2020).
[136] R. Zhang, L. Chen, B. Qiu, X. Sun, S. Qin, B. Wang, F. Li, L. Zhao, and Z. Zhu, Water. Air. Soil Pollut. **232**, (2021).
[137] H. Cheng, J. Zhang, Y. Chen, W. Zhang, R. Ji, Y. Song, W. Li, Y. Bian, X. Jiang, J. Xue, and J. Han, Bioresour. Technol. **346**, 126604 (2022).
[138] X. Zhang, J. Zhang, Y. She, Y. Li, H. Cheng, R. Ji, and Y. Bian, Sci. Total Environ. **846**, 157511 (2022).
[139] X. Fan, X. Wang, B. Zhao, J. Wan, J. Tang, and X. Guo, J. Environ. Chem. Eng. **10**, 107328 (2022).
[140] Z. Sun, X. Wu, K. Qu, Z. Huang, S. Liu, M. Dong, and Z. Guo, Chemosphere **259**, 127389 (2020).
[141] M. Wang, C. Jin, Q. Luo, and E. J. Kim, Ceram. Int. **46**, 18608 (2020).
[142] J. Oyim, E. Amuhaya, R. Matshitse, J. Mack, and T. Nyokong, Carbon Trends **8**, 100191 (2022).
[143] N. P. Wickramaratne, J. Xu, M. Wang, L. Zhu, L. Dai, and M. Jaroniec, Chem. Mater. **26**, 2820 (2014).
[144] L. Xu, L. Guo, G. Hu, J. Chen, X. Hu, S. Wang, W. Dai, and M. Fan, RSC Adv. **5**, 37964 (2015).
[145] D. Gu, R. Ma, Y. Zhou, F. Wang, K. Yan, Q. Liu, and J. Wang, ACS Sustain. Chem. Eng. **5**, 11105 (2017).
[146] K. Xu, Q. Pan, F. Zheng, G. Zhong, C. Wang, S. Wu, and C. Yang, Front. Chem. **7**, 1 (2019).
[147] X. Huang, L. Gou, and L. Yang, J. Alloys Compd. **786**, 91 (2019).
[148] Z. Liang, L. Zhang, H. Liu, J. Zeng, J. Zhou, H. Li, and H. Xia, Results Phys. **12**, 1984 (2019).
[149] X. Li, Y. Song, L. You, L. Gao, Y. Liu, W. Chen, and L. Mao, Ind. Eng. Chem. Res. **58**, 2933 (2019).
[150] S. Zuo, J. Gao, F. Wu, B. Yang, Y. Sun, M. Xie, X. Mi, W. Wang, Y. Liu, and J. Yan, New J. Chem. **44**, 15415 (2020).
[151] X. Ren, H. Li, J. Chen, L. Wei, A. Modak, H. Yang, and Q. Yang, Carbon N. Y. **114**, 473 (2017).
[152] Z. Zhang, X. Gao, M. Dou, J. Ji, and F. Wang, Small **13**, 1 (2017).
[153] L. Bi, S. Ci, P. Cai, H. Li, and Z. Wen, Appl. Surf. Sci. **427**, 10 (2018).
[154] B. Xue, X. Wang, Y. Feng, Z. Chen, and X. Liu, J. Energy Storage **30**, 101405 (2020).
[155] Y. Tang, Q. Chen, W. Li, X. Xie, W. Zhang, X. Zhang, H. Chai, and Y. Huang, J. Hazard. Mater. **388**, 122059 (2020).
[156] S. S. Gunasekaran, A. Gopalakrishnan, R. Subashchandrabose, and S. Badhulika, J. Energy Storage **42**, 103048 (2021).
[157] N. Li, Z. Wang, K. Zhao, Z. Shi, Z. Gu, and S. Xu, Carbon N. Y. **48**, 255 (2010).
[158] V. B. Parambhath, R. Nagar, and S. Ramaprabhu, Langmuir **28**, 7826 (2012).
[159] Y. F. Lu, S. T. Lo, J. C. Lin, W. Zhang, J. Y. Lu, F. H. Liu, C. M. Tseng, Y. H. Lee, C. Te Liang, and L. J. Li, ACS Nano **7**, 6522 (2013).
[160] H. Tian, J. Liu, K. O'Donnell, T. Liu, X. Liu, Z. Yan, S. Liu, and M. Jaroniec, J. Colloid Interface Sci. **476**, 55 (2016).
[161] S. Jia, Y. Wang, G. Xin, S. Zhou, P. Tian, and J. Zang, Electrochim. Acta **196**, 527 (2016).
[162] F. Gao, J. Qu, Z. Zhao, Z. Wang, and J. Qiu, Electrochim. Acta **190**, 1134 (2016).
[163] G. H. An, H. Kim, and H. J. Ahn, Appl. Surf. Sci. **463**, 18 (2019).
[164] H. Song, H. Li, H. Wang, J. Key, S. Ji, X. Mao, and R. Wang, Electrochim. Acta **147**, 520 (2014).
[165] Y. Zhang, L. Chen, Y. Meng, J. Xie, Y. Guo, and D. Xiao, J. Power Sources **335**, 20 (2016).
[166] M. Luo, C. Guo, X. Luo, Z. Li, Y. Qin, and W. Zhang, Int. J. Hydrogen Energy **46**, 2117 (2021).
[167] K. Zhong, M. Li, Y. Yang, H. Zhang, B. Zhang, J. Tang, J. Yan, M. Su, and Z. Yang, Appl. Energy **242**, 516 (2019).
[168] Y. K. and J. C. Minjoon Park, Jaechan Ryu, Energy Environ. Sci. **7**, 3727 (2014).
[169] L. Fang, Q. Xu, X. Zheng, W. Zhang, J. Zheng, M. Wu, and W. Wu, J. Nanoparticle Res. **18**, 1 (2016).
[170] Z. Li, H. Mi, Z. Bai, C. Ji, L. Sun, S. Gao, and J. Qiu, J. Power Sources **418**, 112 (2019).
[171] F. I. Fajarwati, M. Anugrahwati, I. Yanti, R. A. Safitri, Yeni, and E. Yuanita, IOP Conf. Ser. Mater. Sci. Eng. **599**, (2019).
[172] S. Mani and R. N. Bharagava, in *Reviews of Environmental Contamination and Toxicology*, Vol. 237 (2016), pp. 71–104.
[173] W. W. Anku, M. A. Mamo, M. A. Mamo, P. W. Penny, and P. P. Govender, in *Phenolic Compounds: Natural Sources, Importance and Applications* (2017), pp. 419–443.
[174] L. Serwecinska, Water **12**, 1 (2020).
[175] V. R. Kay, C. Chambers, and W. G. Foster, Crit. Rev. Toxicol. **43**, 200 (2013).

[176] K. V. Kumar, V. Ramamurthi, and S. Sivanesan, J. Colloid Interface Sci. **284**, 14 (2005).
[177] N. Ayawei, A. N. Ebelegi, and D. Wankasi, J. Chem. **2017**, 1 (2017).
[178] H. K. Chung, W. H. Kim, J. Park, J. Cho, T. Y. Jeong, and P. K. Park, J. Ind. Eng. Chem. **28**, 241 (2015).
[179] K. Y. Foo and B. H. Hameed, Chem. Eng. J. **156**, 2 (2010).
[180] G. W. Kajjumba, S. Emik, A. Öngen, H. K. Özcan, and S. Aydin, in *Advanced Sorption Process Applications* (2018), pp. 1–19.
[181] M. Ghasemi, N. Ghasemi, G. Zahedi, S. R. W. Alwi, M. Goodarzi, and H. Javadian, Int. J. Environ. Sci. Technol. **11**, 1835 (2014).
[182] K. L. Tan and B. H. Hameed, J. Taiwan Inst. Chem. Eng. **74**, 25 (2017).
[183] W. J. Wolf, J. Agric. Food Chem. **18**, 969 (1970).
[184] Z. He, H. Zhang, and D. C. Olk, PLoS One **10**, 1 (2015).
[185] H. N. Tran, C. K. Lee, T. V. Nguyen, and H. P. Chao, Environ. Technol. (United Kingdom) **39**, 2747 (2018).
[186] F. C. Huang, C. K. Lee, Y. L. Han, W. C. Chao, and H. P. Chao, J. Taiwan Inst. Chem. Eng. **45**, 2805 (2014).
[187] F. Wu, H. Su, K. Wang, W. K. Wong, and X. Zhu, Int. J. Nanomedicine **12**, 7375 (2017).
[188] M. H. Joula and M. Farbod, Appl. Surf. Sci. **347**, 535 (2015).
[189] M. Zaib, A. Akhtar, F. Maqsood, and T. Shahzadi, Arab. J. Sci. Eng. **46**, 437 (2021).
[190] N. A. Alarfaj and M. F. El-tohamy, Int. J. Mol. Sci. **9**, 1162 (2018).
[191] P. Nezhad-Mokhtari, N. Arsalani, M. Ghorbani, and H. Hamishehkar, J. Mater. Sci. **53**, 10679 (2018).
[192] S. Sasrimuang, O. Chuchuen, and A. Artnaseaw, Green Process. Synth. **9**, 340 (2020).
[193] Y. Xie, D. Cheng, X. Liu, and A. Han, Sensors **19**, 3169 (2019).
[194] L. K. Brar, G. Singla, and O. P. Pandey, RSC Adv. **5**, 1406 (2015).
[195] W. Si, J. Zhou, S. Zhang, S. Li, W. Xing, and S. Zhuo, Electrochim. Acta **107**, 397 (2013).
[196] Q. Ma, Y. Yu, M. Sindoro, A. G. Fane, R. Wang, and H. Zhang, Adv. Mater. **29**, 1605361 (2017).
[197] N. Veronica, P. Æ. E. Mun, P. Elizabeth, and D. Æ. J. Rene, J Nanopart Res **12**, 467 (2009).
[198] Z. L. Wang and Z. C. Kang, J. Phys. Chem. **100**, 17725 (1996).
[199] T. Wang, Y. Zhai, Y. Zhu, C. Li, and G. Zeng, Renew. Sustain. Energy Rev. **90**, 223 (2018).
[200] M. Sevilla, W. Gu, C. Falco, M. M. Titirici, A. B. Fuertes, and G. Yushin, J. Power Sources **267**, 26 (2014).
[201] C. He, K. Wang, Y. Yang, P. N. Amaniampong, and J. Y. Wang, Environ. Sci. Technol. **49**, 6872 (2015).
[202] Z. Zhang, W. Zhu, R. Wang, L. Zhang, L. Zhu, and Q. Zhang, J. Mater. Chem. A **2**, 19167 (2014).
[203] H. Qiu, L. Lv, B. C. Pan, Q. J. Zhang, W. M. Zhang, and Q. X. Zhang, J. Zhejiang Univ. Sci. A **10**, 716 (2009).
[204] H. Gong, Z. Tan, L. Zhang, and Q. Huang, Sci. Total Environ. **694**, 133728 (2019).
[205] B. Balagurumurthy, V. Srivastava, Vinit, J. Kumar, B. Biswas, R. Singh, P. Gupta, K. L. N. S. Kumar, R. Singh, and T. Bhaskar, Bioresour. Technol. **188**, 273 (2015).
[206] M. Kwiatkowski and E. Broniek, Colloids Surfaces A Physicochem. Eng. Asp. **529**, 443 (2017).
[207] Y. She, C. Zou, S. Liu, K. Wu, H. Wu, H. Ma, and R. Shi, Green Process. Synth. **10**, 189 (2021).
[208] M. Liang, J. Wang, M. Zhao, J. Cai, M. Zhang, N. Deng, B. Wang, B. Li, and K. Zhang, Mater. Res. Express **6**, 065615 (2019).
[209] D. J. Lane, E. Truong, F. Larizza, P. Chiew, R. De Nys, and P. J. Van Eyk, Energy and Fuels **32**, 4149 (2018).
[210] V. Hernndez-Montoya, J. Garca-Servin, and J. Ivn, in *Lignocellulosic Precursors Used in the Synthesis of Activated Carbon - Characterization Techniques and Applications in the Wastewater Treatment* (2012).
[211] R. Choudhary, O. P. Pandey, and L. K. Brar, Mater. Chem. Phys. **260**, 124174 (2021).
[212] H. Su, K. Wang, and W. Wong, Int. J. Nanomedicine **12**, 7375 (2017).
[213] K. Judai, N. Iguchi, and Y. Hatakeyama, J. Chem. **2016**, 1 (2016).
[214] N. J. Welham and J. S. Williams, Carbon N. Y. **36**, 1309 (1998).
[215] K. Barbera, L. Frusteri, G. Italiano, L. Spadaro, F. Frusteri, S. Perathoner, and G. Centi, Chinese J. Catal. **35**, 869 (2014).
[216] A. Şencan and M. Kiliç, J. Chem. **2015**, 1 (2015).
[217] S. Cheng, A. Huang, S. Wang, and Q. Zhang, BioResources **11**, 4006 (2016).
[218] D. M. Applin, M. R. M. Izawa, E. A. Cloutis, J. J. Gillis-davis, K. M. Pitman, T. L. Roush, A. R. Hendrix, and P. G. Lucey, Icarus **307**, 40 (2018).
[219] T. J. Bandosz and C. O. Ania, Adv. Sci. **5**, 1800293 (2018).
[220] A. Gomis-Berenguer, L. F. Velasco, I. Velo-Gala, and C. O. Ania, J. Colloid Interface Sci. **490**, 879

(2017).
[221] D. B. Schuepfer, F. Badaczewski, J. M. Guerra-Castro, D. M. Hofmann, C. Heiliger, B. Smarsly, and P. J. Klar, Carbon N. Y. **161**, 359 (2020).
[222] J. Zhang, X. Wang, G. Qi, B. Li, Z. Song, and H. Jiang, Carbon N. Y. **96**, 864 (2016).
[223] M. A. Martín-Lara, A. Piñar, A. Ligero, G. Blázquez, and M. Calero, Water **13**, 1188 (2021).
[224] Y. Deng, Y. Xie, K. Zou, and X. Ji, J. Mater. Chem. A **4**, 1144 (2015).
[225] K. Dasgupta, M. Khosravifar, S. Sawant, P. K. Adusei, S. N. Kanakaraj, J. Kasik, and V. Shanov, J. Carbon Res. **6**, 40 (2020).
[226] Z. Lin, G. H. Waller, Y. Liu, M. Liu, and C. ping Wong, Nano Energy **2**, 241 (2013).
[227] Y. Zhang, J. Wang, G. Shen, J. Duan, and S. Zhang, Front. Chem. **8**, 1 (2020).
[228] Y. Gao, Q. Yue, B. Gao, and A. Li, Sci. Total Environ. **746**, 141094 (2020).
[229] P. Thakur, in *Advanced Reservoir and Production Engineering for Coal Bed Methane* (2017), pp. 51–59.
[230] P. Tengvall, in *Comprehensive Biomaterials*, Vol. 4 (Elsevier Ltd., 2011), pp. 63–73.
[231] Q. Zhou, W. Chen, X. Jiang, H. Liu, S. Ma, and B. Wang, Sci. Rep. **10**, 1 (2020).
[232] Prateek, C. Thakur, V. C. Srivastava, and I. D. Mall, Int. J. Chem. React. Eng. **11**, 595 (2013).
[233] V. Fierro, V. Torné-Fernández, D. Montané, and A. Celzard, Microporous Mesoporous Mater. **111**, 276 (2008).
[234] R. Choudhary, O. P. Pandey, and L. K. Brar, Mater. Chem. Phys. **284**, 126037 (2022).
[235] X. L. Su, S. Jiang, G. P. Zheng, X. C. Zheng, J. H. Yang, and Z. Y. Liu, J. Mater. Sci. **53**, 9191 (2018).
[236] M. Polovina, B. Babić, B. Kaluderović, and A. Dekanski, Carbon N. Y. **35**, 1047 (1997).
[237] R. Lafi, I. Montasser, and A. Hafiane, Adsorpt. Sci. Technol. **37**, 160 (2019).
[238] R. Chen, L. Li, Z. Liu, M. Lu, C. Wang, H. Li, W. Ma, and S. Wang, J. Air Waste Manag. Assoc. **67**, 713 (2017).
[239] A. Kumar, A. Ganguly, and P. Papakonstantinou, J. Phys. Condens. Matter **24**, 235503 (2012).
[240] D. Shrestha and A. R. Nyachhyon, Heliyon **7**, e07917 (2021).
[241] D. Lozano-Castelló, J. M. Calo, D. Cazorla-Amorós, and A. Linares-Solano, Carbon N. Y. **45**, 2529 (2007).
[242] Z. Lendzion-Bieluń, Czekajło, D. Sibera, D. Moszyński, J. Sreńscek-Nazzal, A. W. Morawski, R. J. Wrobel, B. Michalkiewicz, W. Arabczyk, and U. Narkiewicz, Adsorpt. Sci. Technol. **36**, 478 (2018).
[243] J. Ma, F. Yu, L. Zhou, L. Jin, M. Yang, J. Luan, Y. Tang, H. Fan, Z. Yuan, and J. Chen, ACS Appl. Mater. Interfaces **4**, 5749 (2012).
[244] L. Wang, G. Chen, C. Ling, J. Zhang, and K. Szerlag, Environ. Prog. Sustain. Energy **36**, 676 (2017).
[245] E. S. I. El-Shafey, H. Al-Lawati, and A. S. Al-Sumri, J. Environ. Sci. (China) **24**, 1579 (2012).
[246] S. Shyam, J. Arun, K. P. Gopinath, G. Ribhu, M. Ashish, and S. Ajay, Chemosphere **286**, 131490 (2022).
[247] S. Singh, A. K. Prajapati, J. P. Chakraborty, and M. K. Mondal, Biomass Convers. Biorefinery **423**, (2021).
[248] A. Öztürk and A. Bayrakçeken Yurtcan, J. Solid State Chem. **296**, 121972 (2021).
[249] D. Díez, A. Urueña, R. Piñero, A. Barrio, and T. Tamminen, Processes **8**, 1 (2020).
[250] Y. K. Choi, T. R. Choi, R. Gurav, S. K. Bhatia, Y. L. Park, H. J. Kim, E. Kan, and Y. H. Yang, Sci. Total Environ. **710**, 136282 (2020).
[251] M. M. Nassarl and G. D. M. MacKay, Wood F~ber Sci. **16**, 441 (1984).
[252] M. Waqas, A. S. Aburiazaiza, R. Miandad, M. Rehan, M. A. Barakat, and A. S. Nizami, J. Clean. Prod. **188**, 477 (2018).
[253] A. Selvarajoo and D. Oochit, Mater. Sci. Energy Technol. **3**, 575 (2020).
[254] R. Chatterjee, B. Sajjadi, W. Y. Chen, D. L. Mattern, N. Hammer, V. Raman, and A. Dorris, Front. Energy Res. **8**, 1 (2020).
[255] Y. Gokce and Z. Aktas, Appl. Surf. Sci. **313**, 352 (2014).
[256] A. Y. Elnour, A. A. Alghyamah, H. M. Shaikh, A. M. Poulose, S. M. Al-Zahrani, A. Anis, and M. I. Al-Wabel, Appl. Sci. **9**, 7 (2019).
[257] J. Eshun, L. Wang, E. Ansah, A. Shahbazi, K. Schimmel, V. Kabadi, and S. Aravamudhan, J. Energy Inst. **92**, 82 (2019).
[258] C. Collett, O. Mašek, N. Razali, and J. McGregor, Catalysts **10**, 1 (2020).
[259] T. W. Osborn, J. Agric. Food Chem. **25**, 229 (1977).
[260] C. Peiris, O. Nayanathara, C. M. Navarathna, Y. Jayawardhana, S. Nawalage, G. Burk, A. G. Karunanayake, S. B. Madduri, M. Vithanage, M. N. Kaumal, T. E. Mlsna, E. B. Hassan, S. Abeysundara, F. Ferez, and S. R. Gunatilake, RSC Adv. **9**, 17612 (2019).
[261] M. Ayiania, A. J. R. Hensley, K. Groden, M. Garcia-Perez, and J. S. McEwen, Carbon N. Y. **152**, 715 (2019).

[262] L. Qi, X. Tang, Z. Wang, and X. Peng, Int. J. Min. Sci. Technol. **27**, 371 (2017).
[263] D. H. Nguyen, H. N. Tran, H. P. Chao, and C. C. Lin, Adsorpt. Sci. Technol. **37**, 607 (2019).
[264] S. Banerjee and M. C. Chattopadhyaya, Arab. J. Chem. **10**, S1629 (2017).
[265] A. Gupta, R. Kour, and L. K. Brar, SN Appl. Sci. **1**, 1 (2019).
[266] X. Liu, W. Y. Huang, Q. Zhou, X. R. Chen, K. Yang, D. Li, and D. D. Dionysiou, Rare Met. **40**, 1086 (2021).
[267] A. Gupta, M. Mittal, M. K. Singh, and S. L. Suib, Sci. Rep. **8**, 13597 (2018).